The QCD phase diagram within effective models

Thorsten Steinert

Dissertation

Institut für Theoretische Physik
Fachbereich 07 Mathematik und Informatik,
Physik, Geographie
Justus-Liebig-Universität Giessen

Contents

Abstract

We study the QCD phase diagram using effective theories with the respective degrees of freedom for the different phases of QCD. In the deconfined phase we employ the dynamical quasiparticle model (DQPM), that is able to describe the dynamics of hot QCD at vanishing chemical potential. We extend to model to momentum-dependent selfenergies in order to match the correct perturbative limit of the propagators at high momenta. Within this generalized quasiparticle approach, denoted as DQPM*, we can simultaneously reproduce the lattice QCD (lQCD) equation of state (EoS) and baryon number susceptibility. Using thermodynamic consistency we extend the model to finite baryon chemical potential exceeding the application range of lQCD by far. We give predictions for the EoS and the most important transport coefficients. In the confined phase the medium is composed of hadrons. At large temperatures they interact predominantly by resonant scatterings, which can be well described in terms of a hadron-resonance gas (HRG). At large chemical potential and low temperature the nature of the interaction changes from resonant scatterings to meson exchange as described by relativistic mean-field theories. We combine both approaches to get an interacting HRG (IHRG), that is compatible to the lQCD EoS ($\mu \approx 0, T > 0$) and the nuclear EoS ($T \approx 0, \mu > 0$). For a complete description of the phase diagram we have to switch between the partonic and the hadronic model. In accordance with heavy-ion simulations we define the transition at lines of constant thermodynamics. The resulting EoS is valid up to $\mu_B \approx 450$ MeV. We perform heavy-ion simulations with the PHSD transport approach and determine the region in the QCD phase diagram that is probed by different collision energies. The EoS constructed from the DQPM* and the IHRG can be used to describe collisions at low beam energies down to $\sqrt{s} \approx 7.7$ GeV. Using simulations at even lower beam energies we determine the conditions necessary for the discovery of the critical point in the QCD phase diagram.

Abstract

Wir untersuchen das QCD-Phasendiagramm unter Verwendung verschiedener Effektiver Theorien. Wir beschreiben die deconfinierte Phase mit einem partonischen Quasiteilchenmodell, dem DQPM, das erfolgreich die Dynamik heißer QCD-Materie reproduzieren kann. Wir erweitern das Modell auf impulsabhängige Selbstenergien um den korrekten störungstheoretischen Grenzwert der Propagatoren zu gewährleisten. Mit diesem generalisierten Quasiteilchenmodell, dem DQPM*, können wir gleichzeitig die von Gitter-QCD Rechnungen prognostizierte Zustandsgleichung sowie die Suszeptibilität beschreiben. Wir nutzen thermodynamische Konsistenz und erweitern das Modell auf endliche chemische Potentiale, die die Anwendbarkeit von Gitter-QCD Rechnungen bei weitem übersteigen, und bestimmen die Zustandsgleichung sowie die wichtigsten Transportkoeffizienten. In der confinierten Phase besteht die Materie nicht aus Partonen sondern aus Hadronen. Bei großen Temperaturen wechselwirken die Hadronen hauptsächlich durch resonante Streuung miteinander. Dies kann durch ein simples Hadron-Resonanz Gas (HRG) beschrieben werden. Bei kleinen Temperaturen und großen chemischen Potentialen dominiert der Austausch von Mesonen die Wechselwirkung. Dieser Mechanismus wird in relativistischen Modellen für unendlich ausgedehnte Kernmaterie beschrieben. Wir kombinieren die beiden Modelle und definieren ein wechselwirkendes HRG (IHRG), das mit der Zustandsgleichung von Gitter-QCD-Rechnungen ($\mu \approx 0, T > 0$) sowie der Zustandsgleichung von unendlich ausgedehnter Kernmaterie ($T \approx 0, \mu > 0$) übereinstimmt. Für eine vollständige Beschreibung des QCD-Phasendiagramms müssen wir an der Phasengrenze von dem partonischen auf das hadronische Modell wechseln. Wir nutzen Erkenntnisse aus Simulationen von Schwerionenkollisionen und definieren die Phasengrenze bei konstanten thermodynamischen Bedingungen. Die resultierende Zustandsgleichung ist bis zu einem Baryonchemischen Potential von $\mu_B \approx 450$ MeV gültig. Wir simulieren Schwerionenkollisionen mit dem PHSD Transportmodell und untersuchen die Regionen des QCD Phasendiagramms die in tatsächlichen Kollisionen zugänglich sind. Die durch das DQPM* und das IHRG definierte Zustandsgleichung kann für Kollisionen mit Schwerpunktsenergien von über $\sqrt{s} = 7.7$ GeV verwendet werden. Wir nutzen Simulationen bei noch geringeren Energien und untersuchen die Bedingungen die nötig sind um den kritischen Punkt des QCD Phasendiagramms nachzuweisen.

1 Introduction

The different phases of matter and their phase diagrams are among the most interesting and challenging fields of modern physics. Phase transition are important for many different phenomena from ultra-cold atoms and solid-states to nuclear matter and cosmology. Especially the early universe features several phase transitions that are connected to the most fundamental aspects of physics like the separation of the four fundamental forces of nature or the decoupling of photons. The conditions in the early universe can be recreated in ultra-relativistic heavy-ion collisions. The matter in the collisions gets compressed and heated up until it reaches temperatures similar to the first few microseconds after the big bang. Heavy-ion collisions probe the properties of quantum chromodynamics (QCD), the theory of the strong interaction, and are the only possible way to create hot and dense QCD matter and to investigate the phase diagram of QCD.

Heavy-ion collisions -performed in the early 2000s at the Relativistic Heavy Ion Collider (RHIC)- reached collision energies not possible in previous heavy-ion experiments. The created matter showed properties never seen at lower beam energies and challenged the current understanding of heavy-ion physics [1, 2, 3, 4]. It was assumed that the collisions created a long predicted state of matter where quarks and gluons have been liberated from confinement [5, 6]. This new phase should appear once the density becomes large enough that individual hadrons overlap each other and the quarks -usually confined in hadrons- could then move freely in the hot and dense medium. This state of matter is called a Quark-Gluon Plasma (QGP).

The QGP can not be studied directly and exists only for a short period of time as an intermediate state in the heavy-ion collision. Once the fireball expands and the density decreases, individual hadrons will form again. Nevertheless, the existence of the QGP has consequences for the dynamics of the medium and will influence the final particle spectra. Possible signals are anomalies in the flow [7, 8, 9, 10], J/Ψ suppression [11], jet quenching [12, 13, 14] and variations in the strangeness production [15, 16, 17]. All these are indirect signals that get affected by the interactions in the hadronic medium. Further important signals are electromagnetic probes like photon and dilepton radiation, because they do practically not interact with the surrounding medium and leave the collision undisturbed [18, 19, 20, 21].

Originally it was believed that the QGP resembles a weakly interacting gas of massless partons, however, the matter created at RHIC, and later also at the Large Hadron Collider (LHC) at CERN, showed properties of a fluid. Indeed, relativistic hydrodynamics has been successful in describing the experimental data [22]. Moreover, viscous hydrodynamics found an almost vanishing ratio of shear viscosity over entropy density η/s close to the theoretical limit $(\eta/s)_{KSS} = 1/4\pi$ [23, 24, 25], which indicates that the QGP is an almost perfect fluid and that the partonic medium is much stronger correlated than ordinary hadronic matter.

The strong interactions provide a big challenge for transport simulations of heavy-ion collisions which have to incorporate the partonic phase to successfully describe the ultra-relativistic collisions. Default hadronic transport models, traditionally based on the Boltzmann transport equation, are not suited for such strongly correlated systems [26, 27, 28, 29]. The QGP phase has to be described by more elaborate transport descriptions [30, 31] or in terms of relativistic hydrodynamics [32, 33, 34]. Both approaches require an underlying equation of state, which serves as direct input into the hydrodynamic simulations while transport approaches need it to define the dynamics of the system.

The calculation of the equation of state for a strongly interacting system is not a trivial task. Perturbative QCD calculations cover only the most extreme temperatures exceeding even the highest beam energies reachable at the LHC while effective models may miss important aspects of QCD. The most reliable source for the equation of state are lattice gauge theories and their application to QCD (lQCD). They provide non-perturbative information from first principle calculations and are the only approach that can solve full QCD. Simulations employing dynamical quarks are numerically very costly and become even more involved if the quark masses are small; only recently calculations with physical quark masses became feasible [35, 36]. At low temperatures the equation of state is well reproduced by a gas of non-interacting hadrons, but as the temperature increases further it shows a steep rise which indicates a change of the degrees of freedom and a transition from hadronic matter to the QGP. This transition is actually no real phase transition, but a smooth crossover at roughly $T_c \approx 155$ MeV at vanishing chemical potential μ [37, 38, 39].

A major drawback of lQCD is its limitation to vanishing chemical potential. However, one can access moderate chemical potentials in terms of Taylor expansions with the expansion coefficients calculated at $\mu = 0$. Currently these coefficients are known up to the 6th order [40, 41, 42] which limits the applicability of the Taylor expansion to $\mu_B/T < 3$. In heavy-ion collisions the realized baryon chemical potential μ_B depends on the available energy in the fireball which gets converted into additional particles that decrease the net-baryon density in the system. The net-baryon densities at RHIC and LHC are almost vanishing and one probes -in good approximation- a system with vanishing chemical potential μ_B where lQCD gives robust results.

With decreasing available energy less particles are produced and the overall net-baryon density increases. If the baryon chemical potential exceeds $\mu_B/T \approx 3$, the conditions can no longer be described by lQCD and one has to use other approaches like effective theories that share the properties and symmetries of full QCD, but allow for calculations at finite chemical potentials. Examples are the Nambu Jona-Lasinio (NJL) [43, 44, 45, 46, 47], Quark-Meson (QM) [48, 49, 50, 51] and chiral sigma models [52, 53, 54, 55] as well as more sophisticated approaches like Dyson-Schwinger Equations [56, 57, 58, 59, 60] and the Functional Renormalization Group [61, 62, 63, 64, 65, 66, 67]. Plenty of these models predict a change in the QCD phase transition to a real first-order transition at large baryon chemical potentials, which implies a critical point in the QCD phase diagram. The possible existence of a critical point renewed the interest in heavy-ion collisions at intermediate beam energies, that probe the QCD phase diagram at large baryon chemical potentials. First experiments have been performed within the scope of the beam-energy scan program (BES) at RHIC [68, 69, 70]. This program performs heavy-ion collisions at varying beam energy which scan the QCD phase boundary at large μ_B. However, the first phase of the BES reached only moderate baryon chemical potentials of $\mu_B < 450$ MeV that are still described by lQCD [71]. Since neither the lQCD predictions nor the experimental data showed signals of a first-order phase transition the critical point has to be located at even larger baryon chemical potentials ($\mu_B > 450$ MeV). These will be probed at even lower beam energies in the second phase of the BES program [72, 73] and at the future facilities FAIR (Facility for Antiproton and Ion Research) [74] and NICA (Nuclotron-based Ion Collider fAcility) [75].

Without lQCD predictions the only theoretical guidance at large baryon chemical potentials comes from effective theories and functional methods. These approaches require certain approximations and do not describe full QCD. Nevertheless, they are applicable to the whole QCD phase diagram. The aim of this thesis is to investigate the equation of state of hot and dense QCD matter using effective models with special emphasis on finite baryon chemical potentials. A substantial problem in the description of QCD is the change of the degrees of freedom with increasing net-baryon or energy density. Most approaches use either hadrons or partons and are not applicable to the other phase. Some approaches, for example Quark-meson models, employ both, but do not describe a dynamical hadron-parton transition [50, 76, 77]. Instead they incorporate quarks and meson as individual degrees of freedom and neglect baryons, which is not justified at large baryon chemical potentials. We will use a different strategy and describe each phase with their respective degrees of freedom, however, we use the equation of state as predicted by lQCD calculations as a guideline for defining the two approaches. This ensures that the hadronic and the partonic model share the same equation of state in the vicinity of the phase transition.

We describe the partonic phase with the Dynamical QuasiParticle Model (DQPM) which treats quarks and gluons as quasiparticles with medium-dependent complex selfenergies and Breit-Wigner spectral functions [78, 79]. The imaginary parts of the selfenergies encode scattering effects that go beyond the mean-field level considered in ordinary quasiparticle models [80, 81, 82, 83]. The DQPM can not only describe the QCD equation of state, it reproduces also the correct behavior of the most important transport coefficients [84]. This ensures that the model is compatible with the bulk properties of partonic matter and reproduces also the correct dynamics in a partonic medium. However, quasiparticle models so far underestimate the equation of state at finite baryon chemical potential [82]. We here extend the DQPM to include momentum-dependent selfenergies that will ensure the correct perturbative limit of the propagators. Within this generalized quasiparticle model, denoted as DQPM*, we can for the first time describe simultaneously the lQCD equation of state and baryon number susceptibility in a single quasiparticle approach [85, 86]. This enables us to apply the DQPM* also to finite baryon chemical potential. We will use thermodynamic consistency to control the extension to higher chemical potentials.

The most common ansatz for hadronic thermodynamics is a gas of non-interacting hadrons. Following the work of Dashen, Ma and Bernstein attractive interactions between the hadrons can be described by the introduction of additional resonances as non-interacting particles [87]. Comparisons with lQCD results showed that this Hadron-Resonance Gas (HRG) can indeed reproduce the equation of state at low temperatures [88, 89, 90, 91]. A shortcoming of the model is the neglect of repulsive interactions. This is incompatible with the nuclear equation of state (at low temperatures) that requires a precise combination of attractive and repulsive interactions to ensure stable nuclear matter [92, 93]. The interactions in nuclear matter are mediated by meson exchange and not by the formation of resonances. We extend a model based on interacting nucleons to finite temperatures and similar to the HRG include the most important resonances as non-interacting particles, but neglect experimentally not well established states. The effects of these resonances are absorbed into the attractive interactions mediated by the scalar σ-meson. At large baryon chemical potentials this picture is indeed physically motivated while at large temperatures one has to interpret it as an attractive mean-field potential. This defines an interacting HRG (IHRG), which is a mean-field approach where the effects of the interactions are described by (real valued) scalar and vector selfenergies in the propagators. This is justified since hadronic matter is not as strongly correlated as partonic matter and the imaginary parts of the selfenergies are much smaller than in the DQPM. The interactions in a hadronic system can be deduced from actual measurements of hadronic cross sections [94, 95, 96, 97, 98, 99], that fix the dynamics of hadronic matter in accordance with experimental data and one can omit the comparison with transport coefficients that are essential in partonic models.

This work is organised as follows: In Sec. 2 we introduce the basics of many-body theory with a focus on the equilibrium state. In Sec. 3 we discuss the DQPM and present its extension to momentum-dependent selfenergies and to finite chemical potentials. The DQPM describes the thermodynamics of QCD, but can not access the order parameters of the QCD phase transition. We discuss the latter in Sec. 4 in terms of the effective Nambu Jona-Lasinio model (NJL). Both, the DQPM and the NJL use partonic degrees of freedom and are not suited to describe QCD at low temperatures. In Sec. 5 we investigate hadronic thermodynamics in terms of the HRG and relativistic mean-field theories. By combining both approaches we define the IHRG as an extension of the standard HRG that describes also the nuclear equation of state at low temperatures. In Sec. 6 we apply the DQPM/DQPM* and the IHRG to the whole QCD phase diagram and discuss the hadron-parton transition of QCD. In order to explore the region of the QCD phase diagram that is probed in central Au+Au (Pb+Pb) collisions for different invariant energies we employ PHSD transport calculations and extract the temperatures and the baryon chemical potentials in the collisions and evaluate the relative fraction of partonic and hadronic matter as a function of time. We will summarize this work in Sec. 7.

---

[1] We use natural units $\hbar = c = k_B = 1$ throughout this thesis.

2 Overview of many-body physics

We investigate in this thesis in particular equilibrium properties of hot and dense QCD matter and give in this section a short introduction into the most important concepts of thermodynamics, many-body theory in and out-of equilibrium and the QCD phase diagram. This introduction is by far not complete and will be extended in the subsequent chapters when necessary.

2.1 Thermodynamic relations

For a many-body system in thermodynamic equilibrium the exact state of the system is not important. It is easier to described it by its energy, particle number and volume. Theoretically this is done by introducing an ensemble of microstates that all belong to the same macrostate defined by the macroscopic properties of the system. The real system is then realized by one of the microstates in the ensemble.

The three most important thermodynamic ensembles are the microcanonical, the canonical and the grand-canonical ensemble. The microcanonical ensemble describes a system with exactly known energy, particle number and volume. Popular examples are spin systems. In a canonical ensemble the energy is not known precisely, just its average value. The real energy of the system may fluctuate due to contact with a different ensemble (bath), but particle number and volume stay fixed. The ideal gas is described by a canonical ensemble and its average energy is determined by the particle number N and the temperature T of the bath,

$$U = \langle E \rangle = \frac{3}{2} N T. \tag{2.1}$$

The temperature is related to the parameter $\beta = T^{-1}$ that has to be introduced as a Lagrange parameter and ensures that the microstates have different energies but give the correct average energy of the macrosystem. The Lagrange parameter β is in terms of statistical mechanics the more fundamental quantity.

The third ensemble is the grand-canonical ensemble which is used to describe systems where neither the energy nor the particle number are fixed and both are only known by their averages. In the description of grand-canonical ensembles a new Lagrange parameter α emerges. It has to be introduced in the same way as β to ensure that the average particle number of the macrostate is fixed. Instead of α one commonly uses the chemical potential $\mu = -\alpha/\beta$. QCD matter in thermodynamic equilibrium is usually treated as a grand-canonical system with fluctuating gluon and quark densities in a fixed volume.

If the energy is only know by average, the system is described by the temperature; if the particle number is only known by average, it is described by the chemical potential. A microcanonical system depends on the energy, the particle number and the volume, a canonical system on the temperature, the particle number and the volume and a grand-canonical system on the temperature, the chemical potential and the volume. If one would additional vary the volume one has to introduce an additional Lagrange parameter that is connected to the pressure of the system. Such a system with varying values of energy, particle number and volume depends on the temperature, the chemical potential and the pressure. The quantities that describe the ensembles are called the natural variables.

In a relativistic theory the chemical potential is no longer coupled to the particle number but to the net-fermion number, i.e. the difference between the fermion and antifermion number. In our everyday world without antimatter this becomes the particle number. Note that the number of bosons is not conserved and, as a consequence, there is no boson number chemical potential. Generally every conserved charge introduces an additional chemical potential. In QCD thermodynamics the relevant charges are the baryon number, the electric charge and the strangeness. The chemical potential μ_i for a given particle reads

$$\mu_i = B_i \; \mu_B + Q_i \; \mu_Q + S_i \; \mu_S, \tag{2.2}$$

where B_i, Q_i and S_i are the baryon number, the electric charge and the strangeness of the particle and μ_B, μ_Q and μ_S the corresponding chemical potentials. Depending on the physical situation the conserved charges can be either known exactly or by average, which requires a separate treatment of each charge. In QCD thermodynamics this emerges from the strangeness conservation of the strong interaction. While the light quarks are treated in a grand-canonical way, the strange quarks are sometimes treated canonically with their particle number fixed to $N_s = 0$.

The probability of a microstate in a canonical or grand-canonical ensemble is given by

$$p_{c,i} = \frac{1}{Z_c} \exp(-\beta E_i), \qquad\qquad p_{g,i} = \frac{1}{Z_g} \exp(-\beta E_i - \alpha N_i), \tag{2.3}$$

where E_i is the total energy of the microstate and N_i the particle number. In a microcanonical ensemble all microstates have the same probability. The normalization constants in Eq. (2.3) are the partition sums of the canonical and the grand-canonical ensemble,

$$Z_c = \sum_i \exp(-\beta E_i), \qquad\qquad Z_g = \sum_i \exp(-\beta E_i - \alpha N_i). \tag{2.4}$$

The sums run over all possible microstates and have to be interpreted either as a summation over discrete quantum states or as an integration over continuous variables or even fields. From the probabilities p_i one can determine the entropy S of the ensembles,

$$S = -\sum_i p_i \ln p_i, \tag{2.5}$$

which can be expressed as a function of the partition sums,

$$S_c = \ln Z_c - \beta \frac{\partial}{\partial \beta} \ln Z_c, \qquad S_g = \ln Z_g - \beta \frac{\partial}{\partial \beta} \ln Z_g - \alpha \frac{\partial}{\partial \alpha} Z_g. \tag{2.6}$$

By rewriting the entropy one can derive the thermodynamic potential, a function of the natural variables of the ensemble from which all other thermodynamic quantities follow by differentiation. The canonical potential is called the free energy F and is a function of the temperature T, particle number N and the volume V, the grand-canonical potential Ω is a function of the temperature T, the chemical potential μ and the volume V. The thermodynamic potentials are always obtained from the logarithm of the partition sums [2],

$$F = -T \ln Z_c = U - TS, \tag{2.7}$$

$$\Omega = -T \ln Z_g = E - TS - \mu N. \tag{2.8}$$

By inserting the thermodynamic definition of the energy

$$E = TS - PV + \mu N \tag{2.9}$$

into the grand-canonical potential one finds the useful relation

$$\Omega = -PV \qquad \text{or} \qquad P = -\frac{\Omega}{V}. \tag{2.10}$$

More important than the actual values of the thermodynamic potentials are their differential forms,

$$dF = -SdT - PdV + \mu dN, \tag{2.11}$$

$$d\Omega = -SdT - PdV - Nd\mu. \tag{2.12}$$

It is important to note, that no other variables are allowed to appear in Eqs. (2.11) and (2.12). That means if a thermodynamic potential depends on an additional function, the derivative with respect to that function has to vanish to preserve the thermodynamic consistency. From the differential forms of the potentials one can read the thermodynamic relations for a canonical

$$\left.\frac{dF}{dT}\right|_{V,N} = -S, \qquad \left.\frac{dF}{dV}\right|_{N,T} = -P, \qquad \left.\frac{dF}{dN}\right|_{T,V} = \mu \tag{2.13}$$

and a grand-canonical system

$$\left.\frac{d\Omega}{dT}\right|_{V,\mu} = -S, \qquad \left.\frac{d\Omega}{dV}\right|_{\mu,T} = -P, \qquad \left.\frac{d\Omega}{d\mu}\right|_{T,V} = -N. \tag{2.14}$$

---

[2] In the grand-canonical ensemble the average energy is abbreviated as E, while in the canonical ensemble it is referred to as the internal energy U. However, both describe the same physical quantity.

The canonical and the grand-canonical ensembles seem equivalent for vanishing particle number, but this is not the case. The average particle number $\langle N \rangle$ may vanish in the grand-canonical ensemble, but its fluctuations are still finite

$$\langle N^2 \rangle - \langle N \rangle^2 \neq 0. \tag{2.15}$$

If the thermodynamic potentials have continuous second derivatives it follows from Schwarz theorem that one can commute the order of the differentials. This leads to a series of thermodynamic relations known as Maxwell relations. Most important for this thesis is the relation between the entropy and the particle number in the grand-canonical framework,

$$\frac{\partial^2 \Omega}{\partial T \partial \mu} = \frac{\partial^2 \Omega}{\partial \mu \partial T} = \frac{\partial S}{\partial \mu} = \frac{\partial N}{\partial T}. \tag{2.16}$$

While all real systems take place in a finite volume it is theoretically easier to work within an infinite volume. This special case is called the thermodynamic limit. We reach it by taking the volume to infinity while simultaneously increasing the energy and the particle number, keeping the energy and particle density as well as the density of the thermodynamic potential fixed:

$$V \to \infty, \quad \Omega \to \infty, \qquad \frac{\Omega}{V} = \text{const.} \tag{2.17}$$

The energy E and particle number N become meaningless in this limit and the relevant quantities are now their densities. To get reasonable quantities we have to divide all formulae by the volume V. Following Eqs. (2.10) and (2.12) we get $P = -\Omega/V$,

$$\frac{dP}{dT} = S/V = s \tag{2.18}$$

and

$$\frac{dP}{d\mu} = N/V = n, \tag{2.19}$$

that hold for grand-canonical systems in an infinite volume. We also have to divide the Maxwell relation (2.16) by the volume and get

$$\frac{\partial s}{\partial \mu} = \frac{\partial n}{\partial T}. \tag{2.20}$$

The energy density follows from Eq. (2.9) and is given by

$$\epsilon = E/V = (TS - PV + \mu N)/V = Ts + \mu n - P. \tag{2.21}$$

Every equilibrium theory that we discuss in this thesis is calculated in the thermodynamic limit. We will therefore no longer differentiate between the density of the potential and the potential itself. Our goal is always to derive the thermodynamic potential, i.e. the negative pressure $(-P)$. We can then apply the relations (2.18), (2.19) and (2.21) and calculate the thermodynamic quantities of the system.

2.2 Systems in equilibrium

After establishing the basic thermodynamic relations we have to answer the question how to calculate the thermodynamic potential for a given theory. For quantum field theories it is common nowadays to use the path integral formalism, see Refs. [100, 101] for an introduction. One defines a generating functional

$$Z' = N \int \mathcal{D}\bar{\Psi}\mathcal{D}\Psi\mathcal{D}\phi \;\exp\left(iS\right) = N \int \mathcal{D}\bar{\Psi}\mathcal{D}\Psi\mathcal{D}\phi \;\exp\left(i \int d^4x \;\mathcal{L}(\bar{\Psi}, \Psi, \phi)\right), \quad (2.22)$$

where S is the action defined by the Lagrangian $\mathcal{L}$ of the theory and N a normalization constant, that we drop from here on. $\mathcal{D}\bar{\Psi}\mathcal{D}\Psi$ stands for a functional integration over all possible paths of the fermion and the antifermion fields while $\mathcal{D}\phi$ is the functional integration over all possible paths of the bosonic fields. In case of gauge theories the bosonic integration includes also the gauge fields. The functional integrations have to be performed for all fields appearing in the Lagrangian. Green's functions, that are the correlation functions of the theory, can be calculated from the generating functional by means of functional derivatives.

Rotating the time integration of the Lagrangian into the complex plane by the substitution $\tau = it$ (Wick rotation) one finds that the generating functional is equal to the partition function of statistical mechanics [100, 102],

$$Z = \int \mathcal{D}\bar{\Psi}\mathcal{D}\Psi\mathcal{D}\phi \;\exp\left(\int_0^\beta d\tau \int d^3x \;\left(\mathcal{L} + \mu \;\Psi^\dagger\Psi\right)\right). \quad (2.23)$$

The temperature is introduced via the inverse parameter $\beta = 1/T$ in the upper integration limit. Thermal Green's functions fulfill certain boundary conditions after the Wick rotation, denoted as Kubo-Martin-Schwinger relations, that turn the infinite integration finite [103, 104]. In case of the grand-canonical partition function one has to introduce a chemical potential μ for every conserved charge in the system. Formula (2.23) connects the underlying dynamics of the theory, defined by the Lagrangian $\mathcal{L}$, with the thermodynamic properties. By taking the logarithm of the partition function one obtains the thermodynamic potential from which all other quantities follow. The generating functional Z' is defined even out-of equilibrium, but the rotation to the imaginary time axis defines Z only for systems in thermodynamic equilibrium [105, 106].

In general it is not possible to evaluate the partition function (2.23) and to access the equation of state. However, there are some cases where the path integral can be solved analytically. The most relevant ones are for non-interacting systems of fermions or bosons. The Lagrangian of free scalar bosons of mass m reads

$$\mathcal{L} = \frac{1}{2}\partial_\mu\phi \;\partial^\mu\phi - \frac{1}{2}m^2\phi^2 \quad (2.24)$$

and the Lagrangian of free spin-1/2 fermions (with mass m) reads

$$\mathcal{L} = \bar{\Psi}\left(i\gamma_\mu\partial^\mu - m\right)\Psi, \quad (2.25)$$

with ϕ denoting the boson field and Ψ the fermion spinor, respectively. The bosonic field ϕ is a scalar that fulfills the Klein-Gordon equation and the fermionic fields Ψ and $\bar{\Psi}$ are Dirac spinors that fulfill the Dirac equation. The four components of Ψ and $\bar{\Psi}$ describe fermions and antifermions with spin 1/2 or spin −1/2. The Dirac matrices γ_μ are 4×4 matrices in spinor space that fulfill the Dirac algebra $\{\gamma^\mu, \gamma^\nu\} = 2g^{\mu\nu}\mathbb{1}_4$ with the Minkowski metric $g^{\mu\nu} = (+ - - -)$.

We will not demonstrate the explicit evaluation of the path integral, for this we refer to Ref. [107], however, we want to emphasize an important intermediate result, i.e. the partition function in terms of the free propagators,

$$\ln Z_B^0 = -\frac{1}{2}\mathrm{Tr}\ln D_0^{-1}, \qquad \ln Z_F^0 = \mathrm{Tr}\ln S_0^{-1}, \tag{2.26}$$

with the free bosonic propagator D_0 and the free fermionic propagator S_0,

$$D_0 = \frac{-1}{p^2 - m^2}, \qquad S_0 = \frac{-1}{\gamma_\mu p^\mu - m} = -\frac{\gamma_\mu p^\mu + m}{p^2 - m^2}. \tag{2.27}$$

The bosonic propagator D_0 is a scalar, the fermionic propagator S_0 is a matrix in spinor space.

The thermodynamic potential for a non-interacting gas of bosons is given by

$$\Omega_0/V = -\frac{T}{V}\ln Z_B^0 = \int \frac{d^3p}{(2\pi)^3}\left[\frac{1}{2}\omega_p + T\ln\left(1 - e^{-\omega_p/T}\right)\right]. \tag{2.28}$$

The first part of the expression (2.28) is divergent but independent from the temperature T and the chemical potential μ. It will vanish when taking any derivatives and one may drop it.

The thermodynamic potential for a non-interacting gas of fermions is given by

$$\begin{aligned}\Omega_0/V = -\frac{T}{V}\ln Z_F^0 = 2\int \frac{d^3p}{(2\pi)^3}\Big[&-\omega_p - T\ln\left(1 + e^{-(\omega_p-\mu)/T}\right) \\ &-T\ln\left(1 + e^{-(\omega_p+\mu)/T}\right)\Big],\end{aligned} \tag{2.29}$$

where we again get a divergent but constant term that we may drop. The factor of two reflects the two spin states of the spin-1/2 fermions. The energy $\omega(\mathbf{p}) = \omega_p$ of the bosons and fermions is given by the dispersion relation for relativistic particles $\omega_p^2 = \mathbf{p}^2 + m^2$, respectively, $\omega_p = \sqrt{\mathbf{p}^2 + m^2}$.

We will now use the thermodynamic potentials for the non-interacting theories to derive the other thermodynamic quantities. We start with the pressure that is identical to the negative potential (2.10). The pressure -without the divergent parts- for a single particle species (without degeneracy) in a unified expression is given by,

$$P = \mp\, T\int \frac{d^3p}{(2\pi)^3}\ln\left(1 \mp \exp\left(-\frac{\omega_p - \mu}{T}\right)\right), \tag{2.30}$$

where the upper/lower sign stands for bosons/fermions. To get the pressure for a gas of bosons one has to omit the chemical potential while for a gas of fermions one has to

add the pressure for negative chemical potentials to account for the antifermions. The entropy density s and the particle density n follow from the pressure by the relations (2.18) and (2.19), the energy density follows from Eq. (2.21).
Another quantity of interest is the "interaction measure" I, which is an indicator for the interaction strength of the system,

$$I = \epsilon - 3P. \tag{2.31}$$

Another name of the "interaction measure" is "trace anomaly" [3]. It is equal to the trace of the energy momentum tensor, that should vanish for an ideal fluid, but has a finite value for QCD. For zero chemical potential it can be written as $I = Ts - 4P$ and fulfills the relation

$$\frac{\partial}{\partial T}\left(\frac{P}{T^4}\right) = \frac{s}{T^4} - \frac{4P}{T^5} = \frac{I}{T^5}. \tag{2.32}$$

The simple form of the pressure (2.30) allows us to give closed expressions for all mentioned quantities. We use additionally partial integration on the logarithms to rewrite them into a simpler form. This leads to the following formulae:

$$P = \frac{1}{2\pi^2}\int_0^\infty dp\ \frac{p^4}{3\omega_p} n_{B/F}(\omega_p), \tag{2.33}$$

$$s = \frac{1}{2\pi^2 T}\int_0^\infty dp\ p^2\left(\frac{\frac{4}{3}p^2 + m^2}{\omega_p} n_{B/F}(\omega_p) - \mu\ n_{B/F}(\omega_p)\right), \tag{2.34}$$

$$n = \frac{1}{2\pi^2}\int_0^\infty dp\ p^2 n_{B/F}(\omega_p), \tag{2.35}$$

$$\epsilon = \frac{1}{2\pi^2}\int_0^\infty dp\ p^2 \omega_p n_{B/F}(\omega_p), \tag{2.36}$$

$$I = \frac{1}{2\pi^2}\int_0^\infty dp\ p^2 \frac{m^2}{\omega_p} n_{B/F}(\omega_p), \tag{2.37}$$

where $n_{B/F}$ are the common Bose/Fermi-distribution functions,

$$n_B(\omega) = \frac{1}{\exp(\omega/T) - 1}, \qquad n_F(\omega) = \frac{1}{\exp((\omega-\mu)/T) + 1}, \tag{2.38}$$

that give the probability that a state with the energy ω is occupied in the thermal medium. The distribution function for antifermions is given by reversing the sign of the chemical potential in the Fermi-distribution function, $n_{\bar{F}}(T, \mu, \omega) = n_F(T, -\mu, \omega)$.
The above formulae are valid as long as the masses of the particles are independent from the temperature, the chemical potential and the momentum. They are a good approximation for systems with very weak interactions. Nevertheless, one can also use them for systems with strong interactions. Plenty of theories (in mean-field approximation) can be rewritten in a form where they resemble a non-interacting theory.

---

[3] Some authors abbreviate the interaction measure/trace anomaly as W.

An important limit of the non-interacting theory is the Stefan-Boltzmann limit of massless particles ($m \to 0$). The energy of the particles is then given by their momentum $\omega_p = |\mathbf{p}|$. The interaction measure vanishes in the Stefan-Boltzmann limit, i.e. $I = 0$, and the energy and the pressure are related by $\epsilon = 3P$. The entropy at vanishing chemical potential becomes $s = 4P/T$. For the special case of vanishing chemical potential we are able to solve the integrals analytically. The Stefan-Boltzmann limit for a single particle species without degeneracy is:

$$\frac{P_B}{T^4} = \frac{\pi^2}{90} \qquad \frac{P_F}{T^4} = \frac{7\pi^2}{720} \tag{2.39}$$

$$\frac{\epsilon_B}{T^4} = \frac{\pi^2}{30} \qquad \frac{\epsilon_F}{T^4} = \frac{7\pi^2}{240} \tag{2.40}$$

$$\frac{s_B}{T^3} = \frac{2\pi^2}{45} \qquad \frac{s_F}{T^3} = \frac{7\pi^2}{180} \tag{2.41}$$

$$\frac{n_B}{T^3} = \frac{\zeta(3)}{\pi^2} \qquad \frac{n_F}{T^3} = \frac{3\zeta(3)}{4\pi^2}. \tag{2.42}$$

The density n in this case is not the thermodynamic density, which has to be zero at vanishing chemical potential, but the actual particle density. The function ζ is the Riemann zeta function with $\zeta(3) \approx 1.202$. Note that the fermionic quantities do not include the antifermion contributions.

The Stefan-Boltzmann limit is the upper limit for any theoretical system since no interacting theory can exceed it. For $N_f = 2 + 1$ QCD, consisting of 36 fermions and 16 bosons, the Stefan-Boltzmann limit is:

$$\frac{P_{SB}^{QCD}}{T^4} = \frac{19}{36}\pi^2, \qquad \frac{\epsilon_{SB}^{QCD}}{T^4} = \frac{19}{12}\pi^2, \qquad \frac{s_{SB}^{QCD}}{T^3} = \frac{19}{9}\pi^2. \tag{2.43}$$

Many physical systems have more than one equilibrium state. If this is the case the system can undergo a phase transition where it changes from one phase into an other. The physical system realized in nature is the one that minimizes the thermodynamic potential. Because the potential depends on the environment, also the thermodynamically stable phase does. Water for example can exist as a gas, a liquid or a solid, depending on the temperature. However, the known transition temperatures of water are not fixed by nature but depend also on the pressure. They might vary considerably from the ones we know under normal atmospheric pressure. The phase structure of a system is summarized in its phase diagram, that indicates the thermodynamic stable phase as a function of the environment. Fig. 2.1 shows the phase diagram of water as a function of the pressure and the temperature.

Different phases are distinguished by an order parameter that changes at the phase boundary. If the change is discontinuous the transition is called a first-order phase transition, if the order parameter changes continuously but one of the derivatives is discontinuous, it is called a second or higher-order phase transition and if the order parameter changes continuously at all orders, it is called a crossover. The water/ice transition is a first-order phase transition with a discontinuity in the density, a popular

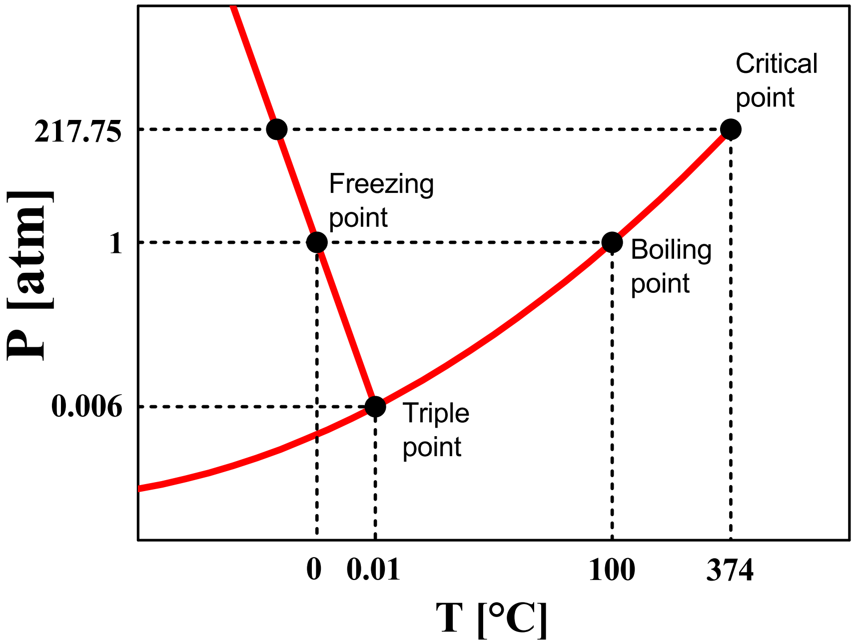

Figure 2.1: Sketch of the phase diagram of water as a function of the temperature in Celsius and the pressure in units of normal atmospheric pressure.

example of a crossover is butter that turns slowly from a solid into a liquid. The order of a phase transition may also change depending on the environment. The liquid/gas transition in water is a first-order phase transition that turns into a crossover at larger temperatures and pressures. The end point of the first-order transition is a critical point where the transition is of second order. Beyond the critical point the gas and the liquid phase are indistinguishable. Water features also a triple point where the gas/water and the water/ice transition meet. At this point all three states coexist in thermodynamic equilibrium.

Phase transitions are often related to symmetries. The transition in ferromagnetic materials between the magnetic and the normal phase can be explained in that way. In the ferromagnetic phase the magnetic moments of the atoms are aligned parallel to each other, which causes a finite magnetization. The material is in a symmetric state. But if this symmetry is lost, i.e. if the magnetic moments are aligned chaotically, the material is no longer magnetic. The order parameter of the transition, the magnetization, changes because the symmetry of the ground state is broken.

2.3 Fundamental properties of QCD

In modern physics all fundamental interactions -except for the gravitation- are described by quantum field theories. The fundamental theory of the strong interaction is quantum chromodynamics (QCD). We will give in this section only a short overview over QCD

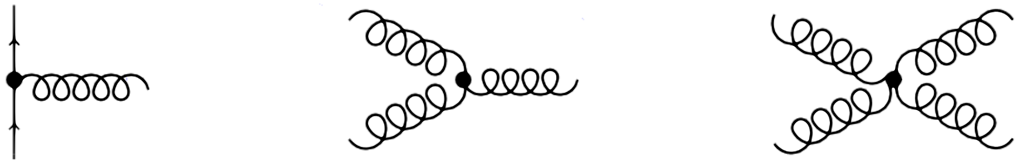

Figure 2.2: The fundamental QCD processes. Straight lines illustrate quarks, curly lines gluons.

and its phase structure; for an extensive introduction we refer to Refs. [100, 108, 109]. QCD describes the interactions between quarks. Each quark carries a color charge and is in one of three different color states denoted as red, blue and green [4]. The interaction is the same for each color and also independent of the quark flavor. A color neutral state can be achieved by two different ways. A color charge can be canceled by the corresponding anticolor or by combining all three color states. The latter is not possible in QED, since the electric charge has only one charge state. Due to the three charge states it is not possible to describe QCD with an abelian gauge theory, instead one has to employ an $SU(N_c)$ non-abelian gauge theory with $N_c = 3$ for the three color states. This causes the exchange bosons of QCD, the gluons, to carry a color and an anticolor. Nevertheless, they can not become color neutral or they could not interact with the quarks. This constraint prohibits one of the possible color-anticolor combinations of the gluons, leading to $N_c^2 - 1 = 8$ different gluon states.

The Lagrangian of QCD is given by

$$\mathcal{L}_{QCD} = \bar{\Psi} \left(i\gamma^\mu \left(\partial_\mu - igT^a \mathcal{A}_\mu^a \right) - \hat{m}_0 \right) \Psi - \frac{1}{4} G_{\mu\nu}^a G^{a\mu\nu}, \tag{2.44}$$

with the gluonic field strength tensor

$$G_{\mu\nu}^a = \partial_\mu \mathcal{A}_\nu^a - \partial_\nu \mathcal{A}_\mu^a + g f^{abc} \mathcal{A}_\mu^b \mathcal{A}_\nu^c, \tag{2.45}$$

where $\mathcal{A}_\mu^a$ denotes 8 massless gauge fields ($a = 1, \cdots, 8$) describing the gluons. The Gell-Mann matrices T^a are traceless matrices in color space and the generators of the $SU(3)$ group. The structure constants f^{abc} are defined by the algebra $\left[T^a, T^b\right] = i f^{abc} T_c$. They vanish in an abelian gauge theories, but are finite in QCD. In (2.44) $\hat{m}_0$ stands for the bare fermion mass matrix.

QCD embeds three fundamental processes, a quark-gluon interaction, a 3-gluon interaction and a 4-gluon interaction, see Fig. 2.2. The gluonic selfinteractions emerge due to the non-abelian nature of the theory in form of the non-vanishing structure constants. The strength of all three interactions is controlled by the coupling constant g. It is very large ($g > 1$) making QCD a strongly interacting theory. However, the gluonic selfinteractions introduce anti-screening effects that decrease the coupling logarithmically for larger energy and smaller length scales [110, 111].

The large coupling constant has severe consequences for the properties of QCD. The

---

[4] Antiquarks carry an anticolor charge denoted as antired, antiblue and antigreen.

attraction between colored particles is so strong, that they form colorless boundstates. The ground state of QCD is not composed of quarks and gluons, but of hadrons. One distinguishes mesons, that are bound states composed of a quark and an antiquark, and baryons, that are composed of three quarks. Quarks and gluons appear only in the most energetic events where the coupling constant becomes small. Unlike other bound states it is not possible to separate a hadron into its constituents and a single quark or gluon has never been observed experimentally. This feature is called confinement [5]. The mechanism behind confinement is still investigated and not fully understood, however, it is sufficient to describe low-energy QCD in terms of hadrons.

The strong interactions between the quarks induces also a non-vanishing quark condensate $\langle \bar{\Psi}\Psi \rangle$. This condensate is created by the spontaneous breaking of chiral symmetry, an exact symmetry of the QCD Lagrangian in the chiral limit of vanishing quark masses $m_q \to 0$. This limit is almost fulfilled if one neglects the heavy quarks and considers only up, down and strange quarks (u, d, s), as usually done in heavy-ion physics. Chiral symmetry breaking is extremely important for the phenomenology of the light mesons [112]. The spontaneous breaking of chiral symmetry leads to eight massless Goldstone bosons, which are the eight mesons of the 0^- octet. Since the symmetry is also explicitly broken by the quark masses, these mesons gain non-vanishing but small masses, which are still considerably smaller than the nucleon mass. A special case is the η' meson, a 0^- meson that belongs to a symmetry which is broken by a quantum anomaly. It is therefore not a Goldstone boson and has a large mass of $m_{\eta'} = 958$ MeV. This highlights the importance of chiral symmetry.

Chiral symmetry breaking introduces differences in hadrons with opposite parities which leads to different masses of the two parity states. Examples are the ρ (1^-) and the a_1 (1^+) and the pion (0^-) and the σ (0^+) meson. The spontaneous breaking has also an effect on the quarks. They gain a dynamically generated mass of $m_{u,d} \approx 350$ MeV, respectively, $m_s \approx 500$ MeV. This explains the huge discrepancy between the bare and the constituent quark masses.

The quark condensate acts as an order parameter of chiral symmetry breaking. It is defined by the trace of the quark propagator or equivalently as the derivative of the thermodynamic potential with respect to the bare quark masses,

$$\langle \bar{\Psi}\Psi \rangle = -\frac{T}{V}\mathrm{Tr}[S] = \frac{\partial \Omega}{\partial m_0}. \tag{2.46}$$

In the vacuum the light quark condensate has a value of $\langle \bar{u}u \rangle = \langle \bar{d}d \rangle \approx (-230\ \mathrm{MeV})^3$. Chiral symmetry gets eventually restored at large temperatures and chemical potentials and the condensate vanishes. This causes the hadrons with opposite parities to become degenerate. As the symmetry gets restored the spectral functions of these hadrons should converge against each other and become identical in case of full restoration of the symmetry, thus changing the properties of the hadrons in a hot and dense medium [51, 113, 114, 115].

A thermal medium has also an effect on confinement. As the system becomes hotter

---

[5] Technically speaking confinement refers to the absence of colored states from the physical spectrum.

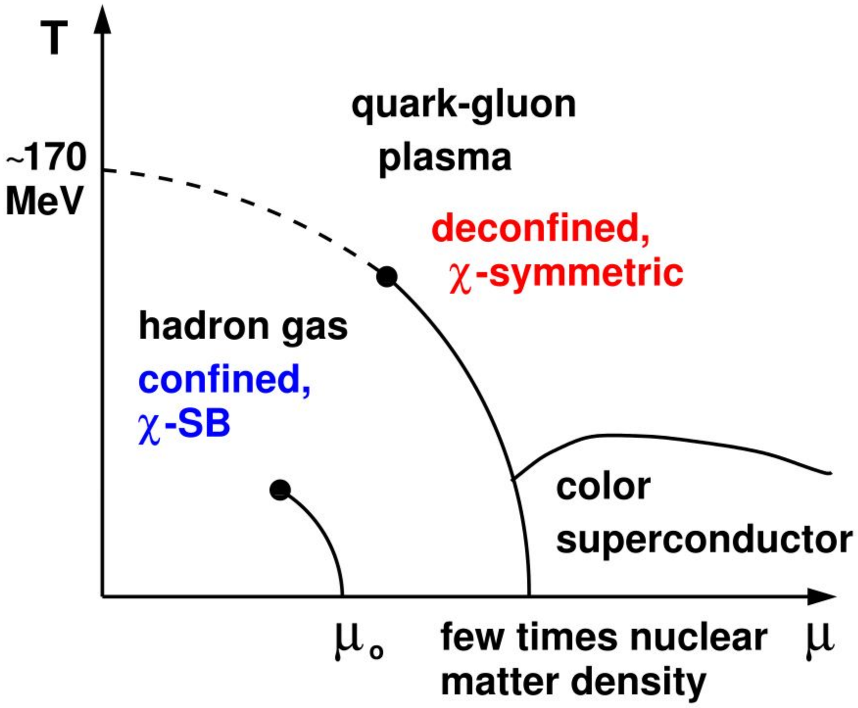

Figure 2.3: Sketch of the QCD phase diagram in the T-μ plane. The dashed line is the crossover transition between the confined hadronic medium with broken chiral symmetry and the deconfined partonic medium with restored chiral symmetry. The full line indicates where the transition might be of first order. The dot between both kinds of transitions is the critical end point. The transition in the confined phase indicates the liquid-gas transition of nuclear matter; the dot shows the end point of the transition. Additional phases like color superconductivity might play a role at large chemical potentials. The figure is taken from Ref. [116].

and denser, the hadrons are packed closer together, eventually overlapping each other. If this happens, one can no longer distinguish between individual hadrons and the quarks can move freely in the medium [5, 6]. This Quark-Gluon Plasma (QGP) is a state of matter where quarks and gluons are no longer confined and act as the normal degrees of freedom. An order parameter of the deconfinement transition is the Polyakov loop $\langle L\rangle$ which is the trace of a Wilson line along a closed loop in the time direction. It is only well defined in Euclidean time. In the heavy-quark limit the Polyakov loop is connected to the free energy of a single quark F_q [117, 118] by

$$\langle L\rangle = \exp\left(-\beta F_q\right) . \tag{2.47}$$

In the confined phase it is not possible to find a single quark, thus F_q is infinite and the Polyakov loop is zero. A non-zero Polyakov loop implies a finite F_q and it would be possible to find single quarks; $\langle L\rangle \neq 0$ is therefore an indication for deconfinement.

QCD will change from a confined phase with broken chiral symmetry in the vacuum to a deconfined phase with restored chiral symmetry at high temperatures and chemical potentials. A still open question is the order of the phase transition. Reliable information are only available at finite temperature and vanishing chemical potential, where the phase transition has been studied using lQCD. It has been shown that both transitions happen around the same critical temperature $T_c \approx 155 \pm 5$ MeV [38, 39]. Furthermore, the transition in both cases is not a real phase transition but a rapid crossover, such that we expect a mixed phase composed of partons and hadrons in the vicinity of the critical temperature. This is consistent with lQCD calculations of the equation of state that show no signals of a phase transition, just a rapid increase of the dimensionless equation of state around T_c, which indicates a change of the degrees of freedom [35]. At finite chemical potential lattice calculations are prevented by the sign problem and the properties of the phase transition are unknown. Arguments from effective QCD-like theories suggest a critical end point at which the crossover transition turns into a real first-order phase transition [43, 50, 60, 76, 119, 120, 121, 122]. Fig. 2.3 shows a sketch of such a QCD phase diagram, where the restoration of chiral symmetry and the deconfinement transition occur always simultaneously. This is only suggested at vanishing chemical potential. There are also indications for a phase where partons are still confined but chiral symmetry is restored [123, 124]. This implies a separation of the two transitions [125]. Also completely new phases like color superconductivity have been predicted at large baryon chemical potentials and low temperatures, see Refs. [44, 126, 127] and references therein. However, neither one of these phases nor the existence of the critical end point have been confirmed experimentally. It is also possible that the transition stays a crossover throughout the whole phase diagram.

2.4 Lattice QCD

Strongly correlated systems like QCD have to be treated in a non-perturbative framework. One of the most powerful non-perturbative approaches are lattice gauge theories. This approach allows for ab initio calculations of any given quantum field theory. A comprehensive introduction into lattice theories can be found in Refs. [128, 129, 130]. Lattice gauge theories use the connection between the generating functional (2.22) and the partition function (2.23), that is given by a Wick rotation $t \to -i\tau$,

$$Z' = \int \mathcal{D}\bar{\Psi}\mathcal{D}\Psi\mathcal{D}A \, \exp\left(iS\right) \quad \underset{t=-i\tau}{\longrightarrow} \quad Z = \int \mathcal{D}\bar{\Psi}\mathcal{D}\Psi\mathcal{D}A \, \exp\left(-S_E\right). \tag{2.48}$$

This rotation corresponds to a change from a Minkowski to an Euclidean metric. The action S in the generating functional is the action in Minkowski space, the action S_E in the partition function is the action in Euclidean space. Also the form of the exponential changes after the Wick rotation. In Z' the exponent is imaginary and the exponential oscillates, in Z the exponential takes the form of a Boltzmann-distribution. This allows the application of methods from statistical physics to evaluate the integral. Paths with small actions give larger contributions to the path integral. The path with the lowest action is the classical path, the other paths describe corrections from quantum fluctuations.

In lattice calculations the path integral is solved on a discretized space-time grid. The discretization introduces an ultra-violet momentum cutoff, that regularizes the theory. The largest possible momentum on the lattice is $p_{max} = \pi/a$, where a is the distance between two grid points. The full theory is only recovered in the continuum limit $a \to 0$ (when possible). In practical calculations one performs simulations for different lattice spacings and extrapolates the results to the continuum limit $a = 0$ [36]. The path integral is approximated by a sum over lattice configurations. Each configuration corresponds to a different path of the fields in the path integral (2.48). They are generated by assigning random numbers for each field to all space-time points on the grid. Each quark field contains four Dirac components for each of the three color charges for each quark flavor. Including up, down and strange quarks this leads to $4 \times N_c \times N_f = 36$ components that have to be assigned to each of the grid points. The gluon fields are not described by the actual gauge fields A_μ, but by link variables U_μ,

$$U_\mu = \exp(igA_\mu a), \tag{2.49}$$

that live on the links between two grid points. The link variables are unitary 3×3 matrices that encode the 8 gluonic degrees of freedom. Every closed loop of link variables is automatically gauge invariant. It is essential to generate configurations with small actions for a good approximation of the full path integral. This is usually done via importance sampling, for example with the Metropolis algorithm [131, 132].

If the different configurations are generated, one calculates observables by weighting them with the exponential of the action,

$$\langle O \rangle = \frac{1}{Z} \int \mathcal{D}\bar{\Psi}\mathcal{D}\Psi\mathcal{D}A \; O(\bar{\Psi}, \Psi, A) \exp\left(-S_E\right) \approx \frac{1}{N_{conf}} \sum_{i=1}^{N_{conf}} O_i \exp(-S_{E,i}). \tag{2.50}$$

The generated configurations and the observables depend on the discretized action. There is no unique choice for the discretized action of QCD, but it has to reproduce the physical action in the continuum limit. As long as the results are not continuum extrapolated they correspond not to real QCD and should only be handled with utmost care.

Due to the discretization of space-time all dimensional observables are given in units of the lattice spacing a. It is therefore common to present results from lattice calculations as dimensionless ratios where the dependences on the lattice spacing cancel. In case of the equation of state, the results are usually scaled by powers of the temperature. However, it is still necessary to determine the value of the lattice spacing. The bare masses of the quarks, which enter the simulations as parameters, are dimensional quantities. To set them to their physical values one requires the value of the lattice spacing [133]. This scale setting has to be done in separate vacuum simulations. One calculates an observable that is experimentally known and the value of the lattice spacing follows from a comparison between the experiment and the value in lattice units. Possible observables for the scale setting are the string tension κ between two heavy quarks or the pion or kaon decay constants (f_π, f_K). Which observable is chosen is not important since each choice should lead to the same result in the continuum limit. However, by determining the scale for different observables, one can check the validity of the continuum extrapolation, see Ref. [36].

One difficulty in lattice QCD (lQCD) simulations is the inclusion of dynamical quarks. While simulations with only gluons (Yang-Mills simulations) and infinitely heavy quarks (quenched simulations) are well established, this is not the case for simulations with fully dynamical quarks (unquenched simulations). In order to describe the correct quantum statistics of fermions, quarks have to be treated as Grassmann variables, scalar numbers that fulfill anticommutation relations. Currently it is impossible to use these variables in actual calculations. To include dynamical quarks in the simulations, one has to transform the Grassmann variables into normal variables. This is done via an integral transformation,

$$\int \mathcal{D}\bar{\Psi}\mathcal{D}\Psi \exp\left(-\bar{\Psi}\hat{M}\Psi\right) = \det(\hat{M}) = \frac{1}{\det(\hat{M}^{-1})} = \int \mathcal{D}\phi^\dagger\mathcal{D}\phi \exp\left(-\phi^\dagger\hat{M}^{-1}\phi\right). \tag{2.51}$$

The fields $\phi^\dagger$ and ϕ are pseudo-fermions that describe fermionic degrees of freedom, but commute like bosonic degrees of freedom. The operator $\hat{M}$ is the inverse quark propagator which in the lattice framework is a high dimensional matrix. For the transformation from Grassmann to normal variables one has to invert this matrix. This step is numerically extremely expensive and the reason for the difficulties in unquenched lattice studies. The inversion becomes even more complicated for lower quark masses. Unfortunately, physical quark masses are very small and unquenched calculations with physical masses require tremendous calculational resources. In actual calculations one sets the heavier strange quark mass to its physical value and uses a fixed ratio between the light and the strange quark mass. The physical light quark mass is reached for a ratio $m_{u,d}/m_s = 1/27$. If the ratio is larger, one will find unphysical heavy pion masses, since they are very sensitive to the actual values of $m_{u,d}$. Note that simulations of full QCD should reproduce the physical pion mass $m_\pi \approx 140$ MeV.

Lattice calculations are subject to two serious limitations. The first restriction concerns the use of an Euclidean metric with an imaginary time. This limits the approach to calculations in the thermodynamic equilibrium [105, 106]. The other restriction concerns simulations at finite chemical potential μ, that are prevented by the infamous sign-problem. If one introduces a chemical potential, the fermion determinant in Eq. (2.51) becomes complex and the exponentiated action loses its interpretation as a probability distribution, which is necessary to connect the approach to statistical physics. So far lQCD calculations are limited to studies with vanishing chemical potential or purely imaginary μ. An introduction to lQCD at finite chemical potential can be found in Ref. [134]. Despite these limitations, lQCD is still among the most powerful tools to study QCD. The results from the calculations are often unrivaled and the only way to study full QCD in a non-perturbative framework.

The most important result for this thesis is the QCD equation of state. One determines

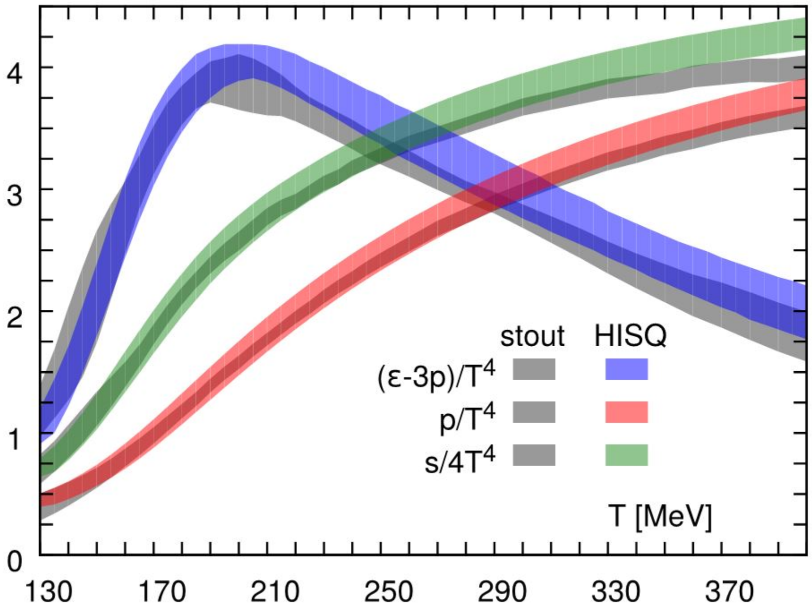

Figure 2.4: Comparison between the lattice equation of state for $s/(4T^4)$, P/T^4 and $(\epsilon - 3P)/T^4$ calculated from the the stout action from Ref. [90] and the HISQ/tree action from Ref. [91]. Both results agree within their error bars. The figure is taken from Ref. [91].

it from the interaction measure, that is (in the lattice framework) the derivative of the thermodynamic potential with respect to the lattice spacing [129],

$$I = \frac{T}{V}\frac{d\ln Z}{d\ln a}. \tag{2.52}$$

Once the interaction measure is known one can use the thermodynamic relations presented in Sec. 2.1 and 2.2 to determine the equation of state. At vanishing chemical potential all thermodynamic functions are connected and it is sufficient to know one function to determine the whole equation of state. This changes at finite chemical potential where one requires at least two thermodynamic functions. The equation of state of QCD was recently calculated by two separate groups, the Wuppertal-Budapest [90] and the HotQCD collaboration [91]. We show their continuum extrapolated predictions in Fig. 2.4. Both groups used different lattice setups, but their results agree within error bars. This led to the common believe that their results describe indeed the proper equation of state of QCD. We will use the equation of state of the Wuppertal-Budapest collaboration from Ref. [90] as benchmark for the QCD equation of state. It was determined in a larger temperature range using physical light quark masses. The HotQCD collaboration had larger light quark masses leading to slightly enhanced pion masses $m_\pi \approx 160$ MeV.

The Wuppertal-Budapest collaboration provided a parametrization of their results in terms of the scaled interaction measure,

$$\frac{I(T)}{T^4} = \exp(-h_1/t - h_2/t^2) \cdot \left(h_0 + \frac{f_0 \left(\tanh \left(f_1 \cdot t + f_2 \right) + 1 \right)}{1 + g_1 \cdot t + g_2 \cdot t^2} \right), \tag{2.53}$$

with $t = T/200$ MeV and:

h_0	h_1	h_2	f_0	f_1	f_2	g_1	g_2
0.1396	-0.18	0.035	1.05	6.39	-4.72	-0.92	0.57

The function (2.53) reproduces the lattice data for temperatures larger than $T \approx$ 130 MeV and is fitted to reproduce the HRG interaction measure at lower temperatures. With the inclusion of the HRG result it gives a valid description for the QCD equation of state at all temperatures even down to the vacuum for $T = 0$. We use Eq. (2.32) and calculate the scaled pressure P/T^4 by integrating I/T^5 over T,

$$\frac{P}{T^4} = \int_0^T \frac{I}{T'^5} dT'. \tag{2.54}$$

The entropy and the energy densities follow from the relations $s = (I - 4P)/T$ and $\epsilon = I + 3P$.

Due to the sign-problem it is not possible to determine the equation of state at finite chemical potential from first principles. However, one can still investigate some properties at $\mu = 0$ in terms of the susceptibilities. They are the Taylor coefficients of the pressure with respect to the chemical potential,

$$\chi_i^n = \left. \frac{\partial^n P}{\partial \mu_i^n} \right|_{\mu_i = 0}, \qquad i = B, Q, S. \tag{2.55}$$

Symmetries of QCD demand that the odd susceptibilities vanish. The even susceptibilities determine the QCD equation of state at small baryon chemical potentials $\mu_B < 3T$,

$$P(T, \mu_B) \approx P(T, 0) + \frac{1}{2} \chi_B^2 \mu_B^2 + \frac{1}{24} \chi_B^4 \mu_B^4 \cdots . \tag{2.56}$$

We will focus in this thesis on the second-order baryon number susceptibility χ_B^2, which is the leading coefficient at finite baryon chemical potential. We will use the results from Ref. [135] as prediction for the susceptibility. They were also determined by the Wuppertal-Budapest collaboration, but from an earlier set of data as the equation of state from Ref. [90]. However, this data set was generated using the same actions and scale settings as the more recent simulations. Furthermore, the equation of state determined from this earlier data set in Ref. [136] agrees up to some small corrections with the more recent equation of state. We expect that the results for the equation of state from Ref. [90] and the susceptibility from Ref. [135] are consistent with each other. The baryon number susceptibility from Ref. [135] is shown in Fig. 2.5. The results can

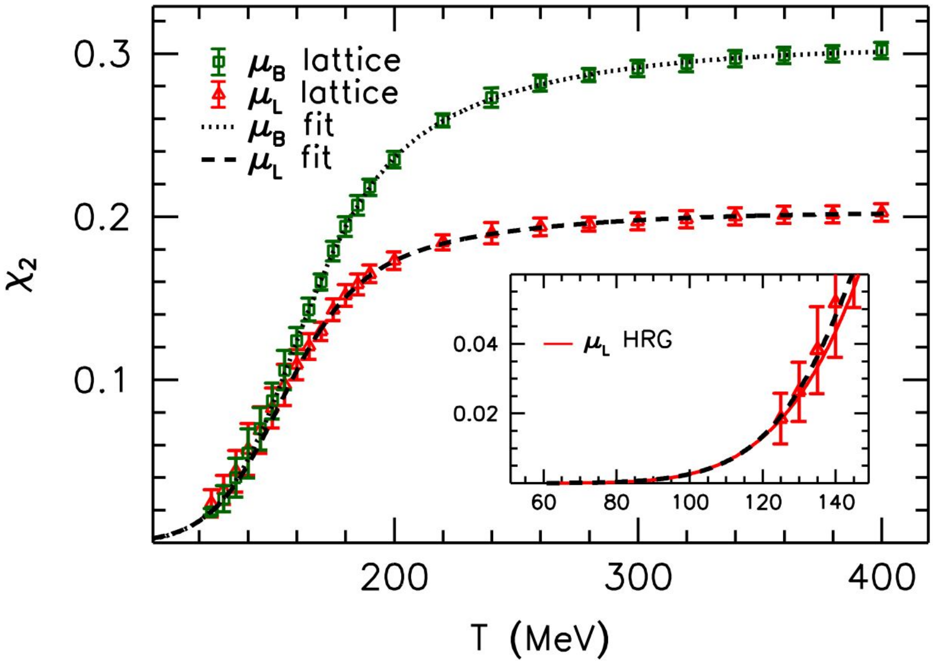

Figure 2.5: The scaled baryon number susceptibility χ_B^2/T^2 as a function of the temperature T from Ref. [135]. The red triangles show the result with and the green squares without strangeness neutrality. The dotted and the dashed line show the fits from Eq. (2.57). The inset zooms into the low temperature region. Here only the result with strangeness neutrality are shown, since the results with and without strangeness neutrality are on top of each other. The red line is the HRG prediction. The figure is taken from Ref. [135].

be fitted with the ansatz

$$\frac{\chi_B^2}{T^2} = \exp(-h_3/t - h_4/t^2) \cdot f_3 \cdot (\tanh(f_4 \cdot t + f_5) + 1)\,, \tag{2.57}$$

with $t = T/200$ MeV and:

μ	h_3	h_4	f_3	f_4	f_5
μ_L	-0.3364	0.3902	0.0940	6.8312	-5.0907
μ_B	-0.5022	0.5950	0.1359	6.3290	-4.8303

The scaled susceptibility shows the same behavior as the scaled pressure and the entropy density in Fig. 2.4, a steep rise at T_c followed by a plateau at large temperatures. At low temperatures the lQCD results are well reproduced by a HRG. The susceptibility differs substantially if strangeness is conserved (μ_L) or not (μ_B). If strangeness is strictly conserved the strange quark density can not fluctuate and its contribution to the susceptibility has to vanish. This is not important at small temperatures because all baryons

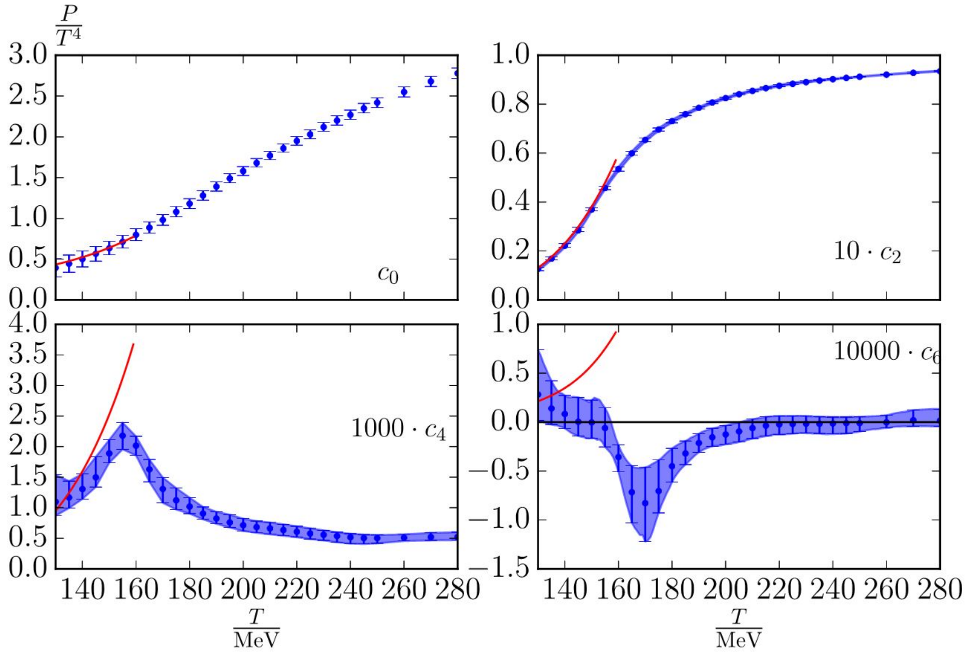

Figure 2.6: The Taylor coefficients of the pressure determined from analytical continuation from Ref. [41] for $N_S = 0$ and $N_Q/N_B = 0.4$. The red lines show the HRG results. The leading coefficient c_0 is the scaled pressure P/T^4 at vanishing chemical potential and was taken from Ref. [90]. The figure is taken from Ref. [41].

carry the same baryon number, regardless of the quark content. Therefore both cases agree with each other, if the medium is composed of hadrons.

Currently the susceptibilities are known up to the 6th order [40, 41, 42]. We show the results from Ref. [41] for the first four non-vanishing expansion coefficients of the scaled pressure P/T^4 in Fig. 2.6. The expansion coefficients are related to the susceptibilities by

$$c_n = \frac{1}{n!}\frac{\chi_B^n}{T^{4-n}}, \qquad n = (0, 2, 4, \cdots). \tag{2.58}$$

The zeroth expansion coefficient is the scaled pressure $c_0 = P/T^4$ and the second coefficient is related to the baryon number susceptibility $c_2 = \chi_B^2/(2T^2)$. So far all results for the higher-order susceptibilities have been obtained for a strangeness-neutral system $N_S = 0$ and a fixed ratio of charge to baryon number density $N_Q/N_B = 0.4$. Note that the derivative $\partial P/\partial \mu_B$ of the pressure (2.56) is not equal to the baryon number density if one puts constraints on the other conserved charges. The system is also described by a charge chemical potential μ_Q and a strangeness chemical potential μ_S. If charge or strangeness are constrained, μ_Q and μ_S become functions of the baryon chemical potential and the derivative will also act on these functions. One has to account for the additional contributions if one wants to determine the actual baryon number density.

With more expansion coefficients one can extend the application range of the lQCD equation of state to larger baryon chemical potentials, at least in the absence of a critical point. One needs much more Taylor coefficients just to enter the vicinity of a possible critical point at high μ_B. This question was studied in Ref. [137] for the NJL and in Ref. [138] for the PQM model. The coefficients beyond the sixth-order become oscillatory and one needs 24 Taylor coefficients just to enter the metastable phase. This is not feasible for present lQCD calculations.

2.5 Systems out-of equilibrium

QCD matter is probed experimentally in relativistic heavy-ion collisions where the nuclear matter is compressed and driven out-of equilibrium. It is unclear if the system reaches a local equilibrium during its time evolution, but this is necessary to relate the properties of the medium to thermodynamics, which is limited to systems in or close to equilibrium. In order to check theoretical results against experimental data it is instructive to study the connection between equilibrium and non-equilibrium physics. Accordingly, we recall in this subsection the basic concepts of transport theory.

2.5.1 Non-relativistic transport

Transport theories describe the time evolution of a given system. The basic quantity in a classical transport theory is the one-particle distribution function $f(\mathbf{r}, \mathbf{p}, t)$. It describes the probability to find a particle at the time t and the position $\mathbf{r}$ with the momentum $\mathbf{p}$. The time evolution of the distribution function is given by the Master equation [139],

$$\frac{df(\mathbf{r},\mathbf{p},t)}{dt} = \int d^3p' \ \left(P_{p'\to p}\ f(\mathbf{r},\mathbf{p}',t) - P_{p\to p'}\ f(\mathbf{r},\mathbf{p},t)\right). \tag{2.59}$$

The left side is the total time-derivative of the distribution function. Using the Hamilton's equations

$$\dot{\mathbf{r}} = \frac{\mathbf{p}}{m}, \qquad \dot{\mathbf{p}} = -\boldsymbol{\nabla}_{\mathbf{r}} U(\mathbf{r}), \tag{2.60}$$

the left side of the Master equation becomes

$$\frac{df(\mathbf{r},\mathbf{p},t)}{dt} = \left(\frac{\partial}{\partial t} + \frac{\mathbf{p}}{m}\cdot\boldsymbol{\nabla}_{\mathbf{r}} - \boldsymbol{\nabla}_{\mathbf{r}} U(\mathbf{r})\cdot\boldsymbol{\nabla}_{\mathbf{p}}\right) f\left(\mathbf{r},\mathbf{p},t\right) \tag{2.61}$$

and describes the motion of particles in the local potential $U(\mathbf{r})$. The right side of the Master equation describes scattering processes that change the distribution function beyond the normal Hamilton dynamics. In Eq. (2.59) $P_{p_1\to p_2}$ is the probability of a scattering event in which the momentum is changed from $\mathbf{p}_1$ to $\mathbf{p}_2$ (or $\mathbf{p}' \leftrightarrow \mathbf{p}$). The two terms on the right side are called "gain" and "loss" term and describe scatterings in and out of the respective phase space cell. The gain term will increase the distribution function for the given momentum and the loss term will decrease it.

A popular approximation for the collision term is the limitation to elastic two-body scatterings. The right side of the Master equation is then approximated by

$$\left.\frac{df(\mathbf{r},\mathbf{p}_1,t)}{dt}\right|_{coll} = \int \frac{d^3p_2}{(2\pi)^3}\int d\Omega\ \frac{d\sigma}{d\Omega}(\mathbf{p}_1+\mathbf{p}_2)\ v_{12} \\ \times \left(f\left(\mathbf{r},\mathbf{p}_3,t\right)f\left(\mathbf{r},\mathbf{p}_4,t\right) - f\left(\mathbf{r},\mathbf{p}_1,t\right)f\left(\mathbf{r},\mathbf{p}_2,t\right)\right). \tag{2.62}$$

The combination of Eqs. (2.61) and (2.62) is the famous Boltzmann equation. The gain and loss-term are now two-body scattering events where one of the particles gets scattered in or out of the momentum state $\mathbf{p}_1$. The probability for a scattering is given by the differential cross section $d\sigma/d\Omega(\mathbf{p}_1+\mathbf{p}_2)$ and the relative velocity $v_{12} = |\mathbf{p}_1 - \mathbf{p}_2|/m$ between the two particles. The momenta of the scattering particles before and after the collision have to fulfill energy-momentum conservation.

An important extension of the Boltzmann equation is the semiclassical Boltzmann-Uehling-Uhlenbeck (BUU) equation. The BUU equation adds quantum-statistical effects into the scattering term (2.62) by considering Pauli-blocking factors $(1-f(\mathbf{r},\mathbf{p}_{f,1},t)) \times (1-f(\mathbf{r},\mathbf{p}_{f,2},t))$ for the final states $\mathbf{p}_{f,1}$ and $\mathbf{p}_{f,2}$ in case of fermions. This is important for simulations of nuclear matter where Pauli-blocking is crucial for the dynamics of the system.

If the system evolves for a sufficient amount of time, it will eventually equilibrate. The equilibrium state is characterized by a static one-particle distribution function,

$$\frac{df_{eq}(\mathbf{r},\mathbf{p},t)}{dt} = 0. \tag{2.63}$$

One can see from Eq. (2.59) that this is the case if the scattering term vanishes. The same amount of particles that get scattered into a specific momentum state will also get scattered out of this state. For the Boltzmann equation (2.62) the equilibrium distribution function is given by a Boltzmann-distribution and for the BUU equation it is given by a Fermi-distribution. Note that in these cases the equilibrium distribution are those for non-interacting particles.

2.5.2 Relativistic transport

The one-particle distribution function is a classical quantity that violates Heisenberg's uncertainty principle. In a quantum mechanical and relativistic framework the one-particle distribution function is replaced by the one-particle Green's function, which is the time ordered expectation value of the operator $\Psi(x)\Psi^\dagger(y)$,

$$G\left(x,y\right) = -i\left\langle \hat{T}_c\left(\Psi(x)\Psi^\dagger(y)\right)\right\rangle, \tag{2.64}$$

where $\Psi(x)$ is the wave function of the particle. The function (2.64) describes the propagation of a particle from the space-time point y to the space-time point x.

Non-equilibrium theories, and therefore also non-equilibrium Green's functions $G\left(x,y\right)$, are defined on a special time-contour [105, 106], see Fig. 2.7. This Keldysh contour runs from $t_0 = 0$ to t on a chronological branch $(+)$ on the real time axis and back from t to

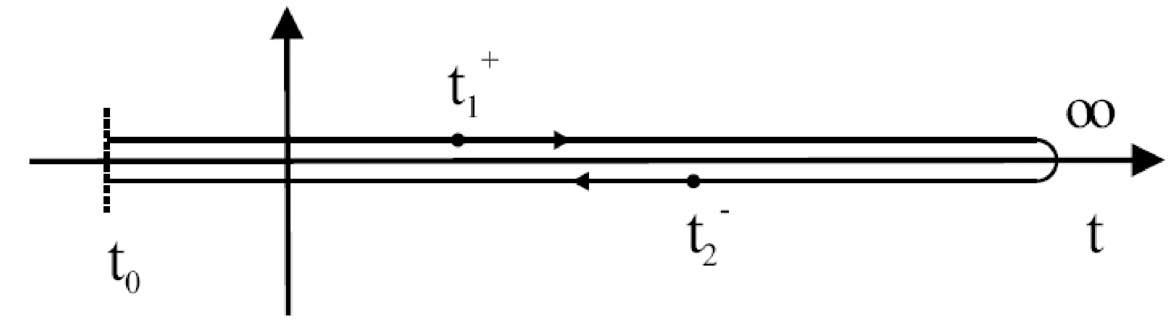

Figure 2.7: The closed time contour in the Schwinger-Keldysh formalism. The figure is taken from Ref. [31].

$t_0 = 0$ on an antichronological branch $(-)$ (and then eventually into the imaginary time axis). The evolution on the real time axis describes the equilibration of the system and the evolution on the imaginary time axis the equilibrium state.

We have to distinguish four different Green's functions based on the location of the two time arguments on the Keldysh contour. Most important are the correlation functions $G^{>}(x,y) = G^{-+}(x,y)$ and $G^{<}(x,y) = G^{+-}(x,y)$ with time arguments on both branches. These contain the statistical information of the system; the Green's functions with both time arguments on the same branch contain only spectral information. The time evolution of the correlation functions $G^{\lessgtr}$ is described by the Kadanoff-Baym equations [30, 31],

$$\begin{aligned}-\left[\partial_\mu^x \partial_x^\mu + m^2\right] G^{\lessgtr}(x,y) =& \Sigma^\delta(x) G^{\lessgtr}(x,y) \\ &+ \int_{t_0}^{x_0} dz_0 \int d^3z \; \left[\Sigma^{>}(x,z) - \Sigma^{<}(x,z)\right] G^{\lessgtr}(z,y) \\ &- \int_{t_0}^{y_0} dz_0 \int d^3z \; \Sigma^{\lessgtr}(x,z) \left[G^{>}(x,z) - G^{<}(x,z)\right],\end{aligned} \tag{2.65}$$

$$\begin{aligned}-\left[\partial_\mu^y \partial_y^\mu + m^2\right] G^{\lessgtr}(x,y) =& \Sigma^\delta(y) G^{\lessgtr}(x,y) \\ &+ \int_{t_0}^{x_0} dz_0 \int d^3z \; \left[G^{>}(x,z) - G^{<}(x,z)\right] \Sigma^{\lessgtr}(z,y) \\ &- \int_{t_0}^{y_0} dz_0 \int d^3z \; G^{\lessgtr}(x,z) \left[\Sigma^{>}(x,z) - \Sigma^{<}(x,z)\right],\end{aligned} \tag{2.66}$$

where Σ are the selfenergies of the correlation functions. They describe the difference between the fully dressed and the non-interacting Green's functions,

$$G^{-1} = G_0^{-1} + \Sigma, \tag{2.67}$$

and contain all possible effects of interactions that are encoded in the full Green's functions.

The Green's functions with two spatial coordinates are not well suited for practical calculations. It is more convenient to Wigner transform the Green's function into its phase-space representation. To this end one introduces center-of-mass coordinates and Fourier transforms the relative coordinates into momentum space. The resulting Wigner transformed Green's functions $\bar{G}^{\lessgtr}(\mathbf{r}, \mathbf{p}, \omega, t)$ depend on the position $\mathbf{r}$, the momentum $\mathbf{p}$, the time t, but also on the energy $\omega = p_0$. The energy dependence originates from the Fourier transformation of the relative time $x_0 - y_0$. The non-equilibrium Green's function $\bar{G}^{\lessgtr}(\mathbf{r}, \mathbf{p}, \omega, t)$ is the off-shell generalization of the one-particle distribution function $f(\mathbf{r}, \mathbf{p}, t)$, which is regained (except for a factor $\pm\frac{i}{2\pi}$) after an integration over the energy ω.

The right side of the Kadanoff-Baym equations contains a convolution and can not be transformed exactly. Instead one transforms the right side in the first-order gradient approximation by expanding the exponential function in the Fourier transformation up to first order. Introducing additionally the Botermans-Malfliet scheme [140] leads to a transport equation for the correlation functions [31],

$$\frac{1}{2}\bar{A}\bar{\Gamma}\left[\left\{\bar{M}, i\bar{G}^<\right\} - \frac{1}{\bar{\Gamma}}\left\{\bar{\Gamma}, \bar{M}\ i\bar{G}^<\right\}\right] = i\bar{\Sigma}^< i\bar{G}^> - i\bar{\Sigma}^> i\bar{G}^<. \tag{2.68}$$

The curly brackets in (2.68) are the relativistic generalization of the Poisson brackets

$$\{\bar{F}(p,x), \bar{G}(p,x)\} = \partial^p_\mu \bar{F}(p,x)\partial^\mu_x \bar{G}(p,x) - \partial^\mu_x \bar{F}(p,x)\partial^p_\mu \bar{G}(p,x), \tag{2.69}$$

$\bar{M}(p,x) = p_0^2 - \mathbf{p}^2 - m^2 - \bar{\Sigma}^\delta(x) - \mathrm{Re}\bar{\Sigma}^R(p,x)$ is the mass function and $\bar{A}$ the spectral function. In first-order gradient expansion the spectral function reads

$$\bar{A} = \frac{\bar{\Gamma}}{[p_0^2 - \mathbf{p}^2 - m^2 - \bar{\Sigma}^\delta - \mathrm{Re}\bar{\Sigma}^R]^2 + \bar{\Gamma}^2/4} \tag{2.70}$$

and has the shape of a relativistic Breit-Wigner function where the width is defined by the imaginary part of the selfenergy $\bar{\Gamma} = -2\ \mathrm{Im}\bar{\Sigma}^R$ [31]. Note that the left side of Eq. (2.68) depends only on the retarded selfenergies $\hat{\Sigma}^R = \hat{\Sigma}^> - \hat{\Sigma}^<$. The transport equation (2.68) is similar to the Master equation (2.59). The left side describes the evolution of the Green's function in a selfgenerated field, the right side contains the usual gain and loss-terms due to scattering processes.

The Kadanoff-Baym equations go beyond the Boltzmann approximation and describe also off-shell effects. This is especially important for theories with broad spectral functions like the DQPM, that we will introduce in Sec. 3. Only the Kadanoff-Baym framework can reproduce the correct equilibrium state for strongly interacting systems! The Boltzmann or the BUU equation will always lead to Boltzmann- or Fermi-distributions in equilibrium, which are the distribution functions of a non-interacting system. The interactions have therefore no influence on the equilibrium state and control only the time scale of the equilibration. This is acceptable only for systems with very weak interactions. In the Kadanoff-Baym framework the equilibrium state is determined by the spectral function [31, 140, 141],

$$i\bar{G}^<_{eq}(\mathbf{r}, \mathbf{p}, \omega) = \bar{A}(\mathbf{r}, \mathbf{p}, \omega) \cdot N_{eq}(\omega), \tag{2.71}$$

$$i\bar{G}^>_{eq}(\mathbf{r}, \mathbf{p}, \omega) = \bar{A}(\mathbf{r}, \mathbf{p}, \omega) \cdot (1 \pm N_{eq}(\omega)), \tag{2.72}$$

where the function N_{eq} is the Bose/Fermi-distribution function $N_{eq} = n_{B/F}(\omega)$. The spectral function itself (2.70) depends on the selfenergies that are defined by the interactions.

At some occasions in this thesis we will use heavy-ion simulations to investigate the properties of QCD matter out-of equilibrium. These simulations are preformed with the Parton-Hadron-String-Dynamics transport approach (PHSD) that is based on the Kandanoff-Baym equations. PHSD is a microscopic covariant transport approach for strongly interacting systems and describes the full time evolution of a heavy-ion collision from the primary hard collisions through the formation of a QGP to the final hadronic scatterings. The interactions/selfenergies are chosen to reproduce the experimental measured cross sections in the hadronic phase and are compatible with the lQCD equation of state and transport coefficients in the partonic phase. PHSD is a special transport approach that treats hadronic and partonic degrees of freedom in the same framework and incorporates a dynamical formation and hadronization of the partonic phase. If the local energy density exceeds a critical energy density of $\epsilon_c \approx 0.5$ GeV/fm^3 the hadrons dissolve into quarks, if the energy density is below this value the partons hadronize by fusion processes. We will use this as a general criterion for the hadron-parton transition throughout this thesis and discuss it explicitly in Sec. 6.1. For further information about PHSD we refer to Refs. [142, 143, 144, 145, 146, 147].

3 The Dynamical QuasiParticle Model

The Dynamical QuasiParticle Model (DQPM) is a phenomenological model that can reproduce the thermodynamics of hot QCD matter in the QGP-phase. The basic idea is to treat quarks and gluons as fully dressed quasiparticles with Breit-Wigner spectral functions. The properties of the quasiparticles are then chosen to reproduce the equation of state obtained from lQCD calculations.

3.1 DQPM

The starting point of the DQPM are the quasiparticle entropy and particle number that follow in a thermodynamically consistent way from the thermodynamic potential in the propagator representation [78, 79, 148, 149, 150], see Appendix A.1:

$$\begin{aligned} s^{dqp} = &- d_g \int_{d^4p} \frac{\partial n_B}{\partial T} \big(\mathrm{Im}(\ln D^{-1}) - \mathrm{Im}\Pi \ \mathrm{Re}D\big) \\ &- d_q \int_{d^4p} \frac{\partial n_F}{\partial T} \big(\mathrm{Im}(\ln S^{-1}) - \mathrm{Im}\Sigma \ \mathrm{Re}S\big) \\ &- d_{\bar{q}} \int_{d^4p} \frac{\partial n_{\bar{F}}}{\partial T} \big(\mathrm{Im}(\ln S^{-1}) - \mathrm{Im}\Sigma \ \mathrm{Re}S\big) , \end{aligned} \tag{3.1}$$

$$\begin{aligned} n^{dqp} = &- d_q \int_{d^4p} \frac{\partial n_F}{\partial \mu} \big(\mathrm{Im}(\ln S^{-1}) - \mathrm{Im}\Sigma \ \mathrm{Re}S\big) \\ &- d_{\bar{q}} \int_{d^4p} \frac{\partial n_{\bar{F}}}{\partial \mu} \big(\mathrm{Im}(\ln S^{-1}) - \mathrm{Im}\Sigma \ \mathrm{Re}S\big) , \end{aligned} \tag{3.2}$$

where D and S are the full quasiparticle propagators of the gluons and the quarks, with the respective selfenergies Π and Σ. The DQPM treats them as scalar particles and neglects the Lorentz structure. The propagator for both particles is taken as

$$G(\omega, \mathbf{p}) = \frac{-1}{\omega^2 - \mathbf{p}^2 - M^2 + 2i\gamma\omega} = \frac{-1}{\omega^2 - \mathbf{p}^2 - \Sigma} \tag{3.3}$$

and satisfies the Dyson equation $G^{-1} = G_0^{-1} + \Sigma$ with the complex selfenergy

$$\Sigma = M^2 - 2i\gamma\omega \tag{3.4}$$

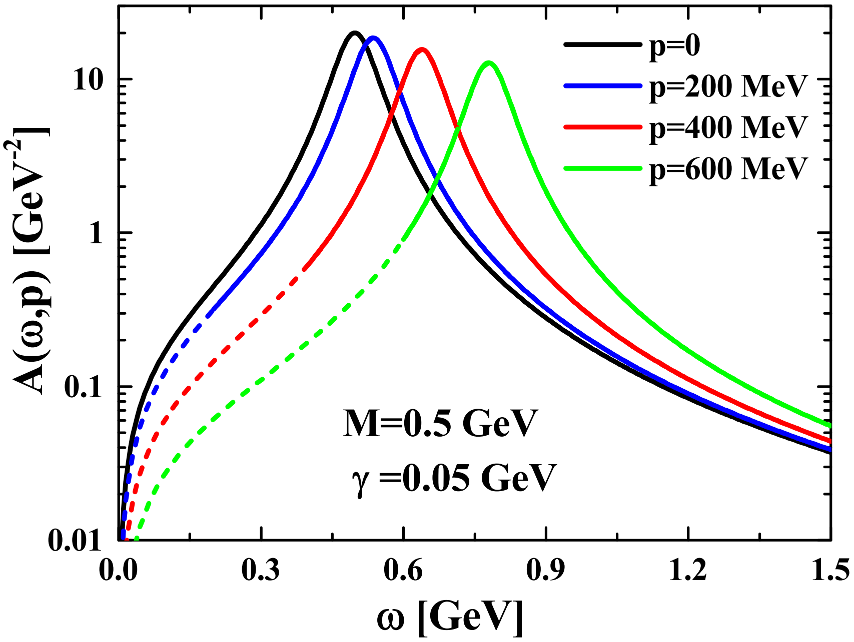

Figure 3.1: Relativistic Breit-Wigner spectral function as a function of the energy ω for different three-momenta $|\mathbf{p}|$ for a mass of $M = 0.5$ GeV and a width of $\gamma = 0.05$ GeV. The dashed part of the curves illustrates the spacelike part $\omega < |\mathbf{p}|$ of the spectral function.

and the bare propagator $G_0 = -1/(\omega^2 - \mathbf{p}^2)$. Here M describes the effective mass and γ the interaction width of the partons. The DQPM supersedes the earliest quasiparticle models that include only an effective mass and neglect the width [151, 152].

The nature of the mass is different from the dynamical mass generation in the nucleon, where quarks get their mass due to dynamical chiral symmetry breaking. Here the effective mass is generated from the interactions with the medium where any particle picks up a contribution to the real part of the selfenergy that is proportional to $\mathrm{Re}\Sigma \sim g^2T^2$ and leads to $M \sim gT$, if the coupling g is large enough [107]. We have dropped the mass in the bare propagator since the bare quark masses are much smaller than the dressed ones. We can easily include them by setting $M^2 = m_0^2 + \mathrm{Re}\Sigma$. This would only change the real part of the selfenergies, while the propagator itself remains unchanged, and has no effect on the thermodynamics.

The imaginary part of the propagator defines the spectral function. For the propagator (3.3) it is given by a relativistic Breit-Wigner spectral function,

$$A(\omega, \mathbf{p}) = \frac{2\gamma\omega}{(\omega^2 - \mathbf{p}^2 - M^2)^2 + 4\gamma^2\omega^2}, \tag{3.5}$$

that is normalized to

$$\int_{-\infty}^{\infty} \frac{d\omega}{2\pi} 2\omega A(\omega, \mathbf{p}) = 1, \tag{3.6}$$

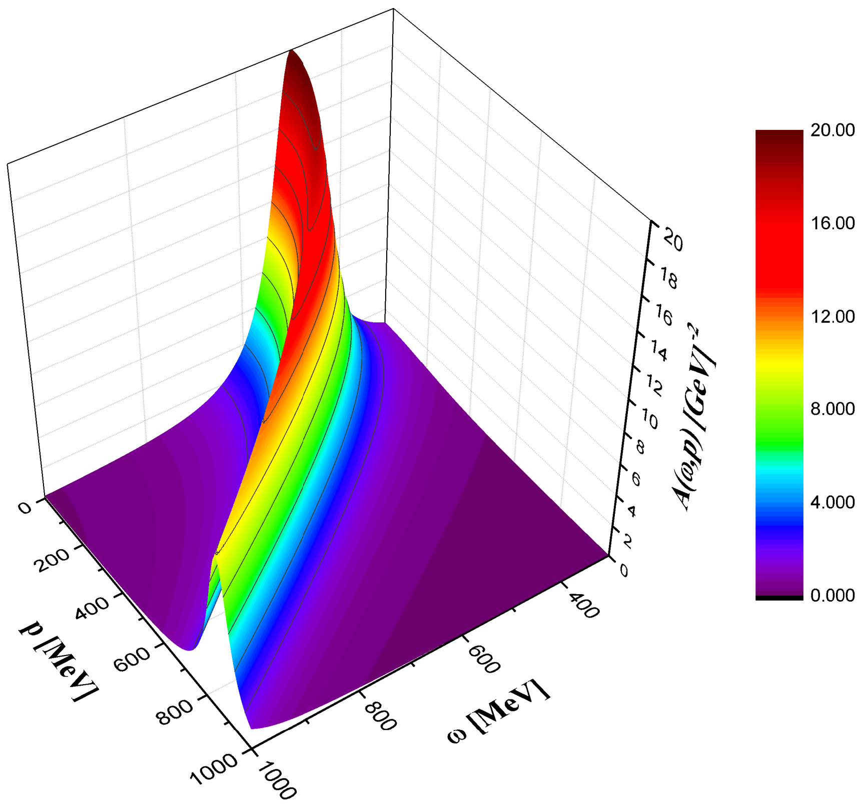

Figure 3.2: Relativistic Breit-Wigner spectral function as a function of the energy ω and the three-momentum $|\mathbf{p}|$ for a mass of $M = 0.47$ GeV and a width of $\gamma = 61$ MeV. This corresponds to the quasiparticle properties of a DQPM quark at $T = 250$ MeV.

for all momenta $\mathbf{p}$. The Breit-Wigner spectral function (3.5) has no poles in the upper half plane and leads to a microcausality conserving retarded propagator [153]. The spectral function for $M = 0.5$ GeV and $\gamma = 50$ MeV as a function of energy ω is shown in Fig. 3.1. It has a maximum at $\omega = \sqrt{\mathbf{p}^2 + M^2}$ and the height of the maximum decreases when the momentum increases. We see that the spectral function decreases rapidly for $\omega \to 0$, but has a non-negligible spacelike contribution for $\omega < |\mathbf{p}|$, shown by the dashed lines. This spacelike part becomes more pronounced with increasing width. Fig. 3.2 shows the spectral function for a mass of $M = 0.46$ GeV and width of $\gamma = 61$ MeV as a function of energy and momentum. This corresponds to a DQPM quark at $T = 250$ MeV and vanishing chemical potential. The peak of the spectral function follows the on-shell dispersion relation $\omega^2 = \mathbf{p}^2 + M^2$ and approaches the light cone $\omega = |\mathbf{p}|$ for high momenta. One sees again that the spacelike part is much smaller than the timelike part and the majority of the spectral function is on the timelike side. Nevertheless, the spacelike part becomes more pronounced as the peak approaches the light cone.

The relativistic Breit-Wigner form (3.5) of the spectral functions was chosen to make the approach compatible with relativistic Kadanoff-Baym dynamics in phase-space representation in first-order gradient expansion [31], where the spectral functions are also of relativistic Breit-Wigner form, see Sec. 2.5.2. This is very important since the quasiparticle properties of the DQPM are used to describe the partonic phase in the PHSD transport approach [144, 145], that is based on the Kadanoff-Baym transport equations [30, 31]. In general the time evolution of every approach with known selfenergies can be simulated in the Kadanoff-Baym framework, if one assumes Breit-Wigner spectral functions.

In Appendix A.2 we apply the explicit form of the propagators and the selfenergies to the entropy and the particle density (3.1) and (3.2). We split them into two parts $s^{dqp} = s^{(0)} + \Delta s$ and $n^{dqp} = n^{(0)} + \Delta n$ where the first part is the on-shell contribution that depends only on the effective mass while the second part is the off-shell contribution that depends also on the width and will vanish in the on-shell limit $\gamma \to 0$. The thermodynamics for vanishing chemical potential follows in a thermodynamic consistent way from the entropy density by

$$P(T) = P(T_0) + \int_{T_0}^{T} s(T')dT'. \tag{3.7}$$

The selfenergies have to be defined such that the model reproduces the lQCD equation of state. This defines the interactions in

accordance with the dynamics of real QCD. We use parametrizations that are motivated by hard-thermal-loop perturbation theory (HTL) [154]. The dressed masses are proportional to the temperature and behave like $M \sim gT$, a standard result from thermal field theory [107]. Including also the correction for finite quark chemical potential the masses are parametrized as [31, 78, 79, 141]:

$$M_g^2\left(T, \mu_q\right) = \frac{g^2}{6}\left(\left(N_c + \frac{1}{2}N_f\right)T^2 + \frac{N_c}{2}\sum_q \frac{\mu_q^2}{\pi^2}\right), \tag{3.8}$$

$$M_{q,\bar{q}}^2\left(T, \mu_q\right) = \frac{N_c^2 - 1}{8N_c} g^2 \left(T^2 + \frac{\mu_q^2}{\pi^2}\right), \tag{3.9}$$

and the widths are given by [141]:

$$\gamma_g\left(T\right) = \frac{1}{3}N_c\frac{g^2 T}{8\pi}\ln\left(1 + \frac{2c}{g^2}\right), \tag{3.10}$$

$$\gamma_{q,\bar{q}}\left(T\right) = \frac{1}{3}\frac{N_c^2 - 1}{2N_c}\frac{g^2 T}{8\pi}\ln\left(1 + \frac{2c}{g^2}\right). \tag{3.11}$$

Here N_c is the number of colors while N_f is the number of flavors. The parameter c is fixed to $c = 14.4$ and has the meaning of a magnetic cutoff, while g^2 is the effective coupling and connected to the coupling constant of QCD ($\alpha_s = \frac{g^2}{4\pi}$). It depends on the temperature and the chemical potential $g^2(T, \mu)$. The masses and widths for quarks and gluons are shown in Fig. 3.3 as a function of temperature at vanishing chemical potential. All quantities have a minimum at $T \approx 200$ MeV and rise almost linearly for

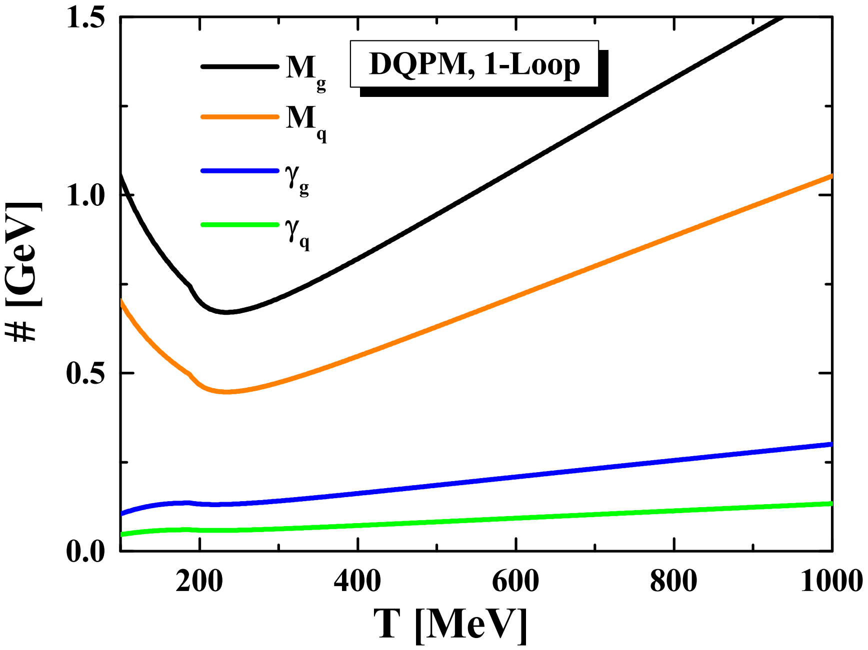

Figure 3.3: The effective masses and widths for quarks and gluons in the DQPM for the 1-loop inspired coupling g^2 taken from Eq. (3.14) and (3.16) at vanishing chemical potential. The kink at $T \approx 190$ MeV comes from the merging of the two parametrizations for the effective coupling. The widths have a minimum at $T \approx 200$ MeV and rise continuously at larger temperatures.

higher temperatures. The ratios between the gluon and the quark properties are

$$\frac{M_g^2}{M_{q,\bar{q}}^2} = \frac{\gamma_g}{\gamma_{q,\bar{q}}} = \frac{9}{4} \tag{3.12}$$

at vanishing chemical potential. They are related to the ratios of the Casimir eigenvalues in color space [31]. The ratio between width and mass is proportional to

$$\frac{\gamma}{M} \sim g \ln\left(1 + \frac{2c}{g^2}\right). \tag{3.13}$$

It increases with temperature up to 250 − 300 MeV while it decreases very slowly for high T. The ratio is approximately $\gamma_g/M_g \approx 0.2$ for the gluons and $\gamma_{q,\bar{q}}/M_{q,\bar{q}} \approx 0.12$ for the quarks at all temperatures larger than 200 MeV.

The widths (3.10) and (3.11) differ from their parametrizations in Ref. [79] where they were first introduced. This is due to the change in the lattice data. When the DQPM was first introduced the only reliable calculations for the lQCD equation of state were provided by the Bielefeld collaboration [155]. These calculations showed a much larger critical temperature of $T_c \approx 190$ MeV than the actual calculations. The lower critical temperature of $T_c \approx 155$ MeV in Refs. [38, 39] was not compatible with the old functional

form, a fate DQPM shared with many other effective theories like NJL and PNJL [84]. The width was changed several times to account for new lQCD results that demanded larger couplings. The actual parametrizations Eqs. (3.10) and (3.11) are positive for arbitrary large couplings and were used to fit the lQCD results from the Wuppertal-Budapest collaboration from Ref. [136]. The latest results from Ref. [90] show only marginal deviations from these. It may seem as if the widths can be chosen arbitrarily and that is, at least for the thermodynamics, true. One can change the width and still get the same equation of state by simply adjusting the effective coupling. On the contrary, the widths have an important impact on the transport coefficients, as we will see in Sec. 3.4. The correct ratios of width to mass (γ/M) are crucial for the proper description of the transport coefficients and one can not choose them independently.
The masses and widths are functions of the temperature and the chemical potential but also of the effective coupling g^2, that contains the non-perturbative information of the system [156] and depends also on the medium. We have to parametrize the coupling as a function of temperature and chemical potential to close the theory. A common parametrization for zero chemical potential is [151, 152]:

$$g^2\left(T, T_c\right) = \frac{48\pi^2}{(11N_c - 2N_f)\ln\left(\lambda^2\left(T/T_c - T_s/T_c\right)^2\right)}, \tag{3.14}$$

with the parameters $\lambda = 2.42$ and $T_s = 0.56\ T_c$ [141]. This parametrization is motivated by the QCD coupling constant α_s in first-order perturbation theory:

$$\alpha_s(p^2) \sim \frac{1}{\ln(p^2/\Lambda^2)}. \tag{3.15}$$

For finite temperature we exchange the momentum with the temperature and obtain roughly Eq. (3.14) [157]. This leads to the right high temperature limit $g^2(T) \to 1/\ln T^2$. One drawback of the parametrization (3.14) is that it breaks down for temperatures slightly above the critical temperature. For this reason one has to use the parametrization

$$g^2(T, T_c) = g^2(\Lambda T_c, T_c) \cdot \left(\frac{\Lambda T_c}{T}\right)^\eta, \tag{3.16}$$

with $\Lambda = 1.19$ and $\eta = 3.1$ for $T < \Lambda \cdot T_c = 188$ MeV [84]. This allows to extend the DQPM even below T_c, although we do not use the correct degrees of freedom and the partons have to become very heavy to compensate for that. The effective coupling from Eq. (3.14) and (3.16) is the blue line shown in Fig. 3.4. The coupling decreases slowly at high temperatures, leading to masses and widths that are almost linear as functions of the temperature, see Fig. 3.3. The parameters given above were achieved by fitting the model to lQCD data from Ref. [136]. A fit to the more recent data from Ref. [90] leads to the parameters

$$\lambda = 3.2, \qquad T_s = 0.84\ T_c, \qquad \Lambda = 1.58, \qquad \eta = 2.75. \tag{3.17}$$

This set gives a better description for the high temperature limit of the equation of state.

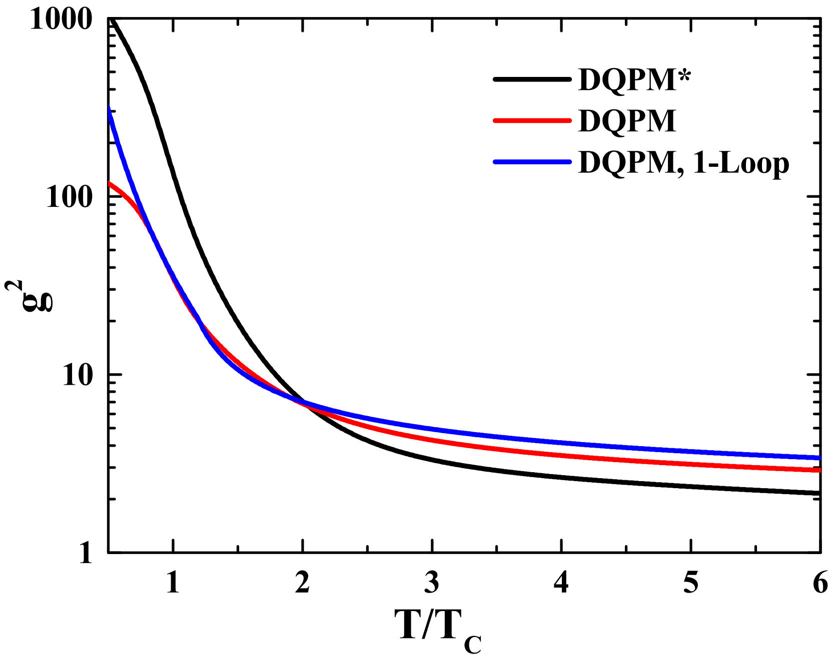

Figure 3.4: The DQPM effective coupling g^2 for different parametrizations as a function of the scaled temperature T/T_c. The blue line shows the parametrization as a function of the temperature from the 1-loop inspired coupling from Eq. (3.14) and (3.16). The switching between both functions happens at $T = 188$ MeV, i.e. $T/T_c = 1.19$. The red line is the parametrization as a function of the entropy density (3.19). Both agree well above the critical temperature. The black line shows the effective coupling for the case of momentum-dependent masses and widths in the DQPM* (3.27) (Section 3.2).

The above ansatz for the effective coupling provides a good description of the lQCD equation of state at vanishing chemical potential [145], but has the drawback, that the coupling is not continuously differentiable, leading to a second-order phase transition at the merging temperature $\Lambda \cdot T_c$. A way to cure this is to determine the coupling for every temperature T to reproduce the entropy density from the lattice. Since this method is very time consuming, we will present a more elegant way:
First we define the masses and widths as a function of both, the temperature and the effective coupling, i.e. $M^2 = M^2(T, g^2)$ and $\gamma = \gamma(T, g^2)$. In this way the masses and widths are proportional to the temperature. If we calculate now the entropy density, which is then also a function of the temperature and the coupling, we see that $s(T, g^2)/T^3$ is a constant for different temperatures but identical g^2. One can also show that $\frac{\partial}{\partial T}(s(T, g^2)/T^3)$ is numerically zero. The entropy density and therefore the complete dimensionless equation of state in the DQPM is a function of only the effective coupling g^2. The function

$$f(g^2) = \frac{1}{(1 + a_1 \cdot (g^2)^{a_2})^{a_3}} \tag{3.18}$$

gives a perfect description of the scaled entropy $s(T, g^2)/s_{SB}(T) = f(g^2)$. We can invert

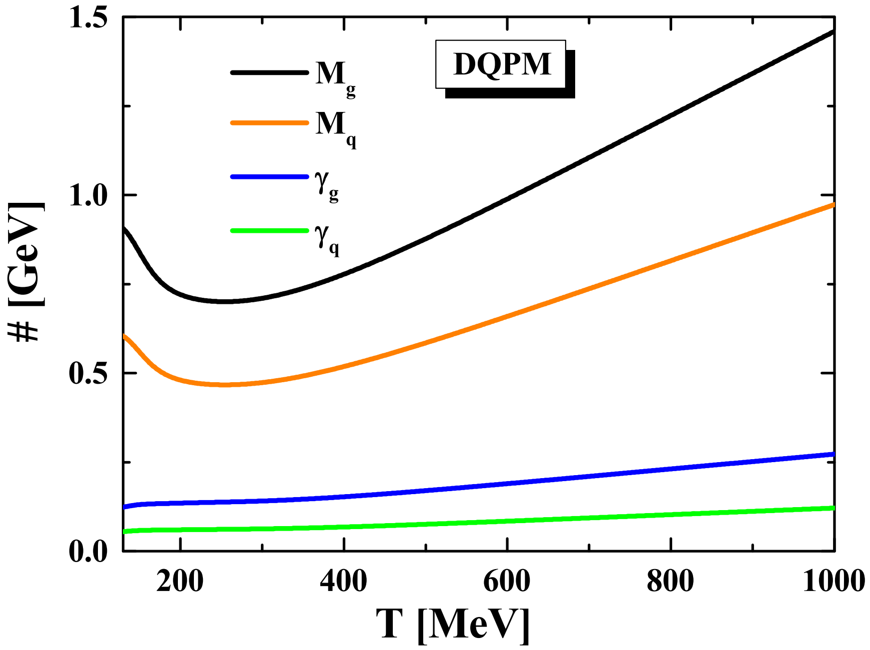

Figure 3.5: The effective masses and widths for quarks and gluons in the DQPM for the effective coupling g^2 from Eq. (3.19). Both widths are continuously rising with temperature. There are no kinks in the parametrizations different to the masses and widths from the 1-loop inspired effective coupling in Fig. 3.4.

$f(g^2)$ and get the effective coupling g^2 as a function of the entropy density,

$$g^2(s/s_{SB}) = g_0 \left(\left(\frac{s}{s_{SB}} \right)^b - 1 \right)^d , \tag{3.19}$$

with $g_0 = 169.934$, $b = -0.178434$, $d = 1.14631$ and $s_{SB}^{QCD} = 19/9\pi^2 T^3$. The parameters are obtained in the range $g^2 < 50$ that belongs to temperatures $T > 100$ MeV. The limit $s = s_{SB}$ gives $g^2 = 0$, therefore consequently $M = \gamma = 0$. Since the lQCD entropy has the right high-temperature limit also the effective coupling obtained from it has the right behavior and decreases like $g^2 \sim 1/\log(T^2)$.

With this new parametrization we can easily adapt to any equation of state and are no longer forced to refit the effective coupling for new lQCD data. We use the equation of state provided by the Wuppertal-Budapest collaboration in Ref. [90] and parametrize the entropy density as discussed in Sec. 2.4. By inserting the entropy density in the coupling (3.19) we get the effective coupling as a function of the temperature $g^2(s) = g^2(s(T)) = g^2(T)$. The result is the red line shown in Fig. 3.4. It decreases faster than the original parametrization (3.14) leading to slightly lower masses and therefore a larger equation of state, but does coincide with the power law from Eq. (3.16) for $T \approx T_c$.

The masses and widths from the coupling (3.19) are shown in Fig. 3.5. The masses still have a minimum at $T \approx 250$ MeV, but the widths are now continuously rising.

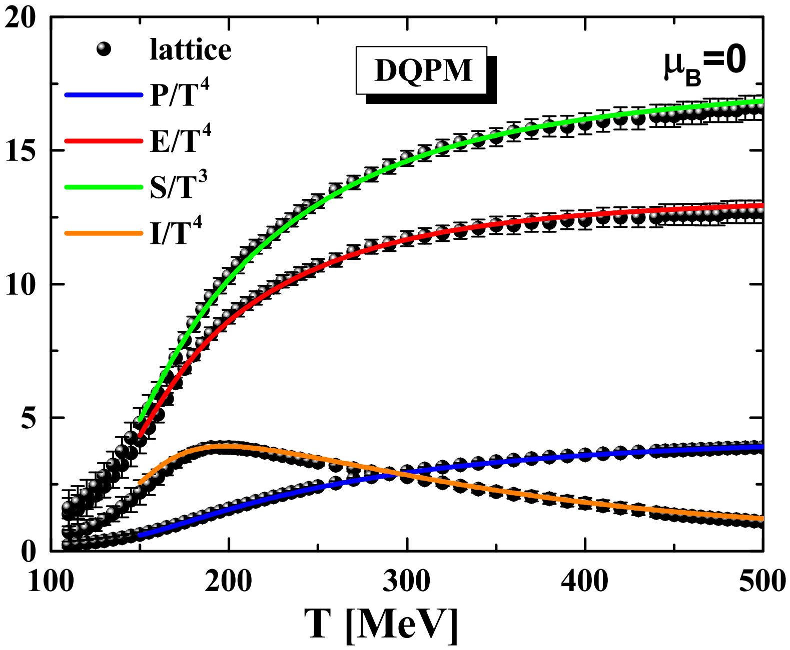

Figure 3.6: The DQPM equation of state as a function of the temperature T for vanishing baryon chemical potential using Eq. (3.19) for the effective coupling. The green line shows the entropy density, the red line the energy density, the blue line the pressure and the orange line the interaction measure. All quantities are scaled by powers of the temperature. The DQPM results are within the error bars of the lQCD data taken from the Wuppertal-Budapest collaboration [90].

Compared to the masses and widths from the 1-loop parametrization, Fig. 3.3, all four quantities rise slower and deviate stronger from the nearly linear rise with T. Most importantly, the masses and widths are now continuously differentiable with respect to the temperature.

With the masses and widths defined we can finally calculate the entropy density and thereof the whole equation of state. The major contribution comes from the on-shell part of the entropy density (A.32), that only depends on the masses. The off-shell contribution (A.35), where also the width enters, is small compared to the on-shell part, see Fig. A.2 in Appendix A.2. Accordingly, the whole equation of state is only sensitive to the masses and gets just a small correction from the width. The equation of state calculated with the effective coupling from the lQCD entropy is shown in Fig. 3.6. We compare it to the lQCD results from Ref. [90], that we also used as input for the coupling. The input entropy density calculated from Eq. (2.53) is perfectly reproduced and we find a perfect agreement between the DQPM and the lQCD equation of state within the error bars. Small deviations from the data originate only from the input parametrization that differs slightly from the data. We are even able to describe the interaction measure, which most quasiparticle models struggle to do. The interaction measure is so hard to reproduce because it is the starting point from which the lQCD

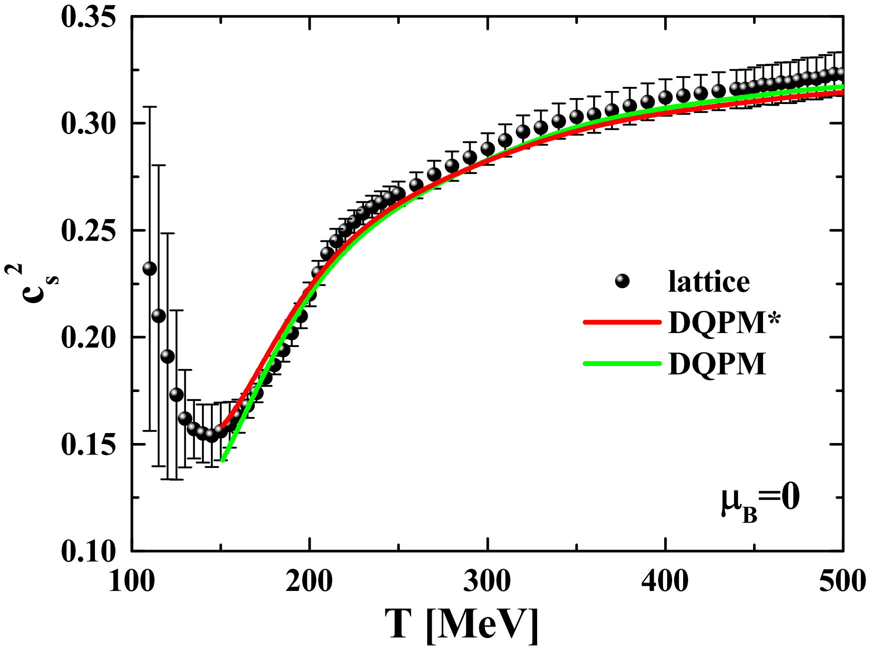

Figure 3.7: The speed of sound squared c_s^2 as a function of the temperature for vanishing baryon chemical potential compared to lQCD results from the Wuppertal-Budapest collaboration from Ref. [90]. The green line is the result for the regular DQPM, the red line from the extended DQPM* (Section 3.2).

entropy is calculated. The entropy density on the other side is the first quantity that quasiparticle models calculate and from which the interaction measure follows. It is therefore extremely sensitive to the effective coupling. The equation of state in Fig. 3.6 is only shown for temperatures larger than $T > 150$ MeV, which is the region where we expect partonic degrees of freedom. However, the effective coupling as a function of the entropy density (3.19) can be used at arbitrary temperatures even down to the vacuum at $T = 0$.

The dimensionless equation of state rises very slowly towards the Stefan-Boltzmann (SB) limit. This is the reason why the parton masses have to rise almost linear with the temperature. If they would increase slower the entropy would approach the SB limit too fast. The slow increase in the scaled entropy density is entirely due to the decrease of the effective coupling g^2 with T.

The entropy density, like the energy density and the pressure, displays a sharp rise in the temperature window $T = 150 - 250$ MeV while the interaction measure has a maximum. This is connected to a change in the degrees of freedom, when the hadrons dissolve into partons. Since there is no real phase transition, only a crossover, we can not identify a phase transition in the equation of state. Possible ways to still determine a transition temperature are when the energy reaches 50% of its Stefan-Boltzmann limit or at the inflection point of the scaled equation of state or at the maximum of the interaction measure. We will discuss this problem in the next section 4 in terms of the NJL model.

In general one should look at the proper order parameters, that is the chiral condensate for chiral symmetry restoration or the Polyakov loop for the deconfinement transition, but we can not access them in the DQPM.

Another important thermodynamic quantity is the speed of sound. The speed of sound squared is defined by the derivative of the pressure with respect to the energy and gives the speed at which turbulences travel through the medium,

$$c_s^2 = \frac{\partial P}{\partial E}. \tag{3.20}$$

The expansion of the fireball in a heavy-ion collision is controlled by the speed of sound which connects it to the elliptic flow v_2 [7, 22, 24]. As one can imagine it is much more sensitive to the equation of state than even the interaction measure. The hadron-resonance gas, a popular model for low temperature QCD, can reproduce the equation of state within error bars, but has the wrong c_s^2, see Sec. 5.1. The DQPM speed of sound squared is shown in Fig. 3.7 and compared to the lQCD data from Ref. [90]. The DQPM describes the rise in c_s^2 after the phase transition and also gives the right behavior in the high temperature regime. The results are completely within the error bars. We mention again, that the speed of sound is a continuous function since the effective coupling is now continuously differentiable.

In conclusion, we showed that the new parametrization of the effective coupling g^2 in terms of the entropy density is able to reproduce the equation of state and the speed of sound. All quantities are within the error bars of the lQCD results in the whole partonic temperature range $T > T_c \approx 158$ MeV. Eq. (3.19) defines the effective coupling for any given entropy density. This will allow us to use any new lQCD equation of state without any novel parameter tuning.

3.2 DQPM*

The masses in the DQPM increase with the temperature due to interactions with the medium. This is a good approximation if the particle has a low momentum but gives the wrong physics if the momentum is large compared to the temperature. In this case perturbation theory becomes accessible and the partons should behave like almost massless particles. This is not taken into account in the standard DQPM.

The momentum dependence of the quark mass is a well known result from Dyson-Schwinger equations [121, 158]. The propagator at small momenta behaves like the propagator of a massive particle and changes as the momentum increases to the bare perturbative propagator for $|\mathbf{p}| \to \infty$. In a simplified picture one could explain this with a momentum-dependent mass that drops from the constituent quark mass down to the bare mass as the 4-momentum p^2 increases. The same should happen in the DQPM where the medium induced selfenergy takes the place of the dynamical generated quark mass (squared). Since the underlying propagators of the DQPM respect causality [153] we can not vary the mass as a function of the 4-momentum, but only with the three-momentum $\mathbf{p}$ relative to the medium at rest,

$$G(\omega,\mathbf{p}) = \frac{-1}{\omega^2 - \mathbf{p}^2 - M^2(\mathbf{p}^2) + 2i\gamma(\mathbf{p}^2)\omega}. \tag{3.21}$$

This ensures that the propagator stays analytic in the upper half plane, the poles are at $\omega = -i\gamma(\mathbf{p}^2) \pm \sqrt{M^2(\mathbf{p}^2) - \gamma^2(\mathbf{p}^2)}$, and causality is preserved. Another constraint on the momentum dependence is that the width of the particle has to vanish in the same way or faster than the mass. This will keep $\sqrt{M^2(\mathbf{p}^2) - \gamma^2(\mathbf{p}^2)}$ real [153].

We assume that the rates, at which the selfenergies vanish with $\mathbf{p}^2$, is similar at finite temperature as in the vacuum Dyson-Schwinger calculations from Refs. [121, 158]. This is supported by the results from Ref. [159] where Dyson-Schwinger equations were solved at finite temperature. One found that the propagator at finite temperature behaves similar to the one in the vacuum with respect to the Euclidean-4-momentum squared $p^2 = \omega^2 + \mathbf{p}^2$.

We have parametrized the momentum dependence already in Refs. [85, 86]. The masses are given by the expressions

$$M_g(T,\mu_q,\mathbf{p}) = \frac{3}{2}\cdot\left[\frac{g^2}{6}\left(\left(N_c + \frac{1}{2}N_f\right)T^2 + \frac{N_c}{2}\sum_q \frac{\mu_q^2}{\pi^2}\right)\right]^{1/2} \cdot h(\Lambda_g,\mathbf{p}) + m_{g0}, \tag{3.22}$$

$$M_{q\bar{q}}(T,\mu_q,\mathbf{p}) = \left[\frac{N_c^2-1}{8N_c}g^2\left(T^2 + \frac{\mu_q^2}{\pi^2}\right)\right]^{1/2} \cdot h(\Lambda_{q\bar{q}},\mathbf{p}) + m_{q0}. \tag{3.23}$$

These are the DQPM masses (3.8) and (3.9) multiplied by a factor $h(\Lambda,\mathbf{p})$ that controls the momentum dependence and an additional factor 3/2 in the gluon mass, that we will explain later. We also added the bare masses to ensure the right limit for $p^2 \to \infty$. The widths are also modified and given by

$$\gamma_g(T,\mu_q,\mathbf{p}) = N_c\frac{g^2T}{8\pi}\log\left(\frac{2c}{g^2} + 1.1\right)^{3/4} \cdot h(\Lambda_g,\mathbf{p}), \tag{3.24}$$

$$\gamma_{q\bar{q}}(T,\mu_q,\mathbf{p}) = \frac{N_c^2-1}{2N_c}\frac{g^2T}{8\pi}\log\left(\frac{2c}{g^2} + 1.1\right)^{3/4} \cdot h(\Lambda_{q\bar{q}},\mathbf{p}). \tag{3.25}$$

The shape of the momentum dependence is inspired by results from Refs. [121, 158]:

$$h(\Lambda,\mathbf{p}) = \frac{1}{\sqrt{1 + \Lambda\cdot\mathbf{p}^2\cdot(T_c/T)^2}}. \tag{3.26}$$

The open parameters are taken as $\Lambda_g = 5$ GeV^{-2}, $\Lambda_{q\bar{q}} = 12$ GeV^{-2}, $m_{g0} = 0.5$ GeV, $m_{u0} = m_{d0} = 0.003$ GeV and $m_{s0} = 0.06$ GeV. This extension of the DQPM will lead to the right perturbative limit for the quasiparticle properties at high momentum with respect to the thermal medium at rest. We call this generalized quasiparticle model DQPM* [85, 86].

Due to the momentum dependence of the quasiparticle properties we can no longer use

	$v(T)$	$w(T)$	$d(T)$
a	-0.0032356	1.20963	0.939529
b	2.88262	1.59028	1.45117
c	0.0116952	0.0728608	0.132123
d	0.411954	0.60418	0.6707
e	0.0850924	0.164018	0.111489

Table 3.1: Parameters for the functions (3.29) in the effective DQPM* coupling (3.27).

Eq. (3.19) for the effective coupling. We can still fit the entropy density as a function of g^2 employing Eq. (3.18), but the fit parameters will change with temperature. This is the effect of the temperature dependence in the function $h(\Lambda, \mathbf{p})$ (3.26). We will therefore turn the fit parameters from Eq. (3.18) into a function of temperature and describe them also by a fitting function. The effective coupling of the DQPM* then is a function of the entropy density and the temperature,

$$g^2(s/s_{SB}, T) = g_0(T) \cdot \left(\left(\frac{s/s_{SB}}{d(T)} \right)^{v(T)} - 1 \right)^{w(T)} . \tag{3.27}$$

We have introduced an additional parameter $d(T)$ compared to Eq. (3.18). The DQPM masses and widths go to zero for $g^2 \to 0$ resulting in the Stefan-Boltzmann limit for the entropy density. In the DQPM* we can not reach this limit as the masses will drop to their bare values and not to zero. The factor $d(T)$ effectively rescales the Stefan-Boltzmann limit.

The prefactor $g_0(T)$ in Eq. (3.27) is given by

$$g_0(T) = 49000 + 30500/T, \tag{3.28}$$

for T in units of GeV. The other parameters $v(T)$, $w(T)$ and $d(T)$ are all fitted with the same function

$$r(T) = \frac{a}{(T^b + c)^d} \cdot (T + e) , \tag{3.29}$$

also for T in units of GeV. The parameters for Eq. (3.29) are shown in Tab. 3.1. The calculation of the fitting functions is computationally expensive as one has to calculate the entropy density for all temperatures and effective couplings and perform several fits. We extracted the parameters in the temperature range between 150 MeV and 500 MeV. The range in the effective coupling was adjusted to this temperature region. One has to redo the fit if one changes the parametrization of the masses, the width or their momentum dependence. We had to iterate this process until we found good results for the equation of state, the susceptibility, that we will discuss later in this section, and also the transport coefficients, that we discuss in Sec. 3.4. The result of the iteration are the formulae shown above. We had to change the coupling in a way, that it no longer reproduces the exact input entropy, but allows for small deviations from it. As long as the input entropy changes not too drastically, one can still reproduce it. Since we expect no large changes in the equation of state to arise from lattice QCD anymore, we can use this fit to describe small corrections to the lQCD equation of state in the future. If we get for some reason a more drastic change in the data, we have to repeat the iteration. Nevertheless, we assume that the chances for this are very small, as different equations of state started to overlap each other [90, 91].

The effective coupling g^2 of the DQPM* is still only a function of the temperature and the chemical potential and not of the three-momentum $\mathbf{p}$. It would be more precise to argue that the high momentum limit alters the coupling and that this gets reflected in the selfenergies. We made the ansatz that we can pull out the momentum dependence and added it directly to the masses and widths, thus keeping the effective coupling momentum independent.

The effective coupling for the DQPM* was already shown as the black line in Fig. 3.4 together with the corresponding coupling of the DQPM (3.19) and the one-loop parametrization of the DQPM coupling (3.14) and shows the same general behavior as the other couplings. It is a very large function at low temperatures that drops down and becomes small at high temperatures. Its functional form at high temperatures is similar to $1/\ln(T^2)$, reproducing the right high temperature limit. Nevertheless, it is different to the DQPM as it is much larger at low temperatures. Since the masses in the DQPM* decrease with the momentum, they have to become larger to reproduce the same entropy density as the regular DQPM. This is reflected in the effective coupling. We show the masses and the width of the DQPM* for $|\mathbf{p}| = 0$ in Fig. 3.8. We see that all quantities are about four times larger than in the DQPM at small temperatures, cf. Fig. 3.5. This changes if the three-momentum increases. The momentum-dependent function $h(\Lambda, \mathbf{p})$ becomes smaller at low temperature and one regains the known functional form of the DQPM. The DQPM* shows the same linear rise at high temperatures as the DQPM. This is kept for all momenta, but the onset of the rise gets shifted towards smaller temperatures as the momentum increases.

We will now discuss the equation of state for the DQPM*. This is similar to our work in Refs. [85] and [86], where we used the lQCD data from the Wuppertal-Budapest collaboration from Ref. [136] as input for the effective coupling (3.27). Throughout this thesis we will always use the more recent results from Ref. [90]. The equation of state of the DQPM* is slightly different from the DQPM, despite the same input entropy. This is a result of the not perfect fit of the effective coupling (3.27) with respect to the entropy density, but we still get a very good reproduction of the lQCD equation of state, as shown in Fig. 3.9. The most outstanding difference is seen at low temperatures just below the transition temperature. The interaction measure I/T^4 is not compatible with the lQCD data for $T < 150$ MeV. The reason for the large difference at this temperatures is due to the fitting procedure, that employed $T = 150$ MeV as the lowest temperature, so the fit is not very reliable close to these temperatures. We find also small differences at very high temperatures. The DQPM* gives a larger entropy, and

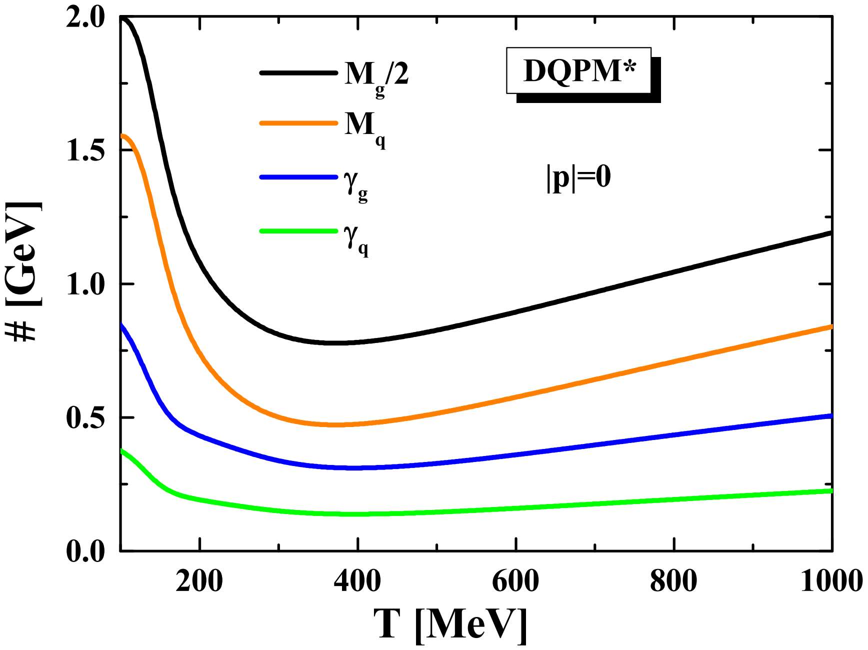

Figure 3.8: The effective masses and widths for quarks and gluons in the DQPM* for $|\mathbf{p}| = 0$ for the effective coupling g^2 taken from Eq. (3.27). The gluon mass, the black line, is divided by a factor 2. All four lines rise continuously for larger temperatures.

therefore energy and pressure, than the DQPM. If we look at the temperature dependence over the whole temperature range we see that the DQPM follows the line of the data much better then the DQPM*, that has some problems with the bending of the equation of state at $T = 200 - 250$ MeV. However, all these deviations are small and the DQPM* above $T = 170$ MeV is completely consistent within the error bars of the lQCD calculations. The speed of sound from both models and the lattice is shown in Fig. 3.7. The red line shows the DQPM* and the green line the DQPM result. We find again that both models are within the error bars in the whole temperature range. The DQPM works better at very high temperatures and near the transition temperature; in between the DQPM* gives better results.

The description of the equation of state for the two quasiparticle models is excellent. Both reproduce the equation of state within the precision of the lQCD calculations and the parametrizations of the effective couplings allow us to adapt to any small corrections of the lattice predictions. All we have to do is to fit the entropy. With the thermodynamics at vanishing chemical potential under control we can now extend the model to finite chemical potential. However, before we discuss the baryon number susceptibilities,

$$\chi_B^n = \left.\frac{\partial^n P}{\partial \mu_B^n}\right|_{\mu_B=0}. \qquad (3.30)$$

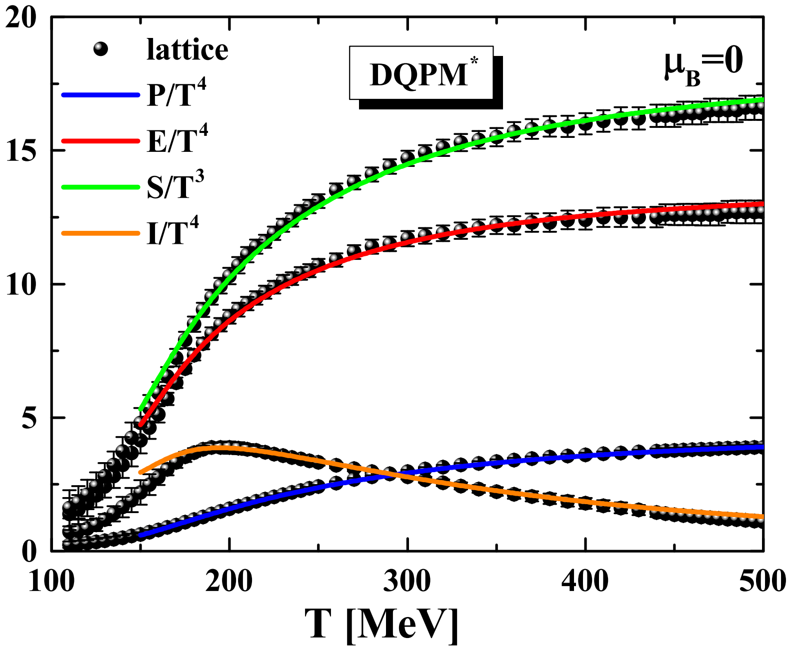

Figure 3.9: The DQPM* equation of state as a function of the temperature T for vanishing baryon chemical potential. The green line shows the entropy, the red line the energy, the blue line the pressure and the orange line the interaction measure. All quantities are scaled by powers of the temperature. The DQPM* results are within the error bars of the lQCD data for $T > 170$ MeV. The lQCD results are taken from the Wuppertal-Budapest collaboration from Ref. [90].

They define the expansion of the pressure for small baryon chemical potentials:

$$\frac{P(T,\mu_B)}{T^4} = \sum_{n=0} \frac{1}{n!}\chi_B^n \left(\frac{\mu_B}{T}\right)^n \approx \frac{P(T,\mu_B=0)}{T^4} + \frac{1}{2}\chi_B^2 \frac{\mu_B^2}{T^2}. \tag{3.31}$$

The susceptibilities are defined at vanishing chemical potential and can be calculated in lQCD simulations [40, 41, 42, 89, 135, 160, 161]. Since QCD is symmetric under $\mu_B \to -\mu_B$ all odd susceptibilities have to vanish, most important is therefore the second-order baryon number susceptibility $\chi_B^2 = \chi_B$. It is the leading term at finite baryon chemical potential and controls the equation of state at small μ_B. We will compare the lQCD susceptibilities with the DQPM and the DQPM* predictions in the following.

The second-order susceptibility is the derivative of the first-order susceptibility, which is the net-baryon density, with respect to the baryon chemical potential:

$$\frac{\partial^2 P}{\partial \mu_B^2} = \frac{\partial}{\partial \mu_B}\rho_B = \frac{1}{9}\frac{\partial n_q}{\partial \mu_q} = \chi_B = \frac{1}{9}\chi_q. \tag{3.32}$$

It is only sensitive to the quark degrees of freedom. Since the quark density in the DQPM consists of two separate contributions $n = n^{(0)} + \Delta n$, the susceptibility consists also of two terms $\chi_q = \chi_q^{(0)} + \Delta\chi_q$. Symmetries demand that the pressure has to be an even function in μ_B, $P(\mu_B) = P(-\mu_B)$, which implies that also the energy and the entropy have to be even in μ_B and the density, that contributes with $\mu_B \cdot \rho_B$ to the pressure, has to be odd. This can only be fulfilled, if the masses, the width and the effective coupling g^2 are even functions of μ_B as well. Therefore their derivatives at $\mu_B = 0$ have to vanish. With this we can analytically evaluate the equations for the quark number susceptibilities $\chi_q = \chi_q^{(0)} + \Delta\chi_q$ that are given by

$$\chi_q^{(0)} = \frac{1}{2\pi^2 T} \int_0^\infty dp\, p^2 \, \frac{1}{1+\cosh\left(\omega_p/T\right)}, \tag{3.33}$$

and

$$\begin{aligned} \Delta\chi_q = \int_{d^4p} & \frac{\sinh\left(\frac{\omega}{T}\right)}{T^2\left(1+\cosh\left(\frac{\omega}{T}\right)\right)^2} \\ & \times \left(2\gamma\omega \frac{\omega^2-\mathbf{p}^2-M^2}{(\omega^2-\mathbf{p}^2-M^2)^2+4\gamma^2\omega^2} - \arctan\left(\frac{2\gamma\omega}{\omega^2-\mathbf{p}^2-M^2}\right)\right), \end{aligned} \tag{3.34}$$

without degeneracy factors, except for the quark/antiquark degeneracy. The Stefan-Boltzmann limit for the susceptibility is $\chi_q = T^2/6$ and $\chi_q^{QCD} = 3\ T^2$ for QCD. In case of the baryon number susceptibility one has to divide it by 9 and finds $\chi_B^{QCD} = T^2/3$. The masses and widths in Eq. (3.33) and (3.34) are the DQPM or DQPM* masses and widths for zero chemical potential. The susceptibility is completely defined by the $\mu_B = 0$ equation of state. The interaction term $\Delta\chi_q$ is, similar to the entropy density, just a small correction and we get the major contribution from the pole term $\chi_q^{(0)}$.

We show the baryon number susceptibility from the DQPM and DQPM* in comparison to the susceptibility from the Wuppertal-Budapest collaboration from Ref. [135] in Fig. 3.10. We display additionally the results from the NJL and the PNJL model, which we will discuss in detail in chapter 4. We choose the parameter set from Ref. [162] for the quark sector and a logarithmic Polyakov potential, cf. Eq. (4.20), with additional quark back reaction for the gluon sector, cf. Eq. (4.26). The DQPM* and the PNJL can roughly describe the lQCD data, while the DQPM and the NJL fail. The NJL susceptibility rises too fast against the Stefan-Boltzmann limit, reflecting the small quark masses at large temperatures. The PNJL, that has almost the same masses, gives a lower result. The reason is, that the distribution function of the PNJL is suppressed by the Polyakov loop. The opposite happens in the DQPM. The quark masses are too heavy, so the susceptibility rises too slow and can not describe the data. The DQPM* masses, that are initially even larger, become smaller due to the momentum dependence and increase the susceptibility compared to the DQPM.

We tried to reproduce the susceptibility and the equation of state with momentum-independent selfenergies. Since it was already reported in Ref. [82] that a normal quasiparticle model is not able to simultaneously reproduce the equation of state and the susceptibility, we investigated the influence of the width. We varied the ratio between the masses and the widths while keeping the equation of state fixed to the lattice.

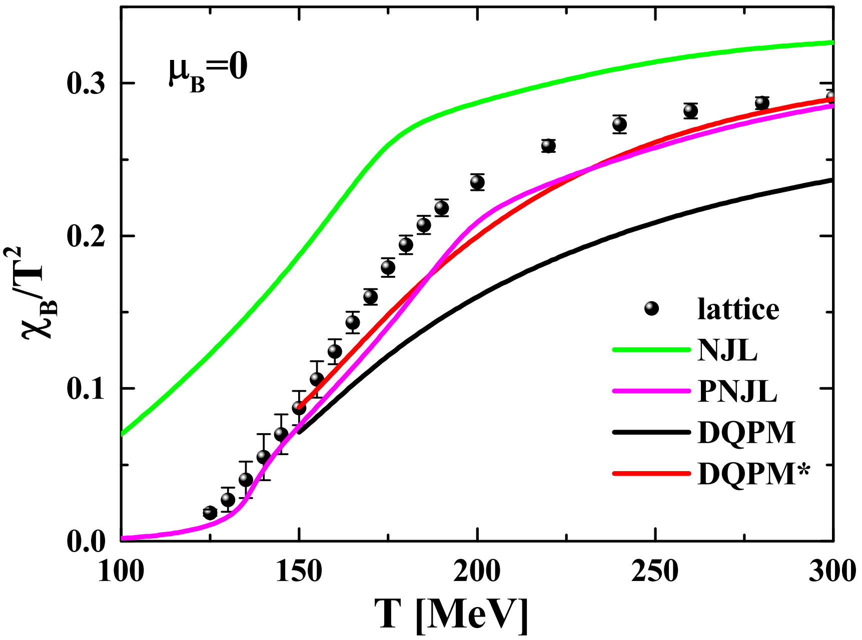

Figure 3.10: The quasiparticle baryon number susceptibility as a function of the temperature T for vanishing baryon chemical potential. The black line is the result from the DQPM, the red line from the extended DQPM*. The green line shows the result from the NJL and the magenta line from the PNJL model with the parameter set from Ref. [162] for the quark sector and the logarithmic Polyakov potential (4.20) with quark back reaction for the gluon sector (4.26). The lQCD results are taken from the Wuppertal-Budapest collaboration from Ref. [135].

Unfortunately, an increase of the width decreases the susceptibility even more. The standard quasiparticle approach with $\gamma = 0$ [81, 82, 163] leads to the best, but still insufficient, result. In a next attempt we fixed the width to zero and took the quark and gluon masses as independent variables. We fitted the quark mass for every temperature to the susceptibility and calculated the entropy. It turned out that the quark entropy density alone was then larger than the total QCD entropy density. This brings us to the conclusion that it is impossible for a quasiparticle model to reproduce simultaneously the equation of state and the susceptibility with momentum-independent selfenergies. For this one has to introduce a momentum dependence as in the DQPM*, that will enhance the distribution function at finite three-momentum. This will affect the susceptibility stronger than the entropy density such that it becomes possible to describe both. Nevertheless, we found that we need more strength in the quark sector and had to add a factor of 3/2 to the gluon mass. This factor breaks the Casimir scaling of the masses in Eq. (3.12). It is not clear if we would need this factor also in the large N_f-limit [164], where the Casimir scaling should hold again [165].
The correct behavior of the susceptibility χ_B is crucial for the extension to finite baryon chemical potential, since it controls the equation of state at small μ_B. Every approach

that can not reproduce the susceptibility will also not be able to reproduce the equation of state at small baryon chemical potentials. It becomes apparent that the DQPM* is the only quasiparticle model with a reasonable extension to finite baryon chemical potential.

3.3 The DQPM at finite chemical potential

The last section was dedicated to vanishing chemical potential but in this section we want to discuss the extension of our quasiparticle models towards finite chemical potential. The entropy $s = s^{(0)} + \Delta s$ in Eqs. (A.32) and (A.35) and the particle density $n = n^{(0)} + \Delta n$ in Eqs. (A.36) and (A.37) are already defined for arbitrary chemical potentials, so we only need to extend our quasiparticle properties to finite μ. The HTL motivated masses (3.8) and (3.9) incorporate also the effects of the chemical potential. They depend on an effective temperature $T^{*2} = T^2 + \mu_q^2/\pi^2$. The widths so far are independent from the chemical potential, since it was found in Ref. [166] that finite μ has no effect on the parton damping rates in the HTL approach, the temperature T is the dominating scale. We will, in accordance with these findings, keep the widths (3.10) and (3.11) μ-independent. This leaves the μ dependence of the effective coupling $g^2(T, \mu)$ as the last missing ingredient for calculations at finite chemical potential.

We can not use the same strategy as for the temperature dependence, since we have no input entropy from lQCD. For the same reason the second-order susceptibility χ_B is of no use, as it is completely defined by the $\mu_B = 0$ equation of state. Only the higher-order susceptibilities are sensitive to finite μ_B and contain non-vanishing contributions from the derivatives of the effective coupling at $\mu_B = 0$. As an example we show here the expression for the pole term of the fourth-order susceptibility χ_B^4 for the DQPM:

$$\begin{aligned}
\chi_B^{4,(0)} &= \frac{d_q}{18\pi^2 T^3} \int_0^\infty dp\, p^2 \left(\frac{1}{1+\cosh\left(\omega_p/T\right)} \right. \\
&\qquad \left. - \frac{1 + \frac{\sinh(\omega_p/T)}{2\omega_p} \left(\frac{2g^2}{\pi^2} T + T^3 \frac{\partial^2 g^2}{\partial \mu_B^2}\big|_{\mu_B=0} \right)}{\left(1+\cosh\left(\omega_p/T\right)\right)^2} \right) \qquad (3.35) \\
&= \frac{\chi_B^{2,(0)}}{T^2} - \frac{d_q}{18\pi^2 T^3} \int_0^\infty dp\, p^2\, \frac{1 + \frac{\sinh(\omega_p/T)}{2\omega_p} \left(\frac{2g^2}{\pi^2} T + T^3 \frac{\partial^2 g^2}{\partial \mu_B^2}\big|_{\mu_B=0} \right)}{\left(1+\cosh\left(\omega_p/T\right)\right)^2} .
\end{aligned}$$

It contains $\frac{\partial^2}{\partial \mu_B^2} g^2$ at $\mu_B = 0$. To access the next non-vanishing derivative we would already need the sixth-order susceptibility. Refs. [40, 41, 42] contain the susceptibilities up to the 6th order, but only under the constraint of strangeness neutrality $N_S = 0$ and a fixed ratio of charge to particle number $N_Q/N_B = 0.4$. The strangeness neutrality would be easy to incorporate, but the charge to particle number ratio is more complicated to consider. Furthermore, the lattice data might not have the necessary precision to extract the derivatives of g^2. In the following we discuss two alternative approaches to solve this problem.

3.3.1 Scaling hypothesis

The first approach was introduced in Ref. [31] and uses phenomenological and scaling arguments. It employs the effective temperature,

$$T_q^* = \sqrt{T^2 + \mu_q^2/\pi^2}, \tag{3.36}$$

that sets the scale for the parton masses at finite μ_B. Note that the chemical potential for the specific quark species enters the effective mass and therefore the effective temperature. It is the same for all quarks as long as only a finite baryon chemical potential $\mu_B = 3\mu_q$ is considered. Additional constraints, that introduce charge or strange chemical potentials, lead to a different T_q^* for different quark species. The scaling hypothesis assumes that the coupling $g^2(T, \mu_B)$ is a function of the ratio of the effective temperature and the critical temperature,

$$g^2(T/T_c, \mu_B) = g^2(T^*/T_c(\mu_B)). \tag{3.37}$$

A finite chemical potential will modify the temperature scale but keeps the coupling itself unchanged. This scaling keeps the parton masses independent from the chemical potential. We refer to Ref. [31] for a detailed discussion of the implications of the scaling hypothesis.

The value of the critical temperature at finite chemical potential $T_c(\mu_B)$, i.e. the phase boundary, is unknown. We will derive an easy approximation for the phase boundary, based on certain assumptions. We assume that the phase transition happens always at the same critical energy density in the whole T-μ_B plane. The critical temperature $T_c \approx 158$ MeV and the corresponding energy density $\epsilon_c = E(T_c) \approx 0.5$ GeV/fm^3 are fixed by lQCD calculations. The resulting phase transition is a monotonic decreasing function, since the energy density is assumed to rise with increasing μ_B. The phase transition will intersect the $T = 0$ axis at the critical chemical potential μ_c. We have studied the energy density at very small temperatures in the simple potential model for nuclear matter, that we will introduce in Sec. 5.2. We found that the lines of constant energy density are perpendicular to the $T = 0$ axis. The same holds at $\mu_B = 0$ since QCD is invariant under the transformation $\mu_B \to -\mu_B$. A simple fit that fulfills all these conditions is the ellipse,

$$\frac{T_c(\mu_B)}{T_c} = \sqrt{1 - \alpha\ \mu_B^2}. \tag{3.38}$$

This function has to vanish at the critical chemical potential μ_c, that is defined by the condition $E(\mu_c) = 0.5$ GeV/fm^3 at zero temperature. We have calculated it for a non-interacting gas of nucleons, which is justified since the energy density in nuclear matter is dominantly a function of the kinetic energy. The potential energy gives only a small correction, see Sec. 5.2. This leads to a critical chemical potential of $\mu_c = 1013.4$ MeV and fixes the parameter $\alpha = 0.974$ GeV^{-2} from the condition $T_c(\mu_c) = 0$.

The critical temperature at finite μ_B is not completely unknown as there is some guidance from lQCD. At small chemical potentials it is controlled by the curvature parameter κ

$$\frac{T_c(\mu_B)}{T_c} = 1 - \kappa \left(\frac{\mu_B}{T_c}\right)^2 + \cdots, \tag{3.39}$$

that can be estimated by lQCD calculations, see Appendix A.3. We perform a Taylor expansion of the critical temperature (3.38) and compare the result to lQCD calculations. We get a value of $\kappa_{DQPM} \approx 0.0122$ which is in line with the curvature parameter from Bonati et al., i.e. $\kappa = 0.0135(20)$ [167].
With the ansatz (3.38) for the critical temperature we can replace the ratio T/T_c in the one-loop parametrization of the effective coupling in Eq. (3.14) to obtain the coupling at finite μ_B,

$$\frac{T}{T_c} \to \frac{T^*}{T_c(\mu_B)} = \frac{\sqrt{T^2 + \mu_B^2/(3\pi)^2}}{T_c(\mu_B = 0) \cdot \sqrt{1 - \alpha\ \mu_B^2}}. \tag{3.40}$$

For the entropy-dependent couplings Eq. (3.19) and (3.27) we replace the temperature with the scaled temperature $\tilde{T}$

$$g^2(s/s_{SB}, T, \mu_B) = g^2(s/s_{SB}(\tilde{T}), \tilde{T}), \qquad \tilde{T} = T^* \frac{T_c}{T_c(\mu_B)}. \tag{3.41}$$

We still use the $\mu_B = 0$ entropy from lQCD since the effects of μ_B are contained in $\tilde{T}$. The finite-μ_B results for the DQPM* in Refs. [85, 86] have been obtained with this method.

3.3.2 Flow equation

The scaling hypothesis uses a phenomenological ansatz to extend the coupling to finite chemical potential. We will show now how to extend the model by using thermodynamic consistency. Since the entropy and the particle density are derived from the same thermodynamic potential in a thermodynamically consistent way, they have to fulfill the Maxwell relation

$$\left.\frac{\partial s}{\partial \mu_B}\right|_T = \left.\frac{\partial n_B}{\partial T}\right|_{\mu_B}. \tag{3.42}$$

Generally this equation is fulfilled at the same order as required for the condition $s' = n' = 0$, that we used to derive the quasiparticle entropy and density in Appendix A.1 [150]. With the masses and widths defined for finite μ_B the evaluation of this equation leads to a differential equation for the effective coupling g^2,

$$a_T \frac{\partial g^2}{\partial T} + a_\mu \frac{\partial g^2}{\partial \mu_B} = a_0. \tag{3.43}$$

We can solve this equation with the coupling at $\mu_B = 0$ as starting values and obtain the effective coupling at finite chemical potential.
The differential equation (3.43) is the result of the T and μ dependence of the masses and the widths. The derivatives that act on the distribution functions in the entropy and the baryon number density lead to the Maxwell relation for a system with constant masses and widths and is always fulfilled. The non-vanishing parts of Eq. (3.42) consist of

derivatives with respect to the masses, widths and the effective coupling. For momentum-independent selfenergies we can rewrite it into the more convenient form,

$$\sum_{g,u,d,s}\left(\frac{\partial s_i}{\partial M_i^2}\frac{\partial M_i^2}{\partial \mu_B}+\frac{\partial s_i}{\partial \gamma_i}\frac{\partial \gamma_i}{\partial \mu_B}\right)=\sum_{u,d,s}\left(\frac{\partial n_i}{\partial M_i^2}\frac{\partial M_i^2}{\partial T}+\frac{\partial n_i}{\partial \gamma_i}\frac{\partial \gamma_i}{\partial T}\right). \tag{3.44}$$

The T and μ_B derivatives of the masses and widths act on the effective coupling and on the explicit dependence of T and μ_B:

$$\frac{\partial M^2}{\partial T}=\frac{\partial M^2}{\partial g^2}\frac{\partial g^2}{\partial T}+\left.\frac{\partial M^2}{\partial T}\right|_{g^2}. \tag{3.45}$$

The first term contributes to a_T, the second to a_0. By explicitly separating these derivatives in Eq. (3.44) we get an equation for the μ_B-derivative of the effective coupling:

$$a_S+a_\mu\frac{\partial g^2}{\partial \mu_B}=a_N-a_T\frac{\partial g^2}{\partial T}\quad\Rightarrow\quad\frac{\partial}{\partial \mu_B}g^2=\frac{\left(a_N-a_S+a_T\,\frac{\partial g^2}{\partial T}\right)}{a_\mu}. \tag{3.46}$$

By substituting $a_0=a_N-a_S$ we retain Eq. (3.43). In the literature this equation is often called "flow equation" for the effective coupling [80, 81]. The abbreviations a_S, a_μ, a_N and a_T are functions of temperature, chemical potential and the effective coupling $g^2(T,\mu_B)$. For momentum-independent selfenergies they are defined as:

$$a_S(T,\mu,g^2)=\sum_{i=g,u,d,s}\left(\frac{\partial s_i}{\partial M_i^2}\left.\frac{\partial M_i^2}{\partial \mu_B}\right|_{g^2}+\frac{\partial s_i}{\partial \gamma_i}\left.\frac{\partial \gamma_i}{\partial \mu_B}\right|_{g^2}\right), \tag{3.47}$$

$$a_\mu(T,\mu,g^2)=\sum_{i=g,u,d,s}\left(\frac{\partial s_i}{\partial M_i^2}\frac{\partial M_i^2}{\partial g^2}+\frac{\partial s_i}{\partial \gamma_i}\frac{\partial \gamma_i}{\partial g^2}\right), \tag{3.48}$$

$$a_N(T,\mu,g^2)=\sum_{i=u,d,s}\left(\frac{\partial n_i}{\partial M_i^2}\left.\frac{\partial M_i^2}{\partial T}\right|_{g^2}+\frac{\partial n_i}{\partial \gamma_i}\left.\frac{\partial \gamma_i}{\partial T}\right|_{g^2}\right), \tag{3.49}$$

$$a_T(T,\mu,g^2)=\sum_{i=u,d,s}\left(\frac{\partial n_i}{\partial M_i^2}\frac{\partial M_i^2}{\partial g^2}+\frac{\partial n_i}{\partial \gamma_i}\frac{\partial \gamma_i}{\partial g^2}\right). \tag{3.50}$$

The extension to momentum-dependent selfenergies is straight forward. The only difference is, that we have to evaluate all the derivatives within the momentum integrals of the entropy and the density. As long as we keep the coupling momentum independent, we can still pull its derivatives out of the integrals, thus retaining the known form of Eq. (3.43) of the flow equation.

It is easy to generalize the flow equation to arbitrary chemical potentials μ_i. For this aim one has to replace the baryon number density with the density assigned to the corresponding chemical potential $\frac{\partial P}{\partial \mu_i}=n_i$,

$$\left.\frac{\partial s}{\partial \mu_Q}\right|_T=\left.\frac{\partial n_Q}{\partial T}\right|_{\mu_Q},\qquad\qquad\left.\frac{\partial s}{\partial \mu_S}\right|_T=\left.\frac{\partial n_S}{\partial T}\right|_{\mu_S}. \tag{3.51}$$

This is important if one wants to consider certain constraints on the strange or charge densities. The densities for the different conserved charges are also connected by Maxwell relations,

$$\left.\frac{\partial n_i}{\partial \mu_j}\right|_{\mu_i} = \left.\frac{\partial n_j}{\partial \mu_i}\right|_{\mu_j}, \qquad i,j = B,Q,S. \tag{3.52}$$

The flow equations derived from Eq. (3.52) are simpler than the ones from Eq. (3.42), because the a_0 term vanishes and the flow equations read

$$\left(\frac{\partial n_i}{\partial g^2}\right)^{-1}\frac{\partial g^2}{\partial \mu_i} = \left(\frac{\partial n_j}{\partial g^2}\right)^{-1}\frac{\partial g^2}{\partial \mu_j}. \tag{3.53}$$

Before we show actual results from the flow equation, we discuss the important case of $\mu_B = 0$. Since the particle density is zero for $\mu_B = 0$, the same holds for its derivatives with respect to the masses and the width. Therefore $a_N = a_T = 0$. On the other side the derivatives of the masses and widths with respect to the chemical potential evaluated at $\mu_B = 0$ also have to vanish, and therefore $a_S = 0$. Only a_μ stays finite. This implies $\partial g^2/\partial\mu_B\ |_{\mu_B=0} = 0$, as expected for QCD.

A more interesting case is the second derivative $\partial^2 g^2/\partial\mu_B^2\ |_{\mu_B=0}$. For this we apply $\frac{\partial}{\partial \mu_B}$ to the flow equation (3.46) and evaluate it at $\mu_B = 0$. Dropping the terms that vanish we get

$$\left.\frac{\partial^2}{\partial \mu_B^2} g^2\right|_{\mu=0} = \left.\frac{1}{a_\mu}\left(\frac{\partial}{\partial \mu_B}\left(a_n - a_s\right) + \left(\frac{\partial}{\partial \mu_B}a_T\right)\frac{\partial g^2}{\partial T}\right)\right|_{\mu_B=0}. \tag{3.54}$$

This quantity is always negative indicating that the effective coupling decreases with chemical potential for fixed T. Note that we needed $\partial^2 g^2/\partial\mu_B^2\ |_{\mu=0}$ to calculate the fourth-order susceptibility (3.35). Using the flow equation we can relate χ_B^4, and all other higher-order susceptibilities, to the equation of state at vanishing chemical potential.

It may seem as if the equation of state at $\mu_B = 0$ contains already the equation of state in the whole T-μ_B plane. This, however, is not true. When we calculate χ_B^4 we probe also the explicit μ_B-dependence of the selfenergies via $\partial^2 M_{q\bar{q}}/\partial\mu_B^2|_{g^2}$. This is a model-dependent input into our theory, that we fixed with the parametrization of the masses. The comparison of higher-order susceptibilities with the lattice is therefore a direct test of the μ_B-dependence of the quark selfenergies, that can only be done with the flow equation.

We solve the flow equation by calculating the derivative $\partial g^2/\partial\mu_B$ (3.46) for all temperatures between $T = 150$ MeV and $T = 600$ MeV while keeping the chemical potential fixed. We then use the Euler method to determine the coupling for an infinitesimal larger chemical potential,

$$g(T,\mu_B + \Delta\mu_B) = g(T,\mu_B) + \frac{\partial g^2}{\partial \mu_B}(T,\mu_B,g^2)\cdot\Delta\mu_B. \tag{3.55}$$

The Euler method is the simplest possible way to solve a differential equation. If the step size is too large, the solution has a huge numerical error. We use a step size of

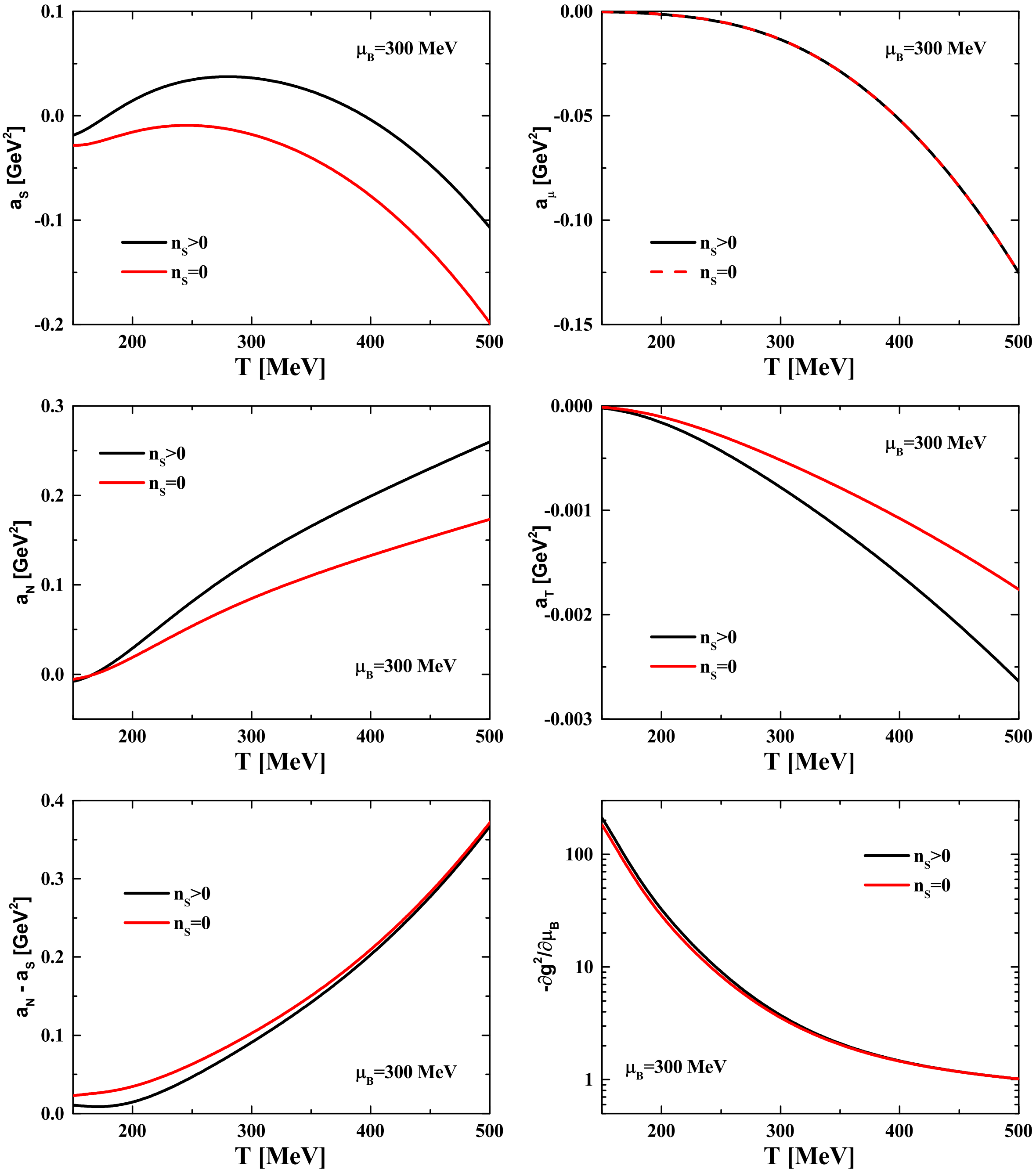

Figure 3.11: The coefficients a_T (top left), a_N (top right), a_S (middle left) and a_μ (middle right) as well as the difference $a_N - a_S = a_0$ (bottom left) and the differential $-\partial g^2/\partial\mu_B$ (bottom right) calculated with the flow equation (3.46) for the DQPM* as a function of temperature for a baryon chemical potential of $\mu_B = 300$ MeV. The red lines show the results obtained with strangeness neutrality and the black lines without. The results for the coefficient a_μ lie on top of each other and can not be distinguished by eye. Nevertheless, they are not exactly equal.

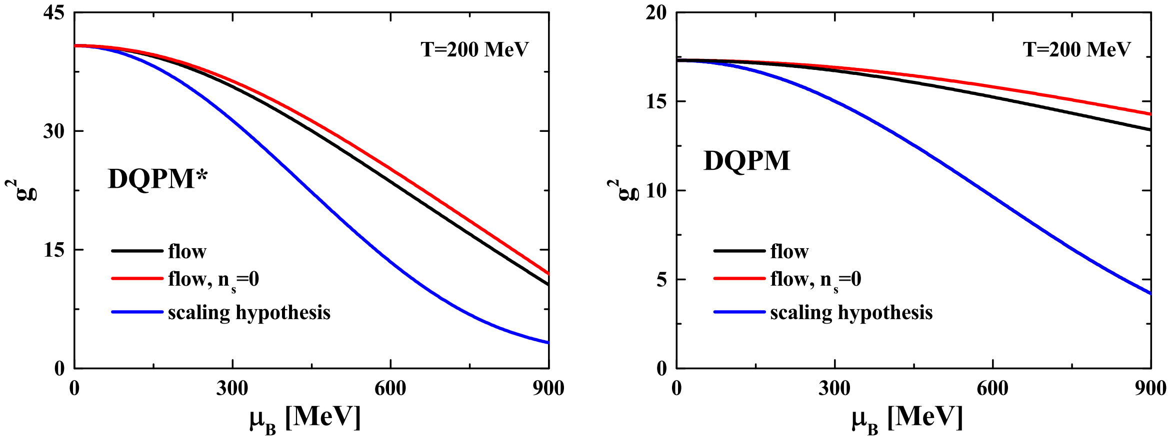

Figure 3.12: The effective coupling for the extended DQPM* (left) and for the regular DQPM (right) as a function of the baryon chemical potential μ_B for $T = 200$ MeV. The red lines show the coupling calculated from the flow equation with strangeness neutrality and the black lines without. We choose the entropy dependent coupling from Eq. (3.19) as the starting coupling at $\mu_B = 0$ for the DQPM. The blue lines show the coupling from the scaling hypothesis.

$\Delta\mu_B = 3$ MeV. A smaller $\Delta\mu_B$ does not lead to a substantial increase in the precision. An alternative way to solve the flow equation is the method of characteristics. With this method one calculates lines on which the coupling stays constant. This was done for an effective quasiparticle model with $\gamma = 0$ in Refs. [80, 81, 165]. The method of characteristics is just a different way to solve the flow equation and does not increase the precision of the solution. Up to now the flow equation was only used in the context of effective quasiparticle models without width. This thesis is the first study in which the flow equation is solved for a quasiparticle model with a finite width. Earlier works on the DQPM at finite chemical potential have used the scaling hypothesis [31, 85, 86, 168, 169, 170].
An important constraint for heavy-ion collisions is strangeness neutrality. This condition is easy to achieve in the DQPM and DQPM*. The only particle that contains strangeness is the strange quark. If the chemical potential of the strange quarks is zero one has automatically zero net strangeness. This fixes the strange chemical potential to $\mu_S = \mu_B$ and therefore $\mu_s = \mu_B - \mu_S = 0$.
The first four panels in Fig. 3.11 show the coefficients a_S, a_μ, a_N and a_T from the flow equation (3.46) as a function of temperature T for a baryon chemical potential of $\mu_B = 300$ MeV. We distinguish the two cases of strict strangeness neutrality $N_S = 0$ and the equivalence of all three flavors $\mu_s = \mu_{u,d}$. In general the coefficients with $N_S = 0$ differ from the coefficients without any constraints. The only difference is $a_\mu = \partial s/\partial g^2$ that is nearly unchanged. The entropy is rather insensitive to finite chemical potentials and even if we incorporate strangeness neutrality, the strange quarks are still in the system and give a contribution to a_μ, since they feel the finite μ_B via the effective coupling $g^2(T, \mu_B)$.
From the behavior of the coefficients in Fig. 3.11 one would expect some influence from

strangeness neutrality on the effective coupling. This, however, is not the case, as only the difference of $a_N - a_S$ enters the flow equation (3.46). The different behaviors of the strange quarks are canceled and the difference $a_N - a_S$ is unaffected by strangeness neutrality, as shown for $\mu_B = 300$ MeV in the bottom left panel of Fig. 3.11. The coefficient a_T, that is also affected by strangeness neutrality, is very small compared to the others. As a result we find that the differential $\partial g^2/\partial\mu_B$ is almost unchanged under the constraint $N_S = 0$ as demonstrated in the bottom right panel of Fig. 3.11, also for $\mu_B = 300$ MeV.

We now compare the results of the coupling from the flow equation with and without strangeness neutrality to the scaling hypothesis. The coupling as a function of the baryon chemical potential is shown in the left panel of Fig. 3.12 for the DQPM* and in the right panel of Fig. 3.12 for the DQPM. The temperature is kept at $T = 200$ MeV. Strangeness neutrality has, as expected, only a small influence on the coupling. We see a similar behavior in both quasiparticle models. The effective coupling decreases as a function of the chemical potential for the flow equation and the scaling hypothesis, but the effect is stronger for the scaling hypothesis. It seems as if the coupling would saturate in the scaling hypothesis at large chemical potentials. The reason is that the ratio $T^*/T_c(\mu_B)$, that controls the coupling, becomes very large as the chemical potential increases. The scaled entropy s/s_{SB} does not change very much at high temperatures, so the coupling does also not change anymore. This illustrates the smaller application range of the scaling hypothesis compared to the flow equation, that does not show such an effect. The coupling keeps decreasing even at $\mu_B = 900$ MeV. The curve looks like a parabola for $\mu_B < 400$ MeV and a linear function for higher μ_B.

A finite chemical potential decreases the coupling, but does not change its functional form. We show g^2 for the DQPM* calculated with the flow equation as a function of temperature for different baryon chemical potentials in Fig. 3.13. The coupling decreases for all μ_B and has the expected $g^2 \sim 1/\ln T^2$ behavior at large temperatures. We find only small deviations between the couplings at $\mu_B = 0$ and $\mu_B = 300$ MeV, which is the range in chemical potential where the lQCD extrapolations can be used. At $\mu_B = 600$ MeV the coupling differs much stronger. This is a region in the phase diagram that can only be accessed with effective theories. The largest chemical potential $\mu_B = 900$ MeV is a region, that for small temperatures $T < 50$ MeV is probed by the nuclear equation of state. Effective theories that employ partonic degrees of freedom have difficulties at these baryon chemical potentials, since baryons become extremely important and it is safer to extend nuclear matter approaches to finite temperature than using effective models that are adjusted to lQCD results at $\mu_B = 0$. The flow equation should still be applicable for these μ_B, if the temperature is not too small compared to the chemical potential. However, we will not apply the flow equation for baryon chemical potentials larger than $\mu_B = 900$ MeV.

We have seen already in the comparison between the flow equation and the scaling hypothesis that the couplings differ. This has also some consequences for the thermodynamics. We compare in Fig. 3.14 the baryon number density from the quasiparticle density $n^{dqp} = n^{(0)} + \Delta n$ calculated from Eqs. (A.36) and (A.37) to the thermodynamic definition $\partial P/\partial\mu_B$. For the flow equation we see no difference between both definitions,

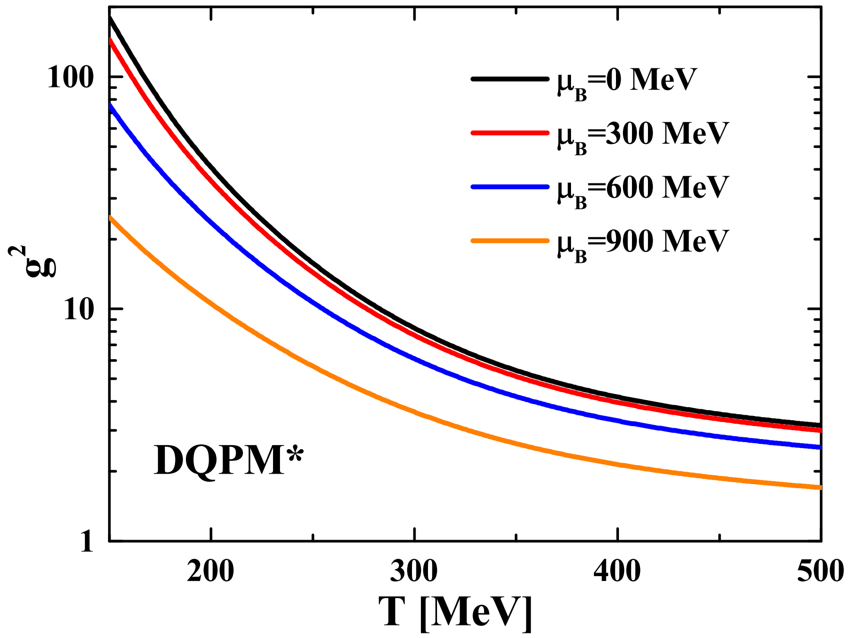

Figure 3.13: The effective coupling g^2 for the DQPM* calculated with the flow equation as a function of the temperature for different baryon chemical potentials.

demonstrating that it leads indeed to a thermodynamic consistent theory, but for the scaling hypothesis we find a larger thermodynamic density than from the quasiparticle density. The scaling hypothesis violates thermodynamic consistency. As a consequence it is not possible to define a unique pressure or energy density. In the following we will always use the flow equation to calculate the effective coupling. However, the quasiparticle density of the scaling hypothesis agrees up to small baryon chemical potential with the density from the flow equation. This shows that the scaling hypothesis is approximately thermodynamic consistent for baryon chemical potentials $\mu_B < 300$ MeV if one uses the quasiparticle density n^{dqp} to define the density. We show additionally the density from the Taylor expansion $n_B \approx \chi_B \cdot \mu_B$. The expansion is consistent with the density from the flow equation and also with the quasiparticle density from the scaling hypothesis at small μ_B. We find no significant deviations from the lQCD equation of state up to $\mu_B \approx 300$ MeV. The range of chemical potentials, where the scaling hypothesis agrees with the flow equation, coincides with the application range of the Taylor expansion because the density at small μ_B is controlled by the susceptibility. We use this fact to construct a thermodynamic consistent extension of the scaling hypothesis in Appendix A.4.

We show in Fig. 3.15 the pressure, the energy density, the entropy density and the interaction measure for $T = 200$ MeV as a function of baryon chemical potential scaled with their values at $\mu_B = 0$. The coupling is calculated with the flow equation without strangeness neutrality. The entropy density is the least affected quantity while the pressure is affected most. As expected, we see only small changes for $\mu_B < 300$ MeV

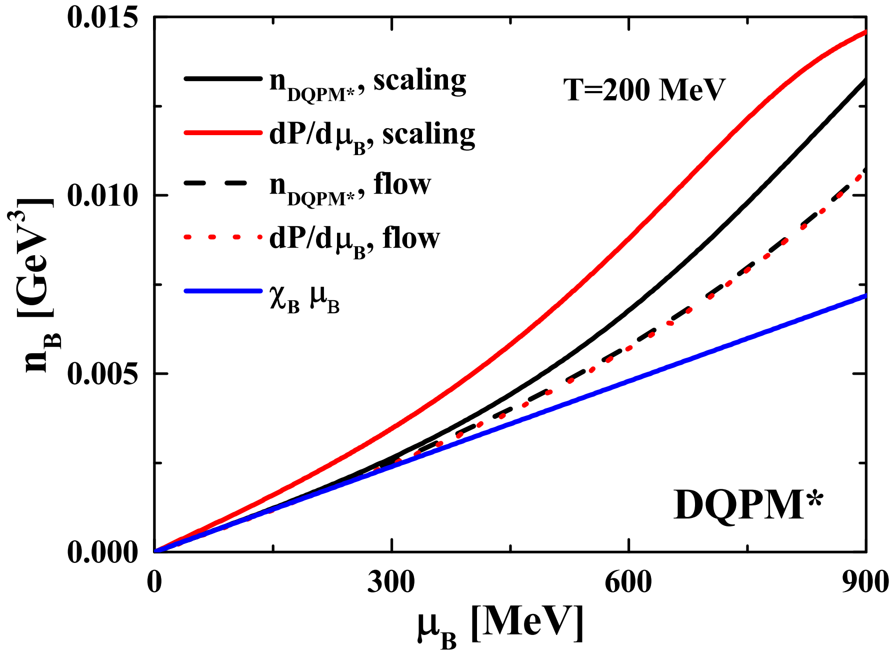

Figure 3.14: The baryon number density for the DQPM* as a function of the baryon chemical potential μ_B for $T = 200$ MeV. The black lines show the results calculated from the quasiparticle density $n_{DQPM} = n^{(0)} + \Delta n = 3\, n_B$, the red lines the results from the thermodynamic definition $\frac{\partial P}{\partial \mu_B}$. Full lines are calculated with the scaling hypothesis and dashed lines with the flow equation. The blue line shows the baryon density in first-order Taylor expansion at zero chemical potential $n_B \approx \chi_B \cdot \mu_B$. The Taylor expansion is compatible with the density from the flow equation up to $\mu_B \approx 300$ MeV.

in all four quantities. The thermodynamics in this region are well described by the fit $P(\mu_B)/P(0) = 1 + a\, \mu_B^2$. This confirms again, that we can trust the lattice expansion for finite μ_B up to $\mu_B \approx 300$ MeV. At larger baryon chemical potentials this is no longer the case, as one sees deviations from this simple fit and one needs more Taylor coefficients to describe the equation of state. The variation of the equation of state at finite chemical potential is usually discussed in terms of the pressure difference,

$$\Delta P = P(\mu_B) - P(0) = \int_0^{\mu_B} n_B \, d\mu_B \approx \frac{1}{2}\chi_B \mu_B^2 + \cdots \, . \qquad (3.56)$$

In first-order Taylor expansion it is defined by the susceptibility $\Delta P \approx \frac{1}{2}\chi_B \mu_B^2$. A deviation from this behavior also indicates that one leaves the applicability range of the Taylor expansion. We will not show the pressure difference since all relevant information are already visible in Figs. 3.14 and 3.15. As long as the baryon density behaves linearly in μ_B one is still in the applicability range of the expansion.

We will finally discuss the equation of state as a function of temperature for finite baryon chemical potential. The left panel in Fig. 3.16 shows the dimensionless equation of state for $\mu_B = 300$ MeV and the right panel for $\mu_B = 600$ MeV. Even if the equation of state

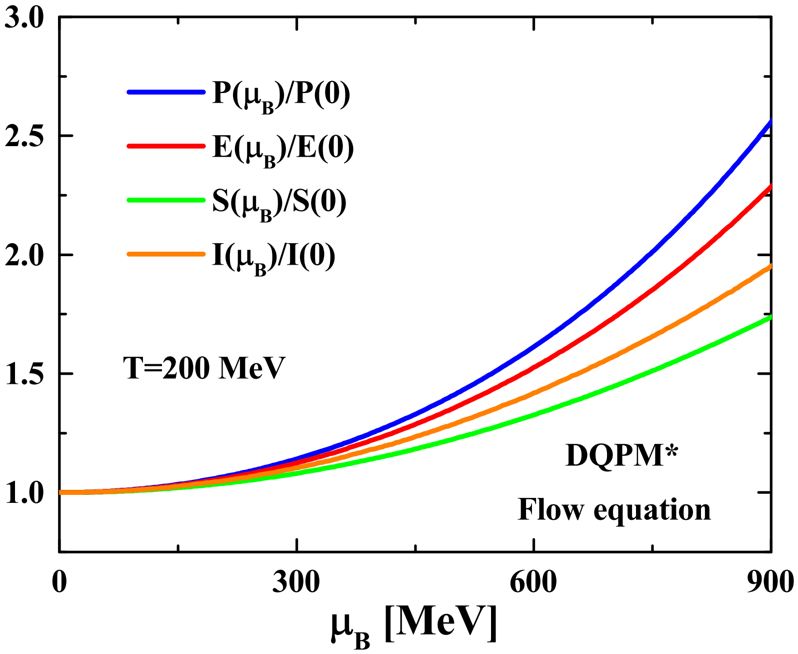

Figure 3.15: The pressure, energy density, entropy density and interaction measure for the DQPM* as a function of the baryon chemical potential μ_B for $T = 200$ MeV. The coupling for finite chemical potential was calculated with the flow equation without strangeness neutrality. All quantities are scaled by their values at $\mu_B = 0$.

for $\mu_B = 600$ MeV follows no longer from the simple Taylor expansion, we see no drastic deviations in the functional form compared to the $\mu_B = 0$ equation of state in Fig. 3.9. The scaled pressure, energy and entropy density are increasing functions but saturate at large temperatures; the interaction measure has a maximum at low temperatures and drops to zero as the temperature increases further. There are, however, small differences. We see that the steep rise in the scaled equation of state, that indicates a change in the degrees of freedom, happens at lower temperatures for finite μ_B and the maximum of the interaction measure is also shifted towards lower temperatures. This suggests that the hadron-parton transition happens at lower temperatures for finite chemical potentials. However, this is not a proof, just an indication. The scaled energy density at $\mu_B = 600$ MeV shows the strongest change compared to $\mu_B = 0$. It appears that the function has already saturated at $T = 200$ MeV. At baryon chemical potentials between 615 MeV and 630 MeV a maximum will emerge. Nevertheless, the unscaled energy density is still a rising function with temperature and chemical potential. The changes in the scaled energy density are closely related to the baryon number density, that gives a contribution of $\mu_B \cdot n_B$ to the energy density. The dimensionless density n_B/T^3 is shown as the black lines in Fig. 3.16. We see that it is very small compared to the other functions. We show it for different μ_B in Fig. 3.17 as a function of the temperature. It has a maximum at $T \approx 230$ MeV for the chemical potentials below 300 MeV. The position of the maximum is shifted towards smaller temperatures as we increase μ_B, similar to the

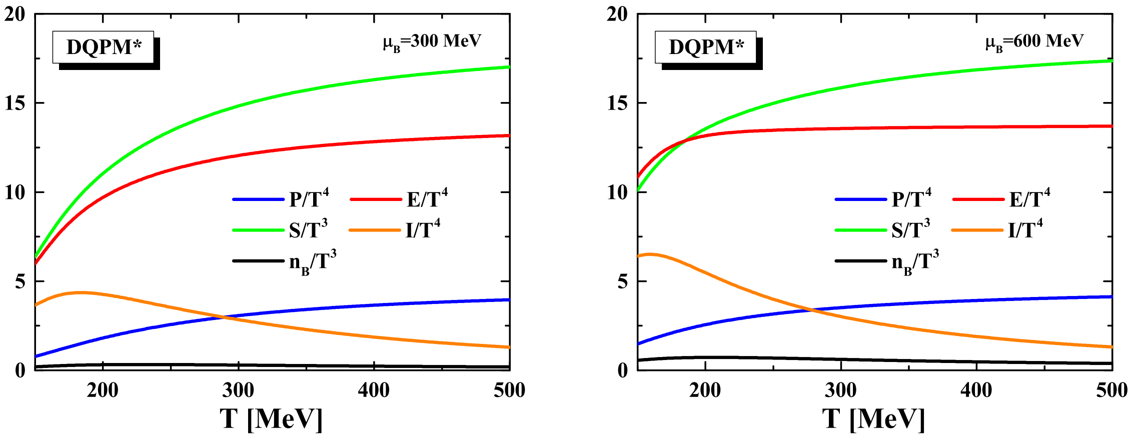

Figure 3.16: The DQPM* equation of state as a function of the temperature T for finite baryon chemical potential. The green lines show the entropy density, the red lines the energy density, the blue lines the pressure, the orange lines the interaction measure and the black lines the baryon number density. All quantities are scaled by powers of the temperature. The left picture shows the results for $\mu_B = 300$ MeV and the right picture for $\mu_B = 600$ MeV. The coupling for finite baryon chemical potential was calculated with the flow equation. The baryon number densities have a maximum at $T \approx 200$ MeV and decrease to zero for larger temperatures. The energy density for $\mu_B = 600$ MeV is still increasing with temperature, but only very slightly.

interaction measure. The maximum for $\mu_B = 600$ MeV is already at $T \approx 210$ MeV. The scaled density decreases with increasing temperature and will vanish at very large T, but increases at least linearly with μ_B; its contribution to the pressure and the energy density is therefore of the order μ_B^2 and the contribution to the scaled equation of state goes with $(\mu_B/T)^2$, so it is most pronounced at low temperatures. This is the reason for the peak in the energy density.

A drawback of the flow equation and also the scaling hypothesis is, that we will never see deviations from the quasiparticle picture, as this is build into the approach. We will also never see a phase transition or a critical point. The flow equation and the scaling hypothesis are blind to different phases of QCD. For this one has to employ more fundamental approaches like Dyson-Schwinger equations [60, 121, 159, 171] or the functional renormalization group [62, 64, 66, 67].

In summarizing this section we have presented two methods to extend our quasiparticle models to finite baryon chemical potential. The scaling hypothesis is based on phenomenology and uses the assumption that the coupling depends only on the ratio T/T_c; the flow equation is based on the Maxwell relations. The flow equation ensures the thermodynamic consistency of the quasiparticle model, but the scaling hypothesis violates it. The scaling hypothesis is therefore not suited to study the equation of state at finite chemical potential, however, it gives still comparable results to the flow equation when applied for baryon chemical potentials $\mu_B < 300$ MeV, where the equation of state is completely defined by the equation of state at $\mu_B = 0$ and the baryon number

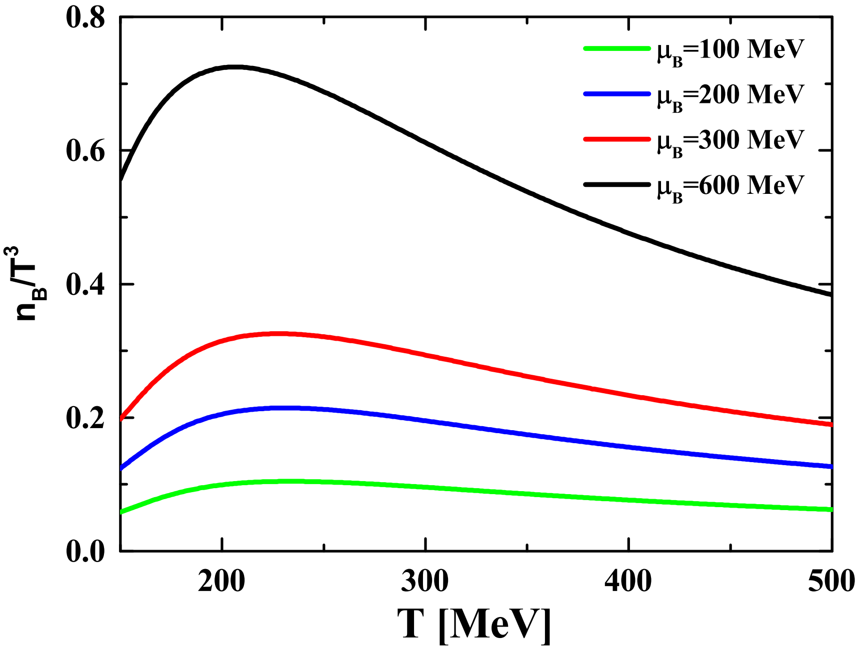

Figure 3.17: The baryon number density (scaled with T^3) for the DQPM* as a function of the temperature T for different baryon chemical potentials. The coupling for finite chemical potential was calculated with the flow equation without strangeness neutrality.

susceptibility χ_B. Using the flow equation for the DQPM* we here predicted the QCD equation of state at large baryon chemical potentials.

3.4 Transport coefficients

So far we studied only thermodynamic, i.e. static properties, but quasiparticle models can also determine dynamical properties. These are encoded in transport coefficients that measure the response of a system to an external perturbation. One of the most commonly known transport coefficients is the electric conductivity σ, that appears in Ohm's law and quantifies the response to an external electric field E,

$$\vec{j}_{em} = \sigma \vec{E}. \tag{3.57}$$

The external field will generate a finite charge current j_{em} that is proportional to the electric field. The strength of the current is determined by the conductivity σ.
Transport coefficients are strictly defined by the Green-Kubo relation [103, 172] that connects a transport coefficient λ with equilibrium fluctuations of the flux J,

$$\lambda = \frac{1}{T}\int d^3r \int_0^\infty dt\, \langle J(0,0)J(\mathbf{r},t)\rangle = \frac{V}{T}\int_0^\infty \langle J(0)J(t)\rangle\, dt. \tag{3.58}$$

The flux is the current created by the external perturbation, i.e. the charge current j_{em} defines the electric conductivity. The quantity $C(t) = \langle J(0)J(t)\rangle$ is the autocorrelation function and relates the observable J to itself at a later time. For $t = 0$ it is identical to the squared flux $\langle J^2(0)\rangle$ and always positive. At large times it will decay to zero as J becomes uncorrelated for $t \to \infty$. Actual calculations show an exponential decay of $C(t)$ [173, 174, 175, 176],

$$C(t) = \langle J(0)J(t)\rangle \approx \langle J(0)J(0)\rangle e^{-t/\bar{\tau}}. \tag{3.59}$$

The relaxation time $\bar{\tau}$ describes the time scale which the system needs to equilibrate after the external force was applied. Substituting (3.59) into Eq. (3.58) defines the transport coefficient as a function of the relaxation time,

$$\lambda = \frac{V}{T}\langle J(0)J(0)\rangle\bar{\tau}. \tag{3.60}$$

Each transport coefficient has its own specific relaxation time that is connected to the underlying microscopic dynamics responsible for the transport process.
The autocorrelation function $C(t)$ is a real-time Green's function and has therefore a spectral representation in terms of a spectral function $\rho(\omega)$. It was shown in Ref. [177] that transport coefficients are related to the low frequency behavior of these spectral functions,

$$\lambda \sim \lim_{\omega\to 0}\frac{\rho(\omega)}{\omega}. \tag{3.61}$$

This Kubo-relation can be used to calculate transport coefficients from lattice simulations because real-time and Euclidean-time Green's functions have the same spectral functions. The Euclidean-time autocorrelation function is defined as

$$C(\tau) = \int d^3x \langle J(0,0)J(\tau,x)\rangle, \tag{3.62}$$

and can be directly calculated on the lattice. The spectral representation of the correlator is given by

$$C(\tau) = \int_0^\infty \frac{d\omega}{2\pi}\rho(\omega)\frac{\cosh\left(\omega\left(\tau - \frac{1}{2T}\right)\right)}{\sinh\left(\frac{\omega}{2T}\right)}. \tag{3.63}$$

By inverting this relation one can determine the spectral function $\rho(\omega)$ that reproduces the calculated Euclidean-time correlators. Unfortunately, the true form of the spectral function for an interacting theory is not known. For a non-interacting theory $\rho(\omega)$ has a δ-peak at $\omega = 0$ [6]. It is expected that this peak gets smeared out by the interaction. The spectral function has to vanish like $\rho(\omega) \sim \omega$ for $\omega \to 0$ to keep the transport coefficient finite. First attempts in Ref. [178] used a simple Breit-Wigner function. This ansatz was confirmed in various approximations like hydrodynamics or the heavy-quark limit [179, 180, 181, 182]. The inversion of relation (3.63) is in general an ill-defined problem. Current approaches are still employing the Breit-Wigner ansatz or use Bayesian methods like the Maximum Entropy Method [183, 184] to determine the spectral functions.

---

[6] This is not the case for the bulk viscosity.

A third way for the calculation of transport coefficients is the relaxation-time approximation (RTA). In this approach the collision term of transport equations is approximated as linear in the distribution function f,

$$I_{Coll} = -\frac{f - f_{eq}}{\bar{\tau}}. \tag{3.64}$$

The distribution function, that was driven out-of equilibrium by the external force, will relax back into the equilibrium distribution f_{eq}. The time scale of the relaxation is governed by the relaxation time $\bar{\tau}$ that describes also the decay of the autocorrelation function (3.59). This approximation allows to derive expressions for various transport coefficients, see Refs. [185, 186].

In the following we will focus on three coefficients: the shear viscosity η, the bulk viscosity ζ and the electric conductivity for static electric fields σ_0.

We start with the discussion of the viscosities. Viscosity is a property that is related to the "thickness" of a fluid. A larger viscosity implies a stiffer behavior; honey has a higher viscosity than water. The QGP created in ultra-relativistic heavy-ion collisions shows properties of a fluid [1, 2, 3, 4]. In fact, first experimental measurements of Au+Au collisions at RHIC are well described by ideal hydrodynamics [22]. This indicates very small viscosities of the created QGP. Calculations using viscous hydrodynamics verified these results. A large shear viscosity of the QGP is incompatible with the observed elliptic flow, a measure of the anisotropy of the particle spectra [23, 24]. A finite shear viscosity decreases this flow anisotropy and only very small η can explain the experimental data. On the contrary, the shear viscosity can not become arbitrarily small. There is a universal lower limit for the ratio of shear viscosity to entropy density derived from infinitely coupled supersymmetric Yang-Mills gauge theories, the so called KSS-limit [25],

$$\frac{\eta}{s} \geq \frac{1}{4\pi}. \tag{3.65}$$

First lQCD calculations found no violations of this limit [187, 188], but the measured ratio was the smallest ever observed for any fluid. This makes the QGP the "most perfect fluid". The shear viscosities in the hadronic and the partonic phases differ substantially. In the hadronic phase η/s is expected to increase for lower temperatures [176, 189, 190, 191, 192], while in the partonic phase the ratio is expected to increase for larger temperatures [141, 193, 194, 195]. This behavior indicates a minimum of η/s in the vicinity of the QCD phase transition which is a universal behavior of strongly correlated fluids and was also seen in the phase transitions of water, helium and ultracold Fermi gases [191, 195, 196].

The other viscosity relevant for heavy-ion physics is the bulk viscosity. A finite bulk viscosity will act against compression or expansion. In heavy-ion collisions it would slow down the expansion of the fireball. The bulk viscosity of QCD matter is expected to be a lot smaller than the shear viscosity and the effects of ζ are therefore much harder to observe. Most viscous approaches concentrate only on the shear viscosity. The QCD bulk viscosity has a different behavior than the shear viscosity. The ratio ζ/s is expected to decrease with temperature at very small [84, 192, 197, 198, 199] but also very large temperatures [173, 200, 201, 202]. However, ζ/s is not a monotonic decreasing function. At a second-order phase transition ζ/s will diverge. This behavior is protected by universality and appears also near a crossover, but in the form of a peak [200]. It is therefore inevitable, that ζ/s rises in the hadronic phase near T_c [203, 204]. The peak causes the fireball to spend more time in the vicinity of the phase transition. This is consistent with the minimum of the speed of sound close to T_c, which has a similar effect. The speed of sound c_s is also connected to the estimated lower bound of the bulk viscosity [205],

$$\frac{\zeta}{\eta} \geq 2\left(\frac{1}{3} - c_s^2\right). \tag{3.66}$$

ζ can only vanish for $c_s^2 \to 1/3$, which occurs in systems with massless particles. A smaller c_s^2 on the other side will imply a larger ζ.

The fluxes corresponding to the viscosities are the components of the energy-momentum tensor $T_{\mu\nu}$. The component T_{00} is the energy density, the T_{0i} are the momentum densities, T_{ii} are the partial pressures P_i and the T_{ij} the momentum fluxes [7]. The momentum fluxes T_{ij} correspond to the shear viscosity and the momentum densities T_{0i} to the "sound mode" given by $\frac{4}{3}\eta + \zeta$, which is a combination of bulk and shear viscosity [206]. The bulk viscosity itself is related to the trace of the energy-momentum tensor $\theta = T_{\mu\mu}$ [201]:

$$\eta = \frac{V}{T}\int_0^\infty \langle T_{xy}(0)T_{xy}(t)\rangle \, dt, \tag{3.67}$$

$$\frac{4}{3}\eta + \zeta = \frac{V}{T}\int_0^\infty \langle T_{0z}(0)T_{0z}(t)\rangle \, dt, \tag{3.68}$$

$$\zeta = \frac{V}{T}\int_0^\infty \langle \theta(0)\theta(t)\rangle \, dt. \tag{3.69}$$

The Kubo formulae for the spectral functions read:

$$\eta = \pi \lim_{\omega\to 0} \frac{\rho_{xy}}{\omega}, \tag{3.70}$$

$$\frac{4}{3}\eta + \zeta = \pi \lim_{\omega\to 0} \frac{\rho_{0z}}{\omega}, \tag{3.71}$$

$$\zeta = \frac{\pi}{9} \lim_{\omega\to 0} \frac{\rho_\theta}{\omega}. \tag{3.72}$$

Here we calculate the viscosities from the RTA formulae derived in Ref. [185]. The shear and bulk viscosity for a system of different quasiparticle species read:

$$\eta = \frac{1}{15T}\sum_i \int \frac{d^3p}{(2\pi)^3}\frac{p^4}{\omega_i^2}\tau_i \; n_{B/F}(\omega_i), \tag{3.73}$$

$$\zeta = \frac{1}{9T}\sum_i \int \frac{d^3p}{(2\pi)^3}\frac{\tau_i}{\omega_i^2}\left[p^2 - 3c_s^2\left(\omega_i^2 - T^2\frac{dM_i^2}{dT^2}\right)\right]^2 n_{B/F}(\omega_i). \tag{3.74}$$

---

[7] i and j denote the spatial components.

The sum runs over all quasiparticle species in the system. In case of deconfined QCD this are 36 quarks and 16 gluons. The distribution function $n_{B/F}$ is either a Fermi- or a Bose-distribution function and τ_i the relaxation time of the quasiparticle. The energy follows from the dispersion relation $\omega_i^2 = p^2 + M_i^2$, with the quasiparticle mass M_i that can depend on the medium. The derivative dM^2/dT^2 explicitly includes these mean-field effects, which are important for the bulk viscosity. They are responsible for the peak at the critical temperature [173].

One can easily evaluate these expressions, if the relaxation times are known. This demonstrates the advantage of the DQPM compared to other quasiparticle approaches. The relaxation times are already defined as the inverse of the quasiparticle widths,

$$\tau_i = \frac{1}{\gamma_i}. \tag{3.75}$$

In approaches without dynamical quasiparticles one needs to estimate the relaxation times, for example from cross sections of parton-parton scatterings $\tau^{-1} = n\sigma_{tot}$ [83, 174, 194]. Note that in the NJL model this procedure leads to a too small η/s that violates the KSS-limit [84].

Eqs. (3.73) and (3.74) define the viscosities for a system of on-shell particles, but the DQPM quasiparticles are off-shell. We extend them to off-shell equations that consider also a finite width. We use the expressions introduced in Refs. [85, 86]. The integral over the distribution function is extended to an integral over the spectral function,

$$\int \frac{d^3p}{(2\pi)^3} n_{B/F}(\omega_p) \to \int \frac{d^3p}{(2\pi)^3} \int_0^\infty \frac{d\omega}{2\pi}\, 4\omega\; A(\omega, \mathbf{p})\; n_{B/F}(\omega), \tag{3.76}$$

with the Breit-Wigner spectral function (3.5). From this we obtain the viscosities for a system of off-shell quasiparticles,

$$\eta = \frac{1}{15T} \sum_i \int \frac{d^3p}{(2\pi)^3} \int_0^\infty \frac{d\omega}{2\pi} \frac{p^4}{\omega} 4\tau_i\; A_i(\omega, \mathbf{p})\; n_{B/F}(\omega)\; \Theta(P^2), \tag{3.77}$$

$$\zeta = \frac{1}{9T} \sum_i \int \frac{d^3p}{(2\pi)^3} \int_0^\infty \frac{d\omega}{2\pi} \frac{4\tau_i}{\omega} \left[p^2 - 3c_s^2 \left(\omega^2 - T^2 \frac{dM_i^2}{dT^2}\right)\right]^2 A_i(\omega, \mathbf{p})\; n_{B/F}(\omega)\; \Theta(P^2). \tag{3.78}$$

In the on-shell limit $\gamma \to 0$ the spectral functions will reduce to a δ-peak $\lim_{\gamma\to 0} A = \pi\delta(\omega^2 - \mathbf{p}^2 - M^2)$ and one recovers the on-shell definitions of the viscosities, Eqs. (3.73) and (3.74).

The factor $\Theta(P^2) = \Theta(\omega^2 - \mathbf{p}^2)$ in Eqs. (3.77) and (3.78) is a step function and excludes spacelike momenta $|\mathbf{p}| > \omega$ from the integration. Spacelike momenta are a natural consequence for off-shell particles, but they "travel" faster than the speed of light. They can therefore not contribute to transport processes and have to be excluded from the calculation of the transport coefficients.

The widths of the DQPM* are momentum-dependent. This implies momentum-dependent relaxation times, but the $\bar{\tau}$ in the Green-Kubo autocorrelation function (3.59) and the

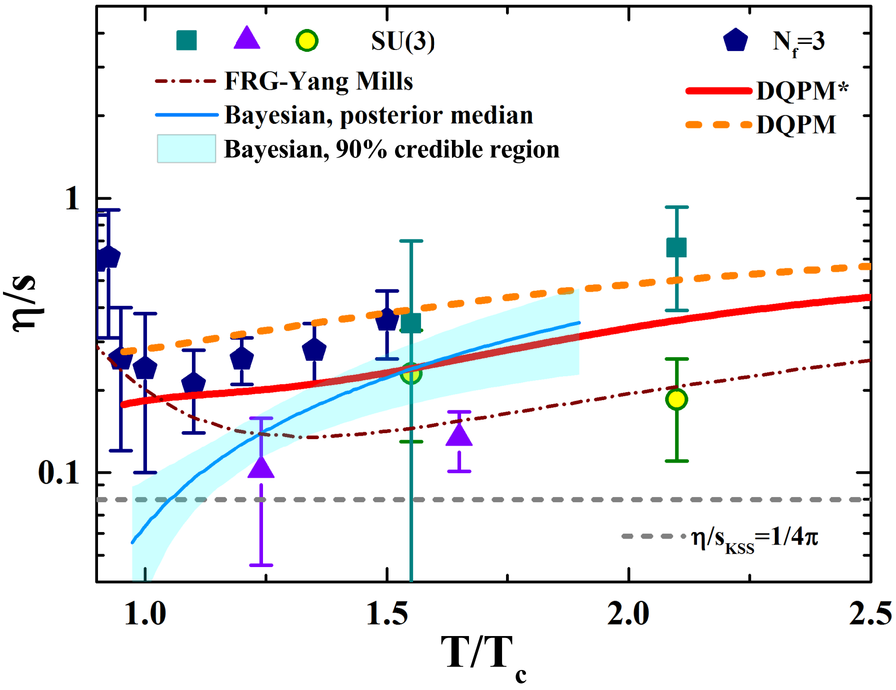

Figure 3.18: The shear viscosity over entropy density ratio η/s as a function of the normalized temperature T/T_c. The full red line shows the DQPM* and the dashed orange line the DQPM result. The symbols show lQCD data taken from Refs. [187] (squares), [188] (triangles), [202] (circles), and [193] (pentagons). The thin brown line shows η/s calculated from the functional renormalization group for pure Yang-Mills theory [207]. The blue line shows the estimate from a Bayesian analysis of experimental heavy-ion data, the blue shaded area is the 90 % credible region [208, 209]. The dashed grey line demonstrates the KSS-limit [25].

RTA approximation (3.64) depend only on the medium. We will therefore define the relaxation times via the ensemble averaged width,

$$\tau_i^{-1} = \langle \gamma_i \rangle = \frac{1}{n_i^{\text{off}}} \int \frac{d^3p}{(2\pi)^3} \int_0^\infty \frac{d\omega}{2\pi}\, 4\omega\, \gamma_i(\mathbf{p})\, A_i(\omega, \mathbf{p})\, n_{B/F}(\omega)\, \Theta(P^2). \tag{3.79}$$

The normalization factor n_i^{off} is the density of timelike off-shell quasiparticles,

$$n_i^{\text{off}} = \int \frac{d^3p}{(2\pi)^3} \int_0^\infty \frac{d\omega}{2\pi}\, 4\omega\, A_i(\omega, \mathbf{p})\, n_{B/F}(\omega)\, \Theta(P^2). \tag{3.80}$$

We have again excluded spacelike momenta from the integration.
We show in Fig. 3.18 the ratio of the shear viscosity to entropy density as a function of T/T_c. Note that we rescaled the temperatures with the specific T_c of the corresponding theory to get a meaningful comparison between different models. The full red line shows the DQPM* and the dashed orange line the DQPM result. In both models η/s

increases with temperature. The DQPM* results differ from the DQPM by a factor of roughly $1.2 - 1.5$. This is essentially due to different relaxation times. The ensemble averaged widths of the DQPM* are larger than the DQPM widths resulting in smaller relaxation times and a smaller η/s. We find that both models respect the KSS-limit. The smallest η/s is twice as large as the KSS-limit. We compare our predictions to different lQCD calculations. The squares [187], triangles [188] and circles [202] are lattice data for pure $SU(3)$ gauge theories. The pentagons show results taken from Ref. [193]. The authors originally determined η/s for pure $SU(3)$ gauge theory, but rescaled their results based on the ratio $(\eta/s)_{QCD}/(\eta/s)_{YM}$ estimated in Ref. [207]. The pentagons show the estimated result for $N_f = 3$ QCD. Their original results are slightly smaller than the shown data points but within the error bars. So far it is not possible to determine the functional form of η/s from the lattice data alone. They vary over more than one order of magnitude and have too large error bars. Only the most recent results from Ref. [193] show a clear functional form. We display also results from other models. The brown line shows η/s predicted for pure $SU(3)$ gauge theory from the functional renormalization group calculated in Ref. [207]. The result features the predicted minimum, but at a too large temperature, despite the proper rescaling of T_c. The η/s from that approach is even smaller than our results and the minimum is extremely close to the KSS-limit. The blue line is the prediction from Refs. [208, 209] that was obtained from a Bayesian analysis of experimental heavy-ion data. They simulated collisions in a hybrid approach with a hydrodynamical evolution of the fireball followed by a hadronic afterburner and determined the best set of parameters to describe experimental data from RHIC and LHC [211, 212]. The transport coefficients extracted by that method are only sensitive to the evolution of the QGP. The blue line shows the best fit of the shear viscosity to the experimental data and the bright blue area is the 90 % credible region of that fit. The η/s ratio is compatible with the DQPM* prediction at temperatures $T/T_c > 1.3$, but shows a very low shear viscosity at small temperatures, violating the KSS-limit near the phase transition. Nevertheless, the 90 % credible region agrees with the limit.

We show in Fig. 3.19 the bulk viscosity over entropy density ζ/s. The DQPM and the DQPM* both exhibit the expected peak close to the critical temperature. The DQPM* maximum is exactly at T_c, the DQPM maximum is at a slightly lower temperature not shown in Fig. 3.19. The peak of the DQPM* bulk viscosity is larger, but the DQPM peak is broader. We find that the maximum of ζ/s in our current models is less pronounced than earlier DQPM results [84, 173]. The bulk viscosities of our quasiparticle models are always smaller than the shear viscosities, even close to the phase transition. We, furthermore, compare the bulk viscosity to available lQCD data. The circles in Fig. 3.19 are taken from Ref. [201] and the squares and triangle from Ref. [202]. They are obtained for pure $SU(3)$ gauge theory. The quasiparticle models can describe the lattice data at larger temperatures, but not the point at $T \approx T_c$ from Ref. [201]. However, this point may be unreliable. It has extremely large error bars and lattice simulations at low temperatures require much larger statistics than simulations at higher T. We compare the bulk viscosity also to predictions from a Bayesian analysis from Ref. [210]. The maximum of the peak at T_c has a value of $\zeta/s \approx 0.075$ agreeing almost with the DQPM and DQPM* predictions, but the ratio drops extremely fast to zero, which is

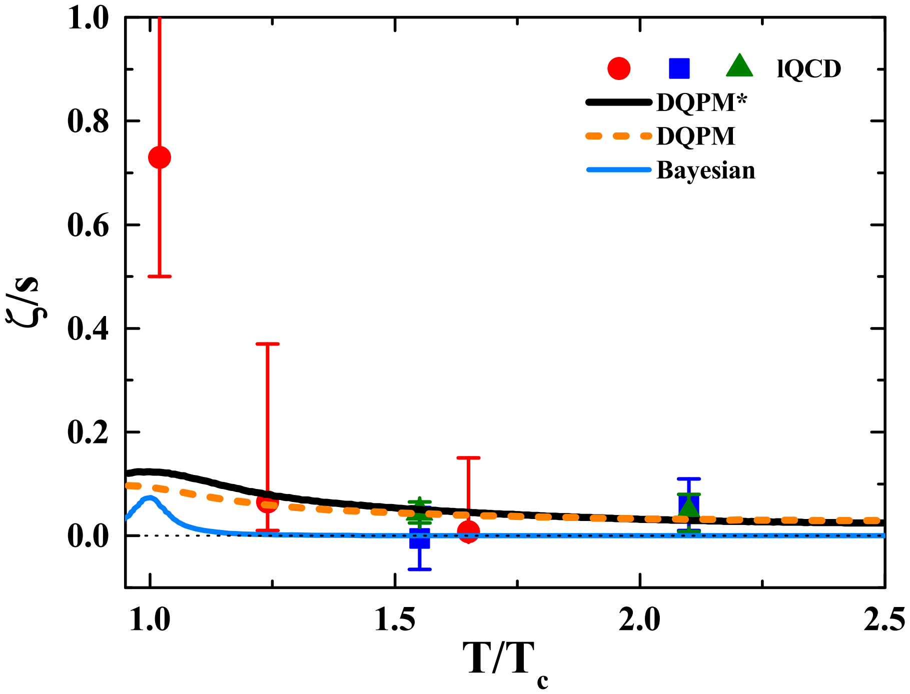

Figure 3.19: The bulk viscosity over entropy density ratio ζ/s as a function of the normalized temperature T/T_c. The full black line shows the DQPM* and the full orange line the DQPM result. The symbols show lQCD data for pure $SU(3)$ gauge theory taken from Refs. [201] (circles) and [202] (squares and triangles). The blue line shows the estimate from a Bayesian analysis of experimental heavy-ion data [210].

incompatible with the small, but non-zero lattice data.

We continue the discussion of transport coefficients with the electric conductivity for stationary electric fields σ_0. We introduced the electric conductivity already in Ohm's law in Eq. (3.57). The conductivity describes the response of a system to an external electric field. Linear response theory demands a linear relation between the field strength and the electric current for small fields. The electric conductivity is the constant of proportionality, $\vec{j}_{em} = \sigma\vec{E}$. Using the Kubo-relation Eq. (3.61) one can calculate the electric conductivity on the lattice. The flux associated with the conductivity is the spatial part of the electric current j^μ_{em}. It is related to the vector currents of the different quark species,

$$j^\mu_{em} = e\sum_f q_f j^\mu_f = \frac{2e}{3}j^\mu_u - \frac{e}{3}j^\mu_d - \frac{e}{3}j^\mu_s. \tag{3.81}$$

The Kubo-relation for the conductivity reads [213, 214]:

$$\sigma_0 = \frac{C_{em}}{6}\lim_{\omega\to 0}\frac{\rho}{\omega}, \tag{3.82}$$

where ρ is the spectral function that belongs to the correlator of the spatial vector current and not the electric current. The electric charges enter via the factor C_{em}. For a partonic system C_{em} is

$$C_{em} = e^2 \sum_f q_f^2, \qquad C_{em}^{N_f=2} = e^2 \frac{5}{9}, \qquad C_{em}^{N_f=3} = e^2 \frac{2}{3}. \tag{3.83}$$

The electric charge in natural units follows from the Sommerfeld constant

$$\alpha = \frac{e^2}{4\pi} \qquad \Rightarrow \qquad e^2 \approx \frac{4\pi}{137} \approx 0.0917. \tag{3.84}$$

The Drude theory gives a simple explanation of the processes leading to a finite σ_0. All charged particles in an electric field feel an additional force proportional to their electric charge. The positive and negative charged particles will be accelerated in opposite directions inducing an electric current. This current is damped by collisions of the particles with each other which limits the acceleration, resulting in a constant value of the electric current. The effects of the collisions are describe by a simple friction term in the equations of motion. The Drude conductivity following from these assumptions is

$$\sigma_0 = \frac{e^2 \tau n_e}{m}, \tag{3.85}$$

where m is the mass of the particle, e the elementary charge and τ the average time between two collisions, i.e. the relaxation time. n_e is the total charge density and should not be confused with the net charge density connected to charge conservation. The Drude formula was first applied to metals but could not describe the measured conductivities. It assumes that all electrons contribute to the electric current, neglecting that some of them are bound to the atomic lattice. The Drude theory is also a classical theory and does not incorporate quantum-statistical effects like Pauli blocking. Fortunately, all these drawbacks do not apply to the QGP. The temperature is so high that quantum-statistical effects are negligible and all particles in the plasma can contribute to the current. We will use the relativistic generalization of the Drude formula to determine the dimensionless ratio σ_0/T for the QGP [85, 86, 215, 216],

$$\frac{\sigma_0}{T} = e^2 \sum_f \frac{q_f^2 \; n_{f+\bar{f}}}{\langle \omega_f \rangle T} \bar{\tau}_f = e^2 \sum_f \frac{q_f^2 \; (n_f^{\text{off}} + n_{\bar{f}}^{\text{off}})}{\langle \omega_f \rangle \cdot \langle \gamma_f \rangle \cdot T}, \tag{3.86}$$

where the sum runs over the three light quark flavors (u, d, s). The q_f are the fractional charges of the quarks and the density $n_{f+\bar{f}} = n_f^{\text{off}} + n_{\bar{f}}^{\text{off}}$ is the sum of the off-shell quasiparticle densities of quarks and antiquarks given by Eq.(3.80). Note that we have to exclude the spacelike parts of the spectral function to preserve causality. As in case of the viscosities we define the relaxation time by the inverse width (3.75) and for the DQPM* by the inverse ensemble averaged width (3.79). The mass in the original Drude formula is replaced by the expectation value of the energy,

$$\langle \omega_i \rangle = \frac{1}{n_i^{\text{off}}} \int \frac{d^3p}{(2\pi)^3} \int_0^\infty \frac{d\omega}{2\pi} \; 4\omega^2 \; A_i(\omega, \mathbf{p}) \; n_{B/F}(\omega) \; \Theta(P^2). \tag{3.87}$$

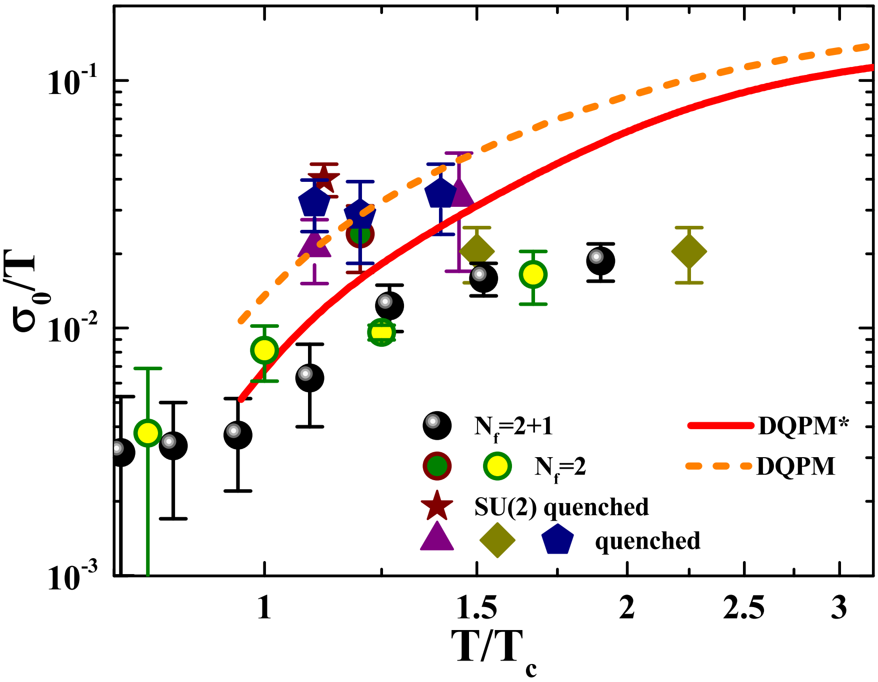

Figure 3.20: The electric conductivity over temperature σ_0/T as a function of the normalized temperature T/T_c. The full red line shows the DQPM* and the dashed orange line the DQPM result. The symbols show lQCD data taken from Refs. [213, 217] (triangles), [218] (diamonds), [219] (pentagons), [220] (star), [221, 222] (green circles with brown borders), [223] (yellow circles with green borders) and [214, 224] (spheres).

The normalization factor is again the particle density of timelike off-shell quasiparticles (3.80). The nonrelativistic limit of $\langle\omega_i\rangle$ is the mass m.

The contribution of each quasiparticle species to the conductivity is proportional to their squared electric charge. The up-quarks with $q_u^2 = 4/9$ give four-times the contribution of the down and the strange quarks with $q_d^2 = q_s^2 = 1/9$. The gluons do not contribute at all. This is different to the viscosities where all particles in the system contribute to the transport process. Electric properties are similar to the thermodynamic density and the susceptibilities and probe only the quark degrees of freedom.

The relativistic Drude formula (3.86) should be well suited to determine the conductivity of the QGP. We confirmed this assumption in Refs. [215, 216] where we simulated the QGP with the PHSD transport approach, a transport realization of the DQPM, in a box with periodic boundary conditions and applied an external electric field to the whole box. After some time a constant electric current emerged, which was proportional to the electric field, thus defining the electric conductivity $\sigma_0 = j_{em}/E$. The results from these dynamical simulations are well described by the Drude conductivity.

We show in Fig. 3.20 the electric conductivity over temperature σ_0/T as a function of T/T_c. The ratio rises almost linearly with temperature above T_c. This is mainly driven by the increasing number of quarks at higher temperatures. Additional charge carriers increase the electric current and therefore the conductivity. We find smaller results in the DQPM* than in the DQPM. The reason is again the smaller relaxation time, but also the larger average energy $\langle\omega\rangle$ in the momentum-dependent DQPM*. The difference is most pronounced close to the phase transition. At larger temperatures the ratio σ_0/T will saturate. The ensemble averaged width and energy rise linearly with the temperature canceling the density which increases like T^3. The saturation value of σ_0/T is similar in both quasiparticle models. We show also various lQCD calculations. It is not possible to determine the conductivity from pure Yang-Mills simulations, because one needs dynamical quarks, i.e. charged particles in the system. This can be done in the quenched approximation or with dynamical fermions. The data from Refs. [213, 217] (triangles), [218] (diamonds), [219] (pentagons) and [220] (star) are calculated in the quenched approximation. In case of Ref. [220] (star) for a $SU(2)$ gauge theory. The data from Refs. [221, 222] (green circles with brown borders) and [223] (yellow circles with green borders) are obtained for $N_f = 2$ and the results from Refs. [214, 224] (black spheres) for $N_f = 2 + 1$ dynamical flavors. The various lattice results differ again by more than one order of magnitude, but the results from Refs. [223] and [214, 224] using dynamical fermions seem to coincide with each other. Both are smaller than the conductivities from the quenched calculations, indicating the importance of dynamical fermions. The σ_0 from the DQPM is too large and incompatible with these lQCD data, but the DQPM* is close at low temperatures. The σ_0/T from the simulations with dynamical quarks seem to saturate at much lower temperatures and at a value one order of magnitude smaller than our quasiparticle models. This is surprising as the saturation takes place far below the perturbative result of $\sigma_0/T \approx 5.97/e^2 \approx 65$, while η/s at comparable temperatures is much closer to its perturbative ratio ≈ 1 [225]. We suppose that the reconstruction of the spectral function at larger temperatures is less precise which might lead to the extremely low lQCD results.

We continue with the discussion of the transport coefficients at finite chemical potential. The Eqs. (3.77), (3.78) and (3.86) incorporate already the effects of a finite μ_B. We use the effective coupling derived from the flow-equation and calculate the transport coefficients also for finite baryon chemical potentials μ_B, but enforce strangeness neutrality to match the conditions in heavy-ion collisions. Fig. 3.21 shows the shear viscosity over entropy density, Fig. 3.22 the bulk viscosity over entropy density and Fig. 3.23 the electric conductivity over temperature for the DQPM* as a function of the temperature and the baryon chemical potential. The ratios η/s and σ_0/T increase with μ_B at all temperatures, but ζ/s only for $T > 300$ MeV. It decreases at low temperatures where the bulk viscosity is dominated by the mean-field effects that enter via dM^2/dT^2. This term depends primarily on the effective coupling. Since g^2 decreases as a function of μ_B, also the mean-field effects become weaker. This leads to a decrease of ζ/s contrary to the other transport coefficients. The mean-field effects become also less pronounced at larger temperatures, resulting in a decreasing ζ/s as a function of temperature. That explains why the μ_B-behavior of the bulk viscosity changes with temperature. When the mean-field effects become subleading, their further decrease has no influence on the bulk viscosity and the ratio ζ/s starts to increase with μ_B as seen for the other transport coefficients.

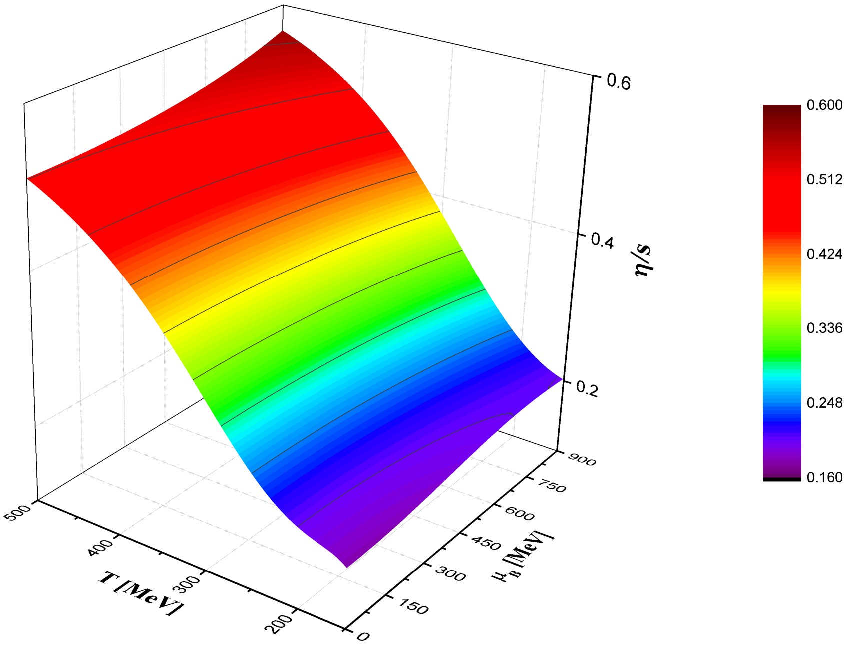

Figure 3.21: Shear viscosity over entropy density from the DQPM* as a function of the temperature T and the baryon chemical potential μ_B.

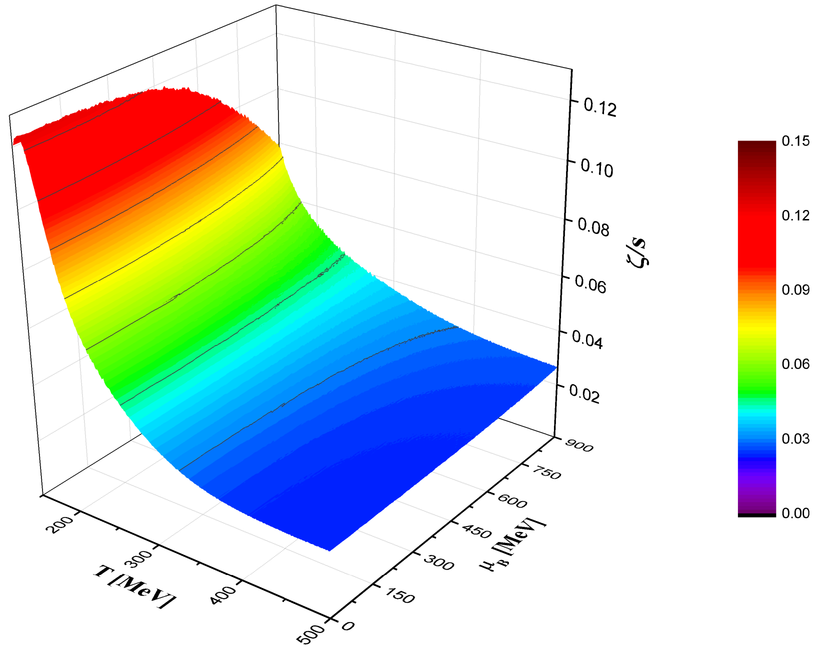

Figure 3.22: Bulk viscosity over entropy density from the DQPM* as a function of the temperature T and the baryon chemical potential μ_B.

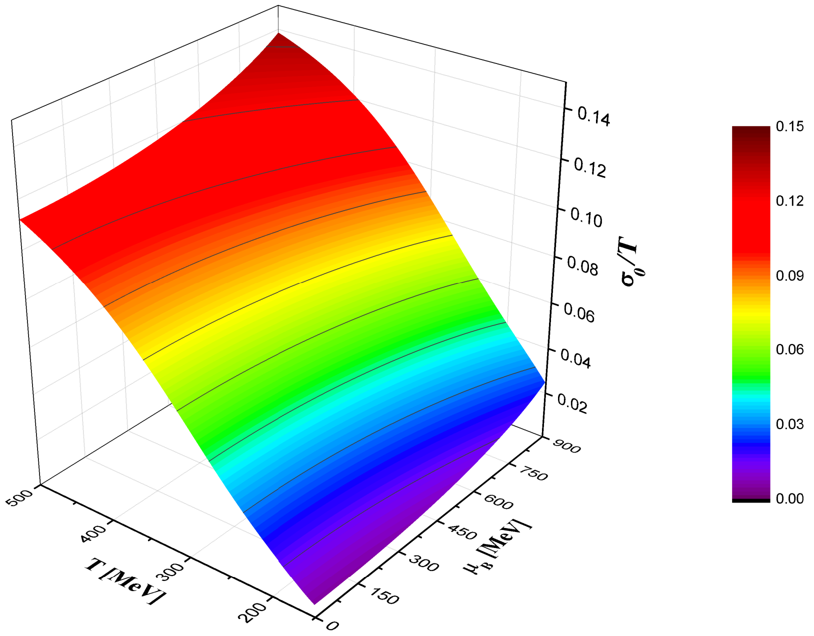

Figure 3.23: Electric conductivity over temperature from the DQPM* as a function of the temperature T and the baryon chemical potential μ_B.

One can easily understand the increase of σ_0/T from the Drude conductivity (3.86). A larger chemical potential increases the quasiparticle density such that more particles contribute to the charge current and the conductivity rises [216]. We will check if the same connection applies also to the viscosities. At small chemical potentials all even functions of μ_B behave like

$$\frac{X(\mu_B)}{X(0)} = 1 + c_X \frac{\mu_B^2}{T^2}. \tag{3.88}$$

We calculate c_X for the different transport coefficients and compare them to the coefficients of the total quasiparticle densities. For the shear viscosity we find $c_\eta = 0.036$ and for the conductivity $c_\sigma = 0.052$. The coefficient for the bulk viscosity depends on the temperature. It takes a constant value after the mean-field effects vanish and one finds $c_\zeta = 0.048$. The coefficient for the light-quark quasiparticle density is $c_l = 0.052$ and for the quasiparticle density of light and strange quarks $c_{l+s} = 0.037$. It is smaller because the strange quarks are suppressed by strangeness neutrality. For the whole system -including also the gluons- we find $c_{l+s+g} = 0.03$. The conductivity scales with the light quark density, more precisely, the up-quark density, because they carry twice the electric charge of the other quarks and are responsible for 2/3 of the QGP conductivity. The shear viscosity scales with the light plus strange quark density. The gluon contribution to η/s is suppressed since they have smaller relaxation times than the quarks. The behavior of the bulk viscosity can not be explained by just the quasiparticle densities. The speed of sound and the mean-field effects change also at finite chemical potential and influence the bulk viscosity. The approximation (3.88) applies only at small chemical potentials. At larger μ_B the masses and widths start to differ from their $\mu_B = 0$ values, additionally influencing the transport coefficients.

Both quasiparticle models, the DQPM and the DQPM*, produce good results for all three transport coefficients. They reproduce the expected temperature dependence and agree with lQCD calculations and experimental predictions. This is an important check for the parametrization of the quasiparticle widths of the DQPM, Eq. (3.10) and (3.11), and the DQPM*, Eq. (3.24) and (3.25). The widths give only small corrections to the thermodynamics, but are crucial for the transport properties. The coefficients depend always linearly on the relaxation times $\bar{\tau}_f$ determined by the inverse width. The agreement between the lQCD predictions and our results justify the chosen parametrizations.

In total the DQPM and the DQPM* can successfully describe the QCD equation of state as well as the most important transport coefficients, thus explaining the dynamics of hot QCD. The DQPM* is the first quasiparticle model that can also reproduce the susceptibility and has a reasonable extension to finite chemical potentials. Using thermodynamic consistency to control the model at finite μ_B we predict the equation of state and the transport coefficients at chemical potentials exceeding by far the current range of lQCD calculations.

4 The effective Nambu Jona-Lasinio model

The DQPM can reproduce the thermodynamics and also to some extend the dynamics of hot QCD matter, but was unable to study the phase structure of QCD and is not applicable in the vicinity of the phase transition. We will study the phase transition and the order parameters of chiral symmetry and confinement using the Nambu Jona-Lasinio and the Polyakov extended Nambu Jona-Lasinio model. Both are effective models that employ only quark degrees of freedom. However, these quarks are fundamentally different from the massive quasiparticles in the DQPM model and much closer to bare perturbative quarks.

4.1 The Nambu Jona-Lasinio model

The Nambu Jona-Lasinio (NJL) model is an effective theory for low-energy QCD designed to model dynamical chiral symmetry breaking. It was first developed by Nambu and Jona-Lasinio as a theory for nucleons [226, 227] but later rediscovered for QCD. The gluons are integrated out from the QCD Lagrangian and the quarks interact via a contact interaction. The interaction has to fulfill the same symmetries as QCD, most important chiral symmetry. This symmetry implies that the left-handed and the right-handed part of the fermionic wavefunction transform independently from each other. It is broken by a non-vanishing quark condensate. In the simple picture of the NJL-model chiral symmetry is conserved if the quarks are massless and broken if the quarks have a finite mass. In QCD chiral symmetry is explicitly broken by the bare quark masses, however, this explicit breaking is small since the masses ($\sim$ 5 MeV) are very small compared to the QCD scale $\Lambda_{QCD} \approx 200$ MeV. The symmetry breaking due to the interaction is much stronger, leads to an increase of the quark masses and explains the difference between the bare masses $m_0 \approx 5-7$ MeV and the constituent quark masses of $M \approx 338-350$ MeV. This mechanism is called dynamical mass generation and is modeled in the NJL approach.

At finite temperature the dynamically generated mass vanishes and chiral symmetry is restored. One knows from lQCD studies that the chiral phase transition at finite temperature and vanishing chemical potential is a crossover [36, 37, 38]. Within the NJL approach one can study the phase transition also at finite chemical potential. It was found that the crossover turns into a first-order phase transition at the critical end point (CEP). The location and even the existence of this CEP is model dependent and it is unknown if there is a CEP in full QCD or not. However, the motivation to search for this point comes from effective models like the NJL.

The NJL model has a variety of applications. It is used to study hadron properties and the phase structure of QCD. Reviews to NJL models can be found in Refs. [44, 162, 228, 229]. We will focus on the thermodynamics of the model. The NJL is a low-energy model for QCD. The gluons are integrated out and the complicated quark-gluon interaction is replaced by local quark interactions. The explicit from of the interaction follows from a Fierz-transformation, but is not unique. One can add more interaction terms, as long as these terms fulfill the same symmetries as QCD, most important chiral symmetry. We use the common three-flavor Lagrangian [44],

$$\begin{aligned}\mathcal{L}_{NJL} =&\bar{\Psi}\left(i\gamma^{\mu}\partial_{\mu}-\hat{m}_0\right)\Psi + G\sum_{a=0}^{8}\left(\left(\bar{\Psi}\lambda^a\Psi\right)^2+\left(\bar{\psi}i\gamma_5\tau_a\Psi\right)^2\right) \\ &-K\left(\det{}_f\left(\bar{\Psi}\left(1+\gamma_5\right)\Psi\right)+\det{}_f\left(\bar{\Psi}\left(1-\gamma_5\right)\Psi\right)\right).\end{aligned} \tag{4.1}$$

The λ^a are the Gell-Mann matrices in flavor space with $\lambda^0=\sqrt{2/3}\,\mathbb{1}_3$ and $\bar{\Psi}=(\bar{u},\bar{d},\bar{s})$, $\Psi=(u,d,s)^T$. The 6-point interaction term with the flavor determinant is the 't Hooft interaction. It belongs to a six-quark interaction that breaks the $U_A(1)$-symmetry and gives rise to the η-η' mass-splitting [230, 231].

The thermodynamic potential in mean-field approximation is derived in Appendix A.5 and reads,

$$\begin{aligned}\Omega_{NJL} =&-2N_c\sum_{u,d,s}\int\frac{d^3p}{(2\pi)^3}\left(\omega_p\,\Theta\left(\Lambda^2-\mathbf{p}^2\right)+\frac{p^2}{3\omega_p}\left(n_F(T,\mu_q,M_q)+n_{\bar{F}}(T,\mu_q,M_q)\right)\right) \\ &+2G\left(\langle\bar{u}u\rangle^2+\langle\bar{d}d\rangle^2+\langle\bar{s}s\rangle^2\right)-4K\langle\bar{u}u\rangle\langle\bar{d}d\rangle\langle\bar{s}s\rangle,\end{aligned} \tag{4.2}$$

with the effective masses

$$M_i = m_{0i}-4G\langle\bar{q}_iq_i\rangle+2K\langle\bar{q}_jq_j\rangle\langle\bar{q}_kq_k\rangle, \tag{4.3}$$

with $i\neq j\neq k$. In contrast to the non-interacting thermodynamic potentials (2.28) and (2.29) we can not neglect the divergent vacuum contribution since the model would not exhibit a finite quark condensate in the vacuum. We regularize the contribution by a three-momentum cutoff Λ. The quark condensates follow from the selfconsistent equation,

$$\langle\bar{q}_fq_f\rangle=\frac{\partial\Omega}{\partial M_f}=-2N_c\int\frac{d^3p}{(2\pi)^3}\frac{M_f}{\omega_p}\left(\Theta\left(\Lambda^2-\mathbf{p}^2\right)-n_F(T,\mu_f,M_f)-n_{\bar{F}}(T,\mu_f,M_f)\right), \tag{4.4}$$

that is equivalent to the stationary condition of the thermodynamic potential (2.12). Note that the Fierz-transformation introduces also a repulsive interaction [228],

$$\mathcal{L}=-G_V\sum_{a=0}^{8}\left(\left(\bar{\Psi}\gamma^{\mu}\lambda^a\Psi\right)^2+\left(\bar{\psi}i\gamma_5\gamma^{\mu}\tau_a\Psi\right)^2\right), \tag{4.5}$$

	RKH [232]	HK [162]	empirical [233]
Λ [MeV]	602.3	631.4	
$G\Lambda^2$	1.835	1.835	
$K\Lambda^5$	12.36	9.29	
$m_{u,d}$ [MeV]	5.5	5.5	3.5 - 7.5
m_s [MeV]	140.7	135.7	110 - 210
$M_{u,d}$ [MeV]	367.7	335	
M_s [MeV]	549.5	527	
$(\langle \bar{u}u \rangle)^{1/3}$ [MeV]	-241.9	-246.9	
$(\langle \bar{s}s \rangle)^{1/3}$ [MeV]	-257.7	-267.0	
T_c [MeV]	171	173	
CEP (μ_c, T_c) [MeV]	$(325, 48)$	$(315, 67)$	
f_π [MeV]	92.4	93.0	92.4 [234]
m_π [MeV]	135.0	138	135.0, 139.6
m_K [MeV]	497.7	496	493.7, 497.7
m_η [MeV]	514.8	487	547.3
$m_{\eta'}$ [MeV]	957.8	958	957.8

Table 4.1: Parameters of the NJL model. The set RKH is taken from Ref. [232], the set HK from Ref. [162]. The empirical properties are taken from Ref. [233], except for f_π from Ref. [234]. The critical temperature T_c is determined from the maximum of $\frac{\partial \langle \bar{q}q \rangle}{\partial T}$. The table is partly taken from Ref. [44].

that has no effect on the results at vanishing chemical potential but serious consequences for the phase boundary! The location of the CEP will shift towards the $T = 0$ axis for an increasing vector coupling G_V [235, 236, 237]. The Fierz-transformation relates the strength of the vector coupling to the scalar coupling G, leading to the relation $G_V = G/2$. This value is so large, that the CEP vanishes for most realistic parametrizations. Despite being fixed by the Fierz-transformation, G_V is mostly taken as an additional free parameter, that is used to improve the behavior at finite chemical potential. We will also use this strategy and set the vector repulsion to zero as in most other studies of the NJL model [162, 232].

The model so far has five parameters, the momentum cutoff Λ, the effective four quark coupling G, the effective six quark coupling K and the bare quark masses $m_{u,d}$ and m_s. To determine the parameters one usually calculates mesonic bound states and fits the results to the measured ones. An interesting feature worth to mention is, that the pseudoscalar meson masses will vanish in the chiral limit, i.e. for massless quarks. This implies that the spontaneous breaking of chiral symmetry leads to massless pseudoscalar particles, i.e. massless pions and kaons, even if the quarks themself gain a huge mass. The NJL model fulfills the Goldstone theorem and is therefore a reliable tool to study chiral symmetry and mesonic properties in low-energy QCD.

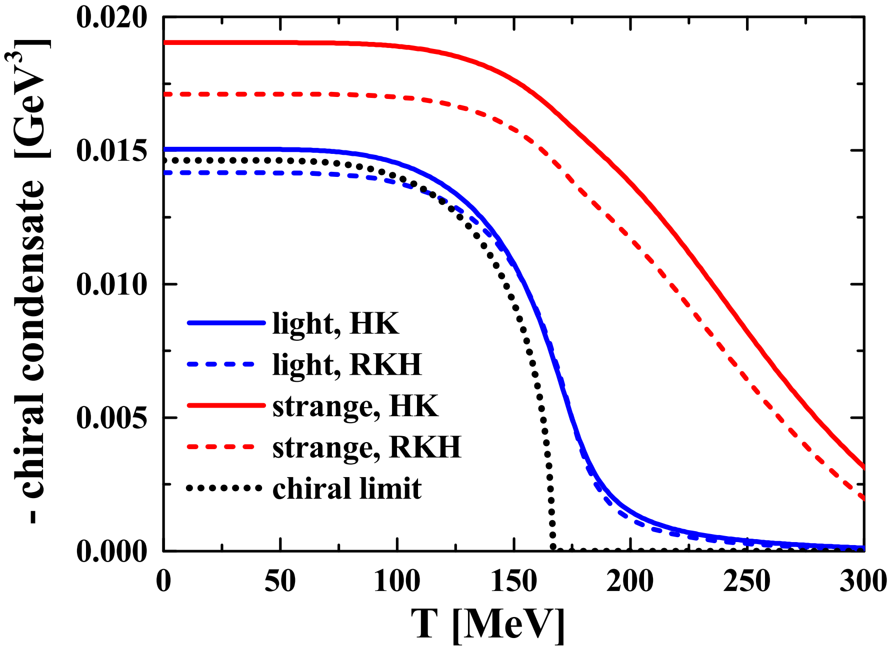

Figure 4.1: The negative chiral condensate from the NJL model as a function of the temperature. The blue lines show the light quark condensate, the red lines the strange quark condensate. Full lines are calculated with the parameter set HK [162], the dashed lines with the set RKH [232]. The black dotted line is the chiral limit $m_{u,d} \to 0$ of HK.

We will not repeat the calculation of hadronic properties and refer to the reviews [44, 162, 228, 229]. We will use the parameters determined in Ref. [162] and Ref. [232] and denote the first set HK and the second RKH. The parameters and the fitting results are shown in Tab. 4.1. Both sets are fitted to the pion mass and decay constant, the kaon mass and the η' mass. The bare light quark mass is taken as the average of the bare up and bare down mass; the mass of the η is a prediction. The empirical properties were taken from the particle data group [233], the pion decay constant f_π from Ref. [234]. $M_{u,d}$ and M_s are the effective masses of the light and strange quarks in the vacuum and thus correspond to the constituent quark masses. The light and the strange condensate for both sets are shown in Fig. 4.1 as a function of the temperature at vanishing chemical potential. The chiral limit refers to the chiral limit of the light quarks, $m_{u,d} \to 0$, the strange quark is kept massive. We show the chiral limit only for the HK parameter set. The condensates stay at their vacuum values up to $T = 100$ MeV. The light quark condensate decreases very rapidly in the temperature window between $T = 130$ MeV and $T = 200$ MeV and stays small at higher temperatures while the strange quark condensate drops slower in the whole temperature range between $T = 130$ MeV and $T = 300$ MeV. We observe a smooth crossover in both parametrizations at vanishing chemical potential $\mu = 0$. Accordingly, the critical temperature T_c in Tab. 4.1 is determined by the maximum of $\frac{\partial\langle\bar{q}q\rangle}{\partial T}$. The condensate in the chiral limit exhibits a second-order transition. At low temperatures it behaves similar

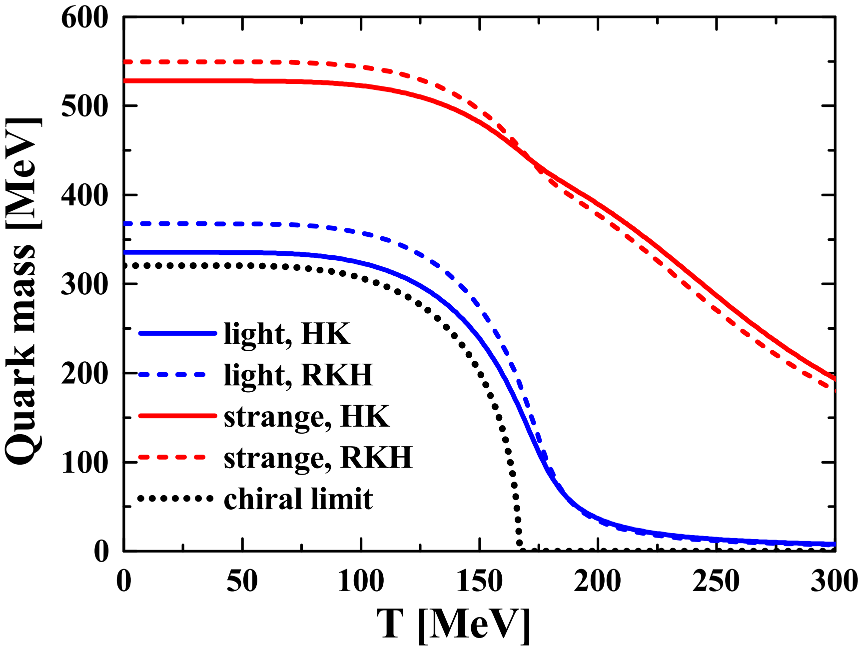

Figure 4.2: The effective quark masses from the NJL model as a function of the temperature. The blue lines show the light quark mass, the red lines the strange quark mass. Full lines are calculated with the parameter set HK [162], the dashed lines with the set RKH [232]. The black dotted line is the chiral limit $m_{u,d} \to 0$ of HK.

to the condensate for finite quark masses but it goes to zero at $T_c = 170$ MeV. The strange quark condensate in the chiral limit behaves exactly like in the massive case at all temperatures, except for the phase transition where it has a small kink due to the vanishing light quark condensate.

Fig. 4.2 shows the effective masses, calculated from Eq. (4.3). The dotted black line is again the chiral limit $m_{u,d} \to 0$ of the HK parameter set. The behavior of the masses is dominated by the four-quark interaction, i.e. by their own condensates. The light quark mass in the vacuum takes a value of approximately one third of the nucleon mass. The masses do vanish with finite temperature in the same way as the condensates in Fig. 4.1. The effective masses will drop only at higher temperatures down to the bare quark masses. In the chiral limit we see that the mass goes to zero at the phase transition. The condensates of the HK set are always larger than the ones from RKH. For the masses we find that the HK masses are smaller than the RKH masses, as expected from the condensates, at small temperatures. However, the order changes for $T = 175$ MeV. The reason is the larger strange-quark condensate of the HK parameter set, that enters the mass by the six-quark coupling.

The NJL has no clear phase transition at vanishing chemical potential $\mu = 0$. This changes if we investigate the model at zero temperature and finite baryon chemical potential. We show the effective quark masses for the HK parameter set for $T = 0$ and $\mu_B \neq 0$ in the left panel of Fig. 4.3 as a function of the light quark chemical poten-

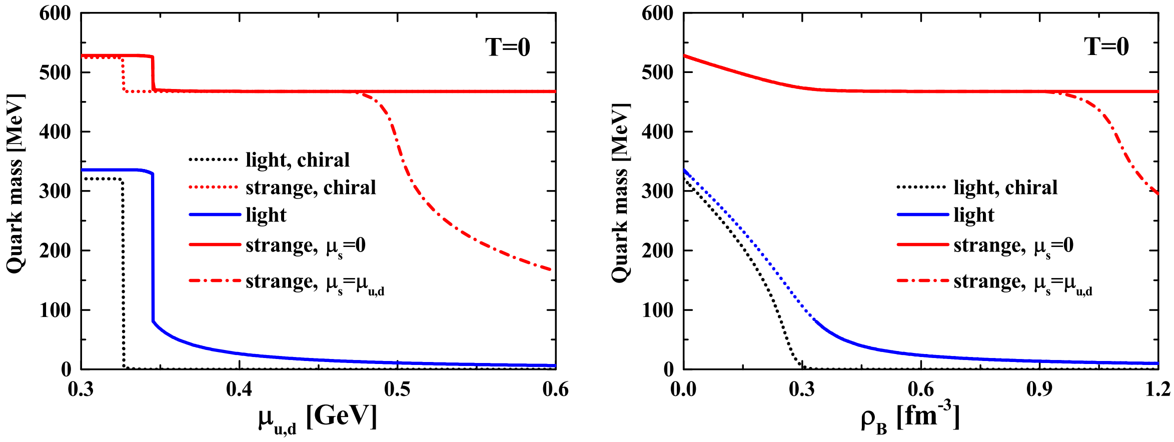

Figure 4.3: The effective quark masses from the NJL model for the HK parameter set [162] at finite chemical potential and $T = 0$ with strangeness neutrality $N_S = 0$, i.e. $\mu_s = 0$. The left panel shows the effective masses as function of the light quark chemical potential, the right panel as function of the baryon density $\rho_B = (n_u + n_d + n_s)/3$. The full blue line is the effective light quark mass and the full red line the effective strange quark mass. The dotted black and the dotted red line are the effective masses in the chiral limit $m_{u,d} = 0$. The dash-dotted red line is the effective strange quark mass without strangeness neutrality. The dotted part of the full blue line in the right panel marks the forbidden region that is inside the phase transition.

tial $\mu_{u,d} = \mu_B/3$. The light quark condensate can be estimated from the effective light quark mass since it has qualitatively the same behavior as the negative effective mass $\langle \bar{q}q \rangle \sim -M_{u,d}$. We employ strangeness neutrality $N_S = 0$ and fix the strange quark chemical potential to $\mu_s = 0$. This has the effect, that we get no thermal contribution to the strange quark condensate. Changes in the strange quark mass are entirely due to the light quark condensate. We find a clear first-order phase transition at $\mu_c = 345$ MeV where the light quark mass drops to a quarter of its vacuum value. The transition in the chiral limit is at a slightly smaller chemical potential $\mu_{c,m_{u,d}=0} = 326$ MeV. The strange quark mass is also feeling the light quark transition, but apart from this, it will stay almost unchanged. We demonstrate this with the red dash-dotted line, that shows the effective strange quark mass without strangeness neutrality, i.e. $\mu_s = \mu_{u,d} = \mu_B/3$. We see no difference to the strangeness neutral case for small chemical potential, but we start to get a thermal contribution after $\mu_{u,d}$ exceeds the strange quark mass for $\langle \bar{q}q \rangle \approx 0$, i.e. $M_{s,\langle \bar{q}q \rangle = 0} = 468$ MeV. The strange effective mass, and also the strange condensate, will then decrease smoothly as for finite temperature and $\mu_B = 0$.

We find a crossover transition at finite temperature and $\mu_B = 0$, but a first-order transition at finite chemical potential and $T = 0$. This implies that the model features a critical point. The CEP for the HK parameter set is at $\mu_c = 325$ MeV and $T_c = 48$ MeV and for the RKH set at $\mu_c = 315$ MeV and $T_c = 67$ MeV.

It is possible to calculate the effective masses also in the forbidden region inside the phase transition. We show in the right panel of Fig. 4.3 the effective masses as a function of

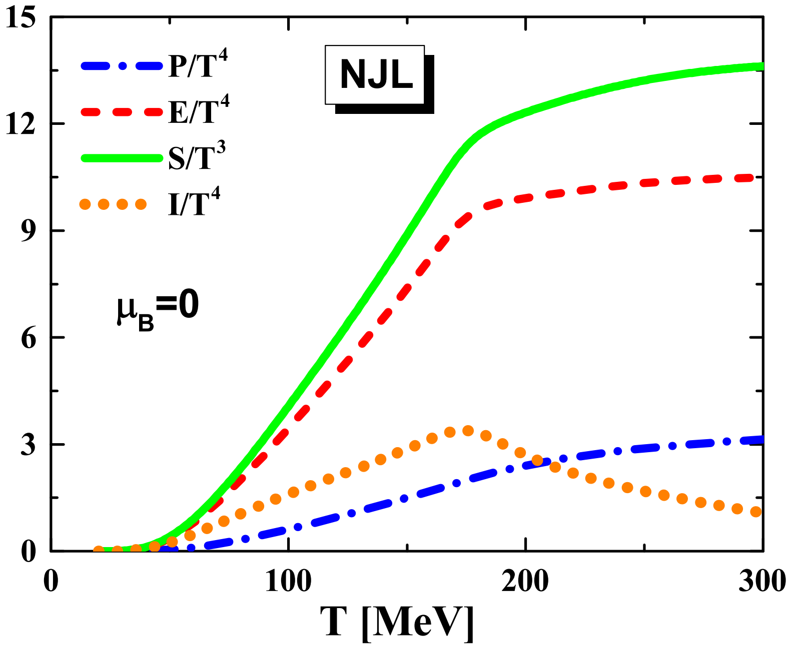

Figure 4.4: The equation of state of the NJL model for the parameter set HK [162] as a function of the temperature T for vanishing chemical potential. The full green line shows the entropy, the dashed red line the energy, the dash-dotted blue line the pressure and the dotted orange line the interaction measure defined by $I = E - 3P$. All quantities are scaled by powers of the temperature.

the baryon density $\rho_B = (n_u + n_d + n_s)/3$ at $T = 0$. The dotted part of the light quark mass (full blue line) indicates the forbidden region $0.01 < \rho_B < 0.33$ fm^{-3}. We employ again strangeness neutrality, but the dash-dotted red line shows the strange quark mass without this constraint. We find that the effective masses decrease almost linearly for small densities. This behavior is similar to the effective nucleon mass in relativistic mean-field theories, see Sec. 5.2, but the NJL model can not reproduce the properties of normal nuclear matter. Stable nuclear matter has a density of $\rho_B = 0.16$ fm^{-3}, which is inside the forbidden region for the NJL. Strange quarks will only contribute at very large densities $\rho_B > 0.9$ fm^{-3}, where one expects already a deconfined system. This indicates that strange quarks, and more important strange hadrons, are unimportant for the nuclear equation of state at small and intermediate densities at $T = 0$.
With the condensates determined we can calculate the equation of state. This is one of the advantages of the NJL model, that it simultaneously provides the thermodynamics and the order parameter of chiral symmetry restoration. The equation of state for zero chemical potential is shown in Fig. 4.4 for the HK parameter set. The scaled entropy density, energy density and interaction measure rise almost linear from $T \approx 50$ MeV to $T \approx 170$ MeV, while lQCD results show a steeper rise and an earlier saturation of all quantities. The linear rise ends after the light quark condensate has almost dropped to zero. From there on the scaled entropy density, energy density and pressure will rise

slowly towards the Stefan-Boltzmann limit while the interaction measure starts to decrease. Note that the Stefan-Boltzmann limit of QCD and NJL are different since NJL does not incorporate gluons. The equation of state for full QCD is always larger, but the NJL is closer to its Stefan-Boltzmann limit.

We see from Fig. 4.4 that the NJL underestimates the equation of state at lower temperatures $T < 100$ MeV, where we expect a gas of non-interacting pions. This can be cured by considering mesonic correlations in the thermodynamic potential [238], that in lowest order are given by the ring sum [239, 240]

$$\Omega_{corr} = \sum_{meson} \frac{d_M}{2} \int d^4p \ln\left(1 - G\,\Pi_M\right). \tag{4.6}$$

Here d_M is the mesonic degeneracy factor and Π_M is the q-$\bar{q}$ polarization loop with the quantum numbers of the respective meson. If the bound state is stable, Eq. (4.6) will turn into the thermodynamic potential of a non-interacting particle with the mass of the bound state pole. The mesonic correlations in the NJL model have been studied in Ref. [241] for the pion and the σ-meson. One found that the equation of state below the transition temperature is indeed equal to a gas of non-interacting pions and σ's and originates entirely from the mesonic correlations. The correlations will vanish as the temperature increases beyond the transition temperature. It might seem as if the NJL describes confinement, but this is not the case. The mesons in the NJL can still decay into a quark-antiquark pair, even at low temperatures, which was never observed in nature.

Since the NJL shows no clear phase transition, we have no real critical temperature. Nevertheless, we find a rapid change in the order parameter where the system goes from a chiral broken to an almost restored phase. There are various approaches how to define a critical temperature for a crossover. The most intuitive way is to define the transition at the most rapid change of the order parameter, i.e. the maximum of the temperature derivative of the condensate,

$$\chi_T = \frac{\partial\langle\bar{q}q\rangle}{\partial T}, \tag{4.7}$$

or the maximum of the chiral susceptibility,

$$\chi_m = \frac{\partial\langle\bar{q}q\rangle}{\partial m_{u,d}} = \frac{\partial^2\Omega}{\partial m_{u,d}^2}. \tag{4.8}$$

Both quantities would diverge at an actual phase transition. The critical temperature in Tab. 4.1 is defined using the maximum of χ_T. The susceptibilities χ_T and χ_m themselves are shown in Fig. 4.5. They have their maximum at the same temperatures and are in general very similar as a function of temperature. Note that we have decreased χ_m by a factor of 20 and reversed the sign since it is a negative real function. The critical temperatures from χ_T are $T_c^{HK} = 171$ MeV for the HK and $T_c^{RKH} = 173$ MeV for the RKH parameter set.

Another possibility to determine T_c is to look at the thermodynamics. A rapid change in the system properties will reflect itself on the equation of state. The maximum of

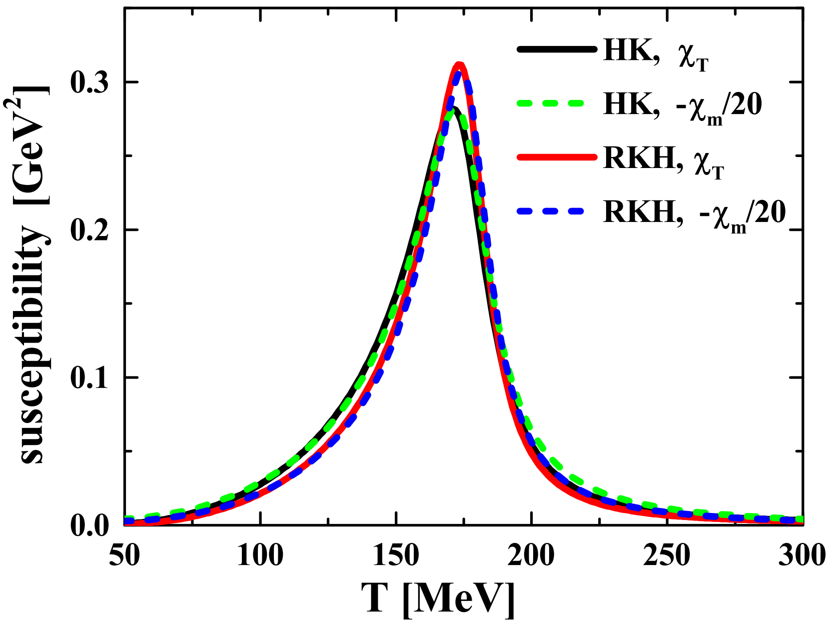

Figure 4.5: The temperature susceptibility χ_T and the negative chiral susceptibility χ_m from the NJL model as a function of the temperature. The full black line and the green dashed line show χ_T and χ_m for the HK parameter set [162], the full red line and the dashed blue line show χ_T and χ_m for the RKH parameter set [232]. The results for the negative chiral susceptibility are divided by a factor of 20.

the susceptibilities coincides with the temperature where the scaled energy turns from a linear rise into an almost constant behavior. One usually uses the inflection point of the dimensionless equation of state to define the critical temperature. The critical temperatures obtained from various methods are summarized in Tab. 4.2. We see that all methods, that use directly the condensate or the effective mass, give roughly the same results in both parametrizations. This is different for the inflection point method where we find lower temperatures. An important exception is the inflection point of the speed of sound squared $c_s^2 = \partial P/\partial E$, that leads to a critical temperature too large compared to the susceptibilities, but gives similar results for both parametrizations. The speed of sound is sensitive to the order parameter since it exhibits a jump at a proper phase transition. The last method used is the maximum of the scaled interaction measure I/T^4. This maximum is between the critical temperature from the susceptibilities and the speed of sound inflection point. The results from Tab. 4.2 imply that one has to be very careful if one wants to define the transition temperature from only the thermodynamics, however, the phase transition has clearly a strong influence on the shape of the equation of state.

Method	T_c [MeV] HK	T_c [MeV] RKH
Max. χ_T	171	173
Max. χ_m	172	174
Max. $dM_{u,d}/dT$	171	173
$\langle \bar{q}q \rangle / \langle \bar{q}q \rangle_0 = 1/2$	166	168
$M_{u,d}/M_{u,d\ 0} = 1/2$	166	168
Inf. point P/T^4	167	173
Inf. point E/T^4	157	164
Inf. point S/T^3	158	165
Inf. point c_s^2	177	179
Max. I/T^4	174	177

Table 4.2: Critical temperature T_c from different methods for the HK [162] and the RKH [232] NJL model. Max. χ_m and Max. $dM_{u,d}/dT$ refer to the maximum of the absolute value as both are negative.

4.2 The Polyakov NJL model

The NJL model describes only quarks and antiquarks and neglects the gluons. It has therefore the wrong number of degrees of freedom with respect to QCD. This is corrected in the so called Polyakov extended Nambu Jona-Lasinio model (PNJL) [45]. The first attempts to merge the NJL model with gluons go back to Meisinger and Ogilvie [242, 243]. The thermodynamics of the gluons are described by an effective potential that is motivated by Yang-Mills lattice results. The gauge field is then coupled back to the quark sector through a covariant derivative.

In the PNJL the gluons are not described by the gauge fields, instead we introduce the Polyakov loop L and the traced Polyakov loop,

$$\phi = \frac{1}{N_c}\mathrm{Tr}_c\, L = \frac{1}{N_c}\mathrm{Tr}_c\, \mathcal{P}\exp\left[i\int_0^\beta d\tau\ A_4(\vec{x},\tau)\right] = \frac{1}{N_c}\mathrm{Tr}_c\ \exp\left[\frac{iA_4}{T}\right], \tag{4.9}$$

that give the model its name. The field $A_4 = -iA^0$ is the temporal component of the Euclidean gauge field $(\vec{A}, A_4)$ while $\mathcal{P}$ is the path ordering operator. The gauge fields $(\vec{A}, A_4)$, and therefore the Polyakov loop L, are 3×3 matrices in color space. In the heavy-quark limit the traced Polyakov loop is an order parameter for confinement [117, 118], which is connected to the free energy F_q of a single quark,

$$\mathrm{Tr}_c\ L \sim e^{-F_q/T}. \tag{4.10}$$

In the confined phase, where one has no free quarks, the free energy is infinite and the traced Polyakov loop is zero, while in the deconfined phase with free quarks the free energy is finite and the traced Polyakov loop larger than zero:

$$\begin{aligned}
&\text{Confinement:} && F_q = \infty && \Rightarrow && \phi = 0 \\
&\text{Deconfinement:} && F_q < \infty && \Rightarrow && \phi > 0.
\end{aligned}$$

The trace of the adjoint Polyakov loop $L^\dagger$ corresponds to the free energy of an antiquark. It is the complex conjugate of the trace of the normal Polyakov loop $\mathrm{Tr}_c\ L^\dagger = \bar{\phi} = \phi^*$. Since there is no difference between quarks and antiquarks at vanishing chemical potential, both are the same ($L = L^\dagger$) and the trace is real. This is different at finite chemical potential where the traces are unequal ($\phi \neq \bar{\phi}$), see Refs. [244, 245].
Similar to the QCD Lagrangian (2.44) we couple the gauge fields to the quark fields by minimal coupling and introduce a covariant derivative,

$$D^\mu = \partial^\mu - iA^\mu, \qquad \text{with} \qquad A^\mu = \delta_0^\mu A^0, \qquad A^0 = g\mathcal{A}_a^0 \frac{\lambda_a}{2}, \tag{4.11}$$

and an effective potential $\mathcal{U}(T, \phi, \bar{\phi})$ that depends on the traced Polyakov loop and has to reproduce the thermodynamics of the pure Yang-Mills limit of QCD [45, 242]. Including them to a two-flavor NJL model leads to a two-flavor PNJL model [45] and including them to a three-flavor NJL model leads to a three-flavor PNJL model [246, 247]. We will use the same three-flavor NJL Lagrangian (4.1) as in the last section. The PNJL Lagrangian is then given by:

$$\begin{aligned}
\mathcal{L}_{PNJL} =& \mathcal{L}_{NJL} + \bar{\Psi}\gamma_\mu A^\mu \Psi - \mathcal{U}(T, \phi, \bar{\phi}) \\
=& \bar{\Psi}\left(i\gamma^\mu D_\mu - \hat{m}_0\right)\Psi + G\sum_{a=0}^{8}\left(\left(\bar{\Psi}\lambda^a\Psi\right)^2 + \left(\bar{\psi}i\gamma_5\tau_a\Psi\right)^2\right) \\
&- K\left(\det{}_f\left(\bar{\Psi}\left(1+\gamma_5\right)\Psi\right) + \det{}_f\left(\bar{\Psi}\left(1-\gamma_5\right)\Psi\right)\right) - \mathcal{U}(T).
\end{aligned} \tag{4.12}$$

We derive the thermodynamic potential for (4.12) in mean-field approximation in Appendix A.6. For $N_c = 3$ the potential reads:

$$\begin{aligned}
\Omega_{NJL} =& -2N_c \sum_{u,d,s}\int \frac{d^3p}{(2\pi)^3}\left(\omega_p\ \Theta\left(\Lambda^2 - \mathbf{p}^2\right) + \frac{p^2}{3\omega_p}\left(n_F^\phi(T, \mu_q, M_q) + n_{\bar{F}}^{\bar{\phi}}(T, \mu_q, M_q)\right)\right) \\
&+ 2G\left(\langle\bar{u}u\rangle^2 + \langle\bar{d}d\rangle^2 + \langle\bar{s}s\rangle^2\right) - 4K\langle\bar{u}u\rangle\langle\bar{d}d\rangle\langle\bar{s}s\rangle + \mathcal{U}(T, \phi, \bar{\phi}),
\end{aligned} \tag{4.13}$$

where the distribution functions get modified by the traced Polyakov loops and have to be replaced by the expressions:

$$n_F^\phi = \frac{\phi\ e^{-\frac{\omega_p - \mu}{T}} + 2\ \bar{\phi}\ e^{-2\frac{\omega_p - \mu}{T}} + e^{-3\frac{\omega_p - \mu}{T}}}{1 + 3\ \phi\ e^{-\frac{\omega_p - \mu}{T}} + 3\ \bar{\phi}\ e^{-2\frac{\omega_p - \mu}{T}} + e^{-3\frac{\omega_p - \mu}{T}}}, \tag{4.14}$$

$$n_{\bar{F}}^{\bar{\phi}} = \frac{\bar{\phi}\ e^{-\frac{\omega_p + \mu}{T}} + 2\ \phi\ e^{-2\frac{\omega_p + \mu}{T}} + e^{-3\frac{\omega_p + \mu}{T}}}{1 + 3\ \bar{\phi}\ e^{-\frac{\omega_p + \mu}{T}} + 3\ \phi\ e^{-2\frac{\omega_p + \mu}{T}} + e^{-3\frac{\omega_p + \mu}{T}}}. \tag{4.15}$$

The modified distribution functions (4.14) and (4.15) have some interesting properties. In the confining vacuum, where the traced Polyakov loops vanish ($\phi = \bar{\phi} = 0$), we get a distribution function with three times the exponent. This can be interpreted as a Fermi-distribution function of a particle with three times the mass and the chemical potential

$$\exp\left(-3\frac{\sqrt{p^2+m^2}-\mu}{T}\right) \qquad \Longrightarrow \qquad \exp\left(-\frac{\sqrt{p^2+(3m)^2}-3\mu}{T}\right). \tag{4.16}$$

This is the distribution function we would expect for a baryon, that has three times the mass and the chemical potential $\mu_B = 3\mu_q$ of a constituent quark. In the perturbative vacuum with $\phi = \bar{\phi} = 1$ we get three times the normal Fermi-distribution function. It seems that the traced Polyakov loop ϕ, which is the order parameter of quark deconfinement, regulates the appearance of quarks and the conjugated traced Polyakov loop $\bar{\phi}$, which is the order parameter of antiquark deconfinement, regulates the appearance of diquarks, that carry an anticolor charge like a single antiquark. The appearance of three quark states, i.e. baryons, is not influenced by the confinement order parameter since these states are colorless and therefore unaffected by confinement. This is reversed in the antiquark distribution function $n_{\bar{F}}^{\bar{\phi}}$ where the antiquarks are regulated by $\bar{\phi}$ and antidiquarks by ϕ. All together this gives a very intuitive picture of confinement in the PNJL model.

To solve the model we have to determine the condensates $\langle \bar{q}_i q_i \rangle$ and the traced Polyakov loops. The quark condensates in the PNJL model follow from the same condition (A.58) as in the NJL,

$$\frac{\partial \Omega_{PNJL}}{\partial \langle \bar{q}_i q_i \rangle} = 0, \tag{4.17}$$

and lead also to the same equations (A.59) for the condensates, but with the PNJL distribution functions (4.14) and (4.15). As for the condensates we will determine the traced Polyakov loops from the stationary condition of the potential,

$$\frac{\partial \Omega_{PNJL}}{\partial \phi} = \frac{\partial \Omega_{PNJL}}{\partial \bar{\phi}} = 0. \tag{4.18}$$

For this we have to define the effective Polyakov potential $\mathcal{U}(T, \phi, \bar{\phi})$. The potential governs the pure gluon interaction without quarks. It has to reproduce the thermodynamics of the pure Yang-Mills theory and the proper temperature dependence of the Polyakov loop. For this it has to meet certain conditions, as summarized in Ref. [45]: The deconfinement transition in quenched QCD emerges from the spontaneous breaking of the $Z(3)$ center symmetry. This has to be reproduced by the potential $\mathcal{U}(T, \phi, \bar{\phi})$ that has to obey the $Z(3)$ symmetry for the same reason as the NJL interaction has to obey chiral symmetry. Pure Yang-Mills QCD has a first-order phase transition. The system is in its confined vacuum state up to the critical temperature $T_0 \approx 270$ MeV and becomes deconfined and gets excited beyond the vacuum if the temperature rises above T_0 [248, 249]. The traced Polyakov loop is zero in the confined and finite in the deconfined phase. The effective potential $\mathcal{U}(T,\phi,\bar{\phi})$ has to reflect these properties. At low temperatures it must have a global minimum at $\phi=\bar{\phi}=0$ and as the temperature increases a second minimum has to emerge that becomes the global minimum at the critical temperature. The physical value of the traced Polyakov loop follows then from the global minimum of the potential

$$\frac{\partial\mathcal{U}(T,\phi,\bar{\phi})}{\partial\phi}=\frac{\partial\mathcal{U}(T,\phi,\bar{\phi})}{\partial\bar{\phi}}=0. \tag{4.19}$$

The differences between the traced Polyakov loops ϕ and $\bar{\phi}$ arise from quantum fluctuations and taking them as equal is equivalent to the mean-field approximation for the Polyakov variables [47]. Keeping them as independent variables induces several problems. Already first calculations of the Polyakov potential in terms of the regular Polyakov loop L in Ref. [250] showed that the effective action might become complex. It was then argued in Ref. [251] that one could rewrite the effective Polyakov potential as a function of just the traced Polyakov loops. The stationary point of such models for $\phi\neq\bar{\phi}$ is a saddle point [244, 245], even in the case $\phi=\bar{\phi}$, since the free energy is not convex. It is believed that these are residues of the sign problem, that manifests itself also in effective models. A convex free energy is also given in effective theories with repulsive interactions. In this cases it is not a problem since the equation that leads to the convex energy follows within the theory [43]. This is different to Eqs. (4.18) and (4.19) that are implications of thermodynamic consistency. The PNJL model was studied without the constraint $\phi=\bar{\phi}$ in Ref. [47] and it was found that the difference between both traces is overestimated in this case. Therefore, it is better to treat the traced Polyakov loops on the mean-field level and take the thermodynamic potential as a function of only ϕ, as done in Ref. [252].

After having discussed the general properties of the Polyakov potential, we will now introduce parametrizations for the effective potential. The parametrization used in the very first PNJL model in Ref. [45] is the simplest possible form that was suggested in Ref. [251], a polynomial in the traced Polyakov loops:

$$\frac{\mathcal{U}_P(T,\phi,\bar{\phi})}{T^4}=-\frac{b_2(T)}{2}\phi\bar{\phi}-\frac{b_3}{6}\left(\phi^3+\bar{\phi}^3\right)+\frac{b_4}{4}\left(\phi\bar{\phi}\right)^2 \tag{4.20}$$

with

$$b_2(T)=a_0+a_1\left(\frac{T_0}{T}\right)+a_2\left(\frac{T_0}{T}\right)^2+a_3\left(\frac{T_0}{T}\right)^3. \tag{4.21}$$

The parameters were fitted to lattice data from pure $SU(3)$ Yang-Mills theory taken from Ref. [248] for the equation of state and Ref. [249] for the temperature dependence of the Polyakov loop. The results of the fit are shown in Tab. 4.3. This parametrization has the problem that the traced Polyakov loop can grow larger than one. This is unphysical since it would indicate negative energies, cf. Eq. (4.10). One can cure this by keeping the kinetic part of the potential $\sim\phi\bar{\phi}$ and replacing the higher polynomials in Eq. (4.20) by a logarithmic term. This logarithmic form of the potential was first suggested in Ref. [253], where the logarithm of the Haar measure associated with the $SU(3)$ group

a_0	a_1	a_2	a_3	b_3	b_4
6.75	-1.95	2.625	-7.44	0.75	7.5

Table 4.3: Parameter set for the effective potential $\mathcal{U}_P/T^4$ (4.20) taken from Ref. [45].

a_0	a_1	a_2	b_4
3.51	-2.47	15.22	-1.75

Table 4.4: Parameter set for the effective potential $\mathcal{U}_L/T^4$ (4.22) taken from Ref. [252].

interaction was used. Ref. [252] introduced an effective potential motivated by this ansatz,

$$\frac{\mathcal{U}_L(T,\phi,\bar{\phi})}{T^4} = -\frac{1}{2}b_2(T)\phi\bar{\phi} + b_4(T)\log\left[1 - 6\phi\bar{\phi} + 4\left(\phi^3+\bar{\phi}^3\right) - 3\left(\phi\bar{\phi}\right)^2\right] \tag{4.22}$$

with

$$b_2(T) = a_0 + a_1\left(\frac{T_0}{T}\right) + a_2\left(\frac{T_0}{T}\right)^2, \qquad b_4(T) = b_4\left(\frac{T_0}{T}\right)^3. \tag{4.23}$$

The parameters were fitted to the same lattice data [249, 248] as the parameters for the polynomial potential (4.20) and the results of this fit are displayed in Tab. 4.4.

The Polyakov loop contributes only to the thermal part of the thermodynamic potential, so we expect no modifications of the vacuum compared to the NJL. This implies that the mesonic properties in the vacuum are the same in both models and that we can keep the parametrizations of the NJL [162, 232] and use them for the quark/antiquark part of the PNJL model.

Even if the vacuum state is the same, we expect some modification at finite temperatures compared to the NJL. We show the order parameters for chiral symmetry restoration, i.e. the light quark condensate, and for confinement, i.e. the traced Polyakov loop, in Fig. 4.6 for the NJL and the PNJL. We use both the polynomial $\mathcal{U}_P$ (4.20) and the logarithmic $\mathcal{U}_L$ (4.22) Polyakov potential. We choose the HK parameter set [162] for the NJL dynamics and normalized the light quark condensates to their vacuum values. Chiral symmetry restoration occurs at a larger temperature in the PNJL model but the transition region itself is much smaller compared to the NJL, where the condensates decrease more slowly around the phase transition. We find that the chiral condensates are not effected by the actual choice of the Polyakov potential and give similar results for both parametrizations. This is different for the traced Polyakov loop ϕ, which depends more strongly on the effective potential. We see that the back coupling from the quark sector, like in real QCD, turns the first-order phase transition into a crossover for both parametrizations. The transition region for the polynomial potential $\mathcal{U}_P$ is broader than for the logarithmic $\mathcal{U}_L$, whose order parameter has a steeper increase. We see also the drawback of the polynomial potential $\mathcal{U}_P$, that leads to Polyakov loops exceeding 1 at larger temperatures. The Polyakov loop from the logarithmic potential $\mathcal{U}_L$ stay always

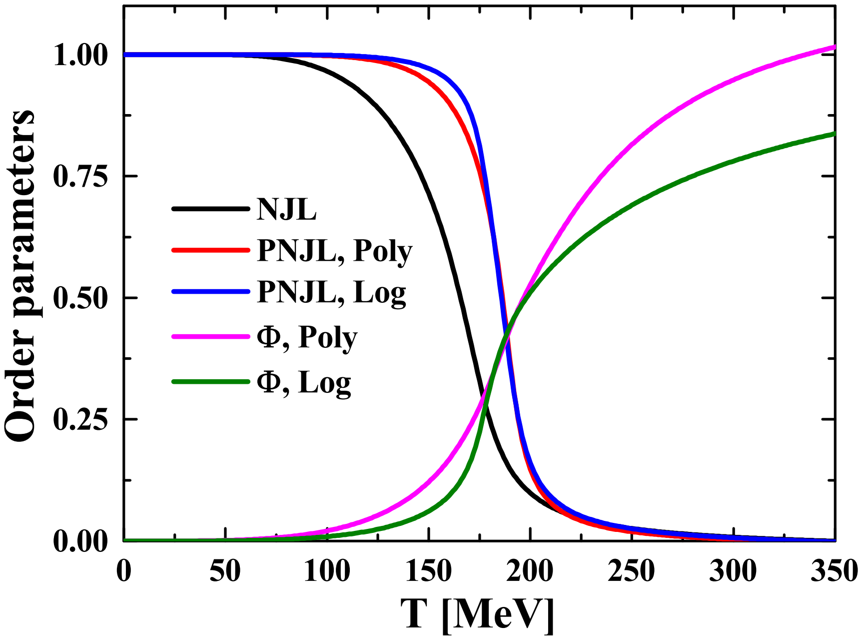

Figure 4.6: The chiral condensate and the traced Polyakov loop of the NJL and PNJL model as a function of the temperature. The red line is the condensate and the magenta line the traced Polyakov loop calculated with the polynomial Polyakov potential (4.20), the blue line is the condensate and the green line the traced Polyakov loop calculated with the logarithmic Polyakov potential (4.22). The black line is the condensate for the NJL model. The NJL parts of the models are parametrized by the HK parameter set from Ref. [162], the chiral condensate is normalized to its vacuum value.

below this limit. We find that the critical temperatures from both, chiral symmetry restoration and deconfinement, are too large compared to full 2+1 flavor QCD, where the transition happens at $T_c \approx 155 - 160$ MeV [38, 39].

4.3 Quark effects on the Polyakov potential

The PNJL considers the couplings of the gluon and the quark sector by the covariant derivative in Eq. (4.11). This has some influence on the glue dynamics as the first-order deconfinement transition at $T_0 = 270$ MeV turns into a crossover at $T_0 \approx 180$ MeV. However, the general form of the potential, i.e. the gluon dynamics, is kept unchanged. It is unlikely that the presence of quarks has no influence on the potential at all and one should also consider the back reaction of the quarks to the glue potential. A first attempt was already done in Ref. [45]. The critical temperature T_0 in the potential was rescaled to shift the phase transition to lower temperatures. Although this rescaling was just done for the purpose of comparing to available lQCD data, it was argued in Ref. [76], that it was indeed justified. The presence of quarks modifies the running coupling

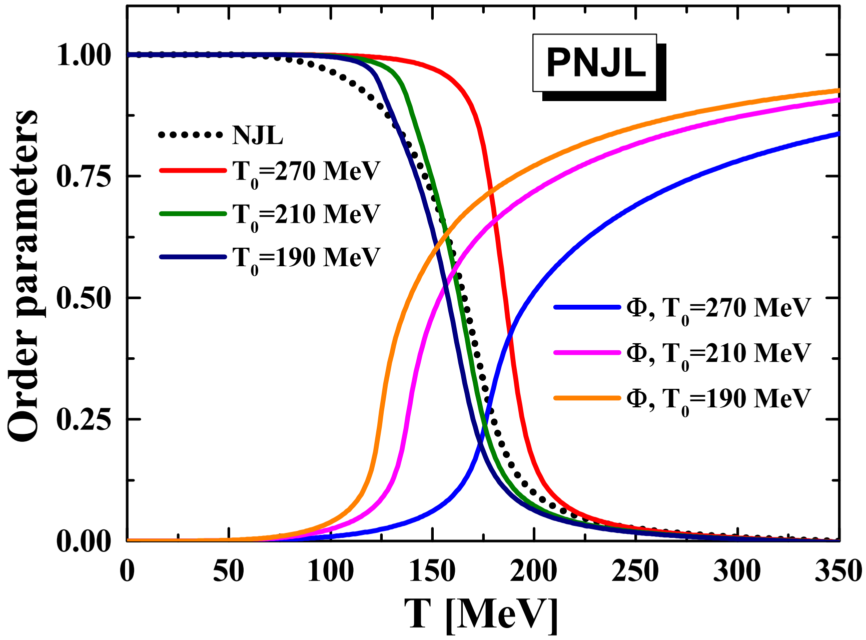

Figure 4.7: The chiral condensate and the traced Polyakov loop of the PNJL model with the logarithmic Polyakov potential (4.22) as a function of the temperature T for different Yang-Mills critical temperatures T_0. The red line shows the condensate for $T_0 = 270$ MeV, the green line for $T_0 = 210$ MeV and the dark blue line for $T_0 = 190$ MeV. The dotted black line shows the condensate from the NJL model. The light blue line shows the traced Polyakov loop for $T_0 = 270$ MeV, the magenta line for $T_0 = 210$ MeV and the orange line for $T_0 = 190$ MeV. The NJL parts of the models are parametrized by the HK parameter set from Ref. [162], the chiral condensate is normalized to its vacuum value.

of QCD and leads to a N_f-dependent decrease of Λ_{QCD} in the vacuum, that translates into a N_f-dependent decrease of T_0 at finite temperatures. The critical temperature for $N_f = 2$ becomes $T_0 = 208$ MeV and $T_0 = 187$ MeV for $N_f = 2 + 1$.

To demonstrate the effects of the rescaling we change the critical temperature in the logarithmic Polyakov potential $\mathcal{U}_L$ to $T_0 = 190$ MeV and $T_0 = 210$ MeV. The effect on the order parameters is shown in Fig. 4.7. The chiral and the confinement/deconfinement phase transition are shifted towards smaller temperatures, but the general form of the curves stays unchanged. The rescaling affects the confinement transition much stronger than the chiral transition. The influence of the rescaled temperatures on the thermodynamics is demonstrated in Fig. 4.8. We show the dimensionless pressure P/T^4 for $T_0 = 270$ MeV, $T_0 = 210$ MeV and $T_0 = 190$ MeV together with the NJL result and the lQCD pressure from the Wuppertal-Budapest collaboration [90]. The NJL pressure increases to early while the PNJL pressure without rescaling increases to late compared to the lQCD result, but the rescaling of T_0 shifts the curves towards smaller temperatures, while keeping their functional form. This improves the description of the pressure, but

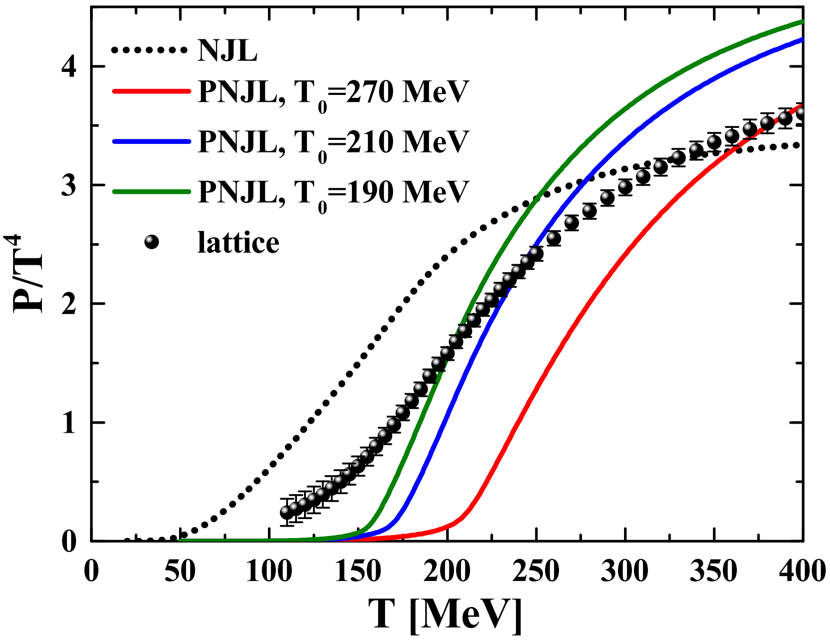

Figure 4.8: The dimensionless pressure P/T^4 for the PNJL model with the logarithmic Polyakov potential (4.22) for different Yang-Mills critical temperatures T_0. The red line shows the results for $T_0 = 270$ MeV, the blue line for $T_0 = 210$ MeV and the green line for $T_0 = 190$ MeV. The dotted black line is the dimensionless pressure from the NJL model for the HK parameter set from Ref. [162]. The lQCD results (full dots) are taken from the Wuppertal-Budapest collaboration from Ref. [90].

the PNJL can still not describe the latest lQCD results from Ref. [90]. We compare the full equation of state of the PNJL for $T_0 = 190$ MeV to the lQCD equation of state from Ref. [90] in Fig. 4.9. We show only a reduced number of the lattice points to increase the readability of the plot, nevertheless, one can clearly see the trend of the data. The PNJL underestimates the equation of state at low temperatures and overestimates it for higher ones and, as a result, has a too steep rise in the transition region. In the NJL one can cure the missing interaction strength at low temperatures with mesonic correlations (4.6). This is also the case in the PNJL [254]. The overestimation of the equation of state at large temperatures can not be resolved so easily. The problem is the almost vanishing light quark mass. The effect is smaller compared to the NJL, since the traced Polyakov loop is smaller than 1 and suppresses colored states in the distribution function, but still too large compared to the lQCD equation of state. This explains why the pressure of the NJL rises at even smaller temperatures, although the light quark condensates, and therefore the light quark masses, are similar to the PNJL, as shown in Fig. 4.7. The simple rescaling of T_0, that worked well for older lQCD results in Ref. [45], can not resolve the discrepancies between the PNJL and the most recent lQCD data. One needs a better description of the back coupling to the Polyakov potential. A detailed study of this question was done in Ref. [255] in the framework of the functional

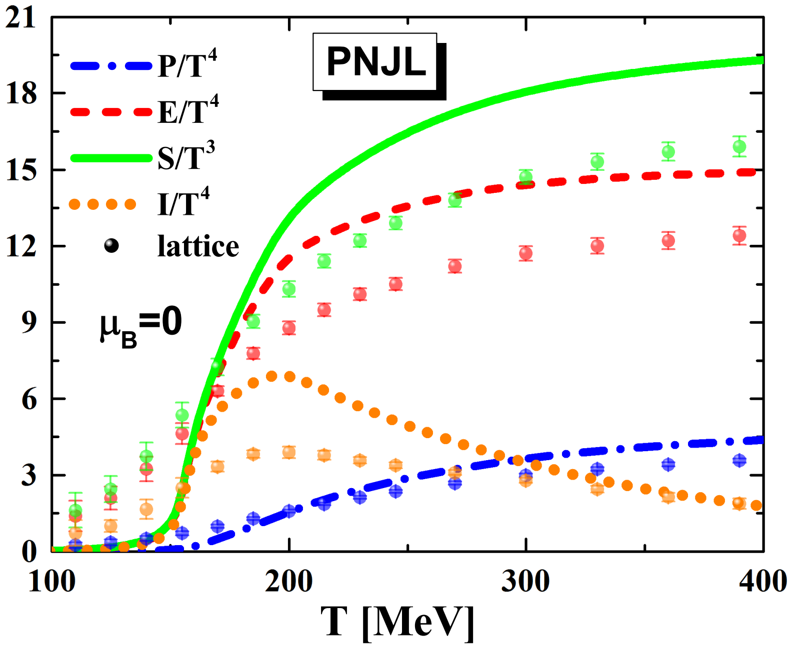

Figure 4.9: The equation of state of the PNJL model with the logarithmic Polyakov potential (4.22) for a Yang-Mills critical temperature $T_0 = 190$ MeV as a function of the temperature T for vanishing chemical potential. The NJL part of the model is parametrized by the HK parameter set from Ref. [162]. The full green line shows the entropy, the dashed red line the energy, the dash-dotted blue line the pressure and the dotted orange line the interaction measure. All quantities are scaled by powers of the temperature. The lQCD results are taken from the Wuppertal-Budapest collaboration from Ref. [90]. We show only every third point from the lattice data. Points and lines of the same color belong to the same quantity.

renormalization group for $N_f = 2$. The effects of the strange quarks were expected to be subleading once the light quarks act on the Polyakov potential. It was found that the inclusion of quarks alters the whole potential but keeps its form as a function of the traced Polyakov loop. The potential in the presence of quarks, called the effective glue potential $\mathcal{U}_{glue}$, can be related to the pure Yang-Mills potential $\mathcal{U}_{YM}$ with a rescaling of the whole temperature scale in terms of the reduced temperature

$$t = \frac{T - T_c}{T_c}, \tag{4.24}$$

that goes beyond the simple rescaling of the critical temperature T_0. The glue potential $\mathcal{U}_{glue}$ follows from the pure Yang-Mills potential $\mathcal{U}_{YM}$ through the simple relation

$$t_{YM}(t_{glue}) = 0.57\ t_{glue} \tag{4.25}$$

and is given by

$$\frac{\mathcal{U}_{glue}}{T^4}(\tau_{glue}, \phi, \bar{\phi}) = \frac{\mathcal{U}_{YM}}{T_{YM}^4}(\tau_{YM}(\tau_{glue}), \phi, \bar{\phi}). \tag{4.26}$$

Note that we had to rescale the whole temperature scale, so we have the actual temperature of the system in the denominator of the glue potential, that is not equal to the temperature in the denominator of the Yang-Mills potential T_{YM}. This temperature depends on the scale of the Yang-Mills calculation and therefore on the exact value of the critical Yang-Mills temperature T_0. In practical calculations we substitute the ratio T_0/T that appears in the parameters of the effective Polyakov potentials in Eq. (4.21) and (4.23) with

$$\frac{T_0}{T} = \frac{1}{1+t} \tag{4.27}$$

and get the dimensionless Polyakov potential $\mathcal{U}/T^4$ as a function of the reduced temperature t. This and Eq. (4.26) define then the effective glue potential $\mathcal{U}_{glue}/T^4$. To set the physical scale we have to determine the critical temperature T_c^{glue} of the glue potential in t_{glue}. As in Ref. [255], we keep T_c^{glue} as an open parameter.

The glue potential (4.26) was first used in PNJL calculations in Ref. [254] together with mesonic correlations. The correlations increased the pressure at low temperatures and the glue potential flattened the pressure at larger temperatures. These two corrections to the standard PNJL model improved the description of the equation of state compared to lQCD, see Figs. 6 and 9 in Ref. [254], but could not resolve the much steeper rise of the PNJL equation of state. The authors in Ref. [254] used the polynomial Polyakov potential $\mathcal{U}_P$ (4.20) and took the NJL parametrization from Ref. [256], that is different from the two parametrizations applied in this thesis. We will therefore check the influence of the glue potential on the logarithmic potential $\mathcal{U}_L$ (4.22) for the HK parameter set [162]. We fix the critical temperature of the glue potential in accordance with the N_f-scaling of Ref. [76] to $T_c^{glue} = 190$ MeV and rescale the critical temperature of the Yang-Mills potential in the standard PNJL approach to the same value. The dimensionless pressure and interaction measure for the two cases are shown in Fig. 4.10. Considering the back reaction on the Polyakov potential softens the rise of the pressure and decreases the interaction measure. Both are in much better agreement with the lQCD results from Ref. [90]. Also the rise of the pressure with increasing temperature is reduced, improving the equation of state especially at high temperatures. Concerning the low temperature region we find only minor improvements. The equation of state is still highly underestimated and has to be described by mesonic correlations.

The mesonic correlations in the PNJL are studied in Ref. [254] and are similar to the ones for the NJL model, see Ref. [241]. The mesons contribute dominantly below the critical temperature, while one finds only small contributions to the thermodynamic potential at higher temperatures. Especially the lighter mesons vanish very early compared to the heavy ones, which can survive even in the deconfined phase. This is a special property of the PNJL model, see Ref. [256]. We will include mesons in a very simple way. The thermodynamic contribution for stable resonances turns into the thermodynamic potential for a non-interacting particle. This was found in Ref. [87] and is the basis of the hadron-resonance gas model. The same holds for the NJL and PNJL model where the thermodynamics of the mesonic correlations follow from Eq. (4.6). The correlations become stable at low temperatures and behave like the lightest mesons, i.e. pions, kaons and the η-meson. To see this, one has to rewrite Eq. (4.6) as in Ref. [254] Eq. (46). By

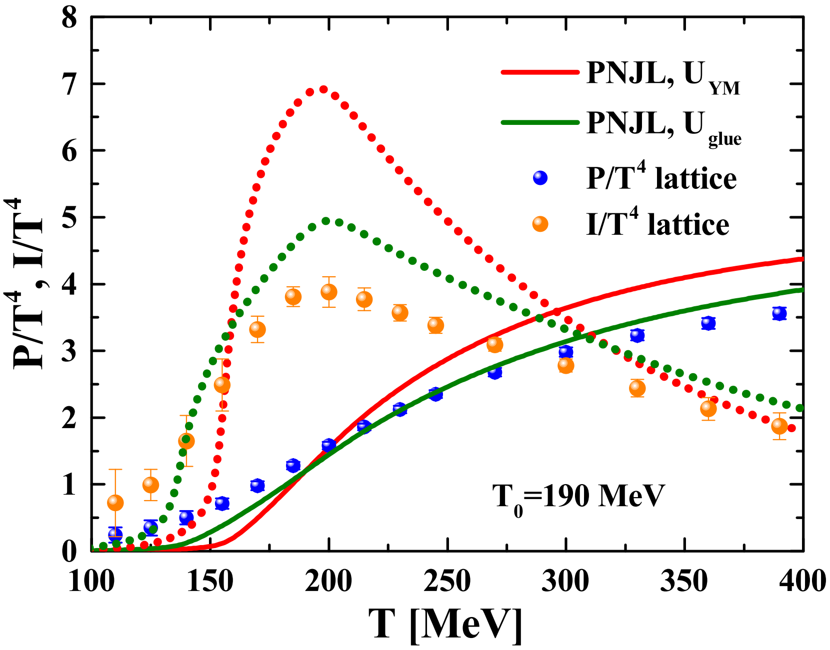

Figure 4.10: The dimensionless pressure P/T^4 and interaction measure I/T^4 of the PNJL model as a function of the temperature T for vanishing chemical potential with and without quark effects in the logarithmic Polyakov potential (4.22). The NJL part of the model is parametrized by the HK parameter set from Ref. [162]. Full lines show the pressure, dotted lines the interaction measure. Red lines show results with the normal Polyakov potential, green lines for the improved glue potential (4.26). The Yang-Mills critical temperature T_0 and the glue critical temperature T_c^{glue} are both taken as 190 MeV. The lQCD results (full dots) are adopted from the Wuppertal-Budapest collaboration from Ref. [90]. We show only every third point from the lattice data.

integrating this equation by parts one introduces the derivative of the scattering phase-shifts, that will jump from 0 to π in the presence of a mesonic bound state. Taking the derivative turns it into a δ-function for the energy of the bound state, $\omega_p = \sqrt{\mathbf{p}^2 + m^2}$, where m is the pole mass of the bound state, that defines the mass of the meson. We will therefore include the mesons just as non-interacting particles,

$$\Omega = \Omega_{PNJL} + \Omega_{0,\pi} + \Omega_{0,K} + \Omega_{0,\eta}. \tag{4.28}$$

This approximation should work well up to the phase transition as shown in Refs. [241, 256], but will fail above as it overestimates the equation of state. Note that the inclusion of mesons as non-interacting particles and not as dynamically generated states changes the Stefan-Boltzmann limit of the theory, so one has to be careful how to interpret the results.

One can improve the description of the equation of state with the last free parameter of the model, the glue critical temperature T_c^{glue}. Guided by Ref. [76] we set it to $T_0^{glue} = 190$ MeV, but the parameter is not fixed by theory. One can use it as a fit

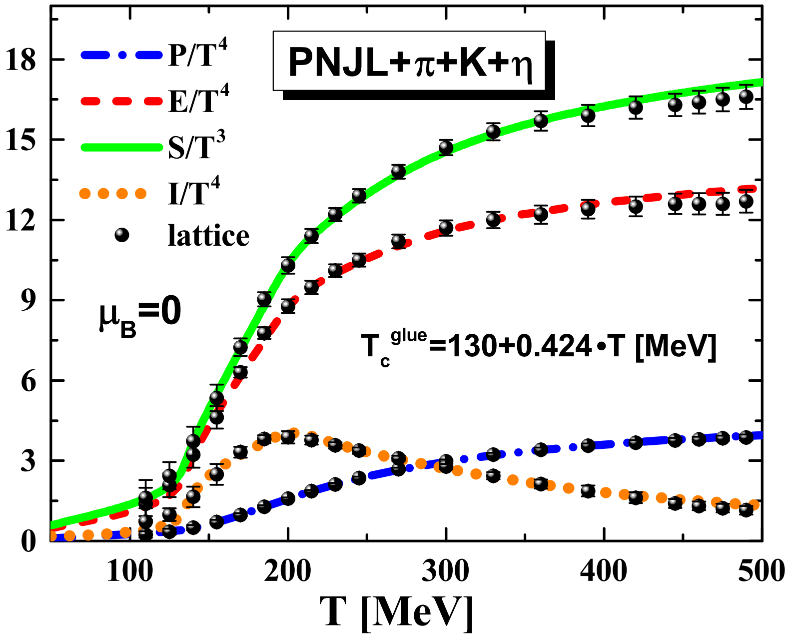

Figure 4.11: The equation of state of the PNJL model with non-interacting pions, kaons and η-mesons as a function of the temperature T for vanishing chemical potential. The effective Polyakov potential is taken as the logarithmic potential (4.22) with quark effects (4.26) for a glue critical temperature $T_c^{glue} = 130 + 0.425\ T$ MeV. The NJL part of the model is parametrized by the HK parameter set from Ref. [162]. The full green line shows the entropy, the dashed red line the energy, the dash-dotted blue line the pressure and the dotted orange line the interaction measure. All quantities are scaled by powers of the temperature. The lQCD results are taken from the Wuppertal-Budapest collaboration from Ref. [90]. We show only every third point from the lattice data.

parameter to find the best agreement with the lQCD equation of state. Doing so we observe that a higher value improves the description at higher temperatures while a lower value of T_c^{glue} favors the agreement with lQCD at lower temperatures. The region of the best agreement changed approximately linear with T_c^{glue}. As an ansatz we choose a linear function for the glue critical temperature. The best result is obtained for

$$T_c^{glue}(T) = 130 + 0.425\ T\ \text{[MeV]}. \tag{4.29}$$

The true critical temperature of the glue potential follows from the solution of $T_c^{glue}(T_c) = T_c$ and is $T_c = 226$ MeV. The equation of state with the ansatz (4.29) is shown in Fig. 4.11. The coincidence with the latest equation of state from the Wuppertal-Budapest collaboration [90] is surprising. The low temperature region is drastically improved by the mesons and the high temperature region gives very good results up to a temperature of $T = 400$ MeV. The model has the right slope at the critical temperature and is within the error bars in the whole temperature range. However, even if this ansatz gives an astonishing reproduction of the lQCD equation of state, there is no physical justification

Method	$T_0 = 270$ MeV	$T_0 = 190$ MeV	$T_c^{glue} = 190$ MeV	$T_c^{glue}(T)$
Max. χ_T	218	194	195	198
Max. $dM_{u,d}/dT$	218	194	194	198
Max. $d\phi/dT$	209	156	137	136
$\langle \bar{q}q \rangle / \langle \bar{q}q \rangle_0 = 1/2$	217	189	189	192
$M_{u,d}/M_{u,d\ 0} = 1/2$	217	189	188	192
$\phi = 1/2$	229	170	158	164
Inf. point P/T^4	232	189	193	196
Inf. point E/T^4	210	157	138	137
Inf. point S/T^4	211	157	138	137
Inf. point c_s^2	223	160	140	139
Max. I/T^4	243	196	200	203

Table 4.5: Critical temperatures T_c of the PNJL for variations of the logarithmic Polyakov potentials (4.22). In the first two columns we rescaled only the critical temperature and in the last two columns the whole temperature scale by Eq. (4.25) with $T_c^{glue} = 190$ MeV and the temperature-dependent $T_c^{glue}(T)$ from Eq. (4.29). The inclusion of non-interacting mesons has no influence on the extracted critical temperatures. The quark sector is parametrized by the HK parameter set [162]. Max. $dM_{u,d}/dT$ refers to the maximum of the absolute value as it is negative.

for stable mesons in the deconfined phase, which is a consequence of the ansatz (4.28). One can improve on this situation by evaluating the mesonic correlations (4.6) explicitly as in Refs. [241, 256], such that they vanish at larger temperatures. This would decrease the equation of state compared to Fig. 4.11, but we assume that one could compensate this by decreasing the slope of T_c^{glue} in Eq. (4.29). However, this investigation is beyond the scope of this thesis.

After having defined the PNJL and its various extensions, we want to study the phase transitions and their relations to the equation of state. We use the HK parameter set [162] and the logarithmic Polyakov potential (4.22) and determine the transition temperature at vanishing chemical potential. As the NJL the PNJL features no real phase transitions, just crossovers, so one can not clearly define the transition temperature. We summarize in Tab. 4.5 the critical temperature determined from the susceptibilities of the order parameters and also from the inflection points of the scaled equation of state. Note that we calculated the equation of state without mesonic correlations, but we checked that the inclusion of the mesons has no influence on the critical temperatures. We compare the standard PNJL to the extension with a rescaled critical temperature T_0 and to the extension with full quark back reaction (4.25) with the glue critical temperature $T_c^{glue} = 190$ MeV and the temperature-dependent glue critical temperature $T_c^{glue}(T)$ from Eq. (4.29). In general we find different transition temperatures for the chiral and the deconfinement phase transition. In the original PNJL model they are relatively close to each other, but in the extensions they differ considerably. The critical temperature for the deconfinement transition seems to agree well with the inflection point of the scaled energy and entropy density and, to some extent, with the inflection point of the speed of sound, the inflection point of the pressure seems to indicate the chiral transition. Contrary to the NJL we can determine the phase transitions from the equation of state in the PNJL, but unfortunately, this is still not possible in full QCD. The PNJL with quark back reaction with the temperature-dependent glue critical temperature and additional mesons can precisely reproduce the equation of state of QCD, therefore, their inflection points have to agree. However, in QCD the chiral and the deconfinement phase transition coincide and are at a critical temperature $T_c^{QCD} \approx 155 - 160$ MeV, which is not reproduced in the PNJL. From this we have to draw two conclusions. First, the PNJL, despite giving an exact reproduction of the QCD equation of state, can not reproduce the proper dynamics of the order parameters and second, it is not possible to deduce the phase transition from the equation of state.

4.4 Accessing the equation of state via the quark condensate

Even if it is not possible to extract the quark condensate from the equation of state, the two quantities are still related to each other. We want to propose a simple approach to connect the quark condensate to the thermodynamic potential. This allows it to determine the equation of state in more elaborate approaches, that can access the quark condensate. We use the NJL and PNJL to illustrate the approach.

The quark condensate is defined as the derivative of the thermodynamic potential with respect to the bare quark mass (2.46). By inverting this relation one finds the thermodynamic potential as an integral over the condensate,

$$\Omega(T,\mu,m_2) - \Omega(T,\mu,m_1) = \int_{m_1}^{m_2} \langle\bar{q}q\rangle(T,\mu,\tilde{m})\ d\tilde{m}. \tag{4.30}$$

This equation is not suitable for actual calculations. One needs the thermodynamic potential for a given mass and more important, the thermodynamic potential and the condensate are in general divergent. We had to introduce a momentum cutoff in the NJL potential (A.57) to regularize the theory. There is an easy solution for the first problem. By setting the upper bound in the integration to infinity, $m_2 \to \infty$, we get an infinitely heavy quark that does not contribute to the thermodynamics of the system. The potential contains then only contributions from the gluons and becomes the thermodynamic potential of the pure Yang-Mills theory,

$$\lim_{m\to\infty} \Omega(m) = \Omega_{YM} = \mathcal{U}_{YM}. \tag{4.31}$$

We have already discussed this potential in Sec. 4.2 and shown two possible parametrizations, Eq. (4.20) and (4.22), that one could use as input.

The second problem is the divergence of the condensate. The quark condensate is only well defined in the chiral limit $m \to 0$, since it is quadratic divergent with the mass. The condensates shown by lQCD calculations are not the actual condensates, but the so called regularized condensates,

$$\Delta_{u,s} = \langle \bar{u}u \rangle - \frac{m_u}{m_s} \langle \bar{s}s \rangle, \tag{4.32}$$

where the divergences from the up/down and the strange quarks cancel each other. The source of the divergent part of the condensate is the vacuum contribution in the thermodynamic potential, that appeared even in a non-interacting theory, see Eqs. (2.28) and (2.29). We neglected this contribution, since it is independent from the temperature and the chemical potential and vanishes if one takes derivatives of the thermodynamic potential. Nevertheless, these terms are not independent from the bare masses and create the divergent part in the quark condensates. As a result we expect that the divergent contribution of the condensate is also independent from T and μ and the derivatives of the condensate with respect to T or μ should therefore be finite. This leads to the following equations,

$$\frac{\partial^2 \Omega}{\partial m \partial T} = \frac{\partial^2 \Omega}{\partial T \partial m} \qquad \Rightarrow \qquad \frac{\partial s}{\partial m} = -\frac{\partial \langle \bar{q}q \rangle}{\partial T}, \tag{4.33}$$

$$\frac{\partial^2 \Omega}{\partial m \partial \mu} = \frac{\partial^2 \Omega}{\partial \mu \partial m} \qquad \Rightarrow \qquad \frac{\partial n}{\partial m} = -\frac{\partial \langle \bar{q}q \rangle}{\partial \mu}, \tag{4.34}$$

that have the same form as a Maxwell relation and should not contain any divergences. If we take the derivative of Eq. (4.30) with respect to the temperature we find

$$s(m_2) - s(m_1) = -\int_{m_1}^{m_2} \frac{\partial \langle \bar{q}q \rangle}{\partial T} d\tilde{m}, \tag{4.35}$$

where the integrand is now finite. We will fix the lower integration limit to the physical bare quark mass and set the upper to infinity. The entropy contribution from the quarks should then disappear and the only offset originates from the Yang-Mills entropy. We know from lattice studies, that the entropy vanishes (almost) below the critical temperature [8] [248, 257], which leads finally to the result,

$$s(m) = \int_m^\infty \frac{\partial \langle \bar{q}q \rangle}{\partial T} d\tilde{m} \qquad \text{for} \quad T < T_{c,YM}, \tag{4.36}$$

$$s(m) = \int_m^\infty \frac{\partial \langle \bar{q}q \rangle}{\partial T} d\tilde{m} + s_{YM} \qquad \text{for} \quad T \geq T_{c,YM}, \tag{4.37}$$

where $T_{c,YM} \approx 270$ MeV is the critical temperature for the pure Yang-Mills theory and s_{YM} the corresponding entropy density. In the same way follows

$$n(m) = \int_m^\infty \frac{\partial \langle \bar{q}q \rangle}{\partial \mu} d\tilde{m}. \tag{4.38}$$

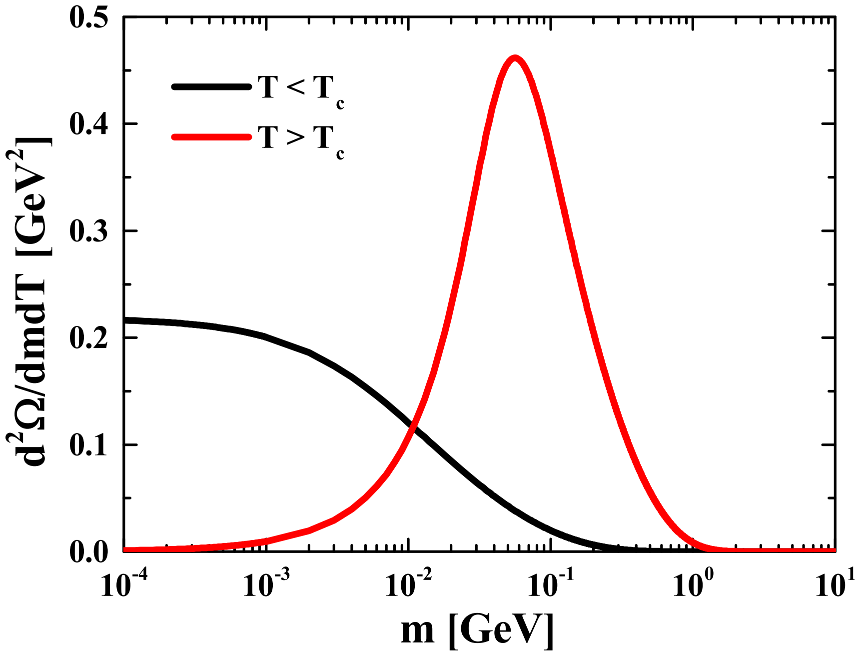

Figure 4.12: The temperature susceptibility $\frac{\partial^2\Omega}{\partial m \partial T} = \chi_T$ of the NJL model for the parameter set HK [162] as a function of the bare quark mass m for vanishing chemical potential. The mass of the strange quark is set to the light quark mass $m_{u,d} = m_s = m$. The black line shows the result for $T = 100$ MeV, which is below the critical temperature in the chiral limit $m = 0$, and the red line for $T = 200$ MeV, which is above the critical temperature.

We show in Fig. 4.12 the quantity $\frac{\partial^2\Omega}{\partial m \partial T} = \frac{\partial\langle\bar{q}q\rangle}{\partial T}$ for the NJL model with three degenerate quark masses $m_{u,d} = m_s = m$, as a function of the bare quark mass m. The black line is the result for $T = 100$ MeV and demonstrates the behavior for temperatures below the critical temperature in the chiral limit T_c, while the red line shows the result for $T = 200$ MeV and illustrates the behavior for $T > T_c$. Both results differ substantially. To explain the differences we have to look at the quark condensate as a function of temperature in the chiral limit $m = 0$, see Fig. 4.1. The condensate vanishes at the critical temperature and is zero for all temperatures $T > T_c$, therefore also its temperature derivative has to be zero. This is different at temperatures $T < T_c$, where the condensate drops to zero from below and has therefore a non-vanishing temperature derivative. The slope of the condensate increases as the temperature approaches the critical temperature and accordingly rises the value of $\frac{\partial\langle\bar{q}q\rangle}{\partial T}(m = 0)$ for $T \to T_c$ until it diverges at the critical temperature. At even higher temperatures we find then $\frac{\partial\langle\bar{q}q\rangle}{\partial T}(m = 0) = 0$ and get the typical behavior shown by the red line in Fig. 4.12. The position of the peak gets shifted to higher masses as the temperature increases while the height of the peak decreases. For very large masses $\frac{\partial\langle\bar{q}q\rangle}{\partial T}$ drops to zero, independent of the temperature,

---

[8] No sizeable contribution to s/T^3 is found below $T \approx 0.8\ T_c$.

since very heavy quarks can not create a sizeable condensate. The quarks behave then like non-interacting particles and freeze out from the system.

In finite temperature QCD one has to consider two light quarks and one heavier strange quark instead of three degenerate quarks. Accordingly one has a light quark condensate $\langle\bar{q}q\rangle$ and a strange quark condensate $\langle\bar{s}s\rangle$. We calculate the entropy density for this case by integrating the mass for all three quarks from infinity to the physical strange quark mass and then two of the quark masses from the physical strange quarks mass to the physical light quark mass,

$$\begin{aligned} s(m_l, m_s) = s_{YM} &+ \int_{m_s}^{\infty} \frac{\partial\left(\langle\bar{q}q\rangle + \langle\bar{s}s\rangle\right)}{\partial T}(\tilde{m}, \tilde{m})\, d\tilde{m} \\ &+ \int_{m_l}^{m_s} \frac{\partial\langle\bar{q}q\rangle}{\partial T}(\tilde{m}, m_s)\, d\tilde{m}. \end{aligned} \tag{4.39}$$

Using Eq. (4.38) one can also determine the particle density and therefore the whole equation of state at arbitrary temperatures and chemical potentials.

The presented approach can only be applied if $\frac{\partial\langle\bar{q}q\rangle}{\partial T}$ is finite. We tested this hypothesis in the framework of Dyson-Schwinger equations. This non-perturbative functional approach can calculate the quark propagator and therefore the quark condensate at finite temperature and chemical potential, but goes beyond the simple NJL approximation [59, 159]. We performed first test calculations on $\frac{\partial\langle\bar{q}q\rangle}{\partial T}$ and found that this quantity is indeed finite and shows the expected behavior as displayed in Fig. 4.12. This indicates that one can apply the ansatz to access the equation of state using Dyson-Schwinger equations. This is so far only possible at zero temperature [258] and in simple approximations [57]. With the presented ansatz one can bypass these limitations and calculate the equation of state regardless of the approximations chosen.

5 Thermodynamics of hadronic systems

The QCD phase diagram has two regions that are relatively well known, while the rest is more or less unknown. These two regions are the axis of $\mu = 0$, that can be studied with lQCD calculations, and the region of $T = 0$, that is described by nuclear physics. Usually one constructs models that can only be applied to one of the two cases, but we want to describe both using the same approach.

We are able to describe QCD-thermodynamics at $\mu = 0$ above the deconfinement transition in terms of the DQPM/DQPM*. In this area the relevant degrees of freedom are quarks and gluons. Below the transition the partons hadronize and the system becomes hadronic. The DQPM can reproduce the thermodynamics in this area but the quarks and gluons have to become very heavy. We will therefore describe the system in terms of hadrons. A common model used in this regime is the Hadron-Resonance Gas model (HRG). It treats the hadrons as a gas of non-interacting particles. The model works at vanishing chemical potential but fails for the description of nuclear matter. For this one needs to consider repulsive and attractive interactions that are missing in the HRG. They are included in relativistic mean-field theories whose interactions are based on the nucleon-nucleon potential. They describe infinite nuclear matter with the right properties of the binding energy but fail for the QCD equation of state at vanishing chemical potential μ. We will combine both approaches in the following to get a model that is consistent with lQCD ($\mu \approx 0,\ T > 0$) and the nuclear equation of state ($T \approx 0,\ \mu > 0$) while using only hadronic degrees of freedom.

5.1 Hadron-Resonance Gas

The number of different degrees of freedom in the partonic phase is rather low. There is only one species of bosons, the gluon (with degeneracy 2×8), and only two different fermions, the light (u, d) and the strange (s) quarks. This becomes much more complicated in the hadronic phase.

In nature the only stable hadron is the proton. Every other hadron will decay under the weak, the strong or the electromagnetic interaction to either protons or leptons. However, all these decays happen at different time scales. In the context of heavy-ion collisions, $t \leq 1000$ fm/c, the weak and the electromagnetic interaction are negligible and only the strong interaction will lead to decays on the timescale of the collision. Thus we will treat all hadrons, that do not decay under the strong interaction, as stable. These are the pseudoscalar 0^- mesons, i.e. the pions, the kaons and the η-meson, and the spin-1/2 baryons, i.e. the nucleons, the Σ, the Λ and the Ξ baryons. Other important hadrons that appear as resonances are the spin-1^- vector mesons, i.e. the ρ, the K^*, the ω and the ϕ meson, and the spin-3/2 baryons, i.e. the Δ, the Σ^*, the Ξ^* and the Ω baryon. The Ω is also stable under the strong interaction. All these hadrons are important for the dynamics of heavy-ion collisions and have to be included to get a reasonable description of finite temperature QCD in the confined phase. Other hadrons that are also important in that context are the axial partner of the ρ, the a_1-meson and the $N(1440)$ and the $N(1535)$ baryon. These are the hadrons contained in the PHSD transport approach [144, 145]. The properties of the mesons are summarized in Tab. A.1 and the properties of the baryons in Tab. A.2 in Appendix A.7.

Another group of hadrons, whose particle nature was discussed over the last years, are the scalar 0^+ mesons [259]. The most prominent is the $f_0(500)$ or σ-meson with a mass of $400 - 550$ MeV, that is now established as a particle and contained in the latest version of the particle list of the Particle Data Group [260]. The other mesons in the scalar 0^+ -multiplet are the $f_0(980)$, the $a_0(980)$ and the strange $\kappa(720)$ meson. They appear to have no real quark-antiquark structure and are potential tetraquark candidates [261]. There is no consensus whether to include them in HRG models or not. An often used argument against the 0^+ mesons is their thermal cancelation by repulsive channels. Calculations for the thermodynamic potential of an interacting pion gas in terms of experimental phase shifts show that the attractive pressure contribution from the σ-mesons gets exactly canceled by the repulsive isotensor channel [262, 263]. The same happens also for the strange κ-mesons. However, the phase shifts used were determined in the vacuum. Studies within effective theories found that the σ-meson is much stronger affected by finite temperature or density than the pions and the ρ-mesons [51, 264, 265, 266] and one can assume that the phase shifts are no longer valid at temperatures above $T \approx 100$ MeV. Further arguments in favor of the scalar mesons come from the statistical hadronization model. In Ref. [267] the σ-meson was explicitly included and improved the description of the K/π ratio, that probes the hadronic medium at finite temperatures and chemical potentials. Even if the scalar mesons are no regular mesons, it was shown in Ref. [259] that neglecting them is inconsistent with respect to causality and unitarity. For all these reasons we will include the scalar nonet into our calculations. The properties of the scalar mesons are summarized in Tab. A.3 in Appendix A.7.

The most frequently used model for hadronic thermodynamics at finite temperature is the HRG. The approach is based on the work of Dashen, Ma and Bernstein [87], who found that one can describe the thermodynamics of a system of particles, which interact through resonant scatterings, by simply including the resonances as stable particles. This is always possible if the widths of the resonances are small compared to the temperature $\gamma \ll T$. An interacting pion gas for example is thermodynamically equivalent to a free gas of pions and ρ-mesons [268]. The HRG generalizes this approach to all possible hadrons. The thermodynamic potential is the sum of all stable hadrons and all known hadronic resonances taken as non-interacting particles,

$$\Omega_{HRG}(T,\mu) = \sum_{\text{hadrons}} \Omega_0(T,\mu,m_i) + \sum_{\text{resonances}} \Omega_0(T,\mu,m_i). \tag{5.1}$$

This approach can only describe attractive interactions. The repulsive interactions, that are important for the equation of state of nuclear matter, are neglected. This version of the HRG is called the ideal HRG. One can introduce repulsive interactions by assuming a finite volume of the particles [269, 270, 271, 272]. The model presented in Refs. [269, 270] assumes the same volume for each particle, so the excluded volume is proportional to the total particle density. The approach in Refs. [271, 272] assumes an excluded volume for each particle that is proportional to its energy. This leads to a limiting energy density similar to the Hagedorn model that has a maximum temperature [273]. The non-relativistic formulation of this approach is the van der Waals model,

$$P = \frac{NT}{V-bN} - a\frac{N^2}{V^2}, \qquad U = \frac{3}{2}NT - a\frac{N^2}{V}, \tag{5.2}$$

with b characterizing the excluded volume and a the strength of the attractive interaction. The repulsive interactions, that are introduced by excluded volume models, are different from repulsive interactions that originate from interactions with vector mesons as, for example, in the Walecka model [92]. The strength of this vector repulsion is proportional to the net particle density and therefore vanishes for zero chemical potential. The excluded volume repulsion is proportional to the total particle density (or pressure) and appears also at vanishing chemical potential.

It is believed that the HRG gives the correct description of hadronic QCD matter at moderate chemical potentials. This is supported by the success of the statistical hadronization model in describing particle ratios from heavy-ion collisions. This model assumes that the medium created in a heavy-ion collision, that probes directly the equation of state of hot QCD matter, equilibrates (to some extent). The system will then continue to interact until it becomes too dilute and freezes out. The particle yields are then fixed by the temperature and the chemical potential at this freezeout. This simple assumption can describe the particle abundances for various collision energies [274, 275, 276, 277]. It becomes even more precise if one assumes additional corrections for non-equilibrium effects [278, 279, 280, 281]. The model is applicable also for $p+p$ [282] and even e^+e^- collisions [283] and was applied to the production of hypernuclei in Ref. [284].

The HRG equation of state and susceptibilities were compared to state of the art lQCD calculations in Refs. [88, 89, 90, 91, 135, 136, 160, 285]. The ideal HRG leads to a satisfying description of the thermodynamics for temperatures below $T \approx 170$ MeV. The quality of the description is improved if one includes an exponential increasing mass spectrum [286], as predicted by Hagedorn, and repulsive interactions [287, 288, 289, 290]. lQCD simulations for temperatures below $T = 100$ MeV are still affected by large errors. Since both approaches match each other almost perfectly in the temperature regime between 100 and 130 MeV, one uses the deviations to set the systematical error of the lattice calculations [136].

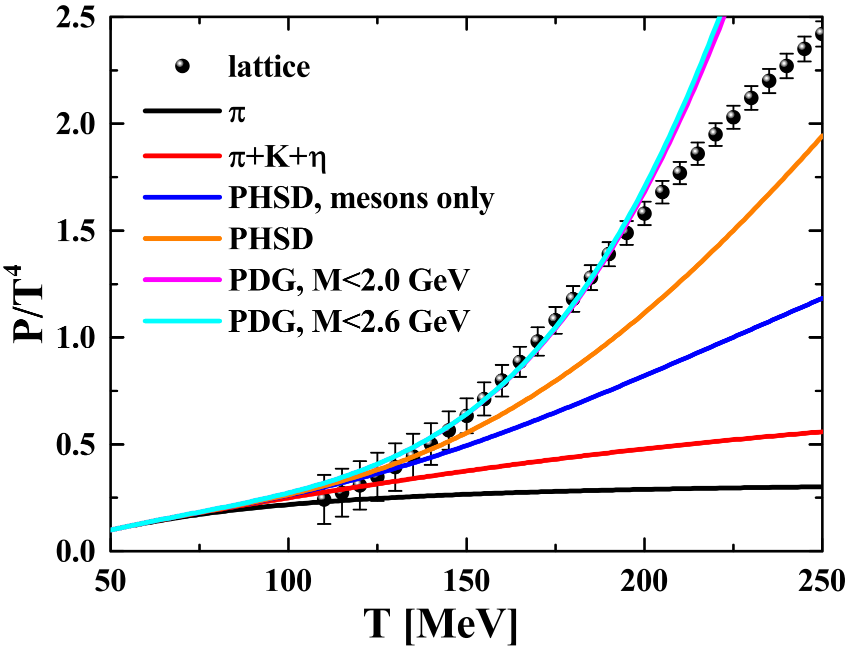

Figure 5.1: The dimensionless pressure P/T^4 for a non-interacting hadron gas as a function of temperature T. The black line shows the pressure if one considers only pions, the red line for pions, kaons and the η. The blue line is the pressure for all mesons that are contained in the PHSD transport approach, see Tab. A.1, and the orange line for all mesons and baryons in PHSD, see Tab. A.2 for the baryons. The magenta line shows the pressure for all hadrons listed by the particle data group [291] with a mass below 2.0 GeV and the light blue line for all hadrons with a mass below 2.6 GeV. The lQCD results are taken from the Wuppertal-Budapest collaboration from Ref. [90].

The only parameters of the HRG are the masses of the hadrons, that are usually taken as the vacuum masses. The model is therefore parameter free in principle, but one has to decide on the amount of particles one wants to include. All versions use at least the stable spin-1/2 baryons and the stable 0^- mesons as well as the spin-3/2 baryons and the 1^- mesons. The standard choice are all hadrons listed by the Particle Data Group [260, 292] with a mass below a certain threshold, mostly 2.0 GeV. We show in Fig. 5.1 the dimensionless pressure P/T^4 of the HRG for vanishing chemical potential,

$$P/T^4 = \frac{1}{6\pi^2 T^4} \sum_i d_i \int_0^\infty dp \, \frac{p^4}{\sqrt{p^2+m_i^2}} \, n_{B/F}\left(\sqrt{p^2+m_i^2}\right) , \tag{5.3}$$

calculated with different amounts of particles and compare it to the latest lQCD data from the Wuppertal-Budapest collaboration [90]. At low temperatures the system is dominated by the lightest mesons, i.e. pions, kaons and the η-meson, which describe the equation of state up to $T \approx 120$ MeV. In general we find that the equation of state is meson dominated and baryons appear only at $T \approx 140$ MeV. The PHSD HRG -based

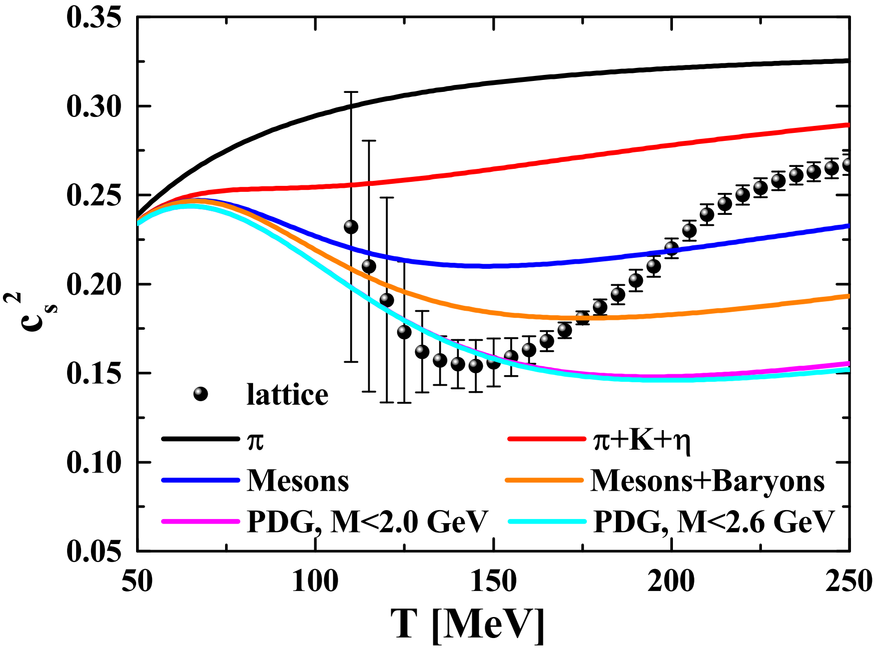

Figure 5.2: The speed of sound squared c_s^2 for a non-interacting hadron gas as a function of temperature. The black line shows the speed of sound if one considers only pions, the red line for pions, kaons and the η. The blue line is the result for all mesons that are contained in the PHSD transport approach, see Tab. A.1, and the orange line for all mesons and baryons in PHSD, see Tab. A.2 for the baryons. The magenta line shows c_s^2 for all hadrons in the 2012 edition of the PDG [291] with a mass below 2.0 GeV and the light blue line for all hadrons with a mass below 2.6 GeV. The lQCD results are taken from the Wuppertal-Budapest collaboration from Ref. [90].

on the hadrons contained in PHSD- describes the lQCD data up to $T = 150$ MeV. At higher temperature it misses additional interaction strength. For this one has to include additional resonances (or interactions). We show the pressure for all hadrons listed by the Particle Data Group [291] with a mass below 2.0 GeV and for all hadrons with a mass below 2.6 GeV [9]. Both are almost on top of each other. The additional hadrons give enough strength to describe the equation of state up to $T = 180$ MeV. This is due to a substantial update of the listed hadrons in the 2014 update of the Particle Data group [292]. The pressure is within the error bars of the lQCD result, but the slope of the line is wrong. This has consequences for the speed of sound defined by

$$c_s(T) = \sqrt{\frac{\partial P(T)}{\partial E(T)}}, \tag{5.4}$$

---

[9] A compact list of the hadrons but without the σ-meson can be found in Ref. [163].

with the energy density

$$E(T) = \frac{1}{2\pi^2} \sum_i d_i \int_0^\infty dp\, p^2 \sqrt{p^2 + m_i^2}\; n_{B/F}\left(\sqrt{p^2 + m_i^2}\right). \tag{5.5}$$

We show the squared speed of sound c_s^2 in Fig. 5.2 with the lQCD data taken from the same simulation as the pressure [90]. The data show a minimum for $T = 140$ MeV, which the HRG can not reproduce, regardless of the hadrons contained. Including more resonances leads to an overall decreasing speed of sound for $T > 150$ MeV. The HRG with the hadronic content of PHSD can not describe the lQCD speed of sound at all, while the full PDG HRG can at least describe the drop down to the minimum, but c_s^2 stays too low for $T > 150$ MeV.

5.2 Nuclear equation of state

We discussed the equation of state at vanishing chemical potential already several times throughout this thesis. In this section we want to introduce the nuclear equation of state at $T = 0$ and $\mu_B \neq 0$. We review the thermodynamics of this special case within a simple mean-field model.

The limit of $T = 0$ and finite chemical potential μ_B is often called "infinite nuclear matter", because this is the scenario found in the interior of all larger atomic nuclei, where the nuclear density is almost constant at $\rho_0 \approx 0.16$ fm^{-3}. When we investigate this limit we have to take into account the special form of the distribution functions. The chemical potential in the Bose-distribution functions has to vanish in order to keep it positive such that the bosons do not contribute to the thermodynamics for $T = 0$. The Fermi-distribution function on the other side turns into a stepfunction

$$n_F(\omega_p) = \frac{1}{e^{\frac{\omega_p - \mu}{T}} + 1} = \Theta(\mu - \sqrt{p^2 + m^2}) = \Theta(p_F - p) \tag{5.6}$$

and the distribution function for antifermions becomes $n_{\bar{F}}(\omega_p) = \Theta(-\mu - \sqrt{p^2 + m^2})$ and is zero for all positive chemical potentials. The highest possible momentum is called Fermi momentum p_F and is connected to the chemical potential via $\omega(p_F) = \epsilon_F = \mu_B$. All states below the Fermi momentum are occupied and all states above are empty. Because of this simple form we can calculate the equation of state analytically. We see directly, that only particles with a mass lower than the chemical potential contribute. This implies that for all chemical potentials below the nucleon mass, the lightest fermion mass, one finds no thermodynamic contributions at all. The system is still in its vacuum state. For this reason it is more convenient to describe the system in terms of the nuclear density rather than the chemical potential,

$$\rho_B = \frac{4}{2\pi^2} \int_0^\infty dp\, p^2\; n_F(\omega_p) = \frac{4}{2\pi^2} \int_0^{p_F} dp\, p^2 = \frac{4}{6\pi^2} p_F^3, \tag{5.7}$$

where the factor 4 stems from the summation over protons and neutrons with two spin projections. Note that the total and the net-baryon density are the same at $T = 0$. The

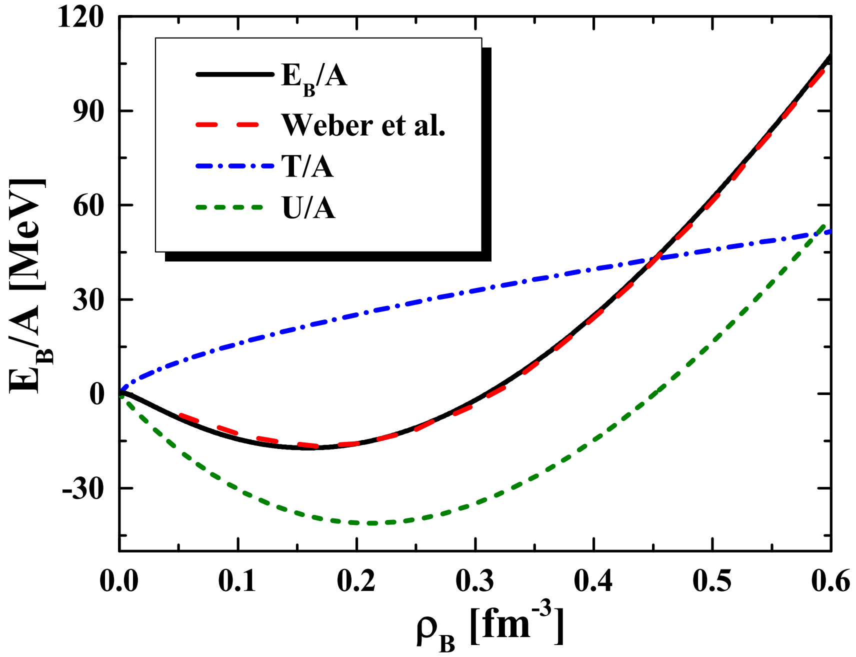

Figure 5.3: The binding energy per particle E_B/A as a function of the nuclear density ρ_B. The solid black line shows the result from the ρ_B-dependent potential model. The potential was fitted to reproduce the equation of state from Ref. [293], given by the red dashed line. The blue dash-dotted line is the binding energy for non-interacting nucleons and the green dotted line shows the potential energy contribution given by Eq. (5.8).

chemical potentials necessary to excite heavier baryons like the Δ's or strange baryons lead to energy densities far above $\epsilon_c = 0.5$ GeV/fm^3, where we expect deconfined matter. For this reason we can restrict ourself to only nucleons.

We know from nuclear physics that the binding energy $E_B/A = E/\rho_B - m_N$ of nuclear matter has a minimum of $E_B/A = -16$ MeV at normal nuclear density $\rho_0 \approx 0.16$ fm^{-3} in order to reproduce the stable nuclear matter inside atomic nuclei. The simple HRG model can not reproduce this minimum, as we see from the blue dash-dotted line in Fig. 5.3, because it discards interactions between the nucleons. We will model the interaction, that emerges from meson exchange, by a simple ρ_B-dependent potential energy density

$$U(\rho_B) = V_2\rho_B^2 + V_3\rho_B^3 + V_4\rho_B^4. \tag{5.8}$$

The energy density for non-interacting nuclear matter follows from Eqs. (2.36) and (5.6) and reads

$$E_0 = \frac{4}{2\pi^2}\left(\frac{p_F}{8}\sqrt{p_F^2+m_N^2}\,(2p_F^2+m_N^2) - \frac{m^4}{16}\ln\left(\frac{\left(p_F+\sqrt{p_F^2+m_N^2}\right)^2}{m^2}\right)\right). \tag{5.9}$$

V_2	V_3	V_4
-0.411 GeV fm^3	1.128 GeV fm^6	-0.478 GeV fm^9

Table 5.1: Parameters of the potential energy density (5.8).

The Fermi momentum p_F is connected to the density by Eq. (5.7); thus the whole binding energy can be written as a function of the nuclear density ρ_B:

$$E_B(\rho_B)/A = E_0(\rho_B)/\rho_B + V_2\rho_B + V_3\rho_B^2 + V_4\rho_B^3 - m_N. \tag{5.10}$$

The parameters V_2, V_3 and V_4 are shown in Tab. 5.1 and are determined in order to reproduce the binding energy from Ref. [293]. The equation of state presented in this work is based on a relativistic effective interaction that is consistent with microscopic Dirac-Brueckner calculations and the experimentally known momentum dependence of the nucleon-nucleus optical potential. Therefore, the approach is not only able to describe nuclear matter at normal nuclear density but can also describe the signals of low-energy heavy-ion collisions that probe the nuclear equation of state at much higher densities. The approach is energy-momentum conserving and most importantly also thermodynamically consistent. Fig. 5.3 shows the results for the binding energy. The simple potential model gives a good fit to the results from Ref. [293] for densities below 0.6 fm^{-3}. The dash-dotted blue line is the kinetic part of the binding energy, which is equal to the HRG result that has no minimum at all and leads to unbound nuclear matter. The attractive interactions due to resonant scatterings are irrelevant in nuclear matter. Instead one requires a precise combination of attractive and repulsive interactions, as seen by the green dotted line in Fig. 5.3.

It is worth mentioning that Fig. 5.3 shows a wide range in the nuclear density up to four times normal nuclear density, but covers actually a very small range in the chemical potential. The smallest densities correspond to a baryon chemical potential $\mu_B = m_N = 938$ MeV; normal nuclear density is reached at $\mu_B = 975$ MeV and the critical energy density $\epsilon_c = 0.5$ GeV/fm^3 is reached for a baryon chemical potential of $\mu_B = 1013.6$ MeV and approximately three times normal nuclear density. Fig. 5.3 shows in terms of baryon chemical potential only the region between $\mu_B = 938$ MeV and $\mu_B = 1023$ MeV. The baryon chemical potential necessary to excite Δ-resonances leads already to densities about 4.5 fm^{-3} $\approx 27\rho_0$. This can change if one includes interactions, but even then one will always find only nucleons up to the critical energy density $\epsilon_c \approx 0.5$ GeV/fm^3. The mentioned chemical potentials are actually model dependent, as we will discuss later, and might get shifted due to repulsive interactions. In fact, the nuclear equation of state is only known as a function of the density and not as a function of the baryon chemical potential.

The simple potential model (5.10) can reproduce the basic features of the nuclear equation of state, but is only valid at very low temperatures where the interaction is not modified by finite temperature effects. In the following we will use relativistic mean-field theories. They can reproduce the well known properties of nuclear matter and are applicable at larger temperatures. Relativistic mean-field theories are the mean-field approximation of the so called quantum hadrodynamics (QHD) [92, 294, 295, 296], that describes the interactions between nucleons by the exchange of mesons. One usually includes isoscalar interactions mediated by the scalar σ-meson and the vector ω-meson and isospin-dependent interactions mediated by the ρ-meson and the δ-meson. The σ-meson describes the attractive part of the nucleon-nucleon potential while the ω-meson describes the short range repulsion. The ρ and the δ-meson are important for asymmetric nuclear matter and neutron star physics, but will give no contribution in isospin symmetric matter. Since this is approximately the case for the hot and dense medium created in heavy-ion collisions, we can neglect them in the following.

The QHD Lagrangian consists of the free Dirac Lagrangian for the nucleons, the Lagrangian for the σ and the ω-field with selfinteractions $U(\sigma)$ and $O(\omega^\mu\omega_\mu)$ and an interaction part of Yukawa type for the nucleon-meson interactions:

$$\begin{aligned}
\mathcal{L} &= \mathcal{L}_B + \mathcal{L}_M + \mathcal{L}_{int}, && (5.11)\\
\mathcal{L}_B &= \bar{\Psi}\left(i\gamma_\mu\partial^\mu - M\right)\Psi, && (5.12)\\
\mathcal{L}_M &= \frac{1}{2}\partial_\mu\sigma\partial^\mu\sigma - U(\sigma) - \frac{1}{4}F_{\mu\nu}F^{\mu\nu} + O(\omega^\mu\omega_\mu), && (5.13)\\
\mathcal{L}_{int} &= g_\sigma\bar{\Psi}\sigma\Psi - g_\omega\bar{\Psi}\gamma^\mu\omega_\mu\Psi. && (5.14)
\end{aligned}$$

The two coupling constants g_σ and g_ω are effective couplings, that are not fixed by theory and chosen to reproduce the main properties of nuclear matter like the saturation density and the binding energy. The selfinteractions are usually taken as polynomials [297, 298] and contain at least the mass terms for the mesons, i.e. $U(\sigma) = \frac{1}{2}m_\sigma^2\sigma^2$, $O(\omega^\mu\omega_\mu) = \frac{1}{2}m_\omega^2\omega^\mu\omega_\mu$. In this case the model reduces to the simple σ-ω model or Walecka model [92]. The main application for relativistic mean-field theories is the calculation of ground state properties of finite nuclei. The model works well for spherical and also deformed nuclei [299, 300], and one can also use it to investigate neutron star properties [301, 302].

An important extension of QHD is the so called density-dependent hadron-field theory [303, 304, 305]. The coupling constants are no longer treated as constants but as functions of the nucleon field,

$$g_\sigma \to \Gamma_\sigma(\bar{\Psi},\Psi), \qquad g_\omega \to \Gamma_\omega(\bar{\Psi},\Psi). \tag{5.15}$$

To preserve Lorentz invariance the couplings have to be Lorentz scalars. The easiest way to ensure this is to write the couplings as a function of a density $\Gamma(\bar{\Psi},\Psi) = \Gamma(\hat{\rho}_0)$, which is again a Lorentz scalar itself. Two physical reasonable choices are $\hat{\rho}_0 = \bar{\Psi}\Psi$ and $\hat{\rho}_0 = \bar{\Psi}u_\mu\gamma^\mu\Psi$, where u_μ is the four-velocity with $u_\mu u^\mu = 1$. The first one is called scalar density dependence (SDD) and will lead to a dependence of the scalar density ρ_s, the second one is called vector density dependence (VDD) and will lead to a dependence of the baryon density ρ_B. It has been shown, that the application of the VDD gives better results when applied to finite nuclei [303, 304]. The interaction part (5.14) of the Lagrangian becomes

$$\mathcal{L}_{int} = \Gamma_\sigma(\hat{\rho}_0)\bar{\Psi}\sigma\Psi - \Gamma_\omega(\hat{\rho}_0)\bar{\Psi}\gamma^\mu\omega_\mu\Psi. \tag{5.16}$$

This has the advantage that one can parametrize a realistic nucleon-nucleon interaction -obtained from Dirac-Brueckner (DB) calculations- but with less numerical effort [304, 305]. This allows to apply Dirac-Brueckner calculations also to finite systems, what is currently out of reach for actual DB calculations. We will need the density-dependent couplings to reproduce the nuclear equation of state and the lQCD equation of state simultaneously in a single approach.

QHD is too complicated to be solved on the many-body level and we will use the mean-field approximation. The meson fields are then no longer independent degrees of freedom but determined by their expectation values. Evaluating the equations of motion one finds the following two coupled selfconsistent equations (see Appendix A.8), that have to be solved simultaneously:

$$\frac{\partial U}{\partial \sigma} = \Gamma_\sigma(\rho_0)\, d \int \frac{d^3p}{(2\pi)^3} \frac{m^*}{\omega_p^*} \left(n_F(T,\mu^*,m^*) + n_{\bar{F}}(T,\mu^*,m^*) \right), \tag{5.17}$$

$$\frac{\partial O}{\partial \omega} = \Gamma_\omega(\rho_0)\, d \int \frac{d^3p}{(2\pi)^3} \left(n_F(T,\mu^*,m^*) - n_{\bar{F}}(T,\mu^*,m^*) \right). \tag{5.18}$$

The density in the couplings is now the normal ordered expectation value of the density $\rho_0 = \langle : \hat{\rho}_0 : \rangle$. The distribution functions depend on $\omega_p^* = \sqrt{\mathbf{p}^2 + m^{*2}}$ with the effective mass

$$m^* = m - \Sigma^s = m_N - \Sigma^{s(0)} - \Sigma^{s(r)} = m - \Gamma_\sigma(\rho_0)\sigma - \Sigma^{s(r)} \tag{5.19}$$

and on the effective chemical potential

$$\mu^* = \mu - \Sigma^0 = \mu - \Sigma^{0(0)} - \Sigma^{0(r)} = \mu - \Gamma_\omega(\rho_0)\omega - \Sigma^{0(r)}. \tag{5.20}$$

Both get effected by the interactions with the mesons. The mass gets modified by the scalar selfenergy Σ^s that originates from the interactions with the σ-meson. The chemical potential gets modified by the vector selfenergy Σ^0 that originates from the interactions with the ω-meson. The selfenergies are split into a normal $\Sigma^{(0)}$ and a rearrangement selfinteraction $\Sigma^{(r)}$. The latter arises from the density dependence of the couplings. Their actual form depends on the choice of ρ_0 that we will specific when necessary. If the couplings are independent from the fields, they will vanish.

With the solution for the selfconsistent Eqs. (5.17) and (5.18) we can evaluate the thermodynamics of the model, see Appendix A.9. The pressure of the density-dependent relativistic mean-field model is given by

$$P = -U(\sigma) + O(\omega) + \Sigma^{0(r)}\rho_B - \Sigma^{s(r)}\rho_s + P_0(T,\mu^*,m^*), \tag{5.21}$$

where P_0 is the pressure for a non-interaction particle evaluated for the effective quantities μ^* and m^*. The model is thermodynamic consistent as long as the selfconsistent equations of motions are fulfilled. We prove this also in Appendix A.9.

We will now continue the discussion of the nuclear equation of state but with the relativistic mean-field model. The basic properties of the binding energy and the saturation density of symmetric nuclear matter are uncontroversial, but there is no consensus on the behavior at larger densities $\rho_B > 1.5\ \rho_0$, as there are no ab-initio calculations to fix it. The parameters of the relativistic mean-field models are usually determined from the ground state properties of nuclei [306, 307, 308, 309, 310, 311], which probe only the region close to the saturation density. The equation of state at higher densities is then a prediction. In general the models contain also the ρ-meson and δ-meson because larger nuclei contain more neutrons than protons $n_n > n_p$ and one has to describe the isospin asymmetry. These models are applicable to symmetric nuclear matter, but their parameters have been fixed in the asymmetric case.

Another method to constrain the equation of state are heavy-ion collisions. A relativistic mean-field model was used in Ref. [312] to study collisions in the energy range of 400 AMeV to 1 AGeV. The model was then extended in Ref. [293] to include also a momentum dependence and to reproduce the momentum dependences of the nucleon-nucleus optical potential. This leads to density-dependent potentials similar to the VDD couplings in the density-dependent relativistic mean-field theory. The density dependence of the potentials is also a well known result from Dirac-Brueckner calculations [313]. The approaches in Refs. [293, 313] probe the equation of state up to $\rho_B \approx 3\rho_0$ exceeding the possibilities of nuclear structure studies. Even larger densities have been probed in Ref. [314] where flow data from heavy-ion simulations have been analyzed to put constraints on the equation of state in the density region between $2\,\rho_0 < \rho_B < 4.5\,\rho_0$. The most extreme densities are reached in neutronstars. They do not contain symmetric nuclear matter but dominantly neutron matter. However, they probe the whole equation of state up to the largest densities. One studies neutron star properties by solving the Tolman-Oppenheimer-Volkoff equation [315, 316], that uses the equation of state as input. This determines the allowed masses and radii for a given equation of state, which is then compared to actual measurements. One can also invert this procedure to determine the equation of state if one could measure the exact mass-radius (M-R) relation [317], but the required precision is currently not possible for the radii. However, for most neutron stars they should be in the range between 10 to 12 km [318]. The recent discovery of two-solar-mass neutron stars [319, 320] ruled out a huge class of equations of state, that were unable to provide such heavy masses. With more precise measurements of the radii one can further constrain the equation of state for highly asymmetric nuclear matter.

In Ref. [301] a testing scheme for nuclear equations of state is suggested that uses also constraints from neutron star phenomenology and the flow-data analysis from Ref. [314]. The authors found that currently no equation of state passes all their tests, but the models employing density-dependent couplings perform better than those without. We use a similar scheme to fix our equation of state, but in a much simpler way. We compare the nuclear equation of state for different parametrizations for relativistic mean-field theories to narrow down the equation of state of symmetric nuclear matter. For this we apply the mesonic selfinteractions in their usual polynomial forms [297, 298],

$$U(\sigma) = \frac{1}{2}m_\sigma^2\sigma^2 + \frac{1}{3}B\sigma^3 + \frac{1}{4}C\sigma^4, \tag{5.22}$$

$$O(\omega) = \frac{1}{2}m_\omega^2\omega^2 + \frac{1}{4}D\omega^4, \tag{5.23}$$

	NL1 [312]	NL3 [312]	MTEC [311]	TM1 [310]	ML2
g_σ	6.91	9.50	6.39	10.03	9.28
g_ω	7.54	10.95	8.72	12.61	10.59
B [1/fm]	-40.6	1.589	-10.76	-7.23	5.1
C	384.4	34.23	-4.05	0.62	9.8
D	0	0	0	71.31	0
m_σ [1/fm]	2.79	2.79	2.03	2.59	2.79
m_ω [1/fm]	3.97	3.97	3.97	3.97	3.97
ρ_0 [fm^{-3}]	0.145	0.145	0.154	0.147	0.164
E_B/A [MeV]	-15.9	-16	-16.3	-16.3	-16.1
K [MeV]	380	373	240	284	358
m^*/m	0.83	0.70	0.78	0.63	0.68
μ_c [MeV]	1125	1258	1097	1175	1207

Table 5.2: Parametrization of different relativistic mean-field models. ρ_0 is the saturation density where the binding energy per nucleon has its minimum and E_B/A is the depth of this minimum, K is the compressibility of nuclear matter, m^* is the effective mass at the saturation density ρ_0 and μ_c is the baryon chemical potential for which the energy density reaches $E(\mu_c) = 0.5$ GeV/fm^3.

and keep the couplings g_σ and g_ω as constants. The parameters are summarized in Tab. 5.2. The parameter sets NL1 and NL3 are taken from Ref. [312], where they were used in heavy-ion simulations. Recently, these parametrizations were also employed in Refs. [147, 321] to investigate chiral-symmetry restoration in heavy-ion collisions. This led to the first microscopic explanation of the K/π ratio in a transport approach and can be used to put further constraints on the equation of state, cf. Sec. 5.5. Note that these sets are not identical to the parameters from Ref. [306] and Ref. [309], that are also called NL1 and NL3, but were fitted to the properties of spherical nuclei. However, it is known that the set NL3 from Ref. [309] is not compatible with neutron star observations [302, 318]. The set MTEC is taken from Ref. [311] and the set TM1 from Ref. [310]. MTEC is fitted to nuclear properties with special emphasis on the isospin-asymmetry coefficient and TM1 to the properties of stable and unstable nuclei. It was checked in Ref. [302] that MTEC and TM1 can reproduce two-solar-mass neutron stars. The last parameter set ML2 is our fit to the equation of state from Ref. [293], shown in Fig. 5.3, that was also used in heavy-ion collisions and is compatible with the nucleon-nucleus optical potential.

We show in Tab. 5.2 the basic properties of the parametrizations like the saturation density ρ_0, where the binding energy per nucleon has its minimum, the depth of the

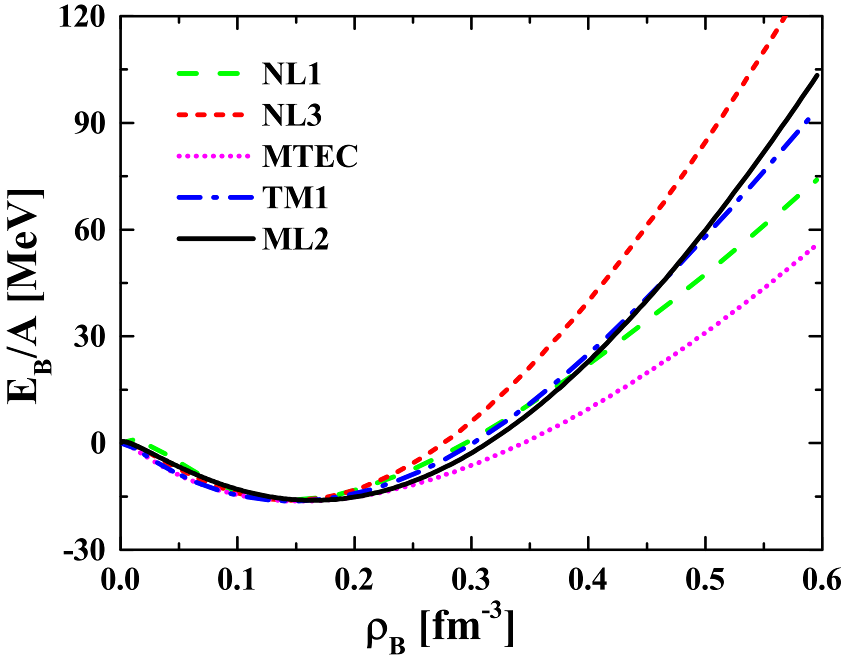

Figure 5.4: The binding energy $E_B/A = E/\rho_B - m_N$ for symmetric nuclear matter as a function of the nuclear density ρ_B for different parametrizations of the relativistic mean-field model.

minimum E_B/A as well as the nuclear compressibility,

$$K = 9\frac{\partial P}{\partial \rho_B}|_{\rho_B=\rho_0}, \tag{5.24}$$

of the different models. The effective mass m^*/m_N denotes here the value of the effective mass at saturation density. We show also the critical chemical potential μ_c for which the energy density reaches $E(\mu_c) = 0.5$ GeV/fm^3. The nuclear densities at μ_c are 0.5 ± 0.01 fm^{-3} for all parametrizations. We recall that the critical chemical potential for non-interacting nucleons is $\mu_c = 1014$ MeV. The much larger μ_c in the relativistic mean-field models is the result of the vector repulsion that pushes the chemical potential to larger values.

The binding energy per nucleon for the five sets is shown in Fig. 5.4 and the pressure in Fig. 5.5. They all reproduce the minimum in the binding energy and give similar results up to $1.5\rho_0$, but differ at larger densities. The findings from Refs. [147, 321] in terms of heavy-ion collisions suggest that the equation of state should be between NL1 and NL3, the findings from Ref. [302] in terms of neutron stars imply that it should be between MTEC and TM1 and at small densities close to ρ_0 the equation of state should be similar to ML2. Comparing the equations of state with each other, we find that the binding energy of ML2 is between the results from NL1 and NL3 and also between MTEC and TM1. This is different for the pressure where ML2 is still between NL1 and NL3 but not between MTEC and TM1. The binding energy and the pressure

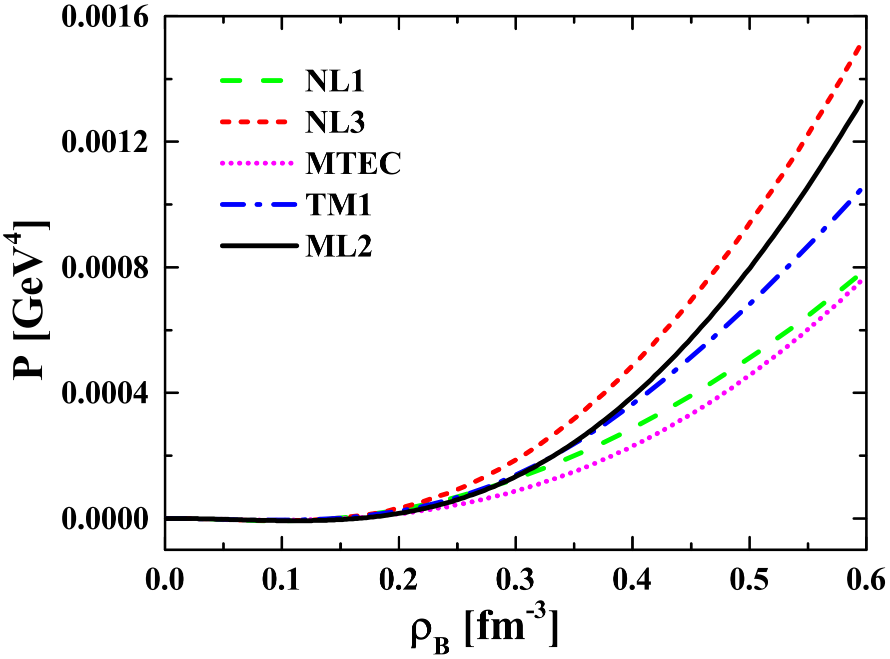

Figure 5.5: The pressure for symmetric nuclear matter as a function of the nuclear density ρ_B for different parametrizations of the relativistic mean-field model.

are sensitive to the combination of the attractive and the repulsive interaction, so we compare the models also for their effective masses $m^*/m_N = 1 - g_\sigma\sigma/m_N$, that is only sensitive to the attractive interaction. The results are shown in Fig. 5.6. The point at $\rho_B = \rho_0 \approx 0.16$ fm^{-3} is the quasi-empirical point which is the effective mass at saturation density and is in the range $0.7 < \tilde{m}/m_B < 0.85$. It is derived from non-relativistic models [322, 323] and is not equal to the effective Dirac mass m^* at the saturation density, that is slightly lower [324]. If we correct the effective point to slightly smaller effective masses we find that only TM1 is unable to reproduce it. Based on all these findings we choose the equation of state from the parameter set ML2 as the "nuclear equation of state". It is compatible with the heavy-ion constraints on the equation of state from Ref. [147, 321] and should be able to feature two-solar-mass neutron stars if one includes the right ρ-meson interaction in the approach.

We close the discussion of the nuclear equation of state with a short remark on the thermodynamic potential. So far we have shown all results as a function of the density and not the chemical potential. As addressed earlier, it is the easiest way to describe the system in terms of the Fermi momentum p_F, that defines also the density $\rho \sim p_F^3$, if the temperature is zero. It is therefore natural to express all thermodynamic quantities as a function of the density. This procedure implies, that we are not working in a grand-canonical ensemble but in a canonical. The thermodynamic potential then is the free energy (2.7), $F = U - TS$, which is equal to the internal energy U at vanishing

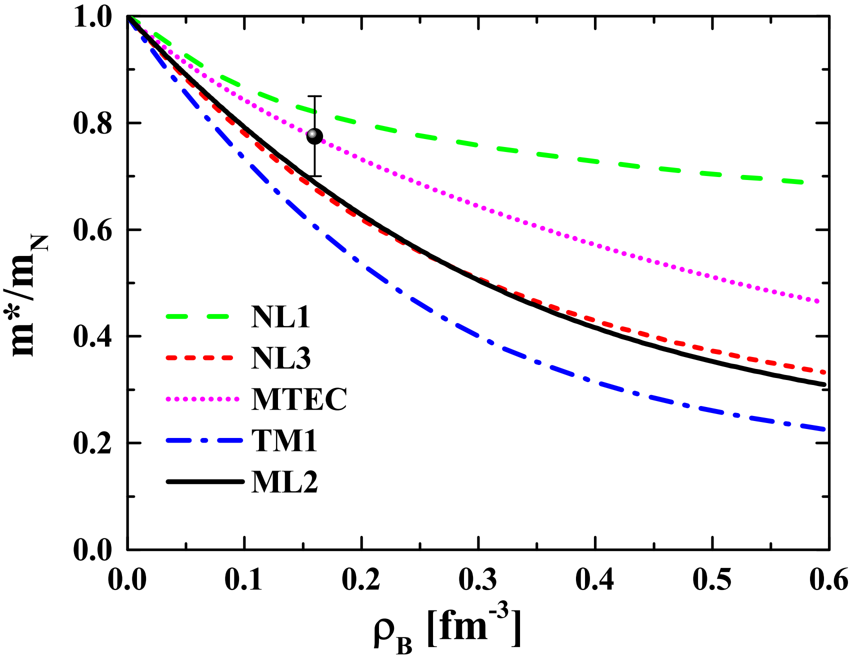

Figure 5.6: The effective mass m^*/m_N as a function of the nuclear density ρ_B for different parametrizations of the relativistic mean-field model. The point at $\rho_B = \rho_0$ is the quasi-empirical point derived from non-relativistic models.

temperature [10]. The pressure of the system in this special case follows from the relation,

$$P = \rho_B^2 \frac{\partial}{\partial \rho_B} \left(\frac{E}{\rho_B} \right) = \rho_B^2 \frac{\partial}{\partial \rho_B} \left(E_B/A \right), \tag{5.25}$$

and is no longer proportional to the thermodynamic potential. As one can see from Eq. (5.25) this implies also negative pressures if the binding energy per nucleon decreases, i.e. for all densities below the saturation density ρ_0, see Fig. 5.5. The system at $\rho_B < \rho_0$ is unstable, since the grand-canonical thermodynamic potential is larger than the vacuum. Another consequence of the canonical nature of the nuclear equation of state is the uncertainty in the chemical potential, which is no longer a natural variable. So far we have defined the phase transition by the condition $\epsilon_c = 0.5$ GeV/fm^3. As shown in Tab. 5.2 this leads to model-dependent critical chemical potentials μ_c that range from $\mu_c = 1014$ MeV in the non-interacting case to $\mu_c = 1258$ MeV for NL3 that incorporates the strongest repulsion. On the other hand one finds the universal value $\rho_c \approx 0.5$ fm^{-3} for the critical density. It might be impossible to define the nuclear equation of state as a function of the chemical potential.

---

[10] In the canonical ensemble one refers to the energy as the internal energy U.

5.3 Interacting Hadron-Resonance Gas

We have now defined all the boundary conditions that our model has to fulfill. At vanishing chemical potential we want to reproduce the most recent equation of state from the Wuppertal-Budapest collaboration [90] and at vanishing temperature we want to reproduce the nuclear equation of state from Ref. [293] that is compatible to Dirac-Brueckner calculations and heavy-ion collisions.

At finite temperature hadrons will interact through resonant scatterings, that we describe in terms of the HRG by including several important resonances as non-interacting particles. We restrict the particles here to those contained in PHSD, that are summarized in Tab. A.1 and A.2 in Appendix A.7. As discussed in Sec. 5.1 we will also include the scalar nonet which is summarized in Tab. A.3 also in Appendix A.7. Furthermore, we incorporate meson-exchange interactions in terms of relativistic mean-field models. This introduces additional attractive interactions mediated by the σ-meson, which will account for the missing higher resonances in the HRG.

The σ and the ω-meson appear in this model also as non-interacting particles, which may seem like a double counting, but the non-interacting contribution plays the role of an s-channel resonant-scattering amplitude. This is missing in the meson-exchange model -where this channel is neglected in the mean-field limit- and the "particles" appear only in the t-channel. The nucleons are included in both models, but in their case it is important to omit them in the HRG to avoid a true double counting.

The thermodynamic potential of the interacting Hadron-Resonance Gas (IHRG) is the sum of the regular HRG and the relativistic mean-field model. Additionally one has to subtract the non-interacting nucleons,

$$\Omega_{IHRG} = \Omega_{HRG} + \Omega_{RMF} - \Omega_{0,N} = \Omega_{RMF} + \sum_{\text{hadrons}\neq N} \Omega_0. \tag{5.26}$$

All other thermodynamical quantities are therefore also just the sum of both models, but without the non-interacting nucleons.

For the description of the nuclear equation of state it is not necessary to extend the model towards more interacting particles, since additional baryons will only appear for $\rho_B \geq 2-3\ \rho_0$ [325, 326, 327]. This changes if we increase the temperature and also other baryons start to interact via meson exchange. The appearance of additional interacting baryons like hyperons and Δ's in the nuclear equation of state is a frequently discussed question in the context of neutron stars, see Ref. [327] and references therein. We will use the findings from this field to extend the IHRG to include more interacting baryons, the mesons are kept non-interacting. Especially important in this context and also for the description of heavy-ion collisions are the Δ-resonances. We describe them through the Lagrangian [325, 326, 328],

$$\mathcal{L}_\Delta = \bar{\Psi}_{\Delta\nu}\left(i\gamma_\mu\partial^\mu - M_\Delta\right)\Psi^\nu_\Delta + \Gamma_{\sigma\Delta}(\hat{\rho}_0)\bar{\Psi}_{\Delta\nu}\sigma\Psi^\nu_\Delta - \Gamma_{\omega\Delta}(\hat{\rho}_0)\bar{\Psi}_{\Delta\nu}\gamma^\mu\omega_\mu\Psi^\nu_\Delta, \tag{5.27}$$

that we add to the Lagrangian of the relativistic mean-field theory (5.11). The couplings Γ_Δ can depend on an arbitrary Lorentz scalar or stay constant. The spinor Ψ^ν_Δ is not a Dirac spinor but a Rarita-Schwinger spinor with 4×4 components that describes a spin-3/2 particle [329], however, the mean-field limit of the theory behaves just like Dirac spinors [325, 326]. The selfconsistent equations (5.17) and (5.18) become

$$\frac{\partial U}{\partial \sigma} = \Gamma_{\sigma N} \rho_s^N(T, \mu_N^*, m_N^*) + \Gamma_{\sigma\Delta} \rho_s^\Delta(T, \mu_\Delta^*, m_\Delta^*), \tag{5.28}$$

$$\frac{\partial O}{\partial \omega} = \Gamma_{\omega N} \rho_B^N(T, \mu_N^*, m_N^*) + \Gamma_{\omega\Delta} \rho_B^\Delta(T, \mu_\Delta^*, m_\Delta^*). \tag{5.29}$$

Here ρ_s^Δ and ρ_B^Δ are the scalar and the particle density for non-interacting Δ-baryons. They depend on the effective mass m_Δ^* and the effective chemical potential μ_Δ^* that are defined by the selfenergies of the Δ's,

$$m_\Delta^* = m_\Delta - \Sigma_\Delta^s, \qquad \mu_\Delta^* = \mu - \Sigma_\Delta^0, \tag{5.30}$$

which follow directly from the effective couplings $\Gamma_{\sigma\Delta}$ and $\Gamma_{\omega\Delta}$ as shown in Appendix A.9. The pressure and the energy density of the system -without the HRG contribution- are given by

$$\begin{aligned} P = &- U(\sigma) + O(\omega) + \Sigma_N^{0(r)} \rho_B^N + \Sigma_\Delta^{0(r)} \rho_B^\Delta - \Sigma_N^{s(r)} \rho_s^N - \Sigma_\Delta^{s(r)} \rho_s^\Delta \\ &+ P_0(T, \mu_N^*, m_N^*) + P_0(T, \mu_\Delta^*, m_\Delta^*) \end{aligned} \tag{5.31}$$

and

$$\begin{aligned} E = &U(\sigma) - O(\omega) + \Sigma_N^{s(r)} \rho_s^N + \Sigma_\Delta^{s(r)} \rho_s^\Delta + \Sigma_N^{0(0)} \rho_B^N + \Sigma_\Delta^{0(0)} \rho_B^\Delta \\ &+ E_0(T, \mu_N^*, m_N^*) + E_0(T, \mu_\Delta^*, m_\Delta^*). \end{aligned} \tag{5.32}$$

The entropy and the particle density are, as expected, the non-interacting expressions but with the respective effective quantities,

$$s = s_0^N(T, \mu_N^*, m_N^*) + s_0^\Delta(T, \mu_\Delta^*, m_\Delta^*), \tag{5.33}$$

$$\rho_B = n_0^N(T, \mu_N^*, m_N^*) + n_0^\Delta(T, \mu_\Delta^*, m_\Delta^*). \tag{5.34}$$

The approach is thermodynamically consistent if the selfconsistent equations (5.28) and (5.29) are fulfilled. The thermodynamic potential of the IHRG with interacting nucleons and Δ's is

$$\Omega_{IHRG} = \Omega_{HRG} + \Omega_{RMF} - \Omega_{0,N} - \Omega_{0,\Delta} = \Omega_{RMF} + \sum_{\text{hadrons} \neq N, \Delta} \Omega_0. \tag{5.35}$$

The extension introduces also two additional couplings $\Gamma_{\sigma\Delta}$ and $\Gamma_{\omega\Delta}$. As for nucleons these couplings are not fixed by theory, but one can impose several constraints on them. The introduction of additional particles like Δ's or hyperons can create a second minimum in the binding energy [325, 326], but since there are no Δ's in the ground state of nuclear matter, this minimum can only describe a metastable state. Furthermore, any contribution from the Δ's has to vanish at saturation density. There is also some guidance from finite density sum-rules which show that the scalar selfenergy of the Δ's is larger and the vector selfenergy smaller than the corresponding values for the nucleon selfenergies [330]. In Ref. [328] all these conditions are used to constrain the model for constant couplings. These findings are summarized by:

$$\frac{\Gamma_{\sigma\Delta}}{\Gamma_{\sigma N}} \leq 1.01 \cdot \frac{\Gamma_{\omega\Delta}}{\Gamma_{\omega N}} + 0.38, \qquad \frac{\Gamma_{\sigma\Delta}}{\Gamma_{\sigma N}} \geq 1, \qquad \frac{\Gamma_{\omega\Delta}}{\Gamma_{\omega N}} \leq 1. \tag{5.36}$$

A popular choice for the couplings -in line with the relations (5.36)- are the conditions $\Gamma_{\sigma\Delta}/\Gamma_{\sigma N} = m_\Delta/m_N$ and $\Gamma_{\omega\Delta} = \Gamma_{\omega N}$. They are based on the argument that the ω-meson has a real quark-antiquark structure and the σ-meson not [326]. This choice leads to a fixed ratio of the effective masses $m^*_\Delta/m^*_N = m_\Delta/m_N$ and keeps the chemical potentials for both baryons the same $\mu^*_\Delta = \mu^*_N$. We will employ this choice whenever we treat the Δ's as interacting particles.
The generalization to even more interacting baryons is straight forward. The spin-1/2 and spin-3/2 particles behave equally in the mean-field limit. We fix the scalar couplings by the ratio of the bare masses and keep the vector couplings identical,

$$\frac{\Gamma_{\sigma X}}{\Gamma_{\sigma N}} = \frac{m_X}{m_N}, \qquad \Gamma_{\omega X} = \Gamma_{\omega N}. \tag{5.37}$$

The selfconsistent equations (5.28) and (5.29) in their generalized form become,

$$\frac{\partial U}{\partial \sigma} = \Gamma_{\sigma N} \sum_X \frac{m_X}{m_N} \rho^X_s(T, \mu^*_N, m^*_X), \tag{5.38}$$

$$\frac{\partial O}{\partial \omega} = \Gamma_{\omega N} \sum_X \rho^X_B(T, \mu^*_N, m^*_X), \tag{5.39}$$

and the pressure reads

$$P = -U(\sigma) + O(\omega) + \sum_X \left(\Sigma^{0(r)}_X \rho^X_B - \Sigma^{s(r)}_X \rho^X_s + P^X_0(T, \mu^*_N, m^*_X) \right). \tag{5.40}$$

The sum runs over all baryons that we include as interacting particles. These baryons have to be omitted in the HRG contribution in case of the IHRG. We will only discuss the cases of interacting nucleons as well as interacting nucleons and Δ's. Another reasonable choice is to use all baryons of the spin-1/2 octet. However, the results are similar to the case of interacting nucleons and Δ's. The reason is that the masses of the Δ and the Σ, Λ and Ξ are all in the vicinity of $m \approx 1200$ MeV. The Δ's are 16-times degenerated, the Σ's, Λ's and Ξ's have in total a degeneracy of 12, thus both cases are fairly similar, but the Δ's are more important in low-energy heavy-ion collisions.
We will now fix the parameters of our model. The right side of the selfconsistent equation (5.39) is proportional to the net-baryon densities of the interacting baryons, that have to vanish for $\mu = 0$. Since symmetries demand that $O(\omega)$ is an even function the left side of the equation vanishes for $\omega = 0$. This fixes $\omega = 0$ for $\mu = 0$ and the repulsive interaction contributes only at finite chemical potential μ_B. As noted before this is different to

	Int. baryons	g_σ	m_σ [MeV]	B [1/fm]	C
DD1	N	28.64	550	-29.67	3837
DD2	$N+\Delta$	20.79	550	-58.29	9690

Table 5.3: Parameters for the scalar interaction in the IHRG at vanishing chemical potential $\mu_B = 0$.

repulsive interactions through excluded volume effects that contribute even at vanishing chemical potential [269, 270, 271, 272]. We can therefore fix the scalar interaction solely with the lQCD equation of state at $\mu_B = 0$ and then tune the repulsive interaction to reproduce the nuclear equation of state at $T = 0$ and $\mu_B \neq 0$.

We use the following strategy to define the scalar interaction. We subtract the non-interacting HRG from the lQCD equation of state and define in this way the contribution from the interacting model. We keep the scalar coupling as a constant $\Gamma_\sigma = g_\sigma$, so we obtain from Eq. (5.37) a constant ratio for the effective masses $m_X^*/m_N^* = m_X/m_N$. The entropy density of the interacting model for a given temperature T is then a function of only the effective nucleon mass m_N^*,

$$s_{\mathrm{Int}} = s_0^N(T, m_N^*) + s_0^\Delta\left(T, \frac{m_\Delta}{m_N} m_N^*\right). \tag{5.41}$$

We demand that the interacting entropy density s_{Int} is equal to the missing entropy density to reproduce the lQCD result. This determines the effective mass $m_N^*(T, \mu_B = 0)$. With $m_N^*(T)$ fixed we can easily calculate the scalar densities and use the selfconsistent equation (5.38) to determine $\partial U/\partial\sigma(T)$ as a function of temperature. The value of the σ-field as a function of temperature follows from the effective mass $\sigma = (m_N - m_N^*)/g_\sigma$. We can then fit $\partial U/\partial\sigma$ as a function of σ, thus defining the σ-selfinteraction. The polynomial ansatz for the selfinteraction, $U(\sigma) = \frac{1}{2}m_\sigma^2\sigma^2 + \frac{1}{3}B\sigma^3 + \frac{1}{4}C\sigma^4$, is able to reproduce the interaction for both nucleons as well as nucleons and Δ's. The value of the scalar coupling g_σ is arbitrary, since σ has no physical meaning, only $g_\sigma\sigma = m_N - m_N^*$. If one rewrites the selfconsistent equations (5.17) and (5.38) in terms of m_N^* instead of σ, one finds for the polynomial ansatz of $U(\sigma)$ that the equation is determined by the ratios m_σ/g_σ, B/g_σ^3 and C/g_σ^4. We fix g_σ by setting the σ-mass to its physical value $m_\sigma \approx 550$ MeV. The parameters in Tab. 5.3 give a good representation of the scalar selfinteraction for the temperature range between $T \approx 130$ MeV and $T \approx 160$ MeV. We denote the set for interacting nucleons DD1 and for nucleons and Δ's DD2. If one compares these values with the parameters for the relativistic mean-field models in Tab. 5.2 one notices the large quartic coefficient C. The scalar selfinteraction in conventional mean-field models is just a small correction, but gives the dominant contribution in our approach at $\mu_B = 0$. Another difference to conventional mean-field models are the much larger values of the scalar density ρ_s probed by our approach, since ρ_s increases with $\rho_s \sim T^3$. This may lead to an unphysical phase transition if $\frac{\partial U}{\partial\sigma}$ is not strictly monotonic increasing, i.e. if the cubic or quartic coefficients B or C are negative. Both parameter

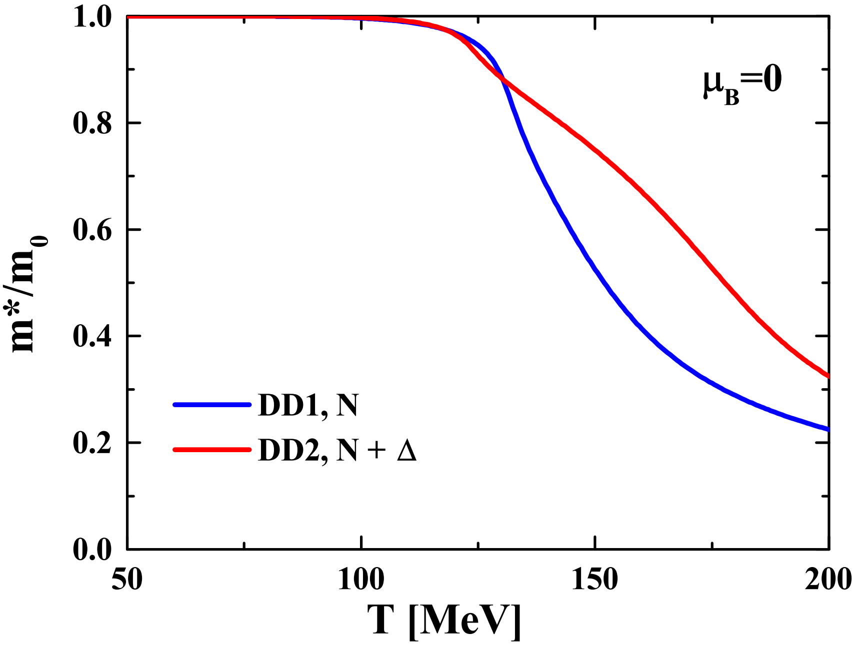

Figure 5.7: The effective baryon masses scaled by their vacuum value as a function of temperature for vanishing chemical potential. The blue line is the result with only interacting nucleons and the red line for the case of interacting nucleons and Δ-resonances.

sets in Tab. 5.3 have repulsive cubic interactions and also the sets NL1, MTEC and TM1 -discussed in the last section- incorporate repulsive cubic interactions; MTEC has even a repulsive quartic interaction. However, in DD1, DD2 and NL1 the repulsive term is not strong enough to introduce a phase transition. This is different for TM1 that has a local minimum and MTEC that even starts to decrease. Nevertheless, these unphysical behaviors appear only at baryon densities much larger than the ones discussed. Note that the lQCD equation of state has no real phase transition, so any model used to describe it can not feature a critical behavior at $\mu_B = 0$. In the same way as a non-monotonic behavior in $\frac{\partial U}{\partial \sigma}$ can introduce a phase transition also a non-monotonic behavior in $\frac{\partial O}{\partial \omega}$ has the potential to introduce one.

We show the ratio of the effective masses to the vacuum masses as a function of the temperature for vanishing chemical potential in Fig. 5.7. The additional interactions are not needed for temperatures below $T \approx 100$ MeV, so the effective masses stay at their vacuum values. As the temperature increases further they begin to decrease. A smaller effective mass results in a larger σ-field and more interaction strength compared to the non-interacting case. The effective mass for DD1 decreases more rapidly than for DD2, because in case of DD1 the whole additional interaction strength has to come from the nucleons alone while for DD2 also the Δ-contribution is enhanced. We show the corresponding entropy densities s/T^3 in Fig. 5.8 and compare them to the non-interacting HRG and the lQCD entropy density from Ref. [90] used to determine the attractive interaction. At small temperatures the interacting models are similar to the

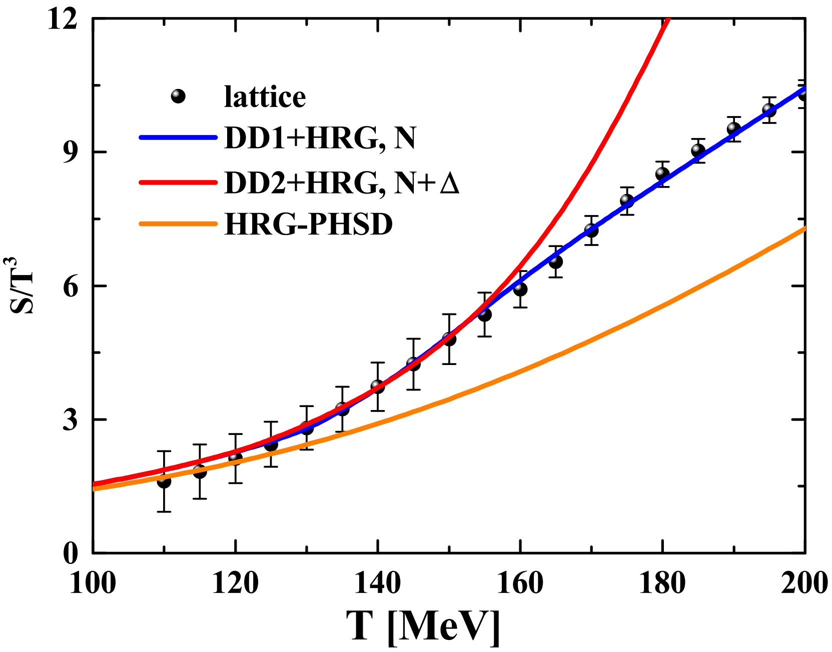

Figure 5.8: The scaled entropy density s/T^3 as a function of the temperature T for vanishing chemical potential. The blue line is the entropy for the IHRG with interacting nucleons and the red line for the IHRG with interacting nucleons and Δ-resonances. The orange line is the entropy density without interactions. The lQCD results are taken from the Wuppertal-Budapest collaboration [90].

non-interacting HRG since the interactions give no contribution. The small offset seen at smaller temperatures is caused by the scalar mesons missing in the PHSD HRG. The additional interaction becomes visible at $T \approx 125$ MeV. Up to temperatures $T \approx 155$ MeV both interacting models by design give the same result and describe the lQCD data within the error bars, however, at larger temperatures (QGP phase) they differ. The model including the Δ's increases too fast and exceeds the lQCD entropy, the model with only nucleons reproduces the entropy density even up to $T = 200$ MeV. This is surprising since we fitted the interaction only for smaller temperatures. Nevertheless, the IHRG can not describe the dynamics at temperatures beyond $T \approx 160$ MeV, because it uses not the right degrees of freedom, however, both models work well in the region where we expect the hadronic phase.

We compare now the equation of state of the two parametrizations. Fig. 5.9 shows the equation of state for DD1 scaled by powers of the temperature. The lQCD equation of state is the same as before. We find an excellent agreement between the model and the data. The thermodynamic consistency of the approach ensures that we get the correct behavior in the pressure and the energy density once the entropy density is fixed. This is the same strategy that we used before in Sec. 3 for the DQPM. We found there that this may lead to some deviations in the interaction measure. This is not the case for the IHRG, which describes the whole equation of state within the error bars of the data, even

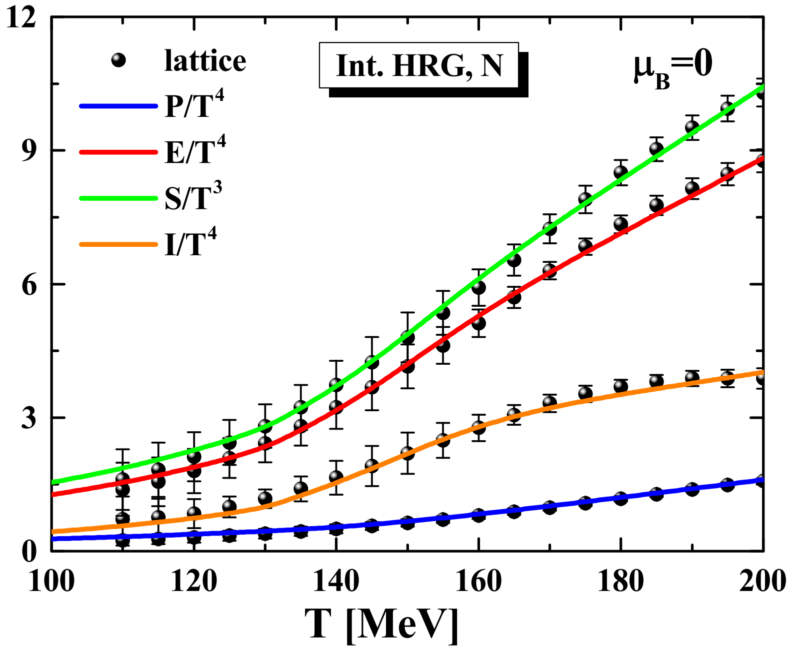

Figure 5.9: The equation of state for the IHRG for the parameter set DD1 as a function of the temperature T. The additional interaction is carried by the nucleons. The green line shows the entropy density, the red line the energy density, the blue line the pressure and the orange line the interaction measure. All quantities are scaled by powers of the temperature. The results are within the error bars of the lQCD data in the whole temperature range shown. The lQCD results are taken from the Wuppertal-Budapest collaboration [90].

at larger temperatures where lQCD becomes more reliable and the error bars shrink. The first differences will appear only for $T > 200$ MeV. The interaction measure I/T^4 has its maximum around this temperature and will then start to decrease, but in the hadronic model it increases further. The IHRG equation of state will then exceed the lQCD data. One finds also small deviations at the lowest temperature of $T = 110$ MeV. This is surprising since lQCD calculations use the non-interacting HRG to fix their equation of state at low temperatures and integrate then over the scaled interaction measure to calculate the equation of state at higher temperatures, see Eq. (2.32). The lQCD results should therefore agree at low temperatures with our predictions. However, most lattice groups use the Boltzmann approximation when they employ the HRG and neglect the quantum statistics. This has only a small influence on the results since most hadron masses are larger than these temperatures, but in case of pions with a mass of $m_\pi = 138$ MeV $\approx T$, it leads to a deviation of roughly 10%. Since pions are the only essential contribution at low temperatures, this explains the deviations between the HRG and the lQCD results.

We show the equation of state for the interacting model with nucleons and Δ-resonances in Fig. 5.10. As mentioned earlier DD1 and DD2 give the same results for tempera-

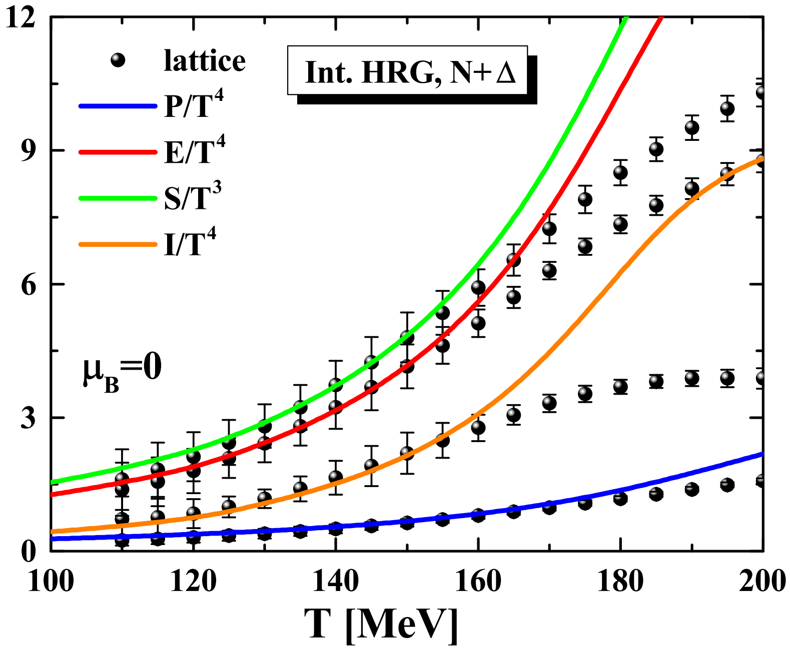

Figure 5.10: The equation of state for the IHRG for the parameter set DD2 as a function of the temperature T. The additional interaction is carried by the nucleons and the Δ-resonances. The green line shows the entropy density, the red line the energy density, the blue line the pressure and the orange line the interaction measure. All quantities are scaled by powers of the temperature. The results are within the error bars of the lQCD data for $T < 160$ MeV. The lQCD results are taken from the Wuppertal-Budapest collaboration [90].

tures below $T = 155$ MeV and the model reproduces the lQCD data within the error bars for all temperatures below $T = 160$ MeV, where we expect a dominantly hadronic system. At larger temperatures DD2 differs substantially from the lQCD results and rises too fast for $T > T_c$ as already seen in Fig. 5.8. One can improve the description at larger temperatures by using a different parametrization for the scalar selfinteraction and fix it also at larger temperatures. Note that we have fixed the interaction only up to $T = 160$ MeV. The excellent results from DD1 at larger temperatures come out as a surprise.

We have seen for the HRG that a reasonable equation of state can still give the wrong behavior in the speed of sound, cf. Sec. 5.1. We compare the speed of sound squared for the IHRG as a function of the temperature in Fig. 5.11 and show again the corresponding results from the non-interacting HRG and also the HRG with all hadrons listed by the Particle Data Group [291] with a mass below 2.0 GeV. We find that only DD1 describes the data properly. It reproduces the minimum at $T \approx 140$ MeV and is within the error bars up to $T = 170$ MeV. Nevertheless, it benefits from the huge error bars at low temperatures. The version DD2 can only describe the data up to $T = 150$ MeV; it has also a minimum in c_s^2, but at a too high temperature, which is also too deep. On the

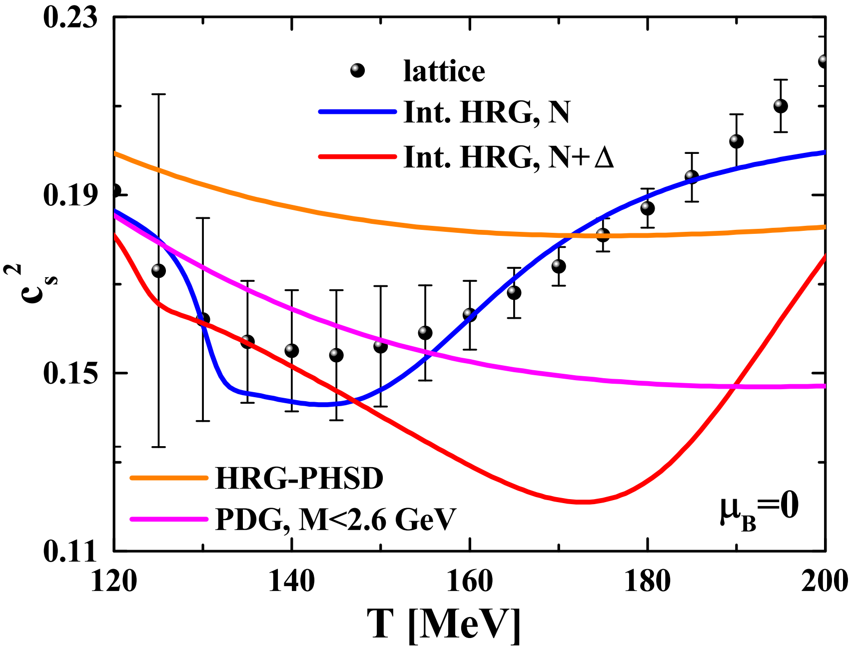

Figure 5.11: The speed of sound squared c_s^2 for the IHRG as a function of the temperature for vanishing chemical potential. The blue line is the result with interacting nucleons, the red line with interacting nucleons and Δ-resonances. The orange line shows c_s^2 for the non-interacting HRG with all the hadrons in the PHSD approach and the magenta line for all hadrons listed by the particle data group [291] with a mass below 2.0 GeV. The lQCD results are taken from the Wuppertal-Budapest collaboration [90].

other hand the non-interacting model is completely off the data and has also the wrong behavior. The other HRG version with much more particles gives a better description but only up to $T = 155$ MeV. From there on it has also the wrong trend. All models except for DD1 fail to describe the rise in the speed of sound at $T \approx 150 - 160$ MeV. For this it is necessary that the models reproduce not only the equation of state but also the inflection points of the scaled equation of state. One will always find a decreasing speed of sound if the pressure P/T^4 has an increasing slope. This is a problem in most hadronic models.

Both parametrizations of the IHRG can reproduce the lQCD equation of state in the hadronic regime $T < T_c$ at vanishing chemical potential. DD1 gives even a satisfying description of the speed of sound while DD2 has the wrong trend in c_s^2 since it does not describe the inflection point of the scaled equation of state. One can repeat the fitting procedure -described in this section- to obtain the scalar selfinteraction for a larger range in σ. The model will then automatically describe the inflection point and c_s^2. However, in the following we will keep DD2 as it is since the deviations appear only close to T_c where one should consider also partonic degrees of freedom. With the scalar interaction defined we can now discuss the repulsive interaction. We fix it in the same way as the scalar interaction but we use the nuclear equation of state at $T = 0$ as input. In this

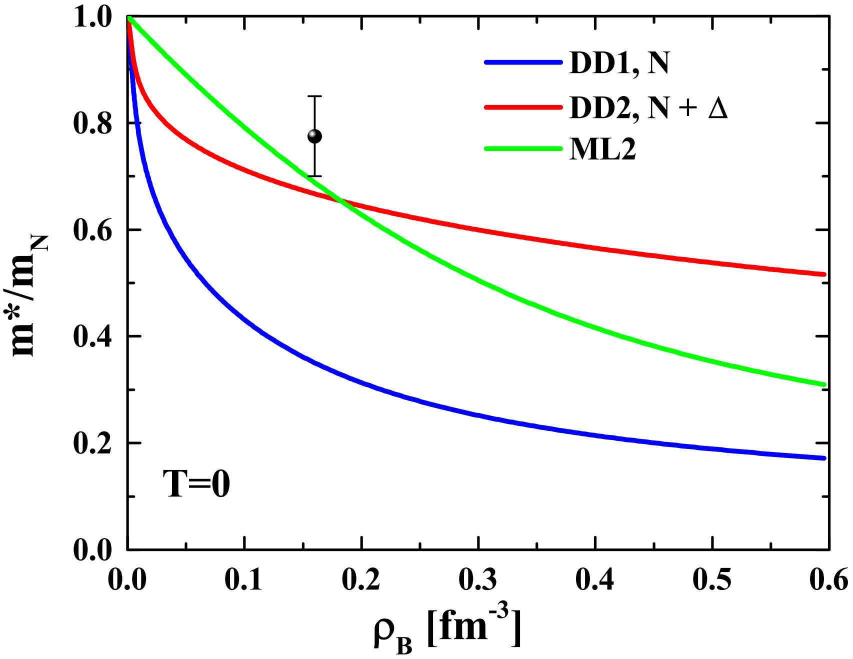

Figure 5.12: The effective mass m^*/m_0 as a function of the baryon density for zero temperature. The blue line follows from the parameter set DD1, the red line from the set DD2 and the green line for the set ML2. The point at $\rho_B = \rho_0$ is the quasi-empirical point derived from non-relativistic models.

limit the HRG contribution of the IHRG vanishes and it reduces to a normal (density-dependent) relativistic mean-field model.

The scalar interaction defines already the effective masses. Fig. 5.12 shows m^*/m_0 for $T = 0$ as a function of the nucleon density for the sets DD1 and DD2, where the scalar interaction is fixed by the lQCD equation of state, and for the parameter set ML2 discussed in Sec. 5.2, that is only valid for the nuclear equation of state. The point at $\rho_B = \rho_0$ is again the quasi-empirical point derived from non-relativistic models. Recall that the relativistic empirical point is at a slightly lower value compared to the non-relativistic one. The effective masses for DD1 and DD2 show not the usual behavior of a relativistic mean-field model, where the effective mass drops linearly as a function of the density for small ρ_B. This is due to the small cubic and quartic corrections in $U(\sigma)$ in the default mean-field models. If these corrections are small one finds an effective mass that decreases almost linearly with the scalar density which at small densities is equal to the nucleon density, $\rho_s \approx \rho_B$. The sets DD1 and DD2 incorporate very large quartic couplings and show therefore a different behavior. However, such a behavior of the effective masses was also observed in a variational approach in Ref. [331] for finite but very small temperatures of $T = 5$ MeV. The results in Fig. 5.7 show the influence of additional interacting hadrons. In DD1 the nucleons carry the whole scalar interaction so the effective mass drops too fast and can not reproduce the quasiempirical point. This is resolved if the scalar interaction is carried by different baryons. In DD2 the in-

	Int. baryons	$\tilde{A}$	$\tilde{B}$	$\tilde{C}$	$\tilde{D}$	$\tilde{E}$	$\tilde{F}$
DD1	N	45.59	3045	$4.90 \cdot 10^7$	$1.40 \cdot 10^{10}$	$6.21 \cdot 10^7$	$7.63 \cdot 10^{10}$
DD2	$N + \Delta$	33.44	50231	$1.99 \cdot 10^7$	$-2.75 \cdot 10^9$	$1.18 \cdot 10^8$	$-1.49 \cdot 10^{10}$

Table 5.4: Parameters for the vector interaction in the IHRG at vanishing temperature. All parameters are in units of GeV.

teraction is shared between nucleons and Δ's, so it is overall weaker. The effective mass is then almost consistent with the quasiempirical point. Note that the nuclear equation of state for DD2 gets no contribution from the interacting Δ's. Even if their mass gets reduced due to the scalar interaction, they are still too heavy to give a thermodynamic contribution. The same holds also if one includes more interacting hadrons, as they would additionally weaken the scalar interaction. The nuclear equation of state of the IHRG is only determined by nucleons, as argued in Sec. 5.2.

The effective mass at $T = 0$ defines the selfinteraction $U(\sigma)$, the scalar selfenergy Σ^s and the non-interacting part E_0 of the energy density of the relativistic mean-field model (A.113). The remaining contributions depend on the repulsive interaction that we determine in the following way. We omit the selfinteractions in the ω-field and keep only the mass term, $O(\omega) = \frac{1}{2}m_\omega^2\omega^2$. Instead we describe the repulsive interaction with a density-dependent vector coupling, that depends on the net-baryon density, $\Gamma_\omega(\rho_B)$. It is important for the consistency of the model that ρ_B contains only the interacting baryons and not the whole baryon density of the IHRG, however, this is naturally the case for the nuclear equation of state. The coupling can not depend on the scalar density, since this would lead to a scalar rearrangement selfenergy that alters the effective mass and therefore the equation of state at finite temperatures and vanishing chemical potentials. The selfconsistent equations for the ω-field (5.18), (5.29) and (5.39) become now $m_\omega^2\omega = \Gamma_\omega(\rho_B)\rho_B$. We use this to rewrite the equation for the energy density (A.113),

$$E(T, \mu_B) - E_0(T, \mu^*, m^*) - U(\sigma) = -O(\omega) + \Sigma^{0(0)}\rho_B = \frac{1}{2m_\omega^2}\Gamma_\omega^2(\rho_B)^2\rho_B^2. \tag{5.42}$$

The left side of the equation is determined by the scalar interaction and the equation of state one wishes to reproduce; the right side is determined by the repulsive interaction. We decided in Sec. 5.2 to adopt the equation of state from the parameter set ML2 as our nuclear equation of state for the IHRG. Note that we describe the equation of state at $T = 0$ as a canonical system where the density is a natural variable and the chemical potential follows as a derivative of the thermodynamic potential. The equation (5.42) is then a function of only the density, so it determines the vector coupling as a function of ρ_B,

$$\Gamma_\omega(\rho_B) = \sqrt{2}\,\frac{m_\omega}{\rho_B}\sqrt{E_{\mathrm{ML2}}(\rho_B) - E_0(\rho_B, m^*) - U(\sigma)}. \tag{5.43}$$

The repulsive interaction is actually determined by the ratio Γ_ω/m_ω. This is similar to the scalar interaction where we fixed m_σ to its physical value. We do the same here

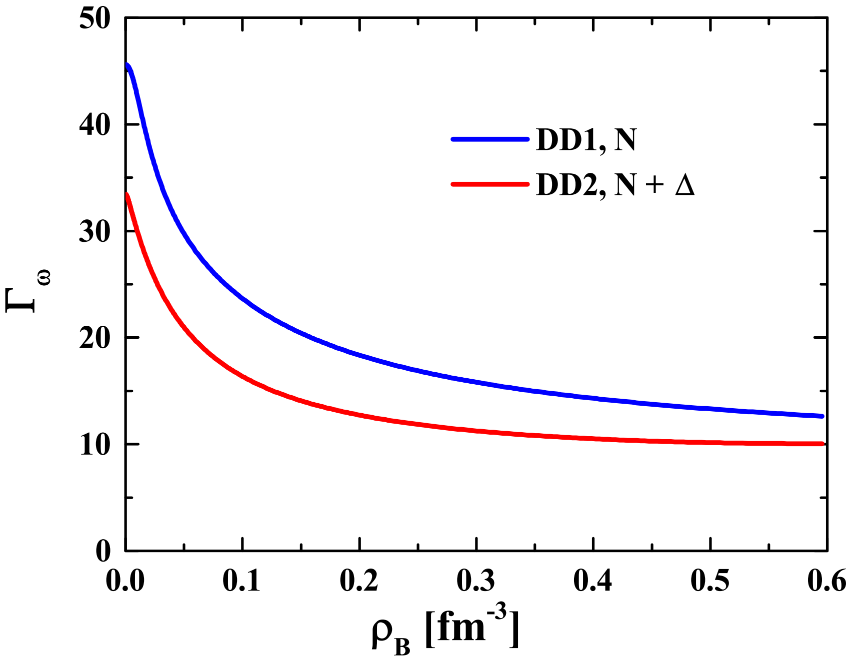

Figure 5.13: The density-dependent vector coupling Γ_ω as a function of the net-baryon density ρ_B. The blue line follows from the parameter set DD1, the red line from the set DD2. The energy density in Eq. (5.43) was taken from ML2 for $T = 0$.

and fix $m_\omega = 783$ MeV. We mentioned already that we use the energy density from the ML2 parameter set, but one can use this procedure to adopt to any possible equation of state. One could directly use Eq. (5.43) in the calculations, but we will fit the function with the ansatz

$$\Gamma_\omega(\rho_B) = \tilde{A} \cdot \frac{1 + \tilde{B}|\rho_B| + \tilde{C}|\rho_B|^2 + \tilde{D}|\rho_B|^3}{1 + \tilde{B}|\rho_B| + \tilde{E}|\rho_B|^2 + \tilde{F}|\rho_B|^3}. \tag{5.44}$$

This function is similar to the ansatz used in Refs. [304, 305] to fit the density-dependence of Dirac-Brueckner calculations, but there are also some important differences. The model in Refs. [304, 305] was only applied to nuclear matter and finite nuclei, i.e. to $T = 0$, but we want to apply our model also to finite temperatures and vanishing chemical potential. It is therefore mandatory that the coupling is an even function of the density. This is guaranteed by the absolute values of the density that lead to $\Gamma_\omega(\rho_B) = \Gamma_\omega(-\rho_B)$, but the function has to be continuously differentiable at $\rho_B = 0$. We ensure this by taking the same linear coefficient in the numerator and denominator of Eq. (5.44). We therefore extend the polynomials in the function to the third order to compensate the lost coefficient in the linear term. The coefficients for the fit are summarized in Tab. 5.4. We show the results of the fits in Fig. 5.13. It may not be possible to see by eye, but both functions fulfill the condition $\Gamma'_\omega(\rho_B = 0) = 0$. The differences in the parametrizations do not follow from the appearance of Δ's but only from the different scalar interactions. Since DD1 has a stronger scalar, i.e. attractive interaction, it needs a stronger repulsive interaction to balance it.

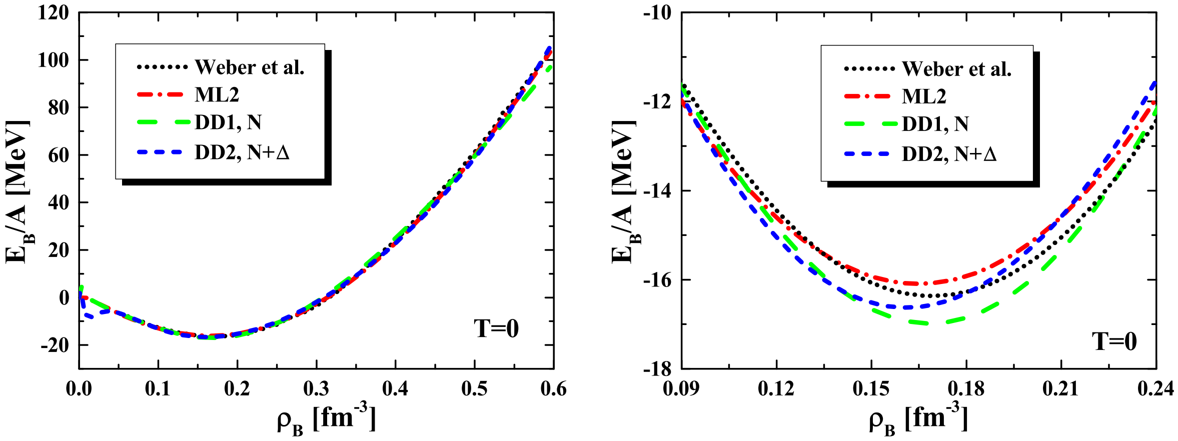

Figure 5.14: The binding energy per nucleon E_B/A as a function of the nucleon density ρ_B for $T = 0$. The dotted black line is taken from Weber et al. [293] and is the benchmark for our nuclear equation of state. It is fitted with the parameter set ML2 shown by the dash-dotted red line. The green dashed line is the result for the parameter set DD1 and the blue short dashed line for the set DD2. The left panel shows the binding energy for a large range in the density from the vacuum up to 3.5 ρ_0 while the right panel focusses on the density region around the saturation density $\rho_0 \approx 0.16$ fm^{-3}.

We can now calculate the nuclear equation of state of the IHRG to check the quality of the fit (5.44). The binding energy per nucleon E_B/A is shown in Fig. 5.14 in comparison to the result from Weber et al. [293], that we used as benchmark for the nuclear equation of state, and the result from the parameter set ML2 that is designed to reproduce this binding energy. The left panel shows the whole density region up to $\rho_B = 0.6$ fm^{-3}, the right panel zooms into the region close to the saturation density. All four lines are approximately on top of each other up to $\rho_B = 3\rho_0$, the vector coupling can successfully reproduce the binding energy. Both DD1 and DD2 give nuclear binding energies in the range of $E_B = -16$ to -17 MeV and a saturation density of $\rho_0 = 0.168$ fm^{-3} for DD1 and $\rho_0 = 0.161$ fm^{-3} for DD2. There are, however, some odd behaviors at very small densities. DD1 has a very small peak and DD2 exhibits a second minimum at $\rho_B = 0.012$ fm^{-3}, but it is higher than the global minimum at the saturation density implying that it describes just a metastable state. These deviations appear also in conventional relativistic mean-field models, but at the smallest densities. They occur due to the singular behavior of the binding energy per nucleon $E_B/A = E/\rho_B - m_N$, if the energy density differs from the form $E \approx m_N \cdot \rho_B$ at small densities. In case of the IHRG they result from the condition $\Gamma'_\omega(\rho_B = 0) = 0$ that constrains the functional form of $\Gamma_\omega(\rho_B)$.

We now have completely defined the IHRG with the scalar interaction given by the parameters in Tab. 5.3 and the vector interaction with the function (5.44) and the parameters in Tab. 5.4. The equation of state for finite temperatures and vanishing chemical potential reproduces the lQCD equation of state and at vanishing temperature and finite density it reproduces the nuclear equation of state from Weber et al. [293].

$\hat{A}$	$\hat{B}$	$\hat{C}$	$\hat{D}$	$\hat{E}$	$\hat{F}$
33.93	18535	$4.49 \cdot 10^7$	$6.80 \cdot 10^9$	$8.97 \cdot 10^7$	$3.90 \cdot 10^{10}$

Table 5.5: Parameters for $\Gamma_\sigma(\rho_s)$ that reproduce the lQCD equation of state at vanishing chemical potential. All parameters are in units of GeV.

We have done this by describing the scalar interaction with selfinteraction terms for the σ-meson and the vector interaction with a density-dependent coupling. This, however, is not unique. The equation of state at finite T and vanishing chemical potential is contained in the effective mass, more precisely in the function $m^*(\rho_s)$, and the nuclear equation of state, for a given scalar interaction, is contained in the effective chemical potential, i.e. in the function $\mu^*(\rho_B)$. We could also describe the scalar interaction with a density-dependent coupling $\Gamma_\sigma(\rho_s)$ and without σ-selfinteractions in $U(\sigma)$, i.e. $B = C = 0$. If it leads to the same effective mass m^*, it will also give the same equation of state. A possible choice is the function

$$\Gamma_\sigma(\rho_s) = \hat{A} \cdot \frac{1 + \hat{B}\rho_s + \hat{C}\rho_s^2 + \hat{D}\rho_s^3}{1 + \hat{B}\rho_s + \hat{E}\rho_s^2 + \hat{F}\rho_s^3} \tag{5.45}$$

with the parameters in units of GeV given in Tab. 5.5. The scalar selfinteraction is then the mass term $U(\sigma) = \frac{1}{2}m_\sigma^2\sigma^2$ with $m_\sigma = 550$ MeV. The σ-selfinteractions are therefore just hidden scalar-density-dependent couplings $\Gamma_\sigma(\rho_s)$. It is also possible to describe the vector interaction through a more complex ω-self-interaction $O(\omega)$ and a constant vector coupling g_ω. The vector rearrangement selfenergy then is zero and one can fix the selfinteraction in the same way as we did with the density-dependent coupling. One can rewrite the equations for the pressure (A.115) and the energy density (A.113) for a given scalar interaction and gets

$$O(\omega) = P - P_0(T, \mu^*, m^*) + U(\sigma) + \Sigma^{s(r)}\rho_s, \tag{5.46}$$

$$g_\omega\omega = \left(P + E - P_0(T, \mu^*, m^*) - E_0(T, \mu^*, m^*)\right)/\rho_B, \tag{5.47}$$

where E and P are the energy density and the pressure for the equation of state one wishes to reproduce. The value of g_ω is arbitrary. Eqs. (5.46) and (5.47) will give the same nuclear equation of state as the density-dependent vector coupling defined by Eq. (5.43). It was already observed when ω-selfinteractions beyond the mass term were first introduced in Ref. [298], that the effects are similar to Dirac-Brueckner calculations. Higher order ω-selfinteractions are just a different way to express density-dependent vector couplings $\Gamma_\omega(\rho_B)$. This justifies mesonic selfinteractions, since density-dependent effective couplings are a standard result from Dirac-Brueckner calculations [313].

We controlled the extension of the model towards finite chemical potential with the nuclear equation of state. This is a different strategy compared to the DQPM* where we used the susceptibilities. The susceptibilities of the IHRG model are the sum of the non-interacting and the interacting susceptibilities

$$\chi_B = \chi_B^{RMF} + \sum_X \chi_{B,0}^X, \tag{5.48}$$

the summation runs over all hadrons that are taken as non-interacting. The susceptibility of the interacting part reads,

$$\chi_B^{RMF} = \frac{\partial n_B^{RMF}}{\partial \mu_B} = \frac{\partial \rho_B}{\partial \mu^*}\frac{\partial \mu^*}{\partial \mu_B} = \tilde{\chi}_B \cdot \left(1 - \frac{\partial \Sigma^0}{\partial \mu_B}\right), \tag{5.49}$$

where $\tilde{\chi}_B$ is the susceptibility for a system without vector repulsion given by the non-interacting susceptibilities (3.33), but with the effective masses m^*. It incorporates only the effects of the scalar interaction, the repulsive interaction is considered by the correction factor $(1 - \partial\Sigma^0/\partial\mu_B)$. The formula is only valid at vanishing chemical potential because it neglects additional correction terms at finite μ_B that originate from the μ_B-dependence of the effective masses. These contributions vanish at $\mu_B = 0$, since $\partial m^*/\partial\mu_B|_{\mu_B=0} = 0$.
In the following we will describe the vector interaction through ω-selfinteractions $O(\omega)$ and a constant coupling g_ω. The vector selfenergy becomes $\Sigma^0 = g_\omega \omega$ and the correction factor reads $(1 - g_\omega \partial\omega/\partial\mu_B)$. We determine the derivative by taking the derivative of the selfconsistent equation (5.39),

$$\frac{\partial}{\partial \mu_B}\frac{\partial O}{\partial \omega} = \frac{\partial^2 O}{\partial \omega^2}\frac{\partial \omega}{\partial \mu_B} = \frac{\partial}{\partial \mu_B}\left(g_\omega \rho_B\right) = g_\omega \chi_B^{RMF}. \tag{5.50}$$

The interacting susceptibility follows then from the relation

$$\chi_B^{RMF} = \tilde{\chi}_B \cdot \left(1 - \frac{g_\omega^2}{\partial^2 O/\partial\omega^2|_{\omega=0}}\chi_B^{RMF}\right). \tag{5.51}$$

Solving the equation for χ_B^{RMF} and replacing the selfinteraction $O(\omega)$ with $O(g_\omega\omega)$ leads to the interacting susceptibility

$$\chi_B^{RMF} = \frac{\tilde{\chi}_B}{1 + \tilde{\chi}_B \cdot \left(O''(g_\omega\omega)|_{\omega=0}\right)^{-1}}. \tag{5.52}$$

This equation shows another way to constrain the vector repulsion for a fixed scalar interaction using lQCD predictions for the susceptibilities. The scalar interaction will increase χ_B compared to a non-interacting system and the vector interaction will suppress it. Both interactions have to be balanced to get a good description of the data. Fig. 5.15 shows χ_B/T^2 for the parameter set DD1 in comparison to the lQCD data from the Wuppertal-Budapest collaboration from Ref. [135], that we used in Sec. 3.2 to determine the parameters for the DQPM*, and the susceptibility for the set DD1 without the suppression effect of the repulsive interaction. We find that our interacting model can not describe the data. The pure scalar interaction overshoots the lQCD result, but the combination of both interactions underestimates it. The repulsive interaction is even so

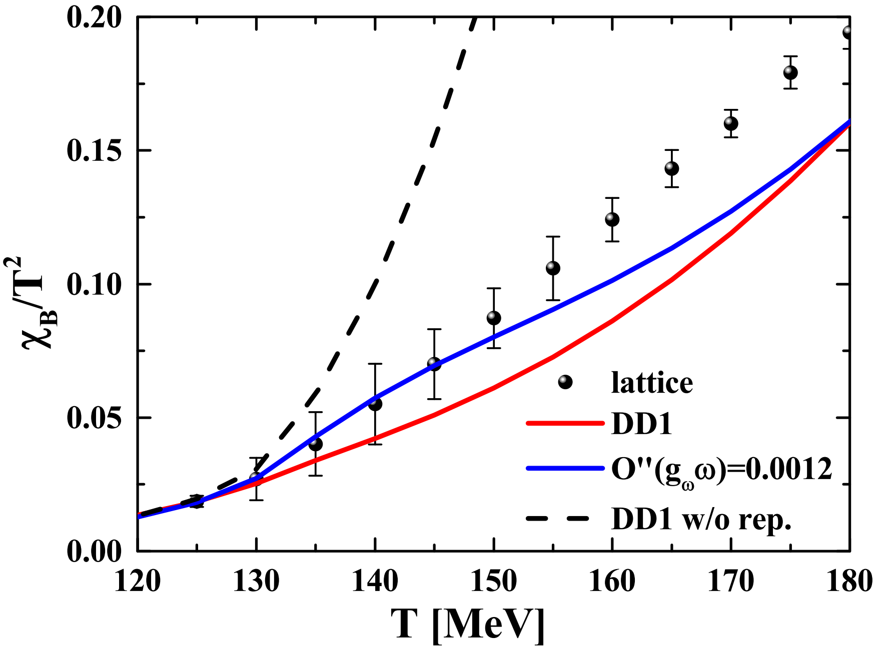

Figure 5.15: The baryon number susceptibility χ_B/T^2 as a function of the temperature T for vanishing baryon chemical potential. The red line is for the IHRG with the set DD1. The blue line is for the IHRG with the scalar interaction from the set DD1 with the repulsive interaction $O(g_\omega\omega) = 0.0006\ (g_\omega\omega)^2$. The dashed black line shows χ_B/T^2 for the set DD1 but without the vector repulsion. The lQCD results are taken from the Wuppertal-Budapest collaboration [135].

strong that the result for χ_B is below the non-interacting HRG. We have used the lQCD data to adjust the vector interaction at small densities and found the best results for $\partial^2 O/\partial(g_\omega\omega)^2|_{\omega=0} = 0.0012\ \text{GeV}^2$, shown by the blue solid line in Fig. 5.15. This ansatz is within the error bars of the data for all temperatures $T < 155$ MeV, but too small at higher temperatures. We have tried to combine the information from the susceptibilities with the nuclear equation of state and model the selfinteraction $O(g_\omega\omega)$ to reproduce both quantities, but unfortunately this is not possible in the current approach. The reason can be best explained by the first derivative of the selfinteraction $O(g_\omega\omega)$. We show in Fig. 5.16 $O'(g_\omega\omega)$ as a function of $g_\omega\omega$. The solid line is the selfinteraction necessary to describe the nuclear equation of state and the dashed line the functional $O'(g_\omega\omega) = 0.0012\ g_\omega\omega$, that gives the best result for the susceptibilities. The saturation density $\rho_0 \approx 0.16\ \text{fm}^{-3}$ is reached for $g_\omega\omega \approx 0.5$ GeV, which is slightly above the $g_\omega\omega$, where $O'(g_\omega\omega)$ for the nuclear equation of state exceeds the function $0.0012\ g_\omega\omega$. The strong rise at small ω, fixed by the susceptibilities, represents a small repulsive interaction, however, this repulsion is too weak to compensate the scalar attraction at small densities and will generate a very deep minimum in the binding energy at small densities $\rho_B \ll \rho_0$. We would still find $E_B/A(\rho_0 = 0.16\ \text{fm}^{-3}) = -16$ MeV, but it will not correspond to a minimum. It is necessary that the repulsion is strong at small

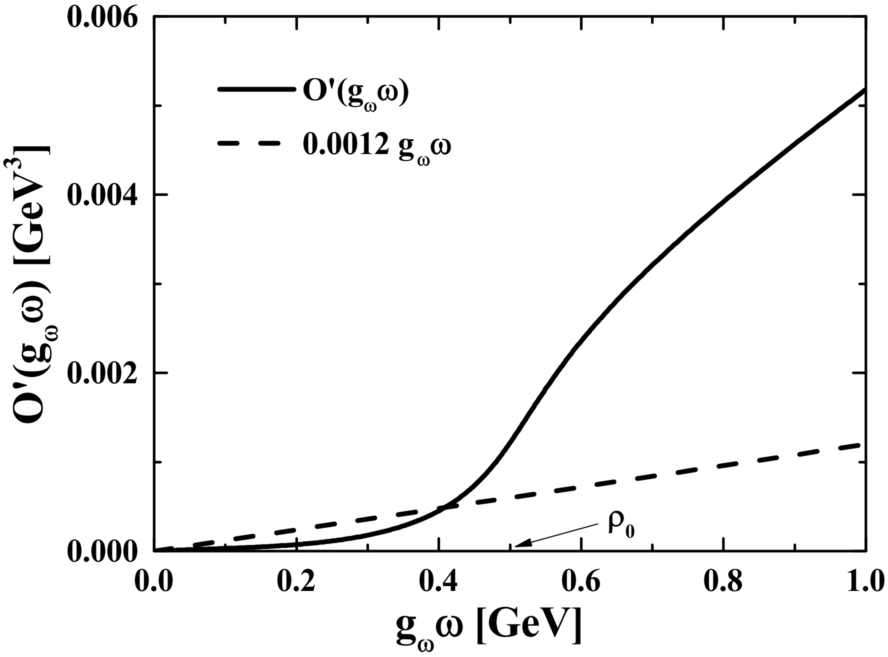

Figure 5.16: The derivative $\partial O(g_\omega \omega)/\partial(g_\omega \omega)$ of the selfinteraction of the ω-meson. The full line shows the result for the interaction needed to reproduce the nuclear equation of state for the parameter set ML2, the dashed line is for $O(g_\omega \omega) = 0.0006\ (g_\omega \omega)^2$. The arrow indicates the value of $g_\omega \omega$ at the saturation density ρ_0.

densities to assure the right minimum in the binding energy, but this is incompatible with the susceptibilities. The only way to achieve both is to decrease $O'(g_\omega \omega)$ after the initial rise, but this introduces an unphysical critical behavior since $O'(g_\omega \omega)$ would not be continuously rising. We will therefore keep $O(g_\omega \omega)$ fixed to the nuclear equation of state. The susceptibilities and the baryon density at larger temperatures and small chemical potentials may be too small, but the description for large chemical potentials and small temperatures is consistent with nuclear matter. This region of the phase diagram is more important for hadronic matter, while the former region is probed by partonic matter [321]. However, if one wants to investigate the region of small chemical potential with the IHRG, one should use the function $O(g_\omega \omega) = 0.0006\ (g_\omega \omega)^2$ for the repulsive interaction. This is sufficient for $\mu_B/T < 2$.

We did not show the susceptibility for the set DD2 where we included the Δ-resonances in the interaction. The reason is that the vector interaction is still too strong. The inclusion of the Δ's leads to a decrease of the scalar interaction, but the necessary repulsive interaction remains strong enough to completely suppress the contribution from both, nucleons and Δ's. The resulting susceptibility is even below the result for DD1.

5.4 Chiral condensate

The IHRG is, similar to the DQPM or DQPM*, a model that describes the equation of state for QCD matter, but can not resolve the complex phase structure of the QCD phase diagram. This can only be done if one has access to the Polyakov loop for confinement/deconfinement and the chiral condensate for chiral symmetry restoration. Both models can never describe the confinement/deconfinement transition, since the fundamental degrees of freedom are fixed to partons for the DQPM and hadrons for the IHRG. However, it is possible to connect the IHRG to the chiral condensate using low-energy theorems of QCD. We consider here only the light quark condensate $\langle \bar{q}q \rangle = \langle \bar{u}u \rangle + \langle \bar{d}d \rangle$ and neglect the strange quark condensate $\langle \bar{s}s \rangle$. Using the Hellmann-Feynman theorem [332, 333],

$$\frac{dE(\lambda)}{d\lambda} = \langle \psi_\lambda | \frac{\partial H(\lambda)}{\partial \lambda} | \psi_\lambda \rangle, \tag{5.53}$$

one can derive an equation for the low temperature and low density behavior of the chiral condensate [334, 335],

$$\frac{\langle \bar{q}q \rangle}{\langle \bar{q}q \rangle_0} = 1 - \frac{\sigma_{\pi N}}{f_\pi^2 m_\pi^2} \rho_s^N. \tag{5.54}$$

In (5.54) ρ_s^N is the scalar density of the nucleons, $m_\pi = 138$ MeV the pion mass, $f_\pi = 92.4$ MeV the pion decay constant [11] and $\sigma_{\pi N}$ the pion-nucleon σ-term. The chiral condensate will drop with the scalar density, but the strength is determined by the hadronic low-energy constants m_π, f_π and $\sigma_{\pi N}$. The value of the pion mass is known with high precision and also the value of the pion decay constant is determined with high accuracy from semileptonic pion decays. Unfortunately, this is not the case for $\sigma_{\pi N}$. The constant is related to the nucleon mass,

$$\sigma_{\pi N} = m \frac{\partial m_N(m)}{\partial m} \bigg|_{m=m_q}, \tag{5.55}$$

and measures the amount of mass, that originates from the explicit chiral symmetry breaking through the finite quark masses m_q. We choose $\sigma_{\pi N} = 45$ MeV which is roughly speaking the world average, see Appendix A.10.

The relation (5.54) is only applicable to nuclear matter ($T = 0$) where the system consists out of nucleons. We have to extend it to include additional hadrons if we want to employ the relation also at finite temperatures. The first generalization of Eq. (5.54) was given in Ref. [336], where it was used to study the evolution of the chiral condensate in heavy-ion collisions. The generalized formula reads

$$\frac{\langle \bar{q}q \rangle}{\langle \bar{q}q \rangle_0} = 1 - \frac{1}{f_\pi^2 m_\pi^2} \sum_h \sigma_h \rho_s^h, \tag{5.56}$$

---

[11] The definition of f_π is not unique. Some authors use an additional factor of $\sqrt{2}$. The Particle Data Group for example gives a value of $f_\pi = 127.13$ MeV [260], using this additional factor.

where ρ_s^h is the scalar density and σ_h the σ-commutator of the hadron species h. The relations (5.54) and (5.56) are model independent and only valid for dilute systems with negligible interactions [335]. But, as argued in Ref. [335], possible extensions are model dependent. To avoid this we will use the relations without further corrections even close to the phase boundary, where we expect strong interactions.

We will now demonstrate that Eq. (5.54) and (5.56) are consistent with the definition of the chiral condensate given by Eq. (A.62) in Appendix A.5. We will assume a hadronic system consisting of nucleons and pions. The definition of the chiral condensate is

$$\frac{\partial\Omega}{\partial m_q} = \langle\bar{q}q\rangle = \langle\bar{q}q\rangle_0 - \frac{\partial P}{\partial m_q} = \langle\bar{q}q\rangle_0 - \frac{\partial P}{\partial m_\pi^2}\frac{\partial m_\pi^2}{\partial m_q} - \frac{\partial P}{\partial M}\frac{\partial M}{\partial m_q}. \tag{5.57}$$

The pressure P corresponds only to the thermal part, the vacuum contribution gives rise to the vacuum condensate $\langle\bar{q}q\rangle_0$. We can evaluate the derivatives of the hadron masses with respect to the bare quark masses with the Gell-Mann-Oakes-Renner relation [337]

$$m_\pi^2 f_\pi^2 = -\frac{1}{2}(m_u + m_d)\langle\bar{q}q\rangle \tag{5.58}$$

and the definition of $\sigma_{\pi N}$ (5.55). This leads to the relation

$$\begin{aligned}\frac{\langle\bar{q}q\rangle}{\langle\bar{q}q\rangle_0} &= 1 - \frac{1}{\langle\bar{q}q\rangle_0}\left(\frac{\partial m_\pi^2}{\partial m_q}\frac{\partial P}{\partial m_\pi^2} + \frac{\partial M}{\partial m_q}\frac{\partial P}{\partial M}\right)\\ &= 1 + \frac{1}{f_\pi^2}\left(\frac{\partial P}{\partial m_\pi^2} + \frac{\sigma_{\pi N}}{m_\pi^2}\frac{\partial P}{\partial M}\right)\\ &= 1 - \frac{1}{2f_\pi^2 m_\pi}\rho_s^\pi - \frac{\sigma_{\pi N}}{m_\pi^2 f_\pi^2}\rho_s^N,\end{aligned} \tag{5.59}$$

which is equivalent to Eq. (5.56) for a system of pions and nucleons. The pion σ-commutator follows from the Gell-Mann-Oakes-Renner relation (5.58) leading to $\sigma_\pi = m_\pi/2$. The vacuum condensate follows also from Eq. (5.58) and is (for a light quark mass of $m_q = 7$ MeV) equal to $\langle\bar{q}q\rangle_0 = -3.2\ \mathrm{fm}^{-3}$. If one wants to generalize the formula to arbitrary hadrons, one has to know the corresponding σ-commutators. In Ref. [336] the commutator for arbitrary baryons was taken as

$$\sigma_h = \frac{Q_i}{Q_N}\sigma_{\pi N}, \tag{5.60}$$

where Q_i is the light-quark content of the baryon. This gives $\sigma_{\Lambda,\Sigma} = 30$ MeV and $\sigma_\Xi = 15$ MeV for the Λ, Σ and Ξ-commutator. The value for kaons, following the same logic, is $\sigma_K = \sigma_\pi/2 = m_\pi/4$.

Eqs. (5.54) and (5.56) may be model independent, but the scalar density is not an observable. This is unproblematic in nuclear matter where at low densities the scalar and the baryon density are equal and the chiral condensate is then controlled by the baryon density,

$$\frac{\langle\bar{q}q\rangle}{\langle\bar{q}q\rangle_0} \approx 1 - \frac{\sigma_{\pi N}}{m_\pi^2 f_\pi^2}\rho_B^N. \tag{5.61}$$

This relation was used in Ref. [336] to access the condensate in a completely model independent way in heavy-ion collisions, but the approximation can only be used in low-energy collisions. Heavy-ion collisions at RHIC or LHC create a very hot medium with an almost vanishing baryon density but large energy densities and the experiments at FAIR and NICA aim for the creation of a very dense medium that exceeds the validity of the low density approximation $\rho_s \approx \rho_B$. If one wants to determine the condensate in such a collision one has to determine the local scalar density. This can be done by means of relativistic mean-field theories as discussed in Refs. [147, 321]. Inserting the selfconsistent equation for the σ-field (A.94) into the relation for the chiral condensate (5.54) relates the condensate to the scalar interaction of the model,

$$\frac{\langle \bar{q}q \rangle}{\langle \bar{q}q \rangle_0} = 1 - \frac{\sigma_{\pi N}}{m_\pi^2 f_\pi^2} \frac{1}{\Gamma_\sigma} \frac{\partial U}{\partial \sigma}. \tag{5.62}$$

This procedure introduces a model dependence, but it will give access to the chiral condensate also in hot systems with vanishing net-baryon density and in heavy-ion collisions at higher energies.

We calculate the condensate with Eq. (5.62) for the parameter sets DD1, DD2 and ML2. These three parametrizations have all the same binding energy per nucleon, see Fig. 5.14, but use different scalar interactions $U(\sigma)$. We show the normalized condensate $\langle \bar{q}q \rangle / \langle \bar{q}q \rangle_0$ calculated for the nuclear equation of state in Fig. 5.17. We show also the condensate for the parameter sets NL1 and NL3, that have been used in Ref. [321] to investigate the influence of the equation of state on the restoration of chiral symmetry. All five models have the same behavior at small densities $\rho_B < 0.1$ fm^{-3}, which is due to the model independent low-density relation (5.61). The condensate for DD1 differs already at $\rho_B \approx 2/3\ \rho_0$ from this approximation, the other parametrizations fulfill it up to $\rho_B \approx 2\rho_0$. The set DD1 has the strongest scalar interaction and therefore the largest condensate. This may seem counter intuitive, but a stronger scalar interaction leads to a smaller effective mass m^*. This translates into a smaller scalar density and therefore to a larger condensate $\langle \bar{q}q \rangle / \langle \bar{q}q \rangle_0$. The condensate for DD2 is similar to the one for NL1, which has the weakest scalar interaction of the parameter sets shown and therefore the smallest condensate. The condensates for ML2 and NL3 are slightly larger than for DD2 and almost identical. This is expected since they have also similar effective masses as shown in Fig. 5.6. Relation (5.62) is also valid at finite temperature. We use the IHRG and calculate the scalar condensate for finite temperature and vanishing chemical potential. Fig. 5.18 shows the normalized condensate $\langle \bar{q}q \rangle / \langle \bar{q}q \rangle_0$ as a function of the temperature. The black dotted line is the contribution from non-interacting pions, which is a continuously decreasing function. It illustrates the contribution from any non-interacting hadron, since ρ_s is a continuously increasing function with temperature for constant masses. The pions are especially important since they give the dominant contribution at low temperatures where the interacting baryons give no contribution at all. This is due to the behavior of the effective masses, shown in Fig. 5.7. The normal baryon masses are too heavy which changes only at $T \approx 120$ MeV where the scalar interaction starts to affect the masses and decreases them. The scalar densities will then increase and therefore also the contribution of the baryons to the chiral condensate. If

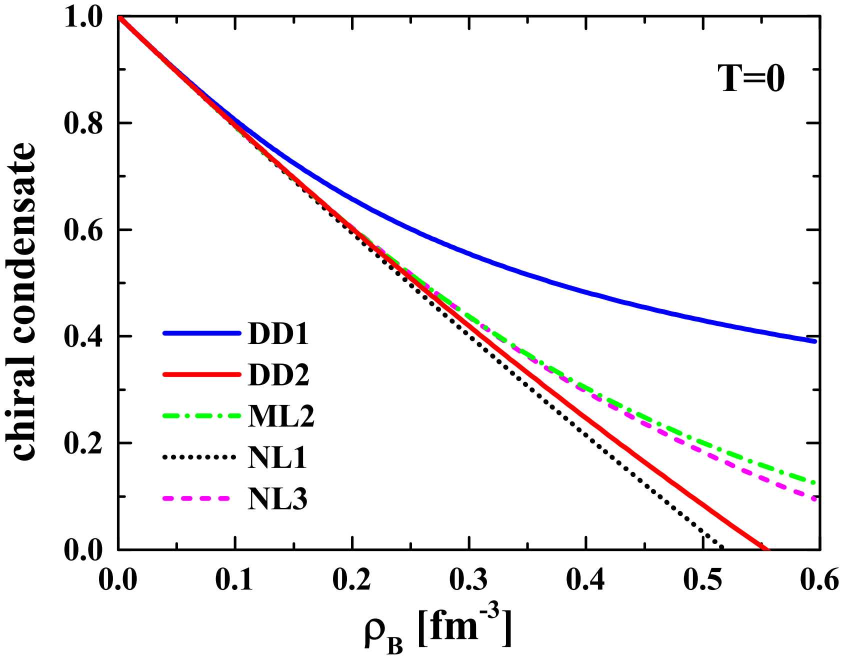

Figure 5.17: The chiral condensate $\langle\bar{q}q\rangle/\langle\bar{q}q\rangle_0$ in nuclear matter as a function of the nucleon density normalized to its vacuum value. The full blue line shows the condensate for the parameter set DD1, the full red line for the set DD2. The green dash-dotted line is the result for the set ML2. All three sets have the same equation of state. The black dotted line is the condensate for the set NL1 and the magenta dashed line for the set NL3.

one compares the results from DD1 and DD2 one should add the contribution from non-interacting Δ's in the set DD1 to get a reasonable comparison using the same degrees of freedom. However, the large Δ-mass suppresses the scalar density and the effect of the non-interacting Δ's becomes only visible for $T > 160$ MeV and can be neglected. We find then the same condensate for both sets up to temperatures of $T \approx 160$ MeV, which is the temperature range where we controlled the scalar interaction. At larger temperatures the normalized condensate for the set DD2 will drop much faster as for DD1 and will even become negative at $T \approx 180$ GeV [12]. This happens also for the set DD1, but at much larger temperatures, and even in nuclear matter at very large densities. The reason is that there is no mechanism that controls $\langle\bar{q}q\rangle/\langle\bar{q}q\rangle_0$ and keeps it positive. However, this effect occurs only at temperatures where we expect a partonic system rather than a hadronic and it is questionable if we can still apply the low-energy relations that we used to access the condensate.

We compare the normalized condensate also to lQCD results from the Wuppertal-Budapest collaboration taken from Ref. [38]. The lattice results show not the normalized

---

[12] The actual condensate $\langle\bar{q}q\rangle$ is negative and will become positive at this temperature.

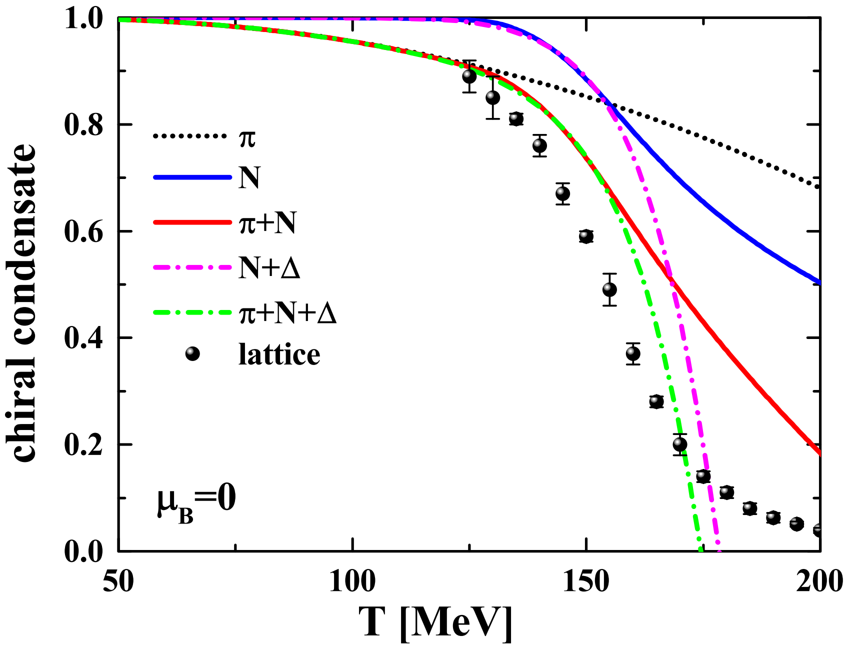

Figure 5.18: The normalized chiral condensate $\langle\bar{q}q\rangle/\langle\bar{q}q\rangle_0$ as a function of the temperature for vanishing chemical potential. The dotted black line shows the reduction of the condensate through non-interacting pions, the full blue line the reduction from the interacting nucleons and the full red line the sum of both contributions. The dash-dotted magenta line is the reduction from interacting nucleons and Δ-resonances and the dash-dotted green line from free pions, interacting nucleons and interacting Δ-resonances. The full lines are calculated with the parameter set DD1 and the dash-dotted lines with the set DD2. The black dots show the regularized condensate $\frac{\langle\bar{u}u\rangle-\frac{m_u}{m_s}\langle\bar{s}s\rangle}{\langle\bar{u}u\rangle_0-\frac{m_u}{m_s}\langle\bar{s}s\rangle_0}$ from the Wuppertal-Budapest collaboration [38].

condensate but the so called regularized condensate defined by

$$\Delta_{u,s} = \frac{\langle\bar{u}u\rangle - \frac{m_u}{m_s}\langle\bar{s}s\rangle}{\langle\bar{u}u\rangle_0 - \frac{m_u}{m_s}\langle\bar{s}s\rangle_0}. \tag{5.63}$$

The strange quark condensate has to be subtracted to regularize the expression, see Sec. 4.4, but is suppressed by the factor $\frac{m_u}{m_s} \approx \frac{1}{27}$ and gives only a small correction to the actual normalized condensate $\langle\bar{q}q\rangle/\langle\bar{q}q\rangle_0$. We find a similar qualitative behavior of both approaches, but the lQCD condensate decreases faster than the IHRG condensate. This is due to the other hadrons in the system that start to give noticeable contributions only near the phase transition, but were neglected in the IHRG condensate. We could include these hadrons but we stress again that the low-energy theorems used to access the condensate are not valid in the vicinity of the phase transition that takes place at $T_c \approx 155 - 160$ MeV for small μ_B.

5.5 Probing the chiral condensate in relativistic heavy-ion collisions

The chiral condensate is, unfortunately, not an observable. This makes it a challenging task to observe the effects of chiral symmetry restoration in an experiment. A possible signal is the effect on the spectral function of hadrons and their chiral partners, who should become equal if the symmetry is restored [51, 113, 338, 339]. Especially the ρ-meson would be very important in this context [114, 115] since the neutral ρ^0 can decay into an e^+e^- pair which leaves the hot and dense medium undisturbed. This makes it possible to measure the in-medium spectral function and any changes compared to the vacuum [340], but unfortunately one was not able to detect any effect of chiral symmetry restoration. The ρ-spectral function becomes broader, but this can be explained by in-medium effects [341, 342, 343]. A clear experimental signal of chiral symmetry restoration is still not discovered in dilepton spectra.

Another effect of the chiral condensate is its influence on the quarks. The chiral condensate determines in first order the effective quark masses,

$$m_q^* = m_q + (M_q - m_q)\frac{\langle\bar{q}q\rangle}{\langle\bar{q}q\rangle_0}, \tag{5.64}$$

$$m_s^* = m_s + (M_s - m_s)\frac{\langle\bar{q}q\rangle}{\langle\bar{q}q\rangle_0}. \tag{5.65}$$

This formula is similar to the effective masses in the NJL model, compare Eq. (4.3). The quark masses in the vacuum are equal to the constituent quark masses $M_q \approx 350$ MeV and $M_s \approx 500$ MeV and will decrease with the scalar condensate. For restored chiral symmetry, i.e. $\langle\bar{q}q\rangle \approx 0$, one recovers the current quark masses $m_q \approx 7$ MeV and $m_s \approx 100$ MeV.

It has been argued in Refs. [147, 321] that these medium-modified effective quark masses will alter the production probability of $s\bar{s}$ pairs from string breaking events and modify the hadron chemistry in a heavy-ion collision.

A string is an excited color-singlet state that is created in high-energy collisions between hadrons or in e^+e^- collision. Most of the initial scatterings in a heavy-ion collision will form such strings. This state consists of a color and an anticolor charge that interact via the color fields consisting of gluons which get pulled together through the gluonic selfinteractions. The field lines form a string that contains vacuum fluctuations and this can create and annihilate quark-antiquark pairs. If the energy is large enough, a real $q\bar{q}$ pair can be formed in a tunneling process, which will break the string into two parts with the newly formed $q\bar{q}$ pair at the ends of the new strings, see Fig. 5.19 for an illustration. This fragmentation will continue until the stored energy can not excite another $q\bar{q}$ pair. The string has then decayed into hadrons.

The $q\bar{q}$ pair created in a specific string breaking event can either be a pair of light quarks or a $s\bar{s}$ pair [13]. The creation of the heavier $s\bar{s}$ pair is suppressed by the factor γ_s, that

---

[13] At higher energies one has to include even charm and bottom quarks.

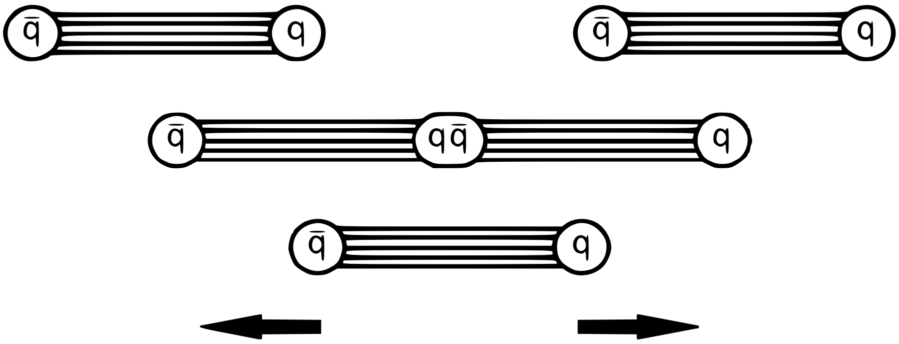

Figure 5.19: Illustration of a string breaking event. While the original $q\bar{q}$ pair moves apart from each other, an additional $q\bar{q}$ pair emerges from the vacuum breaking the original string into two new strings.

can be calculated from the Schwinger mechanism [344],

$$\frac{P(s\bar{s})}{P(u\bar{u})} = \frac{P(s\bar{s})}{P(d\bar{d})} = \gamma_s = \exp\left(-\pi\frac{m_s^2 - m_{u,d}^2}{2\kappa}\right). \tag{5.66}$$

The formula depends only on the string tension $\kappa \approx 0.176\ \mathrm{GeV}^2 \approx 0.9\ \mathrm{GeV/fm}$ and the effective quark masses. One finds, with the constituent quark masses M_q and M_s, a suppression factor of $\gamma_s \approx 0.3$ in the vacuum. This string fragmentation is the basis of the phenomenological LUND string model [345], which leads to a good description of the particle production in elementary high-energy collisions. This fragmentation is implemented in various event generators, most famous is the PYTHIA event generator [346].

The ansatz proposed in Refs. [147, 321] modifies the suppression factor inside the medium by replacing the constituent quark masses with the effective quark masses from Eq. (5.64) and (5.65). The suppression factor depends then, via the chiral condensate, on the medium. We have derived in the last section 5.4 several relations for the condensate. Especially important was Eq. (5.62), which relates the condensate to the scalar interaction of relativistic mean-field theories and enables the calculation of the condensate also for the extreme conditions in a heavy-ion collision. We have already discussed the condensate for finite temperature and chemical potential and will now use these results to determine the suppression factor. Fig. 5.20 shows γ_s in nuclear matter as a function of the energy density, the largest corresponds to $\rho_B \approx 3\rho_0$. The suppression factor shows a strong rise for all five parameter sets and has already increased up to $\gamma_s \approx 0.5$ at normal nuclear density. NL1 gives the largest suppression factor with $\gamma_s \approx 0.9$ for $\rho_B = 3\rho_0$ and DD1 the smallest with $\gamma_s \approx 0.6$. A stronger scalar interaction corresponds to a smaller γ_s. In the limit of a scalar interaction with infinite strength, one would find a constant γ_s, as assumed in the LUND string model. The results imply that the suppression factor will increase when the system becomes denser and/or hotter. This will affect the number of $s\bar{s}$ pairs created in the string fragmentation and enhance the production of strange hadrons in the hot and dense medium inside a heavy-ion collision.

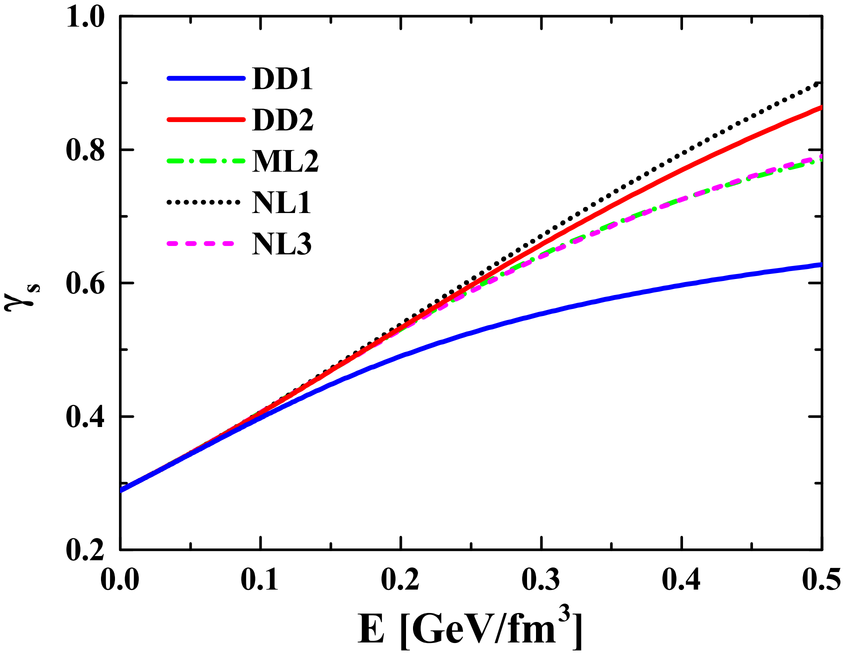

Figure 5.20: The strangeness suppression factor γ_s in nuclear matter as a function of the energy density. The full blue line shows γ_s for the parameter set DD1, the full red line for the set DD2. The green dash-dotted line is the result for the set ML2. The black dotted line is the condensate for the set NL1 and the magenta dashed line for the set NL3.

The rise of the suppression factor at already normal nuclear density suggests a sizable effect on the number of strange particles, which is an observable that can be measured in experiment. The discussed approach converts the effects of chiral symmetry restoration into an observable quantity.

The real influence of the medium-modified strangeness suppression factor can only be determined in heavy-ion simulations. We use the Parton-Hadron-String Dynamics approach (PHSD) for the simulations. PHSD is a microscopic covariant transport approach [144, 145], that is based on the Kadanoff-Baym equations going beyond the common Boltzmann transport description and allowing for off-shell transport [30]. The string fragmentation in PHSD is described by the FRITIOF event generator [347], that is also based on the LUND string model but is tuned towards energetic hadronic collisions [348]. We determine the local value of the scalar condensate and γ_s inside the collision and use them in the string fragmentation routines. This is done on a grid where we divide the volume into small cells and solve the selfconsistent equation for the σ-field (5.38) inside each of these cells. We refer to Ref. [147] for further details about the implementation of the approach and the simulations.

PHSD is a unique transport model that treats hadronic and partonic degrees of freedom in the same framework and dissolves and forms hadrons dynamically in the simulation. If the local energy density inside a cell is larger than a critical energy density

ϵ_c, the hadrons inside the cell will dissolve into quarks. Accordingly, the quarks are hadronizing, if the energy density is lower than ϵ_c. The critical energy density is taken as $\epsilon_c = 0.5$ GeV/fm^3, corresponding to the energy density at the QCD phase transition [91]. The transition from hadronic to partonic matter has serious consequences for the strangeness suppression factor since strings can only appear in confined matter. The string tension κ vanishes in a deconfined medium and the Schwinger mechanism and Eq. (5.66) are no longer valid. Strange quarks are no longer produced in string events, but through the decay of gluons, $g \to s\bar{s}$. The strangeness suppression factor in the partonic phase is therefore independent from the medium and drops to $\gamma_{s,QGP} \approx 1/3$, which is in line with experimental data on the strangeness production measured at RHIC and LHC energies [147]. This drop in γ_s for local energy densities $\epsilon > \epsilon_c$ is not an effect of chiral symmetry restoration, but of deconfinement. The partonic $\gamma_{s,QGP}$ is not sensitive to the effects of chiral symmetry restoration, since the symmetry is expected to be completely restored. The strangeness enhancement can only appear in collisions, where the system is predominantly in the hadronic phase, i.e. at small collision energies. This behavior is indeed reproduced by the simulations. The amount of strange particles is generally increased compared to simulations with a constant γ_s, but the effects are only visible at small center-of-mass energies $\sqrt{s_{NN}} < 20$ GeV. We show in Fig. 5.21 the rapidity distributions for central Au+Au collisions at beam energies of 10.7 AGeV and in Fig. 5.22 the rapidity distributions for central Pb+Pb collisions at beam energies of 30 AGeV for an impact parameter $b = 2.2$ fm. We present the rapidity spectra for protons, $(\Lambda + \Sigma^0)$'s, charged pions and kaons. The experimental data for the Au+Au collisions are taken from Refs. [349, 350, 351, 352, 353, 354] and for the Pb+Pb collisions from Refs. [355, 356, 357]. We have calculated the strangeness suppression factor with the five parametrizations NL1, NL3, ML2, DD1 and DD2, but we show only the results for NL1, NL3 and DD2. ML2 gives exactly the same result as NL3, since both parametrizations have almost the same scalar interaction and therefore identical γ_s, and DD1's γ_s is too low to be compatible with the experimental data. The scalar interaction of DD1 is too strong and can not produce enough additional $s\bar{s}$ pairs. We show additionally also the results without chiral symmetry restoration, i.e. $\gamma_s \approx 1/3$. The K^+ and the $\Lambda + \Sigma^0$ spectra are largely affected by chiral symmetry restoration and both show a clear enhancement through the modified γ_s by up to 30%. The K^- are also increased, but not as strong as the K^+. This asymmetry can be explained with the quark content of the kaons. The K^- contain a strange and the K^+ an antistrange quark. Both could also form baryons, respectively antibaryons, but the fireball at this small collision energies contains much more quarks than antiquarks. The antistrange quarks will primarily form mesons, while the strange quarks form both, mesons and baryons. The increased γ_s has also an effect on the light quark sector. An enhanced production of $s\bar{s}$ pairs implies a lower production of $u\bar{u}$ and $d\bar{d}$ pairs due to energy conservation. This can be seen in the spectra of the nonstrange hadrons. We find slightly less protons and pions than without chiral symmetry restoration. However, both, the increase of strange hadrons and the decrease of non-strange ones, is in line with the experimental measurements. The comparison of the spectra with the measured data shows a striking improvement through the modified γ_s.

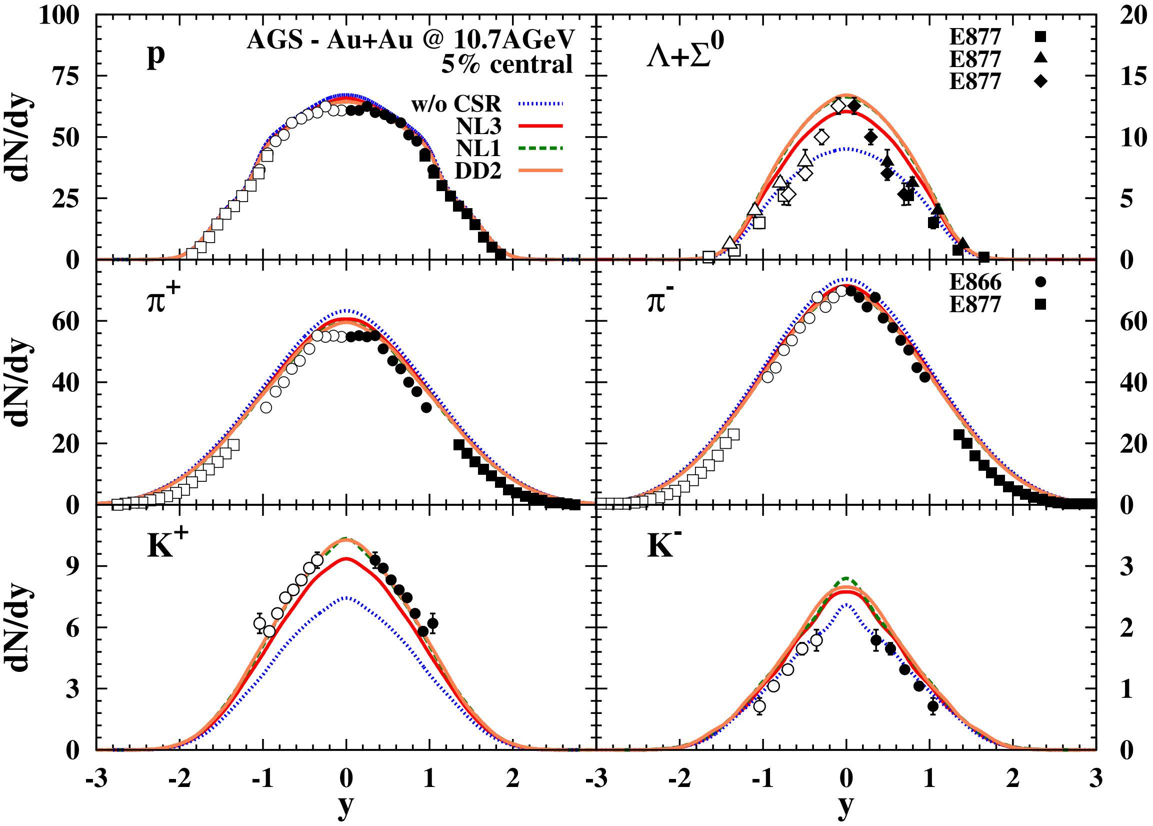

Figure 5.21: The rapidity distribution of protons, $(\Lambda + \Sigma^0)$'s, pions and kaons for 5% central Au+Au collisions at 10.7 AGeV in comparison to the experimental data from Refs. [349, 350, 351, 352, 353, 354]. The solid red lines show the results from PHSD including chiral symmetry restoration with the parameter set NL3, the dashed green lines with the set NL1 and the solid orange line with the set DD2. The blue dotted line shows the result without chiral symmetry restoration.

The strangeness enhancement becomes more pronounced if we look at the total amount of strange particles. We show in Fig. 5.23 the particle ratios K^+/π^+, K^-/π^-, $(\Lambda+\Sigma^0)/\pi$ and the yields of $(\Lambda + \Sigma^0)$ and Ξ^- at midrapidity for central Au+Au collisions as a function of the invariant energy $\sqrt{s_{NN}}$. The experimental data are taken from Refs. [354, 357, 358, 359, 360]. The solid red lines are the results for NL3 and the dashed green lines for NL1. The gray band highlights the area between these two curves and shows the uncertainty of the parametrization of the relativistic mean-field model. The results for DD2 are within this area. The ratios show the same behavior as the rapidity spectra. The K^+/π^+ and the $(\Lambda+\Sigma^0)/\pi$ ratios are strongly enhanced, as well as the two yields, the K^-/π^- ratio shows only minor changes. We find an overall improvement in the simulations with chiral symmetry restoration and are able to reproduce the measured data, which was not possible in earlier studies. Especially the results for the K^+/π^+ ratio are impressive. The peak in the data, called the "horn" [17], imposed a long stand-

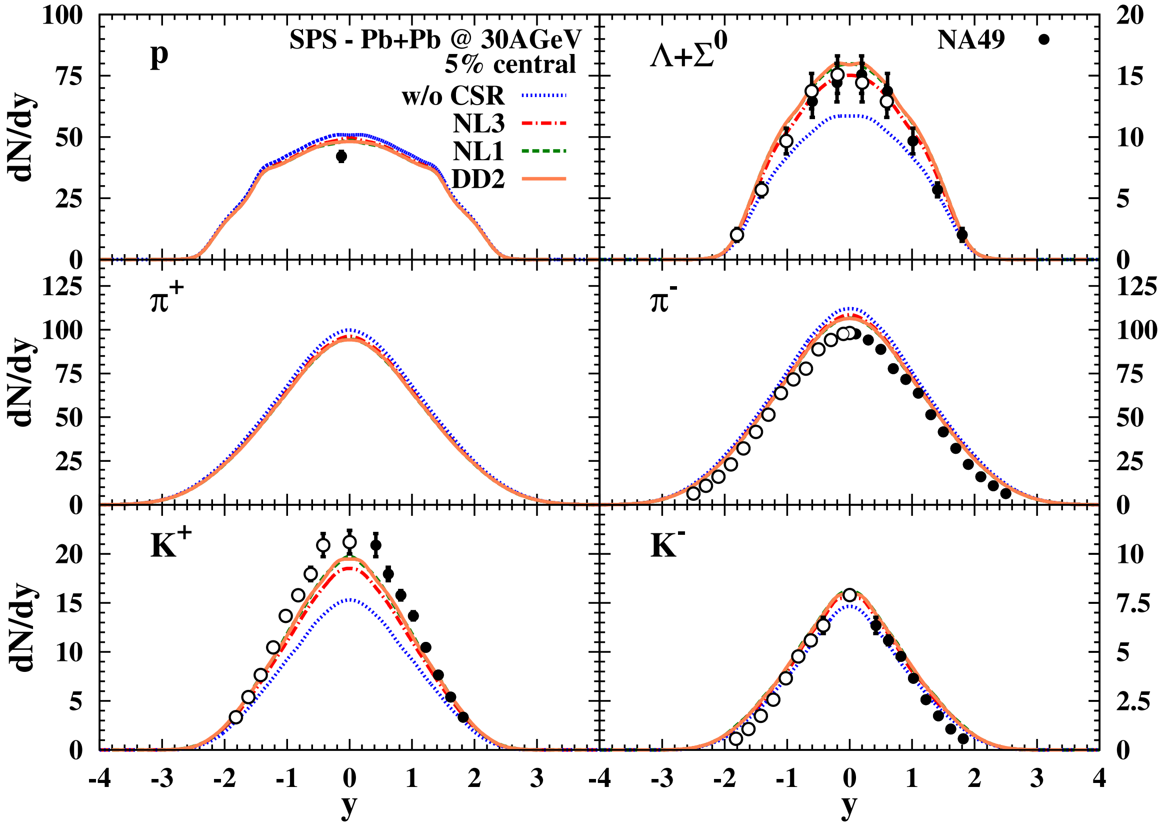

Figure 5.22: The rapidity distribution of protons, $(\Lambda + \Sigma^0)$'s, pions and kaons for 5% central Pb+Pb collisions at 30 AGeV in comparison to the experimental data from Refs. [355, 356, 357]. The solid red lines show the results from PHSD including chiral symmetry restoration with the parameter set NL3, the dashed green lines with the set NL1 and the solid orange line with the set DD2. The blue dotted line shows the result without chiral symmetry restoration.

ing puzzle, as it was not possible to reproduce this structure in a microscopic theory. The enhancement of strange hadrons in heavy-ion collisions compared to $p+p$ collisions was usually seen as a sign of the formation of a QGP [15, 16], while in our approach it originates from the restoration of chiral symmetry and an increasing γ_s compared to the vacuum. The formation of quarks and gluons will even suppress the strangeness enhancement, as found by a comparison between PHSD simulations with and without a partonic phase in Ref. [147], since the strangeness production in the partonic phase is suppressed compared to a hadronic medium with fully restored chiral symmetry. The effects of chiral symmetry restoration are most pronounced for $\sqrt{s_{NN}} \approx 2-12$ GeV. Collisions at lower beam energies can not create the necessary energy densities for the effect, while the energy densities at larger collision energies exceed the critical energy density and the dynamics of the system are dominated by the partonic phase. This explains the convergence of the results with chiral symmetry restoration against the

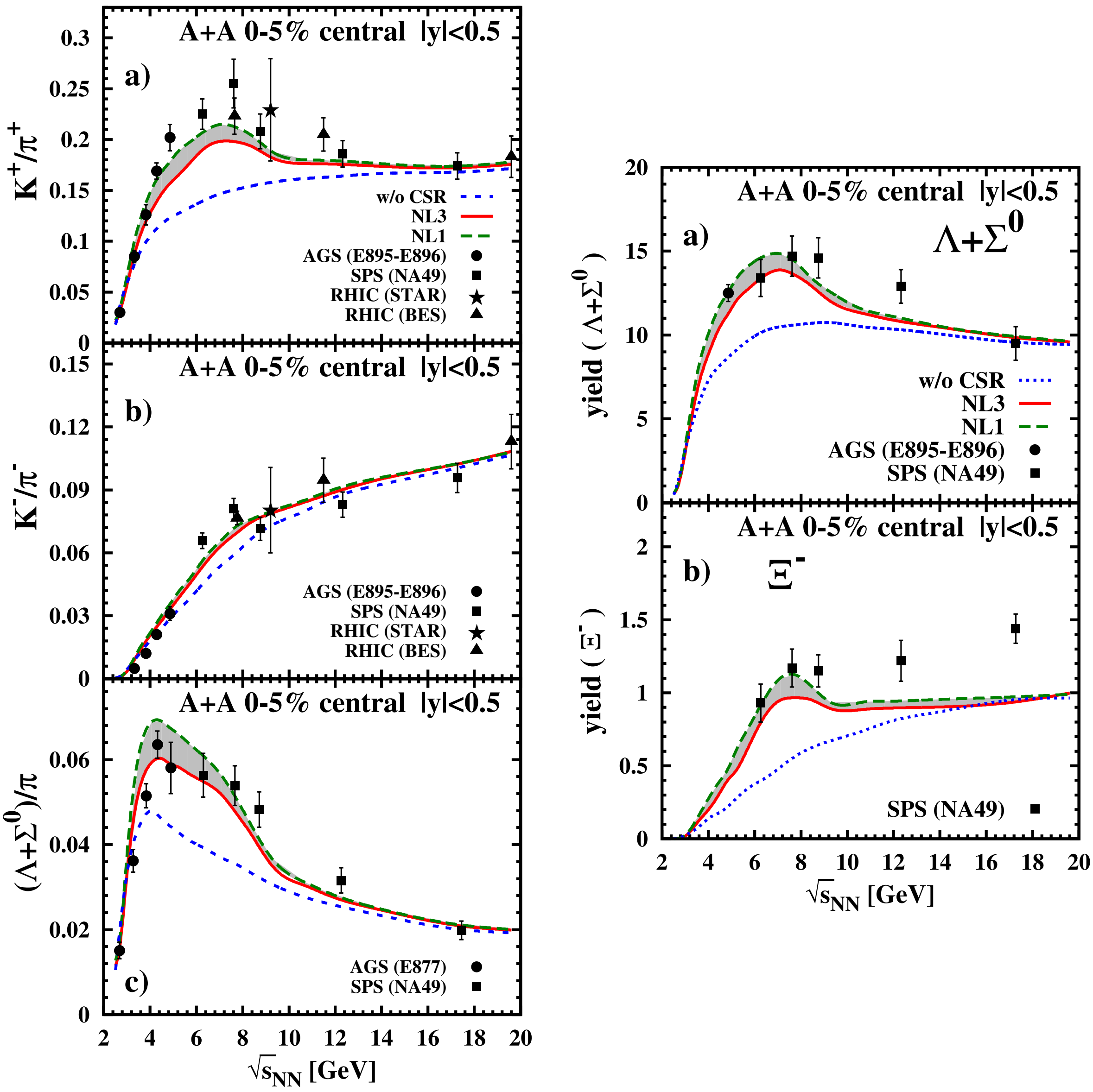

Figure 5.23: The ratios K^+/π^+, K^-/π^-, $(\Lambda + \Sigma^0)/\pi$ (left) and the yields of $(\Lambda + \Sigma^0)$ and Ξ^- (right) at midrapidity from 5% central Au+Au collisions as a function of the invariant energy $\sqrt{s_{NN}}$ up to the top SPS energy in comparison to the experimental data from Refs. [354, 357, 358, 359, 360]. The solid red lines show the results from PHSD including chiral symmetry restoration with the parameter set NL3 and the dashed green lines with the set NL1. The blue dotted line shows the result without chiral symmetry restoration. The grey shaded area represents the uncertainty from the parameters of the relativistic mean-field theory for the scalar interaction. The figures are taken from Ref. [321].

ones without at larger $\sqrt{s_{NN}}$, as seen in Fig. 5.23. The horn emerges only through the combined effects of chiral symmetry restoration and deconfinement. This allows it for the first time to describe the maximum in the K^+/π^+ ratio in a microscopic transport approach.

The results for the rapidity spectra and the ratios show that it was indeed justified to include the Δ-resonances as interacting particles in the IHRG. The amount of additional created strange hadrons depends directly on the scalar interaction and allows to test it against physical observables. The scalar interaction of DD1 is too strong while the interactions of NL1, NL3, ML2 and DD2 have the right strength to reproduce the experimental data. This imposes an upper limit on the scalar interaction of the relativistic mean-field theories, that requires in case of the IHRG the inclusion of additional hadrons beyond the nucleons.

Both, the set DD1 with only interacting nucleons and the set DD2 with interacting nucleons and Δ's can describe the nuclear and the lQCD equation of state. The comparison of the lQCD susceptibilities with the predictions from both sets indicates, that one should not include the Δ's, but they were important to adjust the scalar interaction to the right strength to describe the experimental observed rapidity spectra and particle ratios. We hope to solve this problem by including even more baryons. This will additionally weaken the scalar interaction and therefore also the necessary repulsive interaction, that has to decrease in order to describe the susceptibilities. We can then fix the scalar interaction with the lQCD equation of state, where it is important that we describe the equation of state up to the inflection point of the dimensionless pressure P/T^4 and energy density E/T^4 to get the correct behavior for the speed of sound, control it with the rapidity spectra and fix the repulsive interaction with the nuclear equation of state and control it with the lQCD susceptibilities.

6 The QCD phase boundary

QCD incorporates a change in the degrees of freedom at large energy densities. The quarks, normally confined into hadrons, become liberated. So far we discussed thermodynamic models that describe the equation of state in either the hadronic or the partonic phase, but not in both. In this section we want to study the transition between the two phases.

6.1 A universal hadronization condition

At low temperatures and chemical potentials QCD matter is composed of hadrons, but as the medium becomes hotter and denser the hadrons dissolve and a QGP forms. The transition between these two phases at vanishing chemical potential can be investigated by lQCD methods and was found to be a rapid crossover [35, 36]. The location of the transition is marked by the critical temperature T_c of the inflection point of the order parameter. In the vicinity of T_c one expects a mixed phase composed of hadronic and partonic degrees of freedom.

With the DQPM/DQPM* and the IHRG we have presented models that can reproduce the QCD equation of state at vanishing chemical potential as predicted by lQCD. The IHRG uses hadronic degrees of freedom and describes the equation of state at temperatures below the critical temperature T_c, the quasiparticle models use partonic degrees of freedom and describe the equation of state above T_c. However, it is not possible to extend the models towards the whole temperature axis without using unphysical assumptions. In order to describe the QCD equation of state we have to employ both models and switch between them in the vicinity of the critical temperature.

If the same system can exist in different phases, nature will choose the phase that minimizes the corresponding thermodynamic potential as the physical solution. By calculating QCD thermodynamics in a purely partonic and a purely hadronic medium, one will find the physical solution as the one with the largest pressure. Unfortunately, this approach has several shortcomings. A transition constructed in this manner will always lead to a first-order phase transition [361], see Fig. 6.1 for an illustration, but lQCD calculations revealed that the QCD phase transition should be a crossover. Furthermore, this procedure would lead to a stable hadronic phase at very large temperatures. The reason is the varying number of degrees of freedom in both phases. The total degeneracy factor of the most important hadrons summarized in Tab. A.1 and A.2 in Appendix

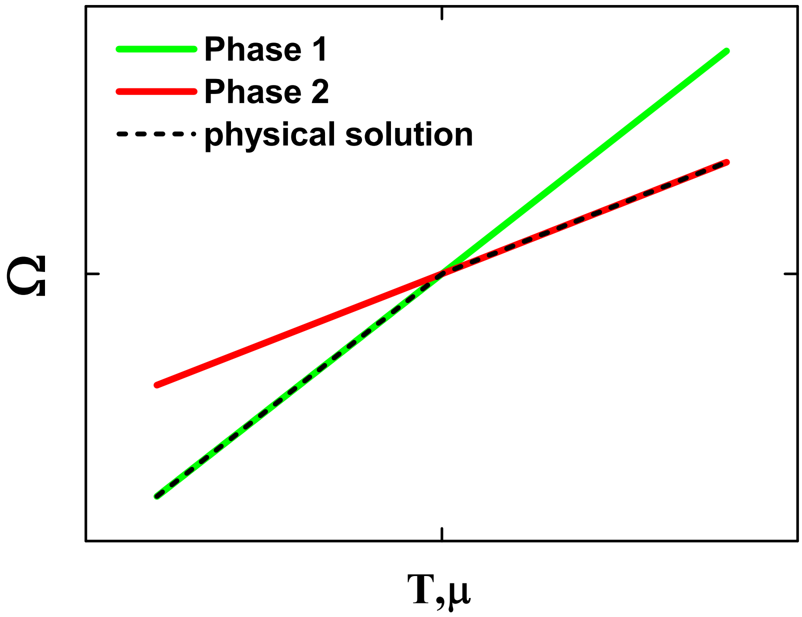

Figure 6.1: Illustration of a first-order phase transition in a grand-canonical system. The red and the green line are different realizations of the same system. The physical solution, indicated by the dashed black line, is the solution that minimizes the grand-canonical potential Ω. It switches from one phase to the other at the intersection of the thermodynamic potentials as function of the natural variables T and μ.

A.7 is 103, but for quarks and gluons we find only a total degeneracy of 52. A HRG at large temperatures will exceed the Stefan-Boltzmann limit of QCD and become the thermodynamically stable phase [362]. This would also happen in the IHRG, where we employ a total of 112 different hadronic degrees of freedom. Only models with large repulsive interactions at vanishing chemical potential -like excluded volume HRG models- can avoid this scenario. The rise of the thermodynamic pressure is suppressed by the excluded volume that limits the amount of particles in the system. It has been shown in Refs. [287, 288, 362] that in such a model the partonic phase is stable at large temperatures.

The transition from hadronic to partonic degrees of freedom can not be explained by thermodynamic arguments alone. It is connected to a fundamental property of QCD, the confinement/deconfinement transition. The IHRG describes always a confined and the DQPM always a deconfined system and the switching between the models has to be associated with the deconfinement phase transition. The expectation value of the Polyakov loop, that we discussed in Sec. 4.2 in terms of the effective Polyakov extended Nambu Jona-Lasinio model (PNJL), serves as an order parameter of this transition [117, 118]. However, we can neither access the Polyakov loop in the DQPM nor in the IHRG and are therefore unable to determine the deconfinement phase transition. Since we can not rely on the proper order parameter we have to define the transition in another way. We have already discussed how to locate a crossover transition from the equation of state in Sec. 4, but the precise location can not be determined. An interesting ansatz for this problem was proposed in Refs. [163, 363, 364]. One defines the pressure of the system as a mixture between a pure hadronic pressure P_h and a pure partonic pressure P_p,

$$P(T, \mu_B) = \phi(T, \mu_B)\ P_p(T, \mu_B) + (1 - \phi(T, \mu_B))P_h(T, \mu_B), \tag{6.1}$$

and interpolates the equation of state between the two phases using the switching function $\phi(T, \mu_B)$ with $\phi(T, \mu_B) = 0$ in the pure hadronic, $\phi(T, \mu_B) = 1$ in the pure partonic and $0 < \phi(T, \mu_B) < 1$ in the mixed phase. The functional form of $\phi(T, \mu_B)$ will be determined by a fit to the lQCD equation of state. A similar ansatz was used in Refs. [365, 366], but the switching function was introduced on the level of the entropy density. Using the ansatz (6.1) with the IHRG and the DQPM leads to an equation of state that is defined at all temperatures. However, we have already used lQCD data to determine the equation of state of our thermodynamic models and included the effects of the phase transition implicitly in the two approaches. Their accuracy is so good, that we can use a step function $\phi(T, \mu_B = 0) = \Theta(T - T_\phi)$ with $T_\phi \approx 150 - 170$ MeV. The transition -defined this way- looks like a first-order phase transition, but the equation of state stays indeed continuous.

It is possible to determine the QCD phase transition at vanishing chemical potential, but this is no longer the case at finite μ_B. Since one is lacking any guidance from lQCD calculations, it is not possible to determine the switching function from first principles. The form of $\phi(T, \mu_B)$ at $\mu_B \neq 0$ is therefore model dependent. We will use the ansatz

$$\phi(T, \mu_B) = \Theta(T - T_\phi(\mu_B)) \tag{6.2}$$

with $T_\phi(0) = T_c$. We choose T_ϕ such that the hadron-parton transition occurs at a constant energy density or pressure. This claim is in line with phenomenological models applied in different regions of the T-μ_B plane:

Heavy-ion simulations at ultra-relativistic collision energies need to incorporate the effects of the partonic phase to describe the experimental measured data. So called hybrid models use relativistic hydrodynamics to describe the evolution of the partonic medium and switch to a hadronic transport description once the system becomes too dilute to apply hydrodynamics [32, 33, 34, 367]. The switching from hydrodynamics to hadronic transport does not mark the hadron-parton transition, but the further evolution of the system is purely hadronic. If the transition is done too early, one has the wrong dynamics and can not describe the experimental results. Models applied at RHIC and LHC energies probe the transition at almost vanishing chemical potentials and use a constant switching temperature [367]. Models applied to FAIR and NICA energies have to describe the medium at a finite baryon chemical potential. These approaches use a constant energy density for the transition [368, 369]. This is similar to PHSD where one switches from a hadronic to a partonic transport description at a critical energy density $\epsilon_c \approx 0.5$ GeV/fm^3. PHSD can reproduce heavy-ion data for a wide range of different beam energies from top RHIC and LHC down to SPS and AGS energies [21, 146, 370, 371, 372, 373, 374]. The most important evidence for the correct transition condition in PHSD can be seen in the K^+/π^+ ratio that we discussed in Sec. 5.5, see Fig. 5.23. The ratio shows a peak at $\sqrt{s} \approx 6 - 8$ GeV. The increase of the ratio at small energies is associated to an enhanced production of strange quarks that occurs only in the hadronic phase. When the medium dissolves into quarks the effects of the strangeness enhancement become less pronounced and the ratio decreases. The position of the peak is therefore sensitive to the hadron-parton transition and the agreement between our predictions and the measured data confirms the correct occurrence of the transition. Further evidence was found in a statistical analysis of heavy-ion collisions. In Refs. [375, 376] heavy-ion collisions are studied within the statistical hadronization model, which determines the temperature and the chemical potential of the fireball at the chemical freezeout. The authors investigated a wide range of beam energies ranging from SPS to RHIC and LHC energies, but the freezeout occurred always at the same pressure $P \approx 82$ MeV and energy density $E \approx 0.5$ GeV/fm^3. Comparing the pressure and the energy density to the lQCD equation of state from Refs. [90] and [91] leads to a transition temperature of $T \approx 162$ MeV. The hadron-parton transition is also important for neutron star physics. The discovery of two-solar-mass neutron stars put new constraints on the equation of state at zero temperature. The authors of Refs. [363, 377] could describe two-solar-mass neutron stars with a crossover equation of state where the transition occurs at roughly three times normal nuclear density. This corresponds to an energy density of $E \approx 3\rho_0 \cdot m_n \approx 0.5$ GeV/fm^3. One can not compare the situation inside a neutron star to the medium in a heavy-ion collision since neutron stars are also effected by the weak interaction, but we find indeed a transition condition similar to heavy-ion collisions.

The hadron-parton transition can not be observed directly and the discussed transition conditions are all based on phenomenology and therefore model-dependent. However, the application range of the discussed models covers almost the whole T-μ_B plane even down to the $T = 0$ axis. It is striking that one finds similar arguments throughout the whole phase diagram. All these models support a hadron-parton transition at a constant energy density.

6.2 The phase boundary between the DQPM* and the IHRG

Based on the evidence from heavy-ion phenomenology we use a constant energy density to define the hadron-parton transition. From the phenomenological assumptions the best choice for the critical energy density seems to be $\epsilon_c \approx 0.5$ GeV/fm^3. However, there is a discrepancy between phenomenology and lQCD predictions. The QCD phase transition was studied in Refs. [36, 37, 38, 39] using lQCD. The transition temperature in these calculations is based on the proper order parameters, the chiral condensate and the Polyakov loop, and one finds a critical temperature of $T_c \approx 155$ MeV. Comparing this temperature to the freezeout line determined from heavy-ion collisions one finds that the freezeout would occur above the critical temperature in the deconfined phase [378, 379, 380]. This inconsistency can be partially explained by the different nature of the medium in a heavy-ion collision and a lattice simulation. Lattice simulations will always describe a system in thermodynamic equilibrium, but the medium in a heavy-ion collision is out-of equilibrium. The success of hydrodynamics suggests a certain degree of equilibration throughout the evolution of the collision, but the lifetime of the fireball is simply too short to achieve a full thermodynamic equilibration. Moreover, in heavy-ion collisions the energy, the baryon number, the total charge and the net strangeness are conserved. Thermodynamically this describes a microcanonical system. The thermodynamic potential of a microcanonical ensemble is the energy density [14] and the hadron-parton transition is therefore associated with a constant value of the thermodynamic potential. If we investigate the transition in a grand-canonical system, it is more plausible that the transition is related to fixed values of the grand-canonical potential, i.e. to constant values of the pressure.

The phenomenological models can only determine the transition for the microcanonical system, so we use the DQPM to relate the transition condition from the microcanonical system to the grand-canonical one. The DQPM discussed in Sec. 3 describes a grand-canonical, the DQPM employed in the PHSD transport approach a microcanonical ensemble, but both realizations are based on the same theory. The dynamical equilibrium state in the PHSD simulations is slightly different from the static equilibrium. This is mostly due to differences in the gluon spectral function in the dynamical simulations [141]. The differences become negligible at large temperatures, but lead to small changes in the equation of state in the vicinity of the phase transition. In the dynamical simulations the critical energy density $\epsilon_c = 0.5$ GeV/fm^3 is reached at a temperature $T \approx 158$ MeV. The static DQPM, that reproduces the lQCD equation of state, has an energy density of $E \approx 0.4$ GeV/fm^3 at this temperature. We define $T_c = 158$ MeV as the critical temperature, such that the transition condition in the microcanonical ensemble is associated with T_c. This fixes the critical energy density for the grand-canonical treatment to $\epsilon_c \approx 0.4$ GeV/fm^3 and the critical pressure to $P_c \approx 63$ MeV/fm^3.

We calculate the lines of constant pressure and energy density for the IHRG and the DQPM* throughout the T-μ_B plane. In case of the IHRG this is straight forward, but we need some adjustments for the DQPM*. We have to use the flow equation (3.43) -introduced in Sec. 3.3- to extend the model to finite chemical potential. The equation requires the effective coupling at vanishing chemical potential as starting values. However, at the low temperatures necessary for this investigation, the DQPM* coupling can not exactly reproduce the lQCD equation of state. This will shift the transition lines compared to the IHRG. Instead of using the standard parametrization of the coupling we will fit it to exactly reproduce the lQCD equation of state and use this coupling as the starting values for the flow equation. In this way we can ensure that the transition condition in the DQPM* and the IHRG are met at the critical temperature $T_c = 158$ MeV at vanishing baryon chemical potential.

---

[14] The real thermodynamic potential of a microcanonical ensemble is the entropy density. However, the entropy density is an entropic thermodynamic potential, that has the dimension of an inverse volume. The canonical and the grand-canonical potentials are energy potentials that have the dimension of an energy density. The energy potential corresponding to the microcanonical ensemble is the energy density.

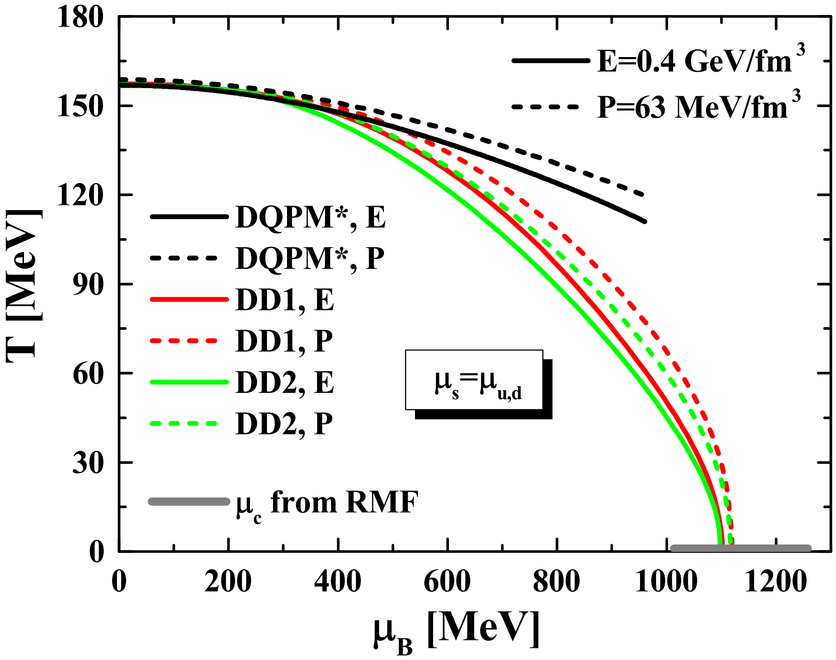

Figure 6.2: Lines of constant pressure and energy density from the DQPM* and the IHRG in the T-μ_B plane. Full lines indicate a constant energy density $E = 0.4$ GeV/fm^3 and dashed lines a constant pressure $P = 63$ MeV/fm^3. Lines of the same color belong to the same model. DD1 is the IHRG with only interacting nucleons and DD2 the IHRG with interacting nucleons and Δ-resonances. The grey line indicates the possible location of the parton-hadron transition at zero temperature for relativistic mean-field theories with different repulsive interactions.

We show the phase boundaries defined by a constant pressure or energy density in Fig. 6.2. Full lines are transitions defined by the energy density and dashed lines defined by the pressure. Both methods give similar results but the lines of constant pressure reach further out into the T-μ_B plane. The IHRG intersects the $T = 0$ axis at $\mu_B = 1100$ MeV for lines of constant energy density and at $\mu_B = 1120$ MeV for the lines of constant pressure. The two different parametrizations, DD1 and DD2, lead to slightly different transitions at $T \neq 0 \neq \mu_B$ with the boundaries of DD1, which uses only nucleons as interacting particles, reaching slightly further into the T-μ_B plane than the boundaries of DD2 that uses additionally the Δ-resonances. However, the different transitions of the IHRG agree close to the axis of the T-μ_B plane and cover almost the same area in the phase diagram.
A large uncertainty in the phase boundaries stems from the transition at low temperatures and large baryon chemical potentials. The nuclear equation of state is known only as a function of the density ρ_B, but not of the chemical potential μ_B. The strength of the repulsive interaction between the nucleons has a large influence on μ_B. The thermodynamics are defined by an effective baryon chemical potential, that gets shifted by the

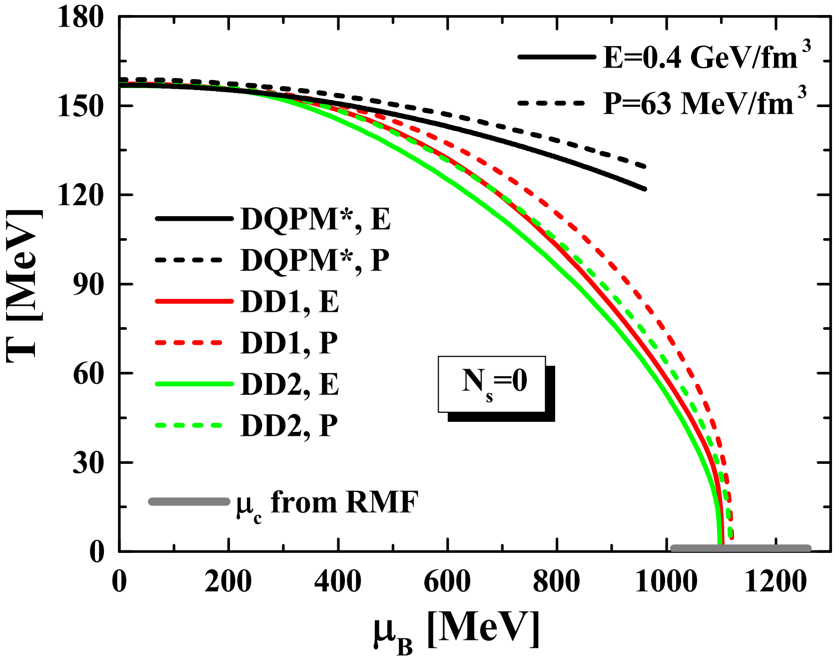

Figure 6.3: Lines of constant pressure and energy density for a strangeness neutral system from the DQPM* and the IHRG in the T-μ_B plane. Full lines indicate a constant energy density $E = 0.4$ GeV/fm^3 and dashed lines a constant pressure $P = 63$ MeV/fm^3. Lines of the same color belong to the same model. DD1 is the IHRG with only interacting nucleons and DD2 the IHRG with interacting nucleons and Δ-resonances. The grey line indicates the possible location of the parton-hadron transition at zero temperature for relativistic mean-field theories with different repulsive interactions.

vector selfenergy,

$$\mu_B^* = \mu_B - \Sigma_B^0(T, \rho_N). \tag{6.3}$$

Models with different interactions can reproduce the same nuclear equation of state as a function of density ρ_B, but for different chemical potentials, see Sec. 5.2. The grey band at $T = 0$ indicates the possible location of the transition as a function of the baryon chemical potential. The lowest chemical potential is the estimate for a gas of non-interacting nucleons, the largest for the parameter set NL3 from Ref. [312], that has the strongest repulsive interaction consistent with the nuclear equation of state.

An important constraint for heavy-ion collisions is strangeness neutrality. Since we did not constrain the strange sector in Fig. 6.2, we have a finite strangeness $N_S > 0$ in the phase diagram. We show in Fig. 6.3 the phase boundaries for a strange neutral medium with the same transition conditions as in Fig. 6.2. Both figures are almost identical, since we have the same amount of strange and antistrange particles at $\mu_B = 0$ and no strange particles at all at $T = 0$. These regions of the phase diagram are always strange neutral and agree in both figures. At $T \neq 0 \neq \mu_B$ we see that the phase boundaries for a strange neutral medium are shifted further into the T-μ_B plane because strangeness neutrality reduces the amount of particles in the strange sector compared to an unconstrained system. This lowers the energy density and the pressure and one needs larger temperatures and baryon chemical potential to reach the same energy densities and pressures as in an unconstrained medium.

We show in Figs. 6.2 and 6.3 also the transitions for the DQPM*. At small baryon chemical potential both models give comparable results, independent of the definition of the transition. In this area of the phase diagram we can indeed define a proper phase boundary between the two models. This changes at larger μ_B. The equation of state of the IHRG increases stronger than the DQPM* and the transition lines split up. We can no longer switch between both models without changing the temperature and the baryon chemical potential and the transition would become a true first-order phase transition. The splitting of the boundaries should not be associated with a critical end point of the QCD phase diagram. Instead they are a result of different constraints for both models at finite baryon chemical potential.

6.3 Partonic quasiparticle models at low temperatures

The splitting of the phase boundaries at large baryon chemical potential prevents us from defining a proper crossover transition between the DQPM* and the IHRG. The phase boundaries between the models agrees only close to the $\mu_B = 0$ axis, where we constrained the equation of state by lQCD data. The IHRG tends much faster towards the $T = 0$ axis than the DQPM* because we force the IHRG to reproduce the nuclear equation of state. On the other side the DQPM and the DQPM* are completely unconstrained at finite chemical potential. We now want to modify our quasiparticle model such that the phase boundary agrees with the IHRG also at larger baryon chemical potentials.

For this we define the phase boundary by a constant pressure $P_c = 63$ MeV/fm^3 and use the equation of state from the IHRG with interacting nucleons, DD1, which gives a slightly better description of the equation of state at vanishing chemical potential than the DD2-IHRG. To match the situation in heavy-ion collisions we enforce strangeness neutrality.

The pressure of the DQPM* is too low to describe the phase boundary defined by the IHRG. To increase the pressure at finite baryon chemical potential a larger baryon number density is required which depends predominantly on the effective quark masses. In the standard DQPM/DQPM* they decrease moderately as a function of the baryon chemical potential, but to match the phase boundary of the IHRG, the masses have to decrease even stronger. This will enhance the density and therefore push the phase boundary closer to the IHRG.

We modify only the μ_B-dependence of the effective light quark mass and keep the standard parametrization of the gluon and the strange quark masses. We use not the full DQPM* but a reduced version. Since the effects of the finite widths are most important for the transport coefficients, but negligible for the equation of state, see Fig. A.2 in Appendix A.2, we neglect them in this exploratory study and control the equation of state with just the effective masses. Furthermore, we drop also the momentum dependence of the selfenergies which is most important at large temperatures. Close to the phase transition the DQPM can describe the lQCD susceptibility as well as the DQPM*, see Fig. 3.10. We take the masses as

$$M_g^2\left(T\right) = \frac{g^2}{6}\left(\left(N_c + \frac{1}{2}N_f\right)T^2 + \frac{N_c}{2}\sum_q \frac{\mu_q^2}{\pi^2}\right), \tag{6.4}$$

$$M_{s,\bar{s}}^2\left(T\right) = \frac{N_c^2-1}{8N_c}g^2\left(T^2 + \frac{\mu_s^2}{\pi^2}\right), \tag{6.5}$$

$$M_{q,\bar{q}}^2\left(T\right) = \frac{N_c^2-1}{8N_c}g^2\left(T^2 + \frac{\mu_q^2}{\pi^2}\right)\cdot F(\mu_q). \tag{6.6}$$

where the light quark mass is modified by the factor $F(\mu_q)$ that controls the mass at finite baryon chemical potential. Symmetries demand that it has to be an even function of μ_q. The factor has to ensure a rapid drop of the effective mass similar to the quark masses in the NJL model or to the nucleon mass in relativistic mean-field theories at $T = 0$. This will increase the net quark density and therefore the pressure at finite chemical potential. We define the factor as

$$F(\mu_q) = \exp\left(-B\mu_q^2 - \frac{1}{2}B^2\mu_q^4\right). \tag{6.7}$$

The parameter B influences the location of the phase boundary. For $B = 0$ we retain the standard DQPM masses while $B = 75$ GeV^{-2} leads to the best agreement between the phase boundaries.

In the actual numerical calculations it is advantageous to use a different parametrization of the effective masses:

$$M_g^2\left(T\right) = \frac{g^2}{6}\left(\left(N_c + \frac{1}{2}N_f\right)T^2 + \frac{N_c}{2}\sum_q \frac{\mu_q^2}{\pi^2}\right)/F(\mu_q), \tag{6.8}$$

$$M_{s,\bar{s}}^2\left(T\right) = \frac{N_c^2-1}{8N_c}g^2\left(T^2 + \frac{\mu_s^2}{\pi^2}\right)/F(\mu_q), \tag{6.9}$$

$$M_{q,\bar{q}}^2\left(T\right) = \frac{N_c^2-1}{8N_c}g^2\left(T^2 + \frac{\mu_q^2}{\pi^2}\right). \tag{6.10}$$

This corresponds to a redefinition of the effective coupling,

$$g^2 \to g^2 \cdot F(\mu_q), \tag{6.11}$$

which has no influence on the physics. All observables stay unchanged, only the effective coupling differs. With the original parametrizations (6.4), (6.5), (6.6) one introduces huge derivatives in the light sector that are now shifted to the strange and the gluon sector, which are far less important. As a result it is much easier to solve the flow equation and to preserve the thermodynamic consistency of the theory.

We show the lines of constant pressure of the IHRG and the modified DQPM in Fig.

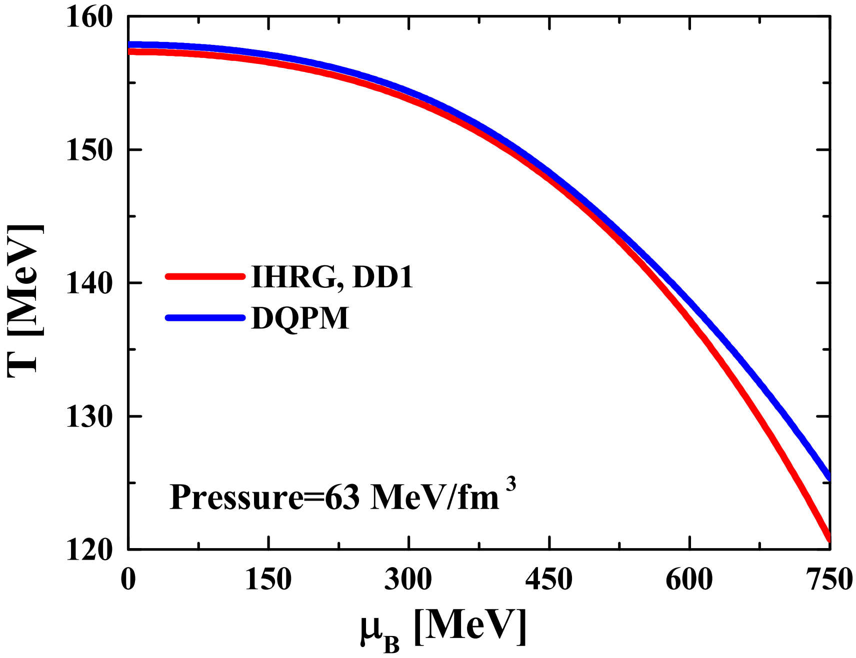

Figure 6.4: Lines of constant pressure $P = 63$ MeV/fm^3 of the IHRG and the DQPM with modified light quark masses in the T-μ_B plane.

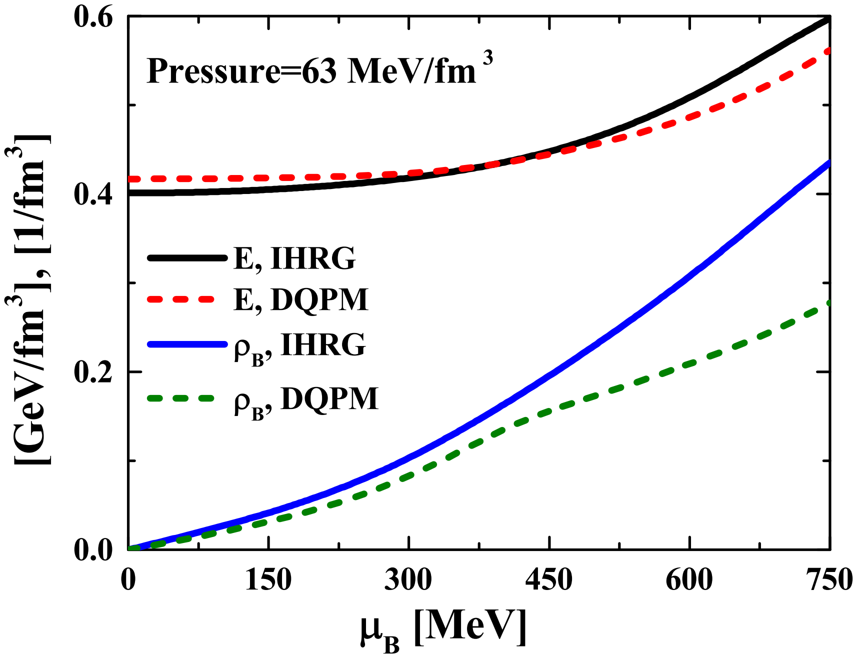

Figure 6.5: Energy and baryon number density on the lines of constant pressure as a function of the baryon chemical potential μ_B. Full lines are results from the IHRG, dashed lines from the modified DQPM.

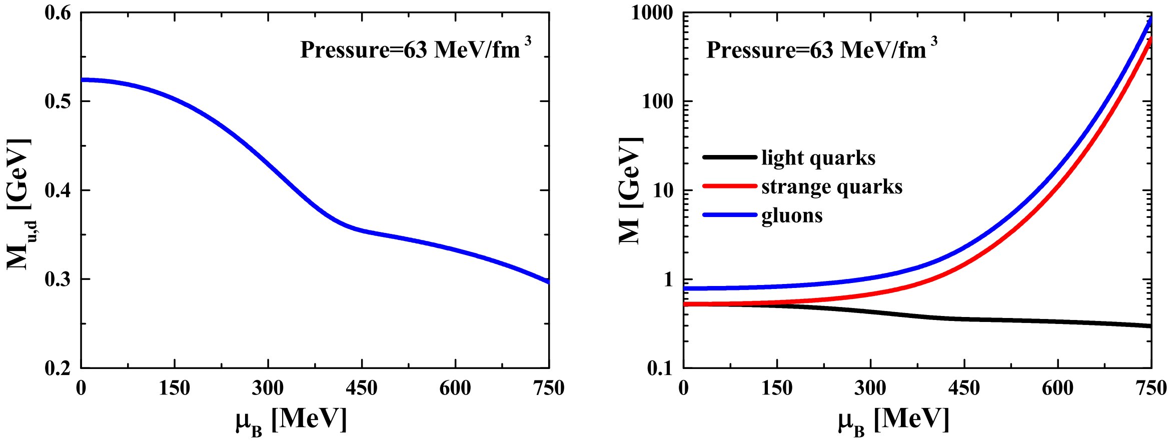

Figure 6.6: The effective masses of the modified DQPM as a function of the baryon chemical potential at the phase boundary defined by a constant pressure $P = 63$ MeV/fm^3. The left figure shows the effective light quark mass and the right side the effective masses of gluons, light and strange quarks on a logarithmic scale.

6.4. The transition line of the DQPM is almost on top of the IHRG transition with a difference of less than 1 MeV. The DQPM has now about the same transition line as the IHRG up to $\mu_B \approx 600$ MeV. At larger chemical potentials we find again a splitting, but we drastically extended the shared phase transition between the models. We show in Fig. 6.5 the energy and the baryon number density at the lines of constant pressure. Both show an acceptable agreement up to $\mu_B \approx 450$ MeV. Based on these results one should be able to construct a crossover transition between the two models up to moderate baryon chemical potentials. Note that microcanonical models -mandatory for heavy-ion simulations- need a perfect agreement of the energy and the particle density, but not necessarily of the pressure.

The phase boundary of the DQPM is only determined by the parametrization of the light quark mass (6.6). We show the effective masses in Fig. 6.6 at the lines of constant pressure as a function of the baryon chemical potential. The left side shows exclusively the light quark mass and the right side the light quark, strange quark and the gluon mass. In the standard DQPM all three decrease as a function of the baryon chemical potential, now this is only the case for the light quark mass. The masses of the strange quarks and the gluons increase. We find a change in the behavior of the light quark mass at $\mu_B \approx 450$ MeV where the slope becomes less steep. This has serious consequences for the phase boundaries, that agreed perfectly up to this point. At $\mu_B = 450$ MeV the phase boundaries start to separate and the energy and the baryon number density of both models deviate more strongly. If the phase boundaries of the two models should agree at even larger baryon chemical potentials, it is necessary that the light quark mass decreases at the same rate as for $\mu_B < 450$ MeV.

The change in the light quark mass is connected to increasing strange quark and gluon masses. We show in Fig. 6.7 the entropy density of gluons and strange quarks in the modified DQPM as a function of the baryon chemical potential at a fixed temperature

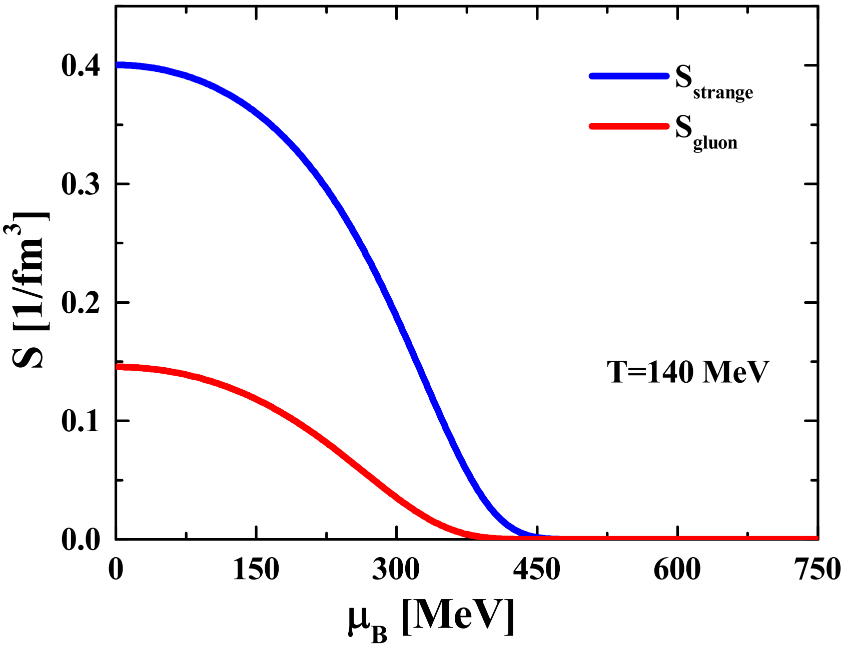

Figure 6.7: The entropy density stemming from only the strange quarks and only the gluons of the modified DQPM as a function of the baryon chemical potential for $T = 140$ MeV.

$T = 140$ MeV. Since the masses increase exponentially as a function of μ_B, the entropy density vanishes. This is contrary to the normal behavior of the entropy density in the standard DQPM where it should increase (see Fig. 3.15 for the entropy density of the DQPM*). At $\mu_B = 450$ MeV the strange quark and gluon masses have become so large, that both no longer contribute to the equation of state. Effectively they disappeared from the system and we have a medium that is composed of only light quarks. We expect this behavior at small temperatures where it would be driven by the small temperatures in the distribution functions, but in this scenario we find a pure light quark system already for $T \approx 140$ MeV. The large strange quark and gluon masses are a direct consequence of the flow equation and the decreasing light quark mass. We show in Fig. 6.8 the specific contributions to the Maxwell relation $\partial s/\partial\mu_B = \partial\rho_B/\partial T$, which is the basis of the flow equation, for each parton species as a function of the baryon chemical potential at $T = 140$ MeV. Since we concentrate on a strange neutral system, the baryon number density is proportional to the light quark density. The full green line shows the right side of the Maxwell relation, $\partial\rho_B/\partial T$, the dashed black line the left side, $\partial s/\partial\mu_B$. Both agree with each other which demonstrates the thermodynamic consistency of the model. The derivative of the light quark entropy density is very large at small baryon chemical potentials, which is due to the decreasing light quark mass, that enhances the derivative beyond its regular value. The derivative of the light quark density, i.e. of the baryon number density, is much smaller. To fulfill the Maxwell relation and counter-balance the light quark contribution, the contributions from the strange quarks and the gluons have

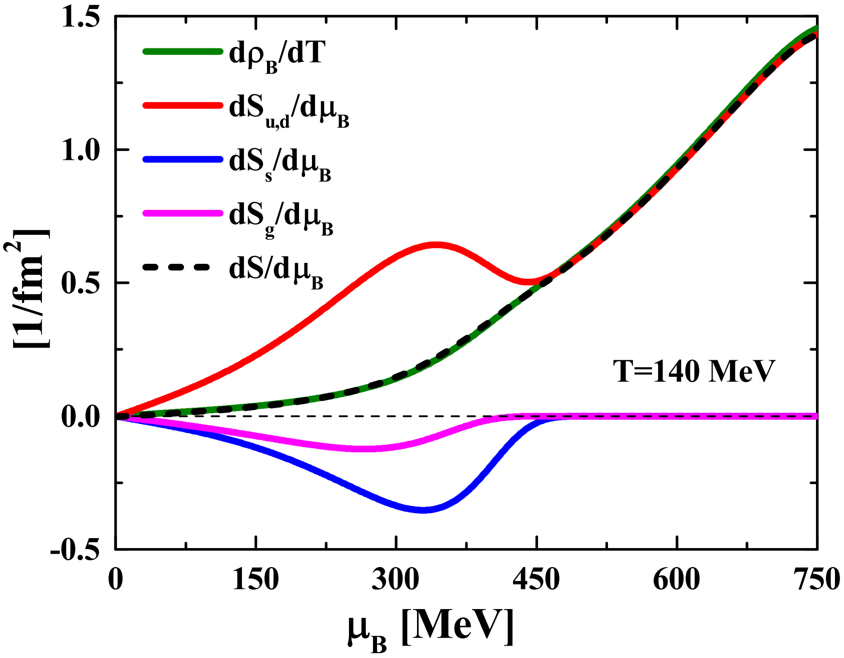

Figure 6.8: Contributions to the Maxwell relation $\partial s/\partial\mu_B = \partial\rho_B/\partial T$ separated into the contribution from the different partons as a function of the baryon chemical potential μ_B at a temperature $T = 140$ MeV. The green line shows the temperature derivative of the baryon number density, the red line the μ_B derivative of the light quark entropy density, the blue line the μ_B derivative of the strange quark entropy density and the magenta line the μ_B derivative of the gluon entropy density. The dashed black line is the μ_B derivative of the total entropy density.

to become negative. This is only possible if the masses increase with μ_B. At around $\mu_B = 450$ MeV, when the strange quarks and the gluons freeze out from the system, also their contribution to the Maxwell relation vanishes. The light quarks become then the only remaining degree of freedom and have to fulfill the Maxwell relation on their own. The behavior of the light quark masses as a function of the temperature and the baryon chemical potential is then solely controlled by thermodynamic consistency which causes the change in the slope. This happens for all possible functional forms of the correction factor $F(\mu_q)$. It is therefore not possible to extend the agreement between the DQPM and the IHRG phase boundary to larger baryon chemical potentials. This limits the application range of a crossover transition to baryon chemical potentials $\mu_B < 450$ MeV. In order to extend the DQPM to larger baryon chemical potentials, one has to introduce a mechanism that generates a nuclear equation of state. In this case the DQPM could reproduce the IHRG phase boundary also at $T = 0$ and hopefully also throughout the whole QCD phase diagram. We speculate that the dynamical generation of diquarks and/or condensates might be a solution to the problem.

6.4 Probing the phase diagram in relativistic heavy-ion collisions

In the previous sections we have studied the location of the hadron-parton transition in the QCD phase diagram. The aim of this section is to investigate which parts of the phase diagram in the T-μ_B plane are probed by heavy-ion collisions for different energies. We simulate collisions with the PHSD transport approach and determine the thermodynamic properties of the fireball. In general it is not straight forward (or even impossible) to connect non-equilibrium dynamics from microscopic transport studies to macroscopic equilibrium properties like temperature and chemical potentials. For this purpose one needs the exact QCD equation of state that relates the energy and the conserved charges to temperature and the chemical potentials of an equilibrated system. As long as lQCD calculations at finite chemical potential are prevented by the sign-problem one has to rely on effective models like the IHRG and the DQPM, making a study of the phase diagram model dependent.
An important issue in this study is the question whether or not the system reaches a local equilibrium during the heavy-ion collision. A common method to decide on kinetic equilibration is the pressure equilibration of the energy momentum tensor $T^{\mu\nu}$. In the local restframe it takes the form

$$T^{\mu\nu} = \begin{pmatrix} \epsilon & 0 & 0 & 0 \\ 0 & P_x & 0 & 0 \\ 0 & 0 & P_y & 0 \\ 0 & 0 & 0 & P_z \end{pmatrix} \tag{6.12}$$

where ϵ is the energy density and P_x, P_y and P_z are the pressure components in x, y and z directions. In the center of the collision they are often labeled as $P_x = P_y = P_\perp$ and $P_z = P_\parallel$, when the beam is in z direction. Due to the initial asymmetry of the collision the longitudinal and the transverse pressure differ significantly. A necessary requirement for kinetic equilibrium is the coincidence of the pressure components $P_\perp \approx P_\parallel$. The behavior of the pressure components in the central region of the collision zone has been studied in Ref. [381] with the UrQMD transport model [382, 383]. It was found that the pressure equilibrates at $t \cong 10$ fm/c after the initial impact of central Au+Au collisions at AGS energies. Additionally, a good agreement between the energy spectra of different hadron species with the predictions of statistical models was found at this time. This indicates that one can indeed find a system with a certain degree of equilibration at AGS energies for times larger than ~ 10 fm/c.
To fix points in the T-μ_B plane we have to determine the temperature T and the baryon chemical potential μ_B of the medium in the expanding fireball. This is usually done by comparing the energy density and the conserved charges in the local cell to the corresponding equation of state [384]. For hadronic matter it is common to use a HRG equation of state. However, it is unclear which hadronic resonances should be included in such a model. We will therefore determine the temperature T and the baryon chemical potential μ_B from the energy density and particle density of nucleons and pions, which

are directly accessible within our transport simulations. Instead of examining the whole fireball we will focus on local cells where strangeness is produced; these cells may be close to thermal equilibrium (at late times) or out-of equilibrium (at early times). The focus on local cells with strangeness production excludes free streaming cells as well as everything that happens after chemical freeze-out. Whenever a new $s\bar{s}$ pair is produced in the hadronic medium we take the nucleon and pion energy densities ϵ_N and ϵ_π and determine the temperature T and the baryon chemical potential μ_B using the expressions for a non-interacting hadron gas in equilibrium:

$$\epsilon_\pi = g_\pi \int \frac{d^3p}{(2\pi)^3} \frac{\omega_\pi}{e^{\omega_\pi/T} - 1}, \tag{6.13}$$

$$\epsilon_N = g_N \int \frac{d^3p}{(2\pi)^3} \frac{\omega_N}{e^{(\omega_N - \mu_B)/T} + 1}, \tag{6.14}$$

where $\omega_i = \sqrt{\mathbf{p}^2 + m_i^2}$ is the energy of the respective particle and $g_\pi = 3$ and $g_N = 4$ are the degeneracy factors of pions and nucleons. By additionally evaluating the particle densities ρ_π and ρ_N,

$$\rho_\pi = g_\pi \int \frac{d^3p}{(2\pi)^3} \frac{1}{e^{\omega_\pi/T} - 1}, \tag{6.15}$$

$$\rho_N = g_N \int \frac{d^3p}{(2\pi)^3} \frac{1}{e^{(\omega_N - \mu_B)/T} + 1}, \tag{6.16}$$

we can check if the local cell is in approximative thermal equilibrium or not. In practical terms, if the temperatures obtained from both methods differ by more than 5 MeV or if the chemical potentials differ by more than 15 MeV we consider the cell to be out-of equilibrium. Within this procedure we can eliminate further cells from the phase diagram, which are out-of equilibrium; however, it does not change the probed area if one considers only times $t \geq 10$ fm/c after the initial impact.

Each point in Figs. 6.9 and 6.10 stands for a local cell in which new strange quarks where produced. The color of the points indicates the time of the production. Red points happened early, yellow and green points at intermediate times and blue points at the end of the time interval. Fig. 6.9 shows the reconstructed temperatures and chemical potentials for a Au+Au collision at 10.7 AGeV with an impact parameter of $b = 2.2$ fm. Fig. 6.9(a) shows the events from 5 to 7 fm/c after the initial collision. These points cover all chemical potentials up to $\mu_B = 750$ MeV and a maximum temperature of $T = 200$ MeV when adopting only nucleons and pions as degrees of freedom. The cells in Fig. 6.9(a) are dominantly out of thermodynamic equilibrium and for low μ_B and high T correspond to partonic cells with some pion content. Fig. 6.9(b) shows the events from 7 to 10 fm/c where the majority of the points are located at baryon chemical potentials larger than $\mu_B = 150$ MeV. The blue points in Fig. 6.9(b) belong to cells that are already in equilibrium. Fig. 6.9(c) shows the events that happened at times $t > 10$ fm/c after the initial collision and are approximately in equilibrium. They cover an area between 150 MeV $< \mu_B <$ 650 MeV and 100 MeV $< T <$ 175 MeV. Fig. 6.9(c) describes indeed a

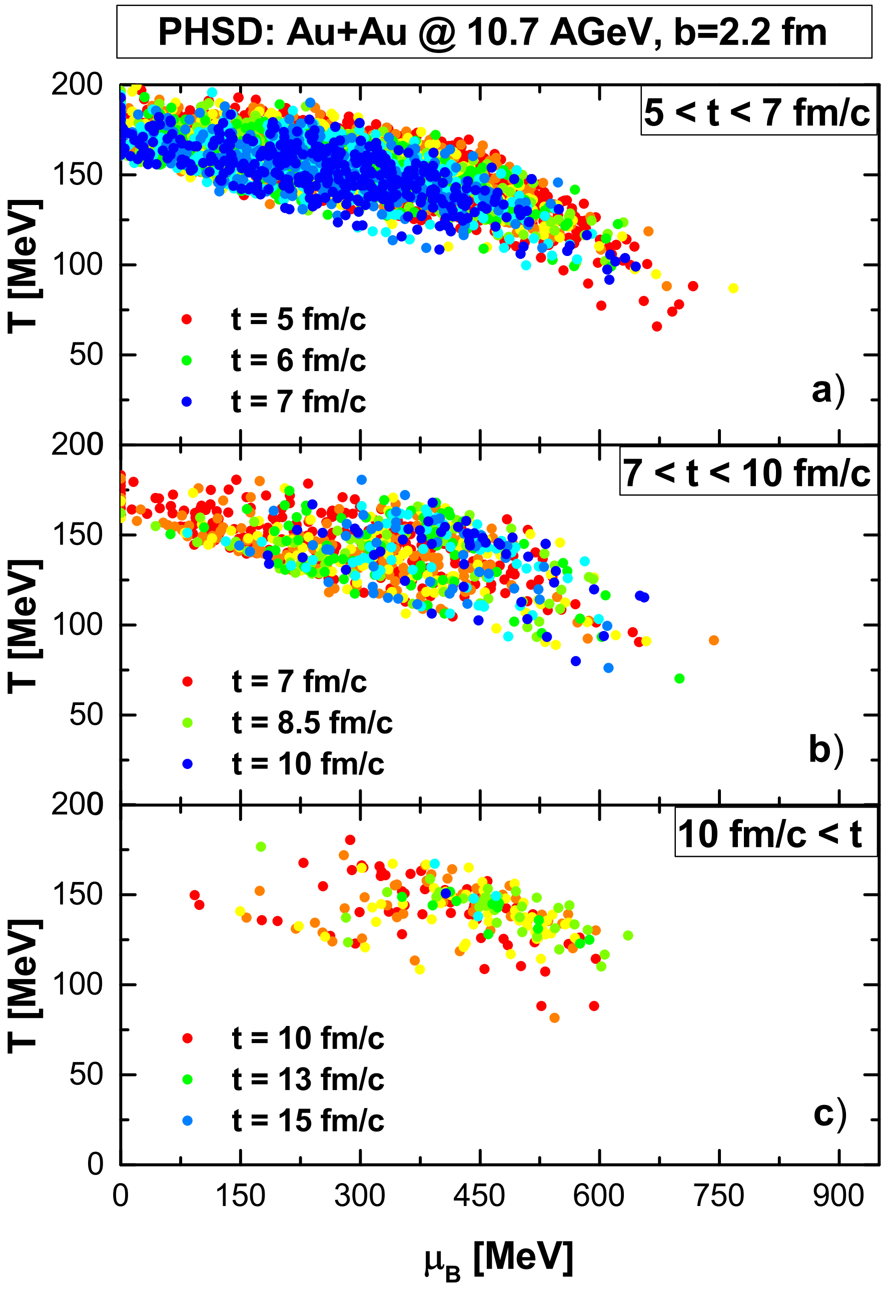

Figure 6.9: Occupancy of the phase diagram for hadronic matter in a central Au+Au collision at 10.7 AGeV for different time intervals. Each point belongs to a cell where strange quarks were produced. The color of the points indicates the time of the events within some varying interval. For times $t > 10$ fm/c the strangeness production occurs in cells that are in approximate thermodynamic equilibrium while the cells in panels (a) and (b) are dominantly out-of equilibrium.

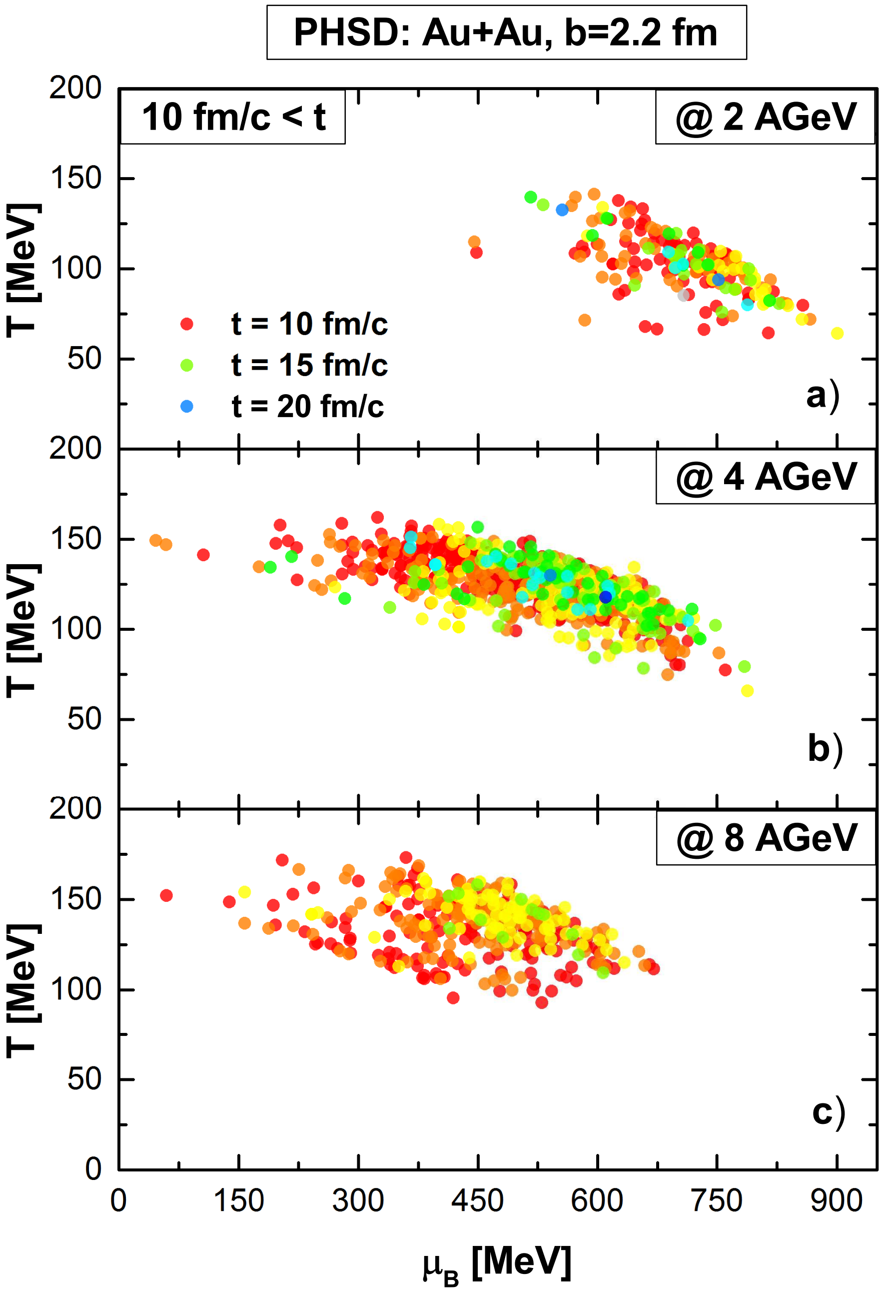

Figure 6.10: Occupancy of the phase diagram for hadronic matter in central Au+Au collisions at different beam energies from 2 to 8 AGeV for times $t > 10$ fm/c. Each point belongs to a cell where strange quarks were produced. The color of the points indicates the time of the events within some interval.

proper phase diagram while Figs. 6.9(a) and 6.9(b) suffer from non-equilibrium effects. We stress again that the temperatures and baryon chemical potentials shown in Figs. 6.9(a) and 6.9(b) cannot be related to any equilibrium properties.

In spite of the restrictions imposed by thermodynamic equilibrium we find that even central Au+Au collisions at 10.7 AGeV explore a wide range of points in the T-μ_B plane for μ_B essentially below 650 MeV. Fig. 6.10, furthermore, shows the occupation of the phase diagrams extracted from Au+Au collisions at 2 [Fig. 6.10(a)], 4 [Fig. 6.10(b)] and 8 AGeV [Fig. 6.10(c)] for an impact parameter $b = 2.2$ fm. All points belong to events that happened at times $t > 10$ fm/c after the initial collision. One sees that the probed region shifts to larger baryon chemical potentials and smaller temperatures when lowering the beam energy. The maximum baryon chemical potential in these plots is $\mu_B = 900$ MeV and the lowest temperature $T = 65$ MeV, however, with a very large spread in T and μ_B. Note that the upper boundary of the probed area in Figs. 6.9(c) and 6.10 correspondes to the (microcanonical) hadron-parton transition in PHSD.

It is important to discuss how these occupancies in the phase diagram relate to the real QCD phase diagram. Due to the model-dependent equation of state, the extracted temperatures and chemical potentials do not represent the real ones for QCD. We recall that the PHSD transport approach uses a critical energy density of $\epsilon_c = 0.5$ GeV/fm^3 to distinguish between a hadronic and a partonic medium. If the local energy density is above this threshold the hadrons dissolve into quarks. The critical energy density ϵ_c marks the largest energy density a hadronic system can reach in our simulations. When compared to the lQCD equation of state from the Wuppertal-Budapest collaboration at $\mu_B = 0$ [90] this translates to a temperature of around $T \approx 162$ MeV. On the other hand, the model used to extract the temperature and chemical potential is based on a HRG with a reduced number of degrees of freedom. We mention that a HRG, which contains all the hadronic particles included in PHSD, reaches the critical energy density at temperature $T \approx 175$ MeV. This indicates that the temperatures shown in Figs. 6.9 and 6.10 are too large compared to full QCD. For the baryon chemical potential we note that the baryon number susceptibilities χ_B of the HRG are smaller than the lQCD results [135]. This implies the corresponding baryon densities, in first order given by $n_B \approx \chi_B \cdot \mu_B$, exceed the HRG densities, thus overestimating the extracted baryon chemical potentials μ_B in comparison to full QCD. Admittedly, we cannot give a definite rescaling for finite chemical potentials; nevertheless, the general trend should be the same in the whole T-μ_B plane shifting the probed area to smaller temperatures and chemical potentials.

We compare our results on the phase diagram to recent experimental data from the RHIC beam-energy-scan program (BES). The BES uses heavy-ion collisions at varying beam energies to probe the phase diagram at different temperatures and chemical potentials [385, 386, 387]. In Ref. [71] the freeze-out temperatures and baryon chemical potentials of the BES were extracted for a strangeness canonical ensemble. We show their results in Fig. 6.11. The freeze-out parameters are only sensitive to the system as a whole and do not distinguish between different conditions in the collisions as we have done in Figs. 6.9 and 6.10. The data cover beam energies ranging from $\sqrt{s} \approx 7.7$ to 200 GeV. The largest beam energies probe the system at almost vanishing baryon chemical potential. As the collision energy is lowered the temperatures drop and the baryon chemical potentials rise. At the lowest energy of $\sqrt{s} = 7.7$ GeV, i.e. beam energies of 30 AGeV, the system reaches $\mu_B \approx 400$ MeV and $T \approx 145$ MeV. This is within the range of baryon

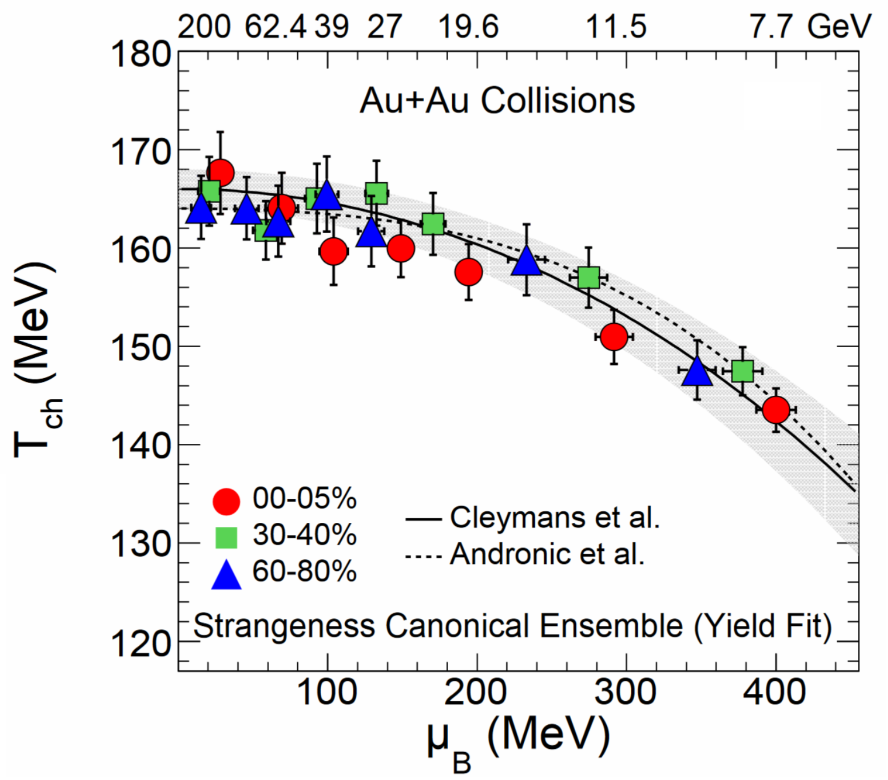

Figure 6.11: Extracted chemical freeze-out temperature as a function of the baryon chemical potential for a strangeness canonical ensemble using particle yields as input for fitting. The curves represent model predictions from Cleymans et al. (full line) [378] and from Andronic et al. (dashed line) [388]. The grey bands represent the theoretical prediction range of the Cleymans et al. model. Uncertainties represent systematic errors. The figure is taken from Ref. [71].

chemical potentials where the IHRG equation of state matches the modified DQPM and the largest μ_B where it matches the DQPM*. One can construct a single equation of state valid in the hadronic as well as in the partonic phase that covers the whole range of temperatures and baryon chemical potentials necessary for the physics of the BES.

The baryon chemical potentials probed in the BES program are still small and do not exceed the ratio $\mu_B/T = 3$, where neither functional methods [121, 389] nor lQCD calculations [42] found evidence for a critical point in the QCD phase diagram. We use the parametrization of the freeze-out curve determined by Cleymans et al. in Ref. [378] to estimate the beam energies necessary to discover the critical point. The freeze-out curve is parametrized as

$$T(\mu_B) = a - b\mu_B^2 - c\mu_B^4, \tag{6.17}$$

$$\mu_B(\sqrt{s}) = \frac{d}{1 + e\sqrt{s}}, \tag{6.18}$$

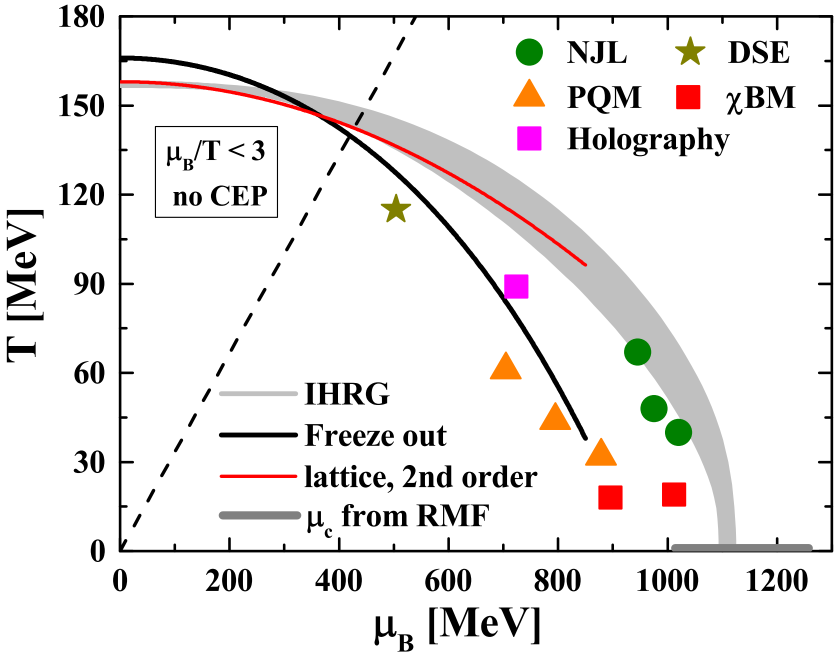

Figure 6.12: Predictions for the critical point in the T-μ_B plane calculated in the Nambu Jona-Lasinio model [43, 162, 232], the Polyakov quark-meson model [50, 67], the Dyson-Schwinger framework [121], a chiral baryon-meson model [390] and a holographic model [122]. The light gray area is the location of the hadron-parton transition as predicted by the IHRG, the dark gray band at zero temperature is the uncertainty due to the nuclear equation of state. The black line shows the freeze-out curve from Cleymans et al. [378] and the red line the lQCD prediction for the chiral phase transition up to second order with the curvature parameter from Bonati et. al [167]. The dashed black line separates the area with $\mu_B/T < 3$ where a critical point is unlikely.

with $a = 0.166 \pm 0.002$ GeV, $b = 0.139 \pm 0.016$ GeV^{-1}, $c = 0.053 \pm 0.021$ GeV^{-3}, $d = 1.308 \pm 0.028$ GeV and $e = 0.273 \pm 0.008$ GeV^{-1}. The fit gives a good description of the BES data in Fig. 6.11 but is also valid for data at much lower $\sqrt{s}$. We show in Fig. 6.12 several predictions for the location of the critical point calculated in the Nambu Jona-Lasinio model [43, 162, 232], the Polyakov quark-meson model [50, 67], the Dyson-Schwinger framework [121], a chiral baryon-meson model [390] and a holographic model [122]. We want to note here again that repulsive interactions lead to huge uncertainties and can push the critical point to smaller temperatures and larger baryon chemical potential, causing it potentially to disappear [235, 236, 237]. We show additionally the freeze-out curve (full black line), our prediction for the hadron-parton transition from the IHRG within uncertainties (gray area) and the chiral phase transition estimated in second order of μ_B by

$$T_c(\mu_B) = T_c \cdot \left(1 - \kappa \left(\frac{\mu_B^2}{T_c^2}\right)\right), \tag{6.19}$$

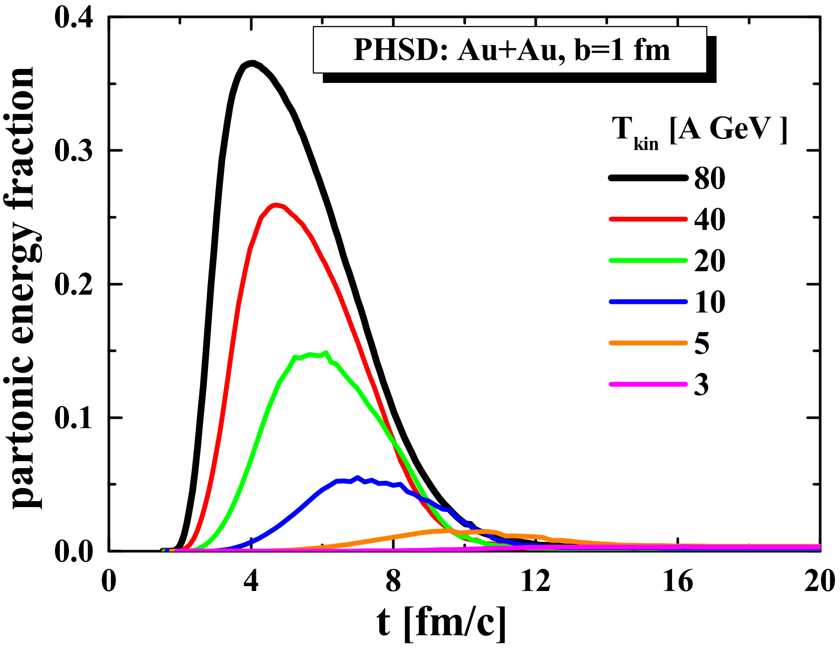

Figure 6.13: The ratio between the energy stored in the partonic phase and the total energy in central Au+Au collisions at different beam energies from 3 to 80 AGeV as a function of time calculated in PHSD simulations.

with the curvature parameter $\kappa = 0.0135$ determined from lQCD calculations by Bonati et al. (full red line) [167]. Apparently, the transition from the IHRG agrees well with the chiral phase transition, while the freeze-out curve shows a much steeper decrease, since it signals the freeze-out for inelastic hadronic scattering.

The locations of the critical points differ substantially, but they are all located at baryon chemical potentials larger than $\mu_B/T = 3$. The Dyson-Schwinger prediction is closest to that line. Apart from this all other predictions are at baryon chemical potentials larger than $\mu_B = 700$ MeV. This corresponds to $\sqrt{s} \approx 3.1$ GeV or a beam energy of $T_{kin} \approx 4$ AGeV. We have shown the occupancy of the phase diagram in such collisions in Fig. 6.10(b). One probes indeed baryon chemical potentials of $\mu_B \approx 700$ MeV at these energies, but dominantly at much lower values of μ_B. The majority of the system will therefore not pass the vicinity of the (potential) critical point.

Another difficulty for the search of the critical point arises from the lower compression rates in heavy-ion collisions at lower beam energies. As the medium gets less compressed, the energy density in the center of the collision will decrease and it becomes more unlikely, that a partonic phase is formed. We show in Fig. 6.13 the partonic energy fraction -defined by the ratio of the energy stored in the partonic phase to the total energy- determined in PHSD simulations of central Au+Au collisions at different beam energies. The largest beam energy of 80 AGeV corresponds to $\sqrt{s} = 12.3$ GeV or a freeze-out chemical potential of $\mu_B = 300$ MeV, the lowest of 3 AGeV to $\sqrt{s} = 2.7$ GeV or $\mu_B = 750$ MeV. As expected we find a decrease in the partonic energy fraction at lower beam energies, at 10 AGeV the fraction has already diminished to 5% and at 5 AGeV to 1.5%. These values will decrease even further if one considers peripheral collisions with a larger impact parameter [145].

The default hadron-parton transition in PHSD is at a constant energy density of $\epsilon_c \approx 0.5$ GeV/fm^3. We calculate additionally the partonic energy fraction for a critical energy density of $\epsilon_c \approx 0.4$ GeV/fm^3 to investigate the dependence on different transition conditions. One would expect a larger partonic phase in this simulations, but the fraction does not change substantially. The results in Fig. 6.13 signal very small fractions of partonic matter in heavy-ion collisions at low beam energies regardless of the precise transition condition. However, if the system does not become partonic, it is impossible to study the deconfinement phase transition. Any transition observed at these energies can only correspond to a chiral phase transition (in the hadronic phase).

It becomes apparent that it will be very hard to identify a critical point in the T-μ_B plane experimentally. With decreasing beam energy, lower temperatures and higher baryon chemical potentials are reached, but the spread in T and μ_B is very large at all bombarding energies of interest and any signal of criticality will be interfered by regular signals. Furthermore, if the critical point is located at large baryon chemical potential, it can only be probed at the lowest beam energies that might not be able to excite the system strong enough to cross the critical point. Theoretical predictions are also not reliable. Ab initio calculations in terms of lQCD simulations are hindered by the sign problem while the predictions from effective models show huge spreads for the locations of the critical point. The biggest uncertainties originate from repulsive interactions that shift the critical point to smaller temperatures or causing it entirely to disappear. Ultimately it is not clarified if QCD features a critical point or not.

7 Summary and Outlook

The QCD equation of state is an important ingredient to understand the physics of relativistic heavy-ion collisions. Collisions at very large beam energies probe systems with almost vanishing net-baryon densities, where lQCD can predict the properties of the medium (in equilibrium). As the beam energy is lowered the collisions create systems with finite net-baryon densities, their equivalent is a medium with a finite baryon chemical potential. The theoretical input for these collisions have to be provided by different models. We discussed in this thesis effective models for the thermodynamic properties of QCD in the confined and the deconfined phase. We used the lQCD equation of state to fix the properties of the models at vanishing baryon chemical potential and discussed their extension to finite μ_B.

In the deconfined phase we employed a partonic quasiparticle model. The DQPM treats quarks and gluons as effective quasiparticles with complex (medium-dependent) selfenergies. The real part of the selfenergies defines the effective mass (squared) of the quasiparticles and the imaginary part the width of the spectral functions. In the mean-field approximation the width is usually neglected and the theory omits off-shell effects that emerge due to interactions of the particles. The width defines the inverse relaxation time of these scattering processes, which allows for a direct calculation of transport coefficients in the relaxation time approximation. The DQPM can not only reproduce the static properties of QCD, i.e. the equation of state, but also the transport dynamics. A known flaw of quasiparticle models is their underestimation of the QCD equation of state at finite baryon chemical potential. It is not possible to tune standard quasiparticle models to describe simultaneously the equation of state and the susceptibilities as provided by lQCD calculations. This is connected to the momentum-independence of the selfenergies. At very high momenta the quark and gluon propagators should resemble their massless bare propagators, but this is not fulfilled in quasiparticle approaches. To this aim we extended the DQPM and introduced an explicit three-momentum dependence into the selfenergies. As the three-momentum (relative to the medium) rises, the selfenergies will vanish which ensures the correct perturbative limit of the propagators. With this generalized quasiparticle model, denoted by DQPM*, we could successfully reproduce the equation of state and the baryon number susceptibility in a single quasiparticle approach. The resulting equation of state at moderate baryon chemical potentials is consistent with the lQCD predictions. To extend the model to even larger μ_B we had to define the effective coupling for finite baryon chemical potentials. At $\mu_B = 0$ we used the lQCD equation of state to determine the coupling, but this is not possible at $\mu_B \neq 0$.

Instead we utilized thermodynamic consistency to control the extension. Quasiparticle models can not directly access the thermodynamic potential, so they are not thermodynamic consistent by design. Using the Maxwell relation between the entropy density and the baryon number density we derived a differential equation for the effective coupling at finite μ_B. By solving this equation we ensured that our quasiparticle model fulfills the Maxwell relation and therefore also thermodynamic consistency, thus defining the model at arbitrary chemical potentials. The equation of state calculated with the effective coupling -derived from the Maxwell relation- agrees with the results from an earlier ansatz for the effective coupling at finite μ_B, which was based on scaling properties, at small baryon chemical potentials $\mu_B < 300$ MeV. This shows that previous DQPM/DQPM* results were indeed thermodynamic consistent for moderate baryon chemical potentials. With the extended DQPM* we predicted the equation of state as well as the shear and bulk viscosity and the electric conductivity at finite baryon chemical potentials up to $\mu_B = 900$ MeV, exceeding previous predictions by far.

The flow equation derived from the Maxwell relation can be easily extended to incorporate also strange and charge chemical potentials. We put no constrains on μ_Q but discussed two important cases for μ_S, i.e. strict strangeness neutrality $N_S = 0$ and the equivalence of all three flavors $\mu_s = \mu_{u,d}$. However, the effective coupling showed only small differences between these two cases. In future works we will also consider the extension to arbitrary charge and strange chemical potentials. Especially the case of $N_S = 0$ and $N_Q/N_B = 0.4$ is of great interest as this is the only case for which higher-order baryon number susceptibilities have been predicted by lQCD. While the susceptibilities of second order are completely defined by the $\mu = 0$ equation of state, the higher-order susceptibilities contain corrections from finite chemical potentials. Comparing them to lQCD predictions allows some insights into the finite μ-behavior of the selfenergies. This should further improve our predictions for large chemical potentials.

The DQPM/DQPM* as an effective approach is not based on the actual symmetries of QCD and uses only partonic degrees of freedom. It can neither describe confinement nor chiral symmetry breaking/restoration. This limits the application range of the model to the fully deconfined part of the QCD phase diagram since it misses the correct dynamics to describe the vicinity of the phase transition or the confined phase. An approach that is based on chiral symmetry is the effective NJL and the Polyakov extended NJL model. Both approaches employ also only partonic degrees of freedom, but these differ substantially from the DQPM quasiparticles, which become very heavy at large temperatures, scaling with $M \sim T$. In the NJL the quarks are massive in the chiral broken phase and become almost massless in the restored phase. This is due to the chiral condensate that generates the quark masses and approximately vanishes when the symmetry gets restored. However, NJL-type models drastically underestimate the equation of state in the chiral broken phase and have an unphysical small shear viscosity in the restored phase that violates the KSS-limit. Nevertheless, they can access the equation of state and the order parameters. We used the models to study the connection between a crossover phase transition and the equation of state. Unfortunately, we could not find a direct relation between the two and it was not possible to define the phase transition from only the equation of state.

At low temperatures and chemical potentials quarks and gluons are not the appropriate degrees of freedom and one should employ hadronic models to describe QCD. At small net-baryon densities the hadrons interact predominantly through resonant scatterings and the effects of the interactions can be easily incorporated by introducing the formed resonances as a non-interacting particles. This HRG, despite being very simple, can describe the lQCD equation of state and susceptibilities. However, to reproduce the data close to the critical temperature one requires an enormous amount of hadrons, many of them not confirmed by experiment. At large densities and small temperatures the nature of the interactions changes and they are dominated by meson exchanges, which are not included in the HRG. At $T = 0$ a precise tuning between attractive and repulsive interactions is necessary to generate stable nuclear matter. The most advanced approach that can reproduce the nuclear equation of state are Dirac-Brueckner calculations. This approach is very complicated and can not be extended towards the whole phase diagram. Nevertheless, it is possible to parametrize the most important results within a relativistic mean-field theory with density-dependent coupling constants, that emerge naturally in the Dirac-Brueckner framework. The attractive interactions are then mediated by the scalar σ-meson and the repulsive interactions by the vector ω-meson. At finite temperature additional hadrons besides nucleons populate the system and will also interact via meson exchange. We treat the mesons as non-interacting and include important baryons into the relativistic mean-field approach. Currently we consider only nucleons and Δ-resonances as interacting particles. The resonant scatterings (emerging at finite temperature) are treated in the same way as in the HRG, by introducing the resonances as non-interacting particles. The resulting interacting HRG is compatible with the lQCD equation of state at $\mu = 0$ and Dirac-Brueckner results at $T = 0$. The IHRG is a purely hadronic model and therefore only applicable to the confined part of the phase diagram. It does not contain chiral symmetry explicitly, but by employing low-energy QCD theorems we calculated the chiral condensate from hadronic low-energy constants. With the approach developed in Ref. [147] we linked the condensate to the strangeness production in heavy-ion collisions. This probes exclusively the attractive interactions. We found a good agreement between PHSD simulations and experimental data. Chiral symmetry restoration had a huge effect on the abundances of strange hadrons produced in the simulations and could drastically improve the predictions of the simulations and led to the first microscopic explanation of the famous "horn" in the K^+/π^+ ratio. This served as an independent verification of the attractive interaction in the IHRG.

The DQPM* and the IHRG are both defined on the level of their selfenergies. This allows an immediate realization of the two approaches in a transport model on the basis of the Kadanoff-Baym equations. For the standard DQPM this is already done and it is used to model the partonic phase in the PHSD transport approach.

With the DQPM* and the IHRG defined in the whole T-μ_B plane we could construct the QCD equation of state from the IHRG in the confined and the DQPM* in the deconfined phase. In order to describe the whole equation of state we had to switch from one model at the other. This corresponds to the change from hadronic to partonic degrees of freedom and is therefore connected to the deconfinement transition. At $\mu = 0$ one can determine the transition condition from lQCD, but at finite chemical potential it is not defined by first principles. Nevertheless, simulations of ultra-relativistic heavy-ion collisions need to incorporate the effects of the partonic phase to achieve a satisfying description of the experimental measurements. An often used transition condition is a constant energy density. In accordance with heavy-ion simulations we defined the transition at a constant value of the energy density or the pressure. This approach might not lead to a mixed phase but is justified if the transition region is very narrow. We calculated the lines of constant pressure and energy density in the T-μ_B plane for both approaches and defined the phase boundary at an energy density of $\epsilon_c \approx 0.4$ GeV/fm^3 or a pressure of $P_c \approx 63$ MeV/fm^3. In this way the transition at $\mu = 0$ is at a critical temperature of $T_c \approx 158$ MeV which is close to the critical temperature predicted by lQCD. We found similar phase boundaries for the IHRG and the DQPM* up to baryon chemical potentials of roughly 400 MeV. In this region it is possible to construct a continuous crossover transition between the two models, but at larger baryon chemical potentials the transition lines split up and a transition would induce rapid changes of the temperature and the chemical potential. The separation of the phase boundary is attributed to different boundary conditions of the two models at large densities. The DQPM* is only constrained by thermodynamic consistency, but the IHRG has to reproduce the nuclear equation of state. This dictates the behavior of the IHRG at large baryon chemical potentials and forces the equation of state to rise much stronger than the DQPM* at finite μ_B. To increase the pressure at $\mu_B \neq 0$ and to describe the IHRG phase boundary the DQPM* requires a much larger net-baryon density which can only be achieved if the light quark masses become smaller compared to the default model. We used a simple quasiparticle model without effective widths and forced the light quark mass to drop at a sufficient rate to reproduce the phase boundary of the IHRG. Unfortunately, thermodynamic consistency required a steep rise of the strange quark and the gluon masses to the point that they became too heavy to contribute to the equation of state. Within the modified quasiparticle model we could describe the IHRG phase boundary up to $\mu_B \approx 450 - 600$ MeV. However, as soon as the strange quarks and gluons decouple from the system, the phase boundaries will separate again. When the light quarks become the only remaining degrees of freedom in the system, the functional form of the light quark mass is constrained by thermodynamic consistency. This restricts the drop of the mass as a function of the chemical potential and the pressure rises too slowly to reproduce the IHRG results. It seems impossible for a quasiparticle model to reproduce the equation of state of a hadronic model with a realistic nuclear equation of state and any transition between the two models would become a first-order transition at large μ_B. However, this is no indication of a critical point in the QCD phase diagram; instead it is merely a shortcoming of the quasiparticle models that are no longer valid under these conditions.

The only possibility to probe the QCD phase diagram is by heavy-ion collisions, but the matter in the collisions is out-of equilibrium and it is therefore not trivial to connect it to equilibrium properties like temperature and chemical potential. We simulated heavy-ion collisions at beam energies between 2 and 11 AGeV with the PHSD transport approach. At late times after the initial collisions it is actually possible to find locally a medium that is close to equilibrium. We extracted the temperatures and the baryon chemical potentials and determined the occupancies of the phase diagram in the collisions. As expected we found lower temperatures and larger baryon chemical potentials at lower beam energies. However, the collisions probe very large fractions of the phase diagram, even at the lowest beam energies of 2 AGeV.

So far the phase diagram has only been studied by collisions at larger beam energies. We compared our results to the freezeout temperatures and chemical potentials extracted from the beam-energy scan (BES) program at RHIC. The freezeout parameters describe the whole system by a single temperature and baryon chemical potential, but they are a reliable indicator of the baryon chemical potentials reached. The lowest energy in the BES corresponded to a center of mass energy of $\sqrt{s} \approx 7.7$ GeV and reached a baryon chemical potential of $\mu_B \approx 400$ MeV. This is still within the range of the crossover transition between the DQPM* and the IHRG. The equation of state defined by these two models can therefore be used to describe the physics at low beam energies down to $\sqrt{s} \approx 7.7$ GeV. With the modified quasiparticle model we could construct a crossover equation of state up to $\mu_B \approx 600$ MeV. This corresponds to a collision energy of $\sqrt{s} \approx 4.3$ GeV or a beam energy of 9 AGeV. Comparing the baryon chemical potential to the phase diagram occupancies from PHSD simulations, we found that the freezeout chemical potential is merely the largest baryon chemical potential probed by the medium in the collisions, the bulk of the fireball probes a much lower μ_B. This has serious consequences for the search of the critical point. The system will only partly cross its location with the majority evolving at different temperatures and chemical potentials. The extraction of the critical signals from the large quantity of non-critical ones will be an extremely difficult task. In the first phase of the BES no signals of a critical point have been found. However, most theoretical models predict it at baryon chemical potentials exceeding $\mu_B \approx 700$ MeV. These conditions can be met at beam energies below 8 AGeV, but the collision energy at these beam energies are very small and might not provide the necessary compression rates to drive the system across the phase boundary. Using PHSD we estimated the fraction of energy that is stored in the partonic phase for heavy-ion collisions at small beam energies and found that at a beam energy of 8 AGeV, less than 5% of the available energy is stored in the partonic medium. This might be insufficient to detect any signals of a critical point or a phase transition. With the necessity for low beam energies on one side and insufficient compression rates at the other, it is obvious that the search for the critical point will be one of the most challenging projects imaginable. However, even if the existence of the critical point can not be confirmed by future experiments, they will still provide valuable data that will help to understand the properties of hot QCD matter also at large baryonic densities.

A Appendix

A.1 Grand-canonical potential in propagator representation

The DQPM has no Lagrangian and defines the thermodynamics from the grand-canonical potential in propagator representation. The potential was originally derived for systems of non-relativistic fermions by Luttinger and Ward [391] and Baym [392] and later extended to relativistic systems with fermions and bosons [393, 394]. An alternative approach, that leads to the same results, is the Cornwall-Jackiw-Tomboulis (CJT) formalism that starts from the effective action [395].

We first introduce the functional W which is the negative logarithm of the generating functional Z. The functional W can also be defined out-of equilibrium but if one considers it for an equilibrium system it is proportional to the thermodynamic potential Ω of the system,

$$-\ln Z = W = \beta\Omega, \tag{A.1}$$

with β denoting the inverse temperature. For a relativistic many-body system in terms of the full propagators it is given by [393]

$$\beta\Omega[D,S] = \frac{1}{2}\mathrm{Tr}[\ln D^{-1} - \Pi D] - \mathrm{Tr}[\ln S^{-1} - \Sigma S] + \Phi[D,S]. \tag{A.2}$$

In this expression D is the fully dressed bosonic propagator describing the gluon degrees of freedom and S the fully dressed fermionic propagator describing the (anti)quark degrees of freedom; Π and Σ are the corresponding selfenergies defined by the Dyson equations,

$$D^{-1} = D_0^{-1} + \Pi, \qquad S^{-1} = S_0^{-1} + \Sigma, \tag{A.3}$$

where D_0^{-1} and S_0^{-1} are the bare propagators and $-\Phi[D,S]$ is the sum of the 2-particle-irreducible "skeleton" diagrams build from the full propagators D and S. The selfenergies follow selfconsistently from Φ by functional variation with respect to the full propagators,

$$\frac{\delta\Phi}{\delta D} = \frac{1}{2}\Pi, \qquad \frac{\delta\Phi}{\delta S} = -\Sigma. \tag{A.4}$$

If the selfenergies are obtained in this way, the approach obeys energy-momentum, angular momentum and particle number conservation, even in non-equilibrium [392].

To prove that W is indeed a thermodynamic potential [15] we have to show that it is stationary under variations of the propagators,

$$\frac{\delta W}{\delta D} = \frac{\delta W}{\delta S} = 0. \tag{A.5}$$

This is equivalent to the stationary condition of the thermodynamic potential from Eq. (2.12). The variation of Φ follows from the definition of the selfenergies

$$\delta\Phi = \frac{1}{2}\mathrm{Tr}\Pi\delta D - \mathrm{Tr}\Sigma\delta S. \tag{A.6}$$

We also use $\delta \ln D^{-1} = \left(D^{-1}\right)^{-1}\delta D^{-1} = D\ \delta D^{-1}$. With this the variation of W reads

$$\begin{aligned}
\delta W &= \frac{1}{2}\mathrm{Tr}[\delta\ln D^{-1} - \delta(\Pi D)] - \mathrm{Tr}[\delta\ln S^{-1} - \delta(\Sigma S)] + \delta\Phi[D,S] \\
&= \frac{1}{2}\mathrm{Tr}\left[D\delta D^{-1} - \Pi\delta D - \delta\Pi D\right] - \mathrm{Tr}\left[S\delta S^{-1} - \Sigma\delta S - \delta\Sigma S\right] + \frac{1}{2}\mathrm{Tr}\Pi\delta D - \mathrm{Tr}\Sigma\delta S \\
&= \frac{1}{2}\mathrm{Tr}\left[D\delta D^{-1} - D\delta\Pi\right] - \mathrm{Tr}\left[S\delta S^{-1} - S\delta\Sigma\right] \qquad (A.7)\\
&= \frac{1}{2}\mathrm{Tr}\left[D\delta\left(D^{-1} - \Pi\right)\right] - \mathrm{Tr}\left[S\delta\left(S^{-1} - \Sigma\right)\right] \\
&= \frac{1}{2}\mathrm{Tr}\left[D\delta D_0^{-1}\right] - \mathrm{Tr}\left[S\delta S_0^{-1}\right] = 0.
\end{aligned}$$

Here we have used the Dyson equations (A.3) and the independence of the bare propagators from the dressed ones.
We will now evaluate the traces in Eq. (A.2) to bring the thermodynamic potential in a form that allows us to derive the entropy and the particle number. We take the trace over the continuous quantum numbers in 4-momentum space. The momentum summation turns into an integration

$$\sum_{\mathbf{p}} \to V\int\frac{d^3p}{(2\pi)^3}, \tag{A.8}$$

while the energy summation has to be performed over Matsubara frequencies,

$$\omega \to i\omega_n = i\pi nT - \mu, \tag{A.9}$$

with n even for bosons and odd for fermions, to include finite temperature effects [396]. We evaluate these by standard techniques and turn the summation via the residue theorem into a contour integration [107]. Therefore we use the Bose- and Fermi-distribution functions,

$$n_B(\omega) = \frac{1}{\exp\left(\frac{\omega}{T}\right) - 1}, \qquad n_F(\omega) = \frac{1}{\exp\left(\frac{\omega-\mu}{T}\right) + 1}, \tag{A.10}$$

---

[15] W is a (dimensionless) entropic thermodynamic potential. The corresponding energy potential is the grand-canonical potential Ω.

that have poles at the Matsubara frequencies. Their residues are given by

$$\mathrm{Res}_{i\omega_n} n_B(i\omega_n) = \frac{T}{\exp(i\omega_n/T)} = T, \qquad \mathrm{Res}_{i\omega_n} n_F(i\omega_n) = \frac{T}{\exp(i\omega_n/T)} = -T. \tag{A.11}$$

With Eq. (A.11) and some deformation of the contour one finds the general relation [397],

$$T\sum_n h(i\omega_n) = \pm \oint_C \frac{dp_0}{2\pi i} n_{B/F}(p_0) h(p_0) = \pm \int_{\mathbb{R}} \frac{dp_0}{2\pi i} n_{B/F}(p_0) \left[h(p_0 + i0^+) - h(p_0 - i0^+)\right], \tag{A.12}$$

where the upper sign is for bosons and the lower for fermions. Since in this case $h(p_0)$ is a function of propagators we can use the general propagator relation [31],

$$G(p_0 + i0^+) - G(p_0 - i0^+) = -iA(p_0) = 2i\ \mathrm{Im}G^R, \tag{A.13}$$

and apply it to h [16]. This leads to the expression,

$$\begin{aligned} \frac{\Omega}{V} =& \mathrm{Tr} \int \frac{d^3p}{(2\pi)^3} \frac{d\omega}{2\pi} n_B(\omega) \mathrm{Im} \left(\ln(D^{-1}) - \Pi D\right) \\ &+ 2\ \mathrm{Tr} \int \frac{d^3p}{(2\pi)^3} \frac{d\omega}{2\pi} n_F(\omega) \mathrm{Im} \left(\ln(S^{-1}) - \Sigma S\right) \\ &+ \frac{T}{V} \Phi[D,S], \end{aligned} \tag{A.14}$$

for the thermodynamic potential. The remaining traces run over the discrete quantum numbers and lead to degeneracy factors $(d_g, d_q, d_{\bar{q}})$ and in case of fermions to a distinction between fermions and antifermions,

$$\begin{aligned} \frac{\Omega}{V} =& d_g \int \frac{d^3p}{(2\pi)^3} \frac{d\omega}{2\pi} n_B(\omega) \left(\mathrm{Im} \ln(D^{-1}) - \mathrm{Im}\Pi\ \mathrm{Re}D - \mathrm{Re}\Pi\ \mathrm{Im}D\right) \\ &+ d_q \int \frac{d^3p}{(2\pi)^3} \frac{d\omega}{2\pi} n_F(\omega) \left(\mathrm{Im} \ln(S^{-1}) - \mathrm{Im}\Sigma\ \mathrm{Re}S - \mathrm{Re}\Sigma\ \mathrm{Im}S\right) \\ &+ d_{\bar{q}} \int \frac{d^3p}{(2\pi)^3} \frac{d\omega}{2\pi} n_{\bar{F}}(\omega) \left(\mathrm{Im} \ln(S^{-1}) - \mathrm{Im}\Sigma\ \mathrm{Re}S - \mathrm{Re}\Sigma\ \mathrm{Im}S\right) \\ &+ \frac{T}{V} \Phi[D,S]. \end{aligned} \tag{A.15}$$

Note that we treat all the fields in the DQPM as scalar particles. This allows for an easy evaluation of the discrete traces although we rather have to sum over spinor indices in case of fermions. We justify this as follows. We have shown the thermodynamic potential for systems without interactions in Sec. 2.2. In the propagator representation

---

[16] We can rewrite the selfenergy term into $\Sigma G = (G^{-1} - G_0^{-1})G = 1 - G_0^{-1}G$, which is linear in G. For the logarithmic part we use the power series $\ln\left(G^{-1}\right) = -\ln G = \sum_i a_i G^i$. The powers G^i are higher-order propagators in the Hartree approximation that fulfill also the propagator relation.

(A.2) this is the limit $\Pi = \Sigma = \Phi = 0$ and $D \to D_0$, $S \to S_0$. The potential is then given by

$$W_0^B = \beta\Omega_0^B = -\ln Z_0^B = \frac{1}{2}\mathrm{Tr}\ln D_0^{-1}, \tag{A.16}$$

$$W_0^F = \beta\Omega_0^F = -\ln Z_0^F = -\mathrm{Tr}\ln S_0^{-1}, \tag{A.17}$$

which is equivalent to Eq. (2.26). Evaluating the traces leads to the formulae (2.28) and (2.29) [107]. We will only get the right degeneracy for the fermions if the fermionic propagator has the full Dirac structure. However, the spinor structure of the fermions does not include any other features into the thermodynamic potential instead of a degeneracy factor and a different quantum statistic, see Eq. (2.33). If the interactions are spin-independent we can assume that this holds also for the interacting potential. We will therefore neglect the Dirac structure of the fermions and include the degeneracy factor for the spin simply into d_q and $d_{\bar{q}}$. In case of QCD this leads to $d_q = d_{\bar{q}} = 2\times N_c\times N_f = 18$ and $d_g = 2 \times (N_c^2 - 1) = 16$.

With Eq. (A.15) we have simplified the thermodynamic potential as far as possible. The integrals could be calculated if the physical solutions of the Green's functions were known, but the functional $\Phi[D, S]$ is too complicated to be solved analytically in general. Nevertheless, we will proceed to determine the entropy density and the particle density from the potential in a thermodynamically consistent way by using Eqs. (2.18) and (2.19). We demonstrate the procedure for the entropy density following the arguments from Refs. [148, 149, 150]. The particle density follows in the same way and uses the same line of arguments [150].

Thanks to the stationary condition of the thermodynamic potential (A.7) we get no contribution from the thermal dependence of the propagators

$$\frac{\partial\Omega}{\partial T} = \left.\frac{\partial\Omega}{\partial T}\right|_{D,S} + \underbrace{\frac{\delta\Omega}{\delta D}}_{=0}\frac{\partial D}{\partial T} + \underbrace{\frac{\delta\Omega}{\delta S}}_{=0}\frac{\partial S}{\partial T}. \tag{A.18}$$

This leads to the entropy density $s = s^{dqp} + s'$ with

$$\begin{aligned} s^{dqp} =& - d_g \int_{d^4p} \frac{\partial n_B}{\partial T}\left(\mathrm{Im}(\ln D^{-1}) - \mathrm{Im}\Pi\ \mathrm{Re}D\right) \\ & - d_q \int_{d^4p} \frac{\partial n_F}{\partial T}\left(\mathrm{Im}(\ln S^{-1}) - \mathrm{Im}\Sigma\ \mathrm{Re}S\right) \\ & - d_{\bar{q}} \int_{d^4p} \frac{\partial n_{\bar{F}}}{\partial T}\left(\mathrm{Im}(\ln S^{-1}) - \mathrm{Im}\Sigma\ \mathrm{Re}S\right), \end{aligned} \tag{A.19}$$

that contains only separate contributions for the different quasiparticle species, and

$$\begin{aligned} s' =& d_g \int_{d^4p} \frac{\partial n_B}{\partial T}\ \mathrm{Re}\Pi\ \mathrm{Im}D + d_q \int_{d^4p} \frac{\partial n_F}{\partial T}\ \mathrm{Re}\Sigma\ \mathrm{Im}S \\ & + d_{\bar{q}} \int_{d^4p} \frac{\partial n_{\bar{F}}}{\partial T}\ \mathrm{Re}\Sigma\ \mathrm{Im}S - \frac{\partial}{\partial T}\left(\frac{T}{V}\ \Phi\right), \end{aligned} \tag{A.20}$$

that contains also residual interactions between the particles. We used here the abbreviation

$$\int_{d^4p} = \int_{d^3p} \int \frac{d\omega}{2\pi} = \int \frac{d^3p}{(2\pi)^3} \frac{d\omega}{2\pi}. \tag{A.21}$$

The contribution of s' containing the functional Φ is still not calculable. Fortunately, it was shown in Refs. [148, 149, 150] that the contributions in s' compensate each other such that s' vanishes at 2-loop order for a scalar theory with cubic and quartic interactions. Furthermore, this is a topological feature that also holds for QCD [78, 79, 150]. The entropy density is then the sum of the gluon, the quark and the antiquark contribution separately, $s = s^{dqp} = s_g + s_q + s_{\bar{q}}$.

By rewriting the imaginary part of the logarithm,

$$\operatorname{Im}\ln(D^{-1}) = \pi \ \operatorname{sgn}(\operatorname{Im}D^{-1})\Theta(-\operatorname{Re}D^{-1}) + \arctan\left(\frac{\operatorname{Im}D^{-1}}{\operatorname{Re}D^{-1}}\right), \tag{A.22}$$

we split the entropy density in two separate parts $s = s^{(0)} + \Delta s$. The first term $s^{(0)}$ does not vanish, when the imaginary part of the propagator, i.e. the interaction, vanishes. We call it the on-shell part,

$$\begin{aligned} s^{(0)} = &- d_g \int_{d^4p} \frac{\partial n_B}{\partial T} \ \pi \ \operatorname{sgn}(\operatorname{Im}D^{-1})\Theta(-\operatorname{Re}D^{-1}) \\ &- d_q \int_{d^4p} \frac{\partial n_F}{\partial T} \ \pi \ \operatorname{sgn}(\operatorname{Im}S^{-1})\Theta(-\operatorname{Re}S^{-1}) \\ &- d_{\bar{q}} \int_{d^4p} \frac{\partial n_{\bar{F}}}{\partial T} \ \pi \ \operatorname{sgn}(\operatorname{Im}S^{-1})\Theta(-\operatorname{Re}S^{-1}). \end{aligned} \tag{A.23}$$

The remaining part Δs is the off-shell contribution to the entropy density, which vanishes if the interaction goes to zero,

$$\begin{aligned} \Delta s = &d_g \int_{d^4p} \frac{\partial n_B}{\partial T} \left(\operatorname{Im}\Pi \ \operatorname{Re}D - \arctan\left(\frac{\operatorname{Im}D^{-1}}{\operatorname{Re}D^{-1}}\right)\right) \\ &+ d_q \int_{d^4p} \frac{\partial n_F}{\partial T} \left(\operatorname{Im}\Sigma \ \operatorname{Re}S - \arctan\left(\frac{\operatorname{Im}S^{-1}}{\operatorname{Re}S^{-1}}\right)\right) \\ &+ d_{\bar{q}} \int_{d^4p} \frac{\partial n_{\bar{F}}}{\partial T} \left(\operatorname{Im}\Sigma \ \operatorname{Re}S - \arctan\left(\frac{\operatorname{Im}S^{-1}}{\operatorname{Re}S^{-1}}\right)\right). \end{aligned} \tag{A.24}$$

Without the contribution from the functional Φ, we can finally evaluate the entropy density for a given set of propagators.

The particle density follows in the same way as the entropy density [150]. We get no contributions from the dependence of the propagators on the chemical potential due to the variational stability of the thermodynamic potential,

$$\frac{\partial \Omega}{\partial \mu} = \left.\frac{\partial \Omega}{\partial \mu}\right|_{D,S} + \underbrace{\frac{\delta \Omega}{\delta D}}_{=0} \frac{\partial D}{\partial \mu} + \underbrace{\frac{\delta \Omega}{\delta S}}_{=0} \frac{\partial S}{\partial \mu}. \tag{A.25}$$

Since the gluon distribution function is independent from the chemical potential, we have only contributions from quarks and antiquarks. Like the entropy, the density can be split into two parts $n = n^{dqp} + n'$, where the contribution n' cancels at 2-loop order [150]. As for the entropy we split n^{dqp} into an on-shell and an off-shell contribution $n = n^{dqp} = n^{(0)} + \Delta n$. The on-shell part is then given by:

$$\begin{aligned} n^{(0)} =& - d_q \int_{d^4p} \frac{\partial n_F}{\partial \mu} \pi \; \mathrm{sgn}(\mathrm{Im}S^{-1})\Theta(-\mathrm{Re}S^{-1}) \\ &- d_{\bar{q}} \int_{d^4p} \frac{\partial n_{\bar{F}}}{\partial \mu} \pi \; \mathrm{sgn}(\mathrm{Im}S^{-1})\Theta(-\mathrm{Re}S^{-1}). \end{aligned} \tag{A.26}$$

The only difference to the on-shell entropy density (A.23) is, that one has the derivative of the distribution function with respect to the chemical potential μ and not with respect to the temperature T. The same holds for the off-shell part:

$$\begin{aligned} \Delta n =& d_q \int_{d^4p} \frac{\partial n_F}{\partial \mu} \left(\mathrm{Im}\Sigma \; \mathrm{Re}S - \arctan\left(\frac{\mathrm{Im}S^{-1}}{\mathrm{Re}S^{-1}}\right)\right) \\ &+ d_{\bar{q}} \int_{d^4p} \frac{\partial n_{\bar{F}}}{\partial \mu} \left(\mathrm{Im}\Sigma \; \mathrm{Re}S - \arctan\left(\frac{\mathrm{Im}S^{-1}}{\mathrm{Re}S^{-1}}\right)\right). \end{aligned} \tag{A.27}$$

The contribution from the antiquarks has always the opposite sign of the quark contribution due to $\frac{\partial n_{\bar{F}}}{\partial \mu} = -\frac{\partial n_F}{\partial \mu}$. In the limit of zero chemical potential, when the propagators for quarks and antiquarks are equal, the densities will cancel and the net quark density is zero.

A.2 DQPM thermodynamics

The DQPM is the combination of the quasiparticle entropy (A.19) with the Breit-Wigner spectral functions (3.5) [78, 79]. It supersedes the earliest quasiparticle models that incorporated only an effective mass [151, 152]. We will now apply the corresponding propagators (3.3) and selfenergies (3.4) to further simplify the entropy density $s = s^{(0)} + \Delta s$ and the particle density $n = n^{(0)} + \Delta n$. Using the explicit form we can rewrite the on-shell entropy density for an arbitrary particle as

$$\begin{aligned} s^{(0)} =& - \int_{d^4p} \frac{\partial n_{B/F}}{\partial T} \pi \; \mathrm{sgn}(\mathrm{Im}D^{-1})\Theta(-\mathrm{Re}D^{-1}) \\ =& - \int_{d^4p} \frac{\partial n_{B/F}}{\partial T} \pi \; \mathrm{sgn}(-2\gamma\omega)\Theta(\omega^2 - \mathbf{p}^2 - M^2) \\ =& \int_{d^3p} \int_0^\infty d\omega \; \frac{\partial n_{B/F}}{\partial T} \Theta(\omega^2 - \mathbf{p}^2 - M^2). \end{aligned} \tag{A.28}$$

In the last line we used that the width γ is always positive such that we can rewrite the sign-function into $\mathrm{sgn}(-2\gamma\omega) = \mathrm{sgn}(-\omega) = -\mathrm{sgn}(\omega)$. The whole integrand is then an even function of ω and we can restrict the integration to positive ω. For the further simplification we introduce a function $\sigma(\omega)$ with $-\frac{\partial\sigma}{\partial\omega} = \frac{\partial n_{B/F}}{\partial T}$:

$$\sigma(\omega) = \frac{\omega-\mu}{T} n_B(\omega) - \ln\left(1 - e^{-(\omega-\mu)/T}\right), \qquad \text{for Bosons,} \tag{A.29}$$

$$\sigma(\omega) = \frac{\omega-\mu}{T} n_F(\omega) + \ln\left(1 + e^{-(\omega-\mu)/T}\right), \qquad \text{for Fermions.} \tag{A.30}$$

We can then explicitly perform the ω-integration by integration by parts. The derivative of the Θ-function is given by

$$\begin{aligned} \frac{\partial}{\partial\omega}\Theta(\omega^2 - \mathbf{p}^2 - M^2) =& 2\omega\delta(\omega^2 - \mathbf{p}^2 - M^2) \\ =& \frac{2\omega}{|2\omega_p|}(\delta(\omega-\omega_p) + \delta(\omega+\omega_p)) \\ =& \delta(\omega-\omega_p) - \delta(\omega+\omega_p), \end{aligned} \tag{A.31}$$

where $\omega_p = \sqrt{\mathbf{p}^2 + M^2}$ is the energy of a relativistic particle with the effective mass M. This leads to:

$$\begin{aligned} s^{(0)} &= \int_{d^3p}\int_0^\infty d\omega\ \frac{\partial n_{B/F}}{\partial T}\Theta(\omega^2 - \mathbf{p}^2 - M^2) \\ &= -\int_{d^3p}\left[\sigma(\omega)\Theta(\omega^2 - \mathbf{p}^2 - M^2)\right]_0^\infty + \int_{d^3p}\int_0^\infty d\omega\ \sigma(\omega)(\delta(\omega-\omega_p) + \delta(\omega+\omega_p)) \\ &= \int_{d^3p}\sigma(\omega_p) \\ &= \frac{1}{2\pi^2}\int_0^\infty dp\ p^2\left(\frac{\omega_p-\mu}{T} n_{B/F}(\omega_p) - S\ln\left(1 - Se^{-(\omega_p-\mu)/T}\right)\right), \end{aligned} \tag{A.32}$$

with $S = 1$ for bosons and $S = -1$ for fermions. The on-shell entropy density is the entropy density for a system of non-interacting particles with the dispersion relation $\omega_p^2 = \mathbf{p}^2 + M^2$. One can further simplify this expression by integrating the logarithm by parts, if the quasiparticle mass M is momentum independent. This gives

$$-S\int_0^\infty dp\ p^2\ln\left(1 - Se^{-(\omega_p-\mu)/T}\right) = \int_0^\infty dp\ \frac{p^4}{3\omega_p T} n_{B/F} \tag{A.33}$$

and leads finally to the on-shell entropy density

$$s^{(0)} = \frac{1}{2\pi^2 T}\int_0^\infty dp\ p^2\left(\frac{\frac{4}{3}p^2 + M^2}{\omega_p} n_{B/F} - \mu\ n_{B/F}\right), \tag{A.34}$$

that is equivalent to Eq. (2.34). The off-shell part Δs, with the explicit form of the selfenergy and the propagator, reads

$$\begin{aligned} \Delta s &= \int_{d^4p}\frac{\partial n_{B/F}(\omega)}{\partial T}\left(\mathrm{Im}\Pi\ \mathrm{Re}D - \arctan\left(\frac{\mathrm{Im}D^{-1}}{\mathrm{Re}D^{-1}}\right)\right) \\ &= \int_{d^4p}\frac{\partial n_{B/F}(\omega)}{\partial T}\left(2\gamma\omega\frac{\omega^2 - \mathbf{p}^2 - M^2}{(\omega^2 - \mathbf{p}^2 - M^2)^2 + 4\gamma^2\omega^2} - \arctan\left(\frac{2\gamma\omega}{\omega^2 - \mathbf{p}^2 - M^2}\right)\right). \end{aligned} \tag{A.35}$$

This part of the entropy contains the imaginary part of the selfenergy and therefore the particle width γ and vanishes in the on-shell limit $\gamma \to 0$.
The particle density is obtained in the same way. Here we use $\sigma(\omega) = n_{B/F}(\omega)$ with $-\frac{\partial \sigma}{\partial \omega} = \frac{\partial n_{B/F}}{\partial \mu}$. The on-shell density then becomes the density of a system of non-interacting particles with the dispersion relation $\omega_p^2 = \mathbf{p}^2 + M^2$,

$$n^{(0)} = -\int_{d^4p} \frac{\partial n_{B/F}}{\partial \mu} \pi \ \mathrm{sgn}(\mathrm{Im}D^{-1})\Theta(\mathrm{Re}D^{-1}) = \frac{1}{2\pi^2}\int_0^\infty dp\ p^2 n_{B/F}(\omega_p), \tag{A.36}$$

which is equivalent to Eq. (2.35). The off-shell part reads

$$\begin{aligned}\Delta n_{B/F} &= \int_{d^4p} \frac{\partial n_{B/F}(\omega)}{\partial \mu}\left(\mathrm{Im}\Pi\ \mathrm{Re}D - \arctan\left(\frac{\mathrm{Im}D^{-1}}{\mathrm{Re}D^{-1}}\right)\right) \\ &= \int_{d^4p} \frac{\partial n_{B/F}(\omega)}{\partial \mu}\left(2\gamma\omega\frac{\omega^2 - \mathbf{p}^2 - M^2}{(\omega^2 - \mathbf{p}^2 - M^2)^2 + 4\gamma^2\omega^2} - \arctan\left(\frac{2\gamma\omega}{\omega^2 - \mathbf{p}^2 - M^2}\right)\right).\end{aligned} \tag{A.37}$$

It has the same form as the off-shell entropy density (A.35) but with the distribution function differentiated with respect to the chemical potential instead of the temperature. It also vanishes in the on-shell limit $\gamma \to 0$.
The entropy and particle density for QCD are obtained by considering gluons and quarks with the corresponding degeneracy factors. The expressions for antiparticles are obtained by replacing $\mu \to -\mu$ and $\frac{\partial n(\mu)}{\partial \mu} \to \frac{\partial n(-\mu)}{\partial \mu}$. This ensures that the density vanishes for zero chemical potential.
The mass and width dependent integrand in Δs and Δn,

$$F(\omega, \mathbf{p}) = 2\gamma\omega\frac{\omega^2 - \mathbf{p}^2 - M^2}{(\omega^2 - \mathbf{p}^2 - M^2)^2 + 4\gamma^2\omega^2} - \arctan\left(\frac{2\gamma\omega}{\omega^2 - \mathbf{p}^2 - M^2}\right), \tag{A.38}$$

has a discontinuity at $\omega^2 = \mathbf{p}^2 + M^2$, where the arctan jumps from $-\pi/2$ to $\pi/2$. We show $F(\omega, \mathbf{p})$ as a function of the momentum in Fig. A.1 for $M = 0.5$ GeV and $\gamma = 50$ MeV. It is positive for all energies smaller than the mass, but these parts are strongly suppressed. The dotted line shows the integrand for $w = M/2$ and is multiplied by a factor of 500 to be visible. If the energy is larger than the mass $F(\omega, \mathbf{p})$ has also negative contributions, but the positive parts are weighted more due to the jacobian $\mathbf{p}^2$ in the momentum integration. From the formula (A.38) alone it is not clear if the momentum integration in Δs and Δn is finite. Nevertheless, it was shown in Ref. [78] that the off-shell contribution to the entropy Δs is finite and positive. This is due to the decrease of $\frac{\partial n}{\partial T}$ for $\omega \to \infty$. For Δn we have $\frac{\partial n}{\partial \mu}$ instead of $\frac{\partial n}{\partial T}$. This function has the same behavior for $\omega \to \infty$ as $\frac{\partial n}{\partial T}$. Therefore, we can conclude that also the off-shell contribution to the density Δn is finite and positive.
In general the rule holds that an increase of the mass decreases the entropy and the density, while they increase with increasing width. If the width becomes as large as the mass $M = \gamma$, one gets the Stefan-Boltzmann limit of a massless particle:

$$\begin{aligned} s(M, \gamma = M) &= s^{(0)}(M) + \Delta s(M, \gamma = M) = s^{(0)}(M = 0), \\ n(M, \gamma = M) &= n^{(0)}(M) + \Delta n(M, \gamma = M) = n^{(0)}(M = 0).\end{aligned} \tag{A.39}$$

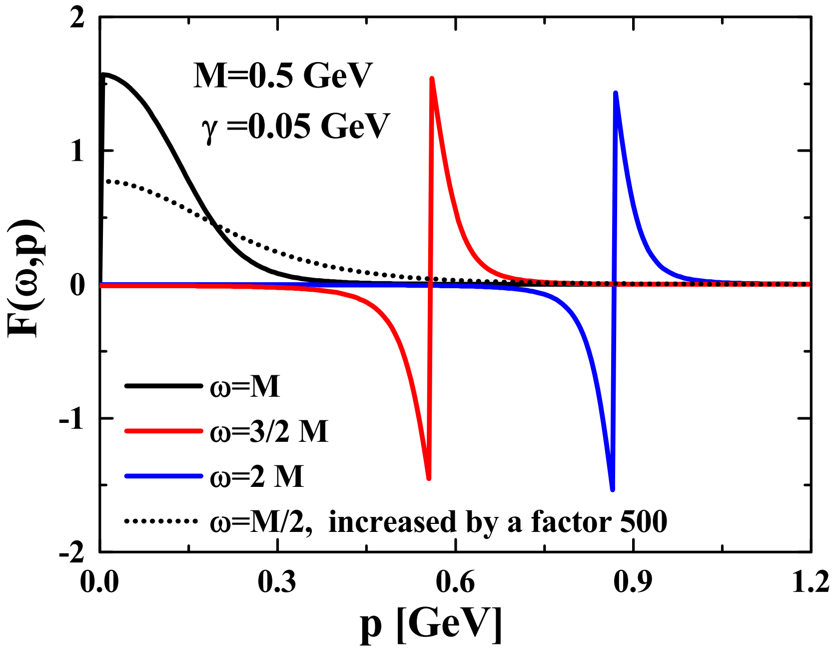

Figure A.1: The integrand (A.38) as a function of the three-momentum $|\mathbf{p}|$ for a mass of $M = 0.5$ GeV and a width of $\gamma = 50$ MeV, for various energies. The dotted line for an energy of $\omega = M/2$ is multiplied by a factor of 500. The discontinuity at $p^2 = \omega^2 - M^2$ is a finite jump from $-\pi/2$ to $\pi/2$. The black line for the energy $\omega = M$ jumps to zero for $|\mathbf{p}| = 0$.

The reason is, that the propagator inside the light cone vanishes for $M = \gamma$, so one retains only the parts directly on the light cone [153]. This is characteristic for a massless particle.

To demonstrate the impact of the off-shell contribution we show in Fig. A.2 the ratio of the off-shell and the on-shell entropy $\Delta s/s^{(0)}$ from the DQPM for QCD, i.e. 36 quarks and 16 gluons, at vanishing chemical potential $\mu = 0$. The entropy is dominated by the on-shell contribution, the off-shell part gives only a small contribution of a few percent. The ratio decreases for increasing temperatures until it falls below 1% at $T = 500$ MeV. This explains the success of default quasiparticle models, that neglect the imaginary part of the selfenergies [81, 82, 163].

The pressure of the DQPM is unknown as we are still not able to calculate the functional Φ in Eq. (A.2) (see Appendix A.1), but we derived the entropy and the density using the thermodynamic relations

$$-\frac{\partial \Omega}{\partial T} = \frac{\partial P}{\partial T} = s, \qquad\qquad -\frac{\partial \Omega}{\partial \mu} = \frac{\partial P}{\partial \mu} = n. \tag{A.40}$$

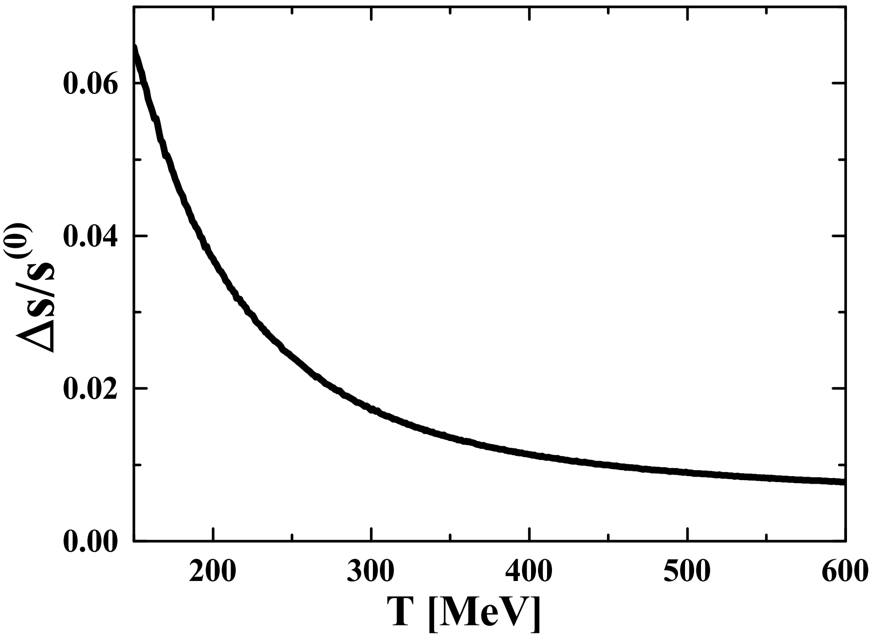

Figure A.2: The ratio between the off-shell Δs and the on-shell contribution $s^{(0)}$ to the DQPM entropy density for QCD at vanishing chemical potential.

We calculate the pressure in a thermodynamically consistent way by integrating s over T or n over μ, respectively. At zero chemical potential the pressure is then given by

$$P(T) = \int_0^T s(T')dT' = \int_{T_0}^T s(T')dT' + P_0, \tag{A.41}$$

where $P_0 = P(T_0, \mu = 0)$ is an input parameter taken as $P_0 = 0.0003$ GeV^4 at $T_0 =$ 150 MeV in accordance with lQCD calculations from Ref. [90]. If we further integrate over the particle density we also get the pressure at finite μ,

$$P(T, \mu) = \int_0^T s(T', 0)dT' + \int_0^\mu n(T, \mu')d\mu'. \tag{A.42}$$

The energy density follows in a thermodynamically consistent way from Eq. (2.21).
An alternative approach suggested in Ref. [398] sets T_0 to infinity and uses the well-known Stefan-Boltzmann pressure for P_0. The equation of state then follows by integrating down in T from infinitely large temperatures. This has the advantage, that one does not need P_0, but one has to make several assumptions to define the equation of state at the large temperatures needed.

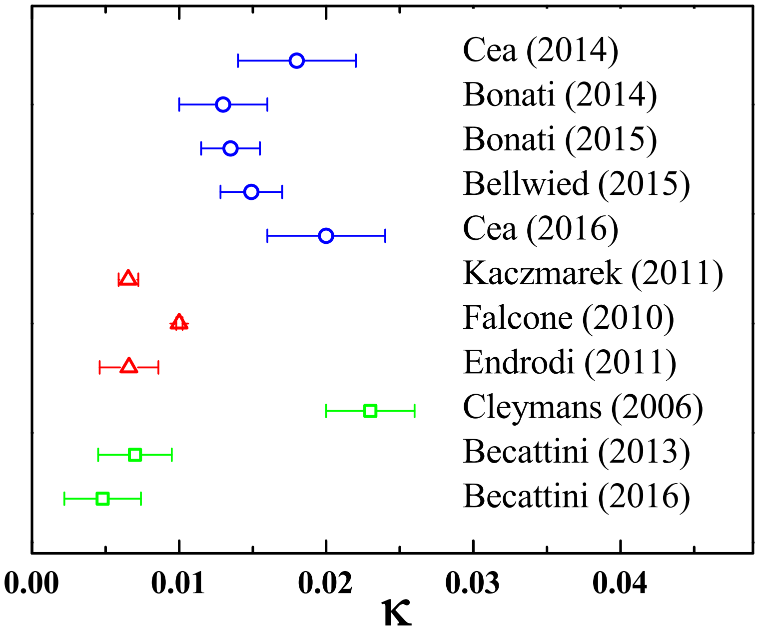

Figure A.3: Curvature parameter κ from lQCD calculations and heavy-ion phenomenology. The blue circles were obtained from lattice calculations by analytic continuation from imaginary chemical potential [167, 399, 400, 401, 402], the red triangles from lattice calculations via Taylor expansions [403, 404, 405] and the green squares from freezeout analysis of heavy-ion collisions [378, 379, 380].

A.3 Curvature parameter

The critical temperature of QCD is known only at vanishing chemical potential. At small chemical potentials it can be estimated by the curvature parameter κ,

$$\frac{T_c(\mu_B)}{T_c} = 1 - \kappa \left(\frac{\mu_B}{T_c}\right)^2 + \cdots . \tag{A.43}$$

This parameter can be calculated in lQCD simulations in terms of analytic continuation from imaginary chemical potentials or by Taylor expansions. It is also possible to determine the parameter from freezeout analysis of heavy-ion collisions where it follows from the freezeout temperature obtained by the statistical hadronization model. We show the curvature parameter from different groups in Fig. A.3. The blue circles are results from lattice calculations by analytic continuation [167, 399, 400, 401, 402], the red triangles from lattice calculations via Taylor expansions [403, 404, 405] and the green squares from a freezeout analysis from heavy-ion collisions [378, 379, 380].

The result from Cea et al. [399, 402] used $N_f = 2 + 1$ staggered fermions and the HISQ/tree gauge action. They fixed the ratio $m_l/m_s = 1/20$ and put the strange quark to its physical mass. Bonati et al. [167, 400] used $N_f = 2 + 1$ stout improved staggered fermions and a tree level Symanzik gauge action. They used physical quark masses and implied strangeness neutrality. The latter work used also a fixed ratio of charge to baryon number density of $N_Q/N_B = 0.4$ to match the conditions in Au+Au collisions. The result from Bellwied et al. [401] was obtained with $N_f = 2{+}1{+}1$ four times smeared staggered fermions and a tree level Symanzik gauge action with physical quark masses and strangeness neutrality. Kaczmarek et al. [403] used $N_f = 2 + 1$ staggered fermions and the p4 action with physical quark masses and strangeness neutrality. Falcone et al. [404] used the same action but with a pion mass of $m_\pi = 220$ MeV and without strangeness neutrality. Endrodi et al. [405] used stout improved staggered fermions and a Symanzik improved gauge action with physical quark masses and strangeness neutrality.

There is a clear difference between the curvature parameters obtained from analytic continuation and from the Taylor expansion with the κ's from the analytic continuation being larger by a factor of two. The curvature parameters from the freezeout analysis κ^f do not correspond to the QCD phase transition but to the freezeout line, which marks the region in the phase diagram at which the system becomes so dilute, that inelastic collisions stop and the particle yields of the different hadron species do not change anymore. The κ^f from Ref. [378] agrees with the κ's from the analytic continuation and the more recent κ^f's from Refs. [379, 380] agree with the Taylor expansion. There is a recent analysis of freezeout data in terms of lQCD results that constrained the κ^f's to $\kappa^f < 0.011$ [406]. This, however, is incompatible with the κ^f from Cleymans et al. [378] and the κ's from analytic continuation and would favor the smaller curvatures from the Taylor expansion. Nevertheless, when using freezeout data there are several limitations to consider, see Ref. [407] for a recent discussion. The freezeout curve should be below the phase transition, which implies $\kappa^f > \kappa$, but the freezeout temperature at vanishing chemical potential is usually above the critical temperature expected from lQCD calculations. One should also consider that the hadron yields after hadronization get influenced by the final (elastic) interactions, that change the extracted freezeout parameters. Moreover, since the medium in heavy-ion collisions is not in a thermodynamic equilibrium, different observables freeze out under different conditions and one can not define a unique freezeout temperature. All this problems have to be taken into account before one can relate the freezeout data to the real QCD phase transition.

Given all the uncertainties in the freezeout analysis we assume the freezeout κ^f's to not represent the actual trend of the critical temperature at small chemical potential. We will use the curvature parameters from analytic continuation that are more recent than the κ's from Taylor expansions. After rescaling the κ's of the two results from Cea et al. [399, 402] with a factor 2/3 to account for the missing strangeness neutrality, we see that all five results are consistent with each other $\kappa \approx 0.0135$.

A.4 Thermodynamic consistent scaling hypothesis

The flow equation ensures the thermodynamic consistency of the DQPM/DQPM*, but is numerically much more expensive than the scaling hypothesis. Comparing the results from both approaches in Fig. 3.14 shows that the scaling hypothesis can indeed repro-

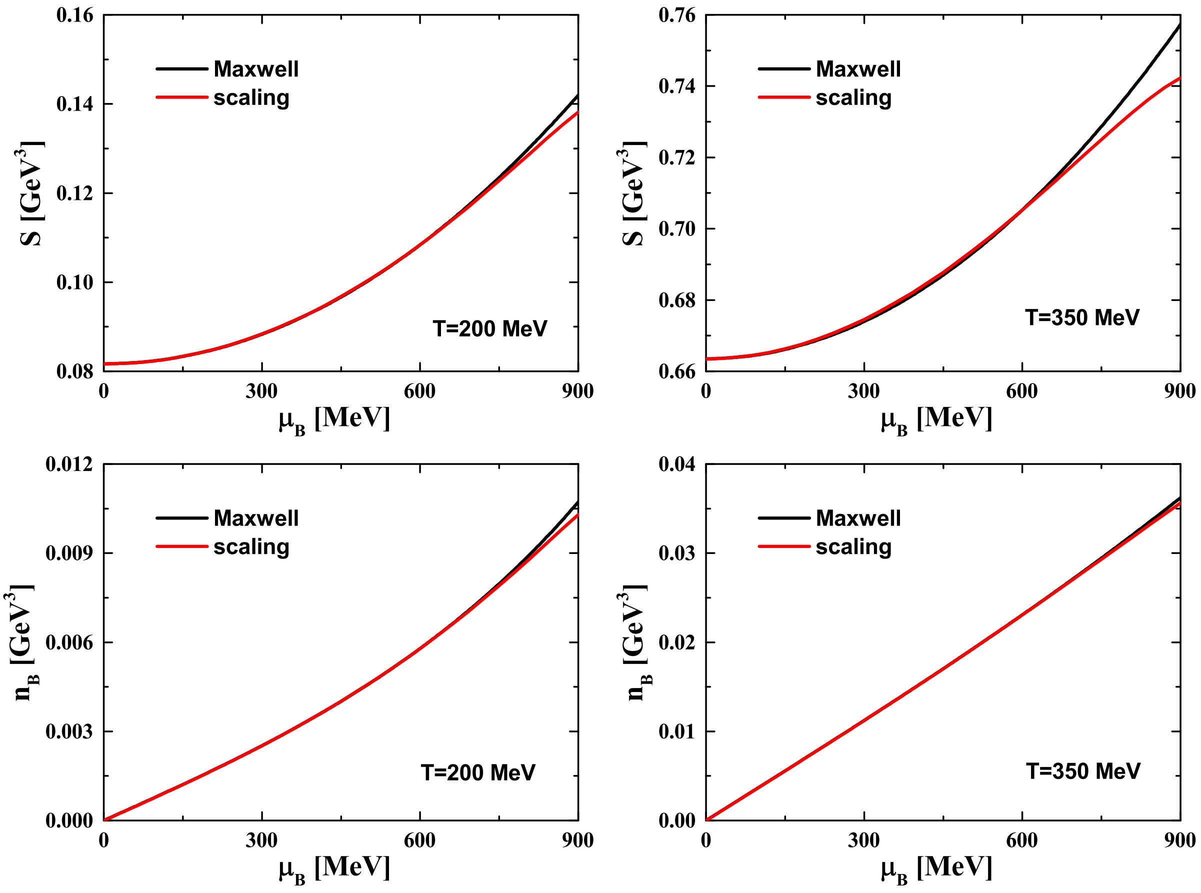

Figure A.4: Entropy and baryon number density for different temperatures as a function of the baryon chemical potential. The black lines show the thermodynamic consistent results derived from the flow equation and the black lines the results from the modified scaling hypothesis.

duce the baryon number density of the flow equation at small baryon chemical potentials, if the density is calculated from the quasiparticle density $n^{dqp} = n^{(0)} + \Delta n$ given by Eqs. (A.36) and (A.37). This seems surprising at first, since the effective couplings of both approaches differ significantly even at small μ_B, see Fig. 3.12. However, the density at small baryon chemical potentials is controlled by the susceptibility χ_B,

$$n_B \approx \chi_B \cdot \mu_B, \tag{A.44}$$

that is independent from the actual values of the effective coupling at finite μ_B. These influence the density only at baryon chemical potentials larger than the temperature. We can use this fact to extend the agreement between the flow equation and the scaling hypothesis up to much larger chemical potentials. The scaling hypothesis assumes an elliptic shape of the critical temperature $T_c(\mu_B)$ at finite baryon chemical potential, cf. Eq. (3.38). The curvature of the ellipse is controlled by the parameter $\alpha = 0.974$ GeV^{-2}, that we determined from phenomenology. We change the value of the parameter such

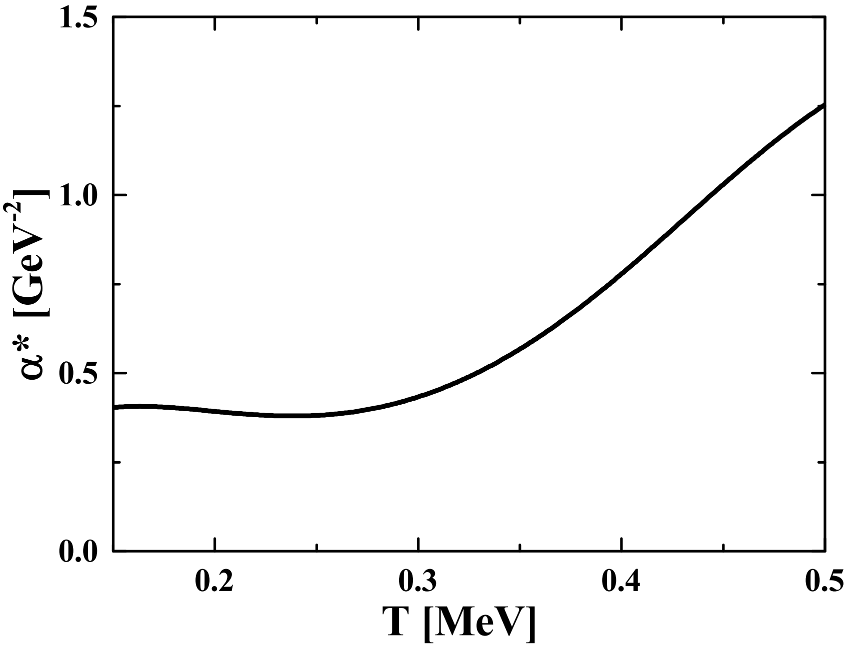

Figure A.5: The effective α^* as a function of temperature.

that the effective coupling coincides with the coupling from the flow equation at $\mu_B =$ 600 MeV:

$$g^2_{scaling}(T, \mu_B = 600 \text{ MeV}) = g^2_{flow}(T, \mu_B = 600 \text{ MeV}). \tag{A.45}$$

We show in Fig. A.4 the entropy and the baryon number density for $T = 200$ MeV and $T = 350$ MeV with the modified α^*. The results coincide with the predictions from the flow equation up to $\mu_B \approx 700$ MeV. Unfortunately, it is not possible to use the same value of α^* for all temperatures. Instead, we take the parameter as a function and determine its value for each temperature. The resulting $\alpha^*(T)$ is shown in Fig. A.5. The function can be fitted by a polynomial of order 5 with the coefficients given by:

$a_0 = -0.679$ $a_1 = 19.45$ $a_2 = -122.99$

$a_3 = 321.65$ $a_4 = -307.79$ $a_5 = 63.55.$

The equation of state calculated from this modified scaling hypothesis agrees with the equation of state from the flow equation for all baryon chemical potentials smaller than 700 MeV and is therefore also thermodynamic consistent.

A.5 Thermodynamic potential of the NJL model

The NJL model contains no gluons only quarks. The NJL Lagrangian is the free Dirac Lagrangian (2.25) with a space-time local 4-point-interaction that emerges from a Fierz-transformation of the QCD Lagrangian (2.44) [228, 229]. For one flavor it reads

$$\mathcal{L}_{NJL} = \bar{\Psi}\left(i\gamma^{\mu}\partial_{\mu} - m_0\right)\Psi + G\left(\left(\bar{\Psi}\Psi\right)^2 + \left(\bar{\Psi}i\gamma_5\Psi\right)^2\right). \tag{A.46}$$

We solve the model in the mean-field approximation. For this we replace the fields in the interaction term by their expectation value:

$$\bar{\Psi}\Psi = \langle\bar{\Psi}\Psi\rangle + \delta\bar{\Psi}\Psi \qquad \Rightarrow \qquad \left(\bar{\Psi}\Psi\right)^2 \approx \langle\bar{\Psi}\Psi\rangle^2 + 2\langle\bar{\Psi}\Psi\rangle\delta\bar{\Psi}\Psi = 2\langle\bar{\Psi}\Psi\rangle\bar{\Psi}\Psi - \langle\bar{\Psi}\Psi\rangle^2. \tag{A.47}$$

The expectation value $\langle\bar{\Psi}\Psi\rangle$ is the definition of the chiral condensate. The terms quadratic in the fluctuations are neglected in this approximation $\left(\delta\bar{\Psi}\Psi\right)^2 \approx 0$; the expectation value of the term in the isovector channel vanishes and gives no contribution $\langle\bar{\Psi}i\gamma_5\Psi\rangle = 0$. The Lagrangian in mean-field approximation is then given by

$$\mathcal{L}_{\langle NJL\rangle} = \bar{\Psi}\left(i\gamma^{\mu}\partial_{\mu} - \left(m_0 - 2G\langle\bar{\Psi}\Psi\rangle\right)\right)\Psi - G\langle\bar{\Psi}\Psi\rangle^2. \tag{A.48}$$

We have pulled parts of the interaction in the mass term of the free Lagrangian where it gives rise to an effective quark mass $M = m_0 - 2G\langle\bar{\Psi}\Psi\rangle$. This mass is independent from the fields but does depend on the medium. It illustrates the relation between chiral symmetry breaking and the constituent quark mass.

The NJL Lagrangian is not unique and one can add additional terms that give contributions in the mean-field limit. We use the three-flavor Lagrangian [44]:

$$\begin{aligned}\mathcal{L}_{NJL} =& \bar{\Psi}\left(i\gamma^{\mu}\partial_{\mu} - \hat{m}_0\right)\Psi + G\sum_{a=0}^{8}\left(\left(\bar{\Psi}\lambda^a\Psi\right)^2 + \left(\bar{\psi}i\gamma_5\tau_a\Psi\right)^2\right) \\ &- K\left(\det{}_f\left(\bar{\Psi}\left(1+\gamma_5\right)\Psi\right) + \det{}_f\left(\bar{\Psi}\left(1-\gamma_5\right)\Psi\right)\right).\end{aligned} \tag{A.49}$$

The λ^a are the Gell-Mann matrices in flavor space with $\lambda^0 = \sqrt{2/3}\,\mathbb{1}_3$ and $\bar{\Psi} = (\bar{u}, \bar{d}, \bar{s})$, $\Psi = (u, d, s)^T$. The mean-field approximation of this Lagrangian reads,

$$\mathcal{L}_{\langle NJL\rangle} = \sum_{u,d,s}\bar{q}_f\left(i\gamma^{\mu}\partial_{\mu} - M_f\right)q_f - 2G\left(\langle\bar{u}u\rangle + \langle\bar{d}d\rangle + \langle\bar{s}s\rangle\right) + 4K\langle\bar{u}u\rangle\langle\bar{d}d\rangle\langle\bar{s}s\rangle, \tag{A.50}$$

with the effective masses

$$M_i = m_{0i} - 4G\langle\bar{q}_iq_i\rangle + 2K\langle\bar{q}_jq_j\rangle\langle\bar{q}_kq_k\rangle, \tag{A.51}$$

with $i \neq j \neq k$. The model is solved once we determine the quark condensates $\langle\bar{q}_fq_f\rangle$ and solve the gap equations (A.51). There are various methods to derive the equations for the condensates. The standard way is to write down the Dyson equation, as shown in the reviews [44, 162, 228, 229]. The interaction term in mean-field or Hartree-Fock approximation is just a closed quark loop that gives the expectation value of the quark propagator, i.e. the quark condensate. One has to evaluate this expectation value using methods from thermal field theory which leads to the equations for the condensates.

Since we are interested in the condensates for finite temperature and chemical potential, we will use thermodynamic consistency to derive the equations for the condensates. This approach leads to the same result and gives us also access to the thermodynamics. We will first derive the thermodynamic potential of the NJL model in mean-field approximation. We use that the condensates $\langle \bar{q}_f q_f \rangle$ in (A.50) are independent from the fields $\bar{q}_f$ and q_f and therefore just normal $\mathbb{C}$-numbers. We split the Lagrangian in a part that contains the operators and a part that contains the mean-fields $\mathcal{L}_{MF}$. The mean-field Lagrangian is thus also a $\mathbb{C}$-number. The other part $\mathcal{L}_{Dirac}$, that contains the operators, is the free Lagrangian of a Dirac field with the effective masses (A.51). Thanks to this simple Lagrangian,

$$\mathcal{L}_{\langle NJL \rangle} = \mathcal{L}_{Dirac} + \mathcal{L}_{MF}, \tag{A.52}$$

we can use the results from Sec. 2.2 where we already calculated the thermodynamic potential for the free theory. The additional term $\mathcal{L}_{MF}$ is easy to consider. As a $\mathbb{C}$-number it commutes with the free Lagrangian. We will insert the separated Lagrangian $\mathcal{L}_{\langle NJL \rangle}$ in the path integral for the partition function (2.23) and evaluate directly the thermodynamic potential

$$\begin{aligned} \Omega &= -\frac{T}{V} \ln \left(\int \mathcal{D}\bar{\Psi}\mathcal{D}\Psi \; \exp \left(\int_0^\beta d\tau \int d^3x \; \mathcal{L}_{\langle NJL \rangle} \right) \right) \\ &= -\frac{T}{V} \int_0^\beta d\tau \int d^3x \; \mathcal{L}_{MF} - \frac{T}{V} \ln \left(\int \mathcal{D}\bar{\Psi}\mathcal{D}\Psi \; \exp \left(\int_0^\beta d\tau \int d^3x \; \mathcal{L}_{Dirac} \right) \right). \end{aligned} \tag{A.53}$$

The integration of $\mathcal{L}_{MF}$ has to be evaluated in the context of thermal field theory where we use the imaginary-time formalism with $\tau = it$ in the boundaries $0 \leq \tau \leq \beta$ [229, 396], but since $\mathcal{L}_{MF}$ is a $\mathbb{C}$-number, we simply get

$$\int_0^\beta d\tau \int d^3x \; \mathcal{L}_{MF} = \beta V \mathcal{L}_{MF} = \frac{V}{T} \mathcal{L}_{MF}. \tag{A.54}$$

The thermodynamic potential is then the sum of the non-interacting potential (2.29) with the effective masses (A.51) and the mean-field Lagrangian

$$\Omega = \Omega_0 - \mathcal{L}_{MF}. \tag{A.55}$$

All field-independent parts of the Lagrangian are simply transferred into the thermodynamic potential with a sign change. This is a general statement that holds in all theories and not only in the NJL model. The thermodynamic potential of the three flavor NJL-models is therefore given by:

$$\begin{aligned} \Omega &= \sum_{u,d,s} \Omega_0(T, \mu_f, M_f) + 2G \left(\langle \bar{u}u \rangle^2 + \langle \bar{d}d \rangle^2 + \langle \bar{s}s \rangle^2 \right) - 4K \langle \bar{u}u \rangle \langle \bar{d}d \rangle \langle \bar{s}s \rangle \\ &= \Omega_{vac} - \sum_{u,d,s} P(T, \mu_f, M_f) + 2G \left(\langle \bar{u}u \rangle^2 + \langle \bar{d}d \rangle^2 + \langle \bar{s}s \rangle^2 \right) - 4K \langle \bar{u}u \rangle \langle \bar{d}d \rangle \langle \bar{s}s \rangle. \end{aligned} \tag{A.56}$$

The divergent vacuum part of the potential Ω_{vac}, that we dropped in the non-interacting theory, is more complicated to deal with in the NJL model. Simply neglecting this term

-as we did for the non-interacting theory- would mean that we have no interaction in the vacuum and thus the wrong hadron phenomenology. Unfortunately, the four-quark interaction has a dimensional coupling constant, that prevents the proper renormalization of the model. The vacuum part is therefore divergent but unrenormalizable.
There exist many different ways of regularization for the vacuum part like the three dimensional momentum cutoff, the four dimensional momentum cutoff, Pauli-Villars regularization, proper-time regularization and dimensional regularization. These five regularization schemes where compared in Ref. [408] for the two flavor NJL model. All methods showed a similar behavior for the meson properties and the phase structure, but differ for the location of the critical endpoint. We will use the most common approach, i.e. the three dimensional momentum cutoff or short 3D cutoff. The divergent integral is regularized by the introduction of a momentum cutoff in the integration:

$$\Omega_{vac} = -2N_cN_f \int \frac{d^3p}{(2\pi)^3}\,\omega_p \quad \to \quad \Omega_{vac}^{\mathrm{3D}} = -\frac{N_cN_f}{\pi^2}\int_0^\Lambda dp\; p^2\,\omega_p. \tag{A.57}$$

This is only necessary in the vacuum part since the other integrals are finite. With the thermodynamic potential at hand we can now derive the equations for the condensates. We remember that the differential form of the potential was fixed to contain only derivatives with respect to the temperature and the chemical potential, see Eq. (2.12). Thermodynamic consistency requires that the differentials of the potential with respect to additional parameters have to vanish. The condensates that enter the effective masses (A.51) are such additional parameters. By evaluating these equations we find the definition of the condensates,

$$\begin{aligned}
0 \overset{!}{=} \frac{\partial\Omega}{\partial\langle\bar{q}_iq_i\rangle} =& 4G\langle\bar{q}_iq_i\rangle - 4K\langle\bar{q}_jq_j\rangle\langle\bar{q}_kq_k\rangle \\
&+ \frac{\partial\Omega}{\partial M_i}\frac{\partial M_i}{\partial\langle\bar{q}_iq_i\rangle} + \frac{\partial\Omega}{\partial M_j}\frac{\partial M_j}{\partial\langle\bar{q}_iq_i\rangle} + \frac{\partial\Omega}{\partial M_k}\frac{\partial M_k}{\partial\langle\bar{q}_iq_i\rangle} \\
=& 4G\langle\bar{q}_iq_i\rangle - 4K\langle\bar{q}_jq_j\rangle\langle\bar{q}_kq_k\rangle - 4G\rho_s(T,\mu_i,M_i) \\
&+ 2K\langle\bar{q}_kq_k\rangle\rho_s(T,\mu_j,M_j) + 2K\langle\bar{q}_jq_j\rangle\rho_s(T,\mu_k,M_k), \\
=& 4G\left(\langle\bar{q}_iq_i\rangle - \rho_s(T,\mu_i,M_i)\right) + 2K\left(\langle\bar{q}_kq_k\rangle\rho_s(T,\mu_j,M_j)\right. \\
&+ \left.\langle\bar{q}_jq_j\rangle\rho_s(T,\mu_k,M_k) - 2\langle\bar{q}_jq_j\rangle\langle\bar{q}_kq_k\rangle\right),
\end{aligned} \tag{A.58}$$

with the definition of the scalar density $\frac{\partial\Omega}{\partial M_i} = \rho_s(T,\mu_i,M_i)$. Eq. (A.58) is fulfilled if the condensates are equal to the scalar density of the corresponding quark species,

$$\langle\bar{q}_fq_f\rangle = \frac{\partial\Omega}{\partial M_f} = -2N_c\int\frac{d^3p}{(2\pi)^3}\frac{M_f}{\omega_p}\left(\Theta\left(\Lambda^2-\mathbf{p}^2\right) - n_F(T,\mu_f,M_f) - n_{\bar{F}}(T,\mu_f,M_f)\right). \tag{A.59}$$

The evaluation of the thermal expectation value of the quark propagator in terms of thermal field theory leads to the same result, see Ref. [229]. The first term in Eq. (A.59) emerges from the vacuum part of the pressure and is therefore regularized in the same way. The other two terms contribute only at finite temperature and chemical potential. Here we can clearly see why we could not neglect the vacuum part. In this case the condensate in the vacuum would be zero. The NJL is solved numerically by iterating Eq. (A.59) together with Eq. (A.51).

We can rewrite Eq. (A.59) by using $\frac{\partial M_f}{\partial m_f} = 1$ to get the well know definition of the scalar condensate as the derivative of the thermodynamic potential with respect to the bare quark mass,

$$\langle \bar{q}_f q_f \rangle = \frac{\partial \Omega}{\partial M_f} = \frac{\partial \Omega}{\partial m_f}. \tag{A.60}$$

This is a general statement for QCD, while Eq. (A.59) applies only to the NJL model. We can derive Eq. (A.60) from the definition of the thermodynamic potential in propagator representation (A.2). We use the Dyson equation (A.3) to replace the fermionic selfenergy with the difference of the full and the bare inverse propagator $\Sigma S = S^{-1}S - S_0^{-1}S = 1 - S_0^{-1}S$. The bare fermionic propagator is the only quantity in Eq. (A.2) that depends explicitly in the bare quark mass m_0. All other quantities depend only implicitly on m_0 via the full propagator. However, the variation of the functional W with respect to the full propagators have to vanish (A.7). The derivative of the functional $W = \beta\Omega$ with respect to the bare quark mass is therefore given by the simple formula

$$\frac{\partial W}{\partial m_0} = \frac{\partial}{\partial m_0}\left(-\mathrm{Tr}\left[S_0^{-1}S\right]\right) = -\mathrm{Tr}\left[S\right], \tag{A.61}$$

with $\partial S_0^{-1}/\partial m_0 = 1$. The trace has to be evaluated in the same manner as the functional W in Appendix A.1. This leads to

$$\frac{\partial \Omega}{\partial m_0} = -\frac{T}{V}\,\mathrm{Tr}\left[S\right] = i\int \frac{d^4p}{(2\pi)^4}\mathrm{Tr}\left[S(p)\right] = \langle \bar{q}q \rangle, \tag{A.62}$$

which is the definition of the quark condensate (in the vacuum) [229, 409] [17]. Evaluating the equation at finite temperature leads to Eq. (A.59) [44].

The derivations so far where done considering only attractive scalar interactions. A rigorous treatment of the Fierz-transformation will also introduce repulsive interactions in the vector channel, see Ref. [228]. In the same way -as the scalar interaction leads to an effective mass- the vector interaction introduces an effective chemical potential,

$$\mu^* = \mu - G_V\langle q^\dagger q \rangle = \mu - G_V n, \tag{A.63}$$

that enters the thermal integrals instead of the actual chemical potential. The thermodynamic potential in the presence of a vector interaction is modified according to,

$$\Omega(T,\mu)_V = \Omega(T,\mu^*) - \frac{G_V}{2}n^2, \tag{A.64}$$

where n is the quark density corresponding to the chemical potential, $\langle q^\dagger q \rangle = n = -\frac{\partial \Omega}{\partial \mu}$. The repulsive interactions add the density as an additional parameter in the thermodynamic potential. It has therefore to fulfill the condition $\frac{\partial \Omega}{\partial n} = 0$. The solution of

---

[17] The definition of the condensate may change depending on the sign of the propagator.

this equation does minimize the potential but is a saddle point which, however, is not a problem. If one evaluates the thermal expectation value $\langle q^\dagger q\rangle$ one finds an equation that is equivalent to the condition $\frac{\partial\Omega}{\partial n} = 0$. The density is therefore not just an additional parameter but rooted deeper inside the theory [43]. If the equation has several solutions the physical solution is still the one that belongs to the smallest thermodynamic potential.
The strength of the vector coupling is related to the scalar coupling by $G_V = G/2$, but is mostly neglected since it has no effect on the results at vanishing chemical potential [162, 232]. We will also use this strategy and set the vector repulsion to zero. Note that a finite vector coupling has serious consequences for the location of the critical point that might even disappear for large repulsive interactions [235, 236, 237].

A.6 Polyakov loop in the PNJL

The PNJL Lagrangian is similar to the NJL Lagrangian but contains also the effective potential $\mathcal{U}(T,\phi,\bar{\phi})$ and the coupling to the gauge fields A^μ,

$$\begin{aligned}\mathcal{L}_{PNJL} =&\mathcal{L}_{NJL} + \bar{\Psi}\gamma_\mu A^\mu \Psi - \mathcal{U}(T,\phi,\bar{\phi})\\ =&\bar{\Psi}\left(i\gamma^\mu D_\mu - \hat{m}_0\right)\Psi + G\sum_{a=0}^{8}\left(\left(\bar{\Psi}\lambda^a\Psi\right)^2 + \left(\bar{\psi}i\gamma_5\tau_a\Psi\right)^2\right)\\ &- K\left(\det{}_f\left(\bar{\Psi}\left(1+\gamma_5\right)\Psi\right) + \det{}_f\left(\bar{\Psi}\left(1-\gamma_5\right)\Psi\right)\right) - \mathcal{U}(T,\phi,\bar{\phi}).\end{aligned} \tag{A.65}$$

Since we describe the gauge field A^μ by the traced Polyakov loop, it is not independent but an additional parameter like the chiral condensates $\langle \bar{q}_f q_f\rangle$ in the NJL-model. This implies that the partition function of the PNJL model contains no path integral over the gauge fields,

$$Z_{PNJL} = \int \mathcal{D}\bar{\Psi}\mathcal{D}\Psi\ \exp\left(\int_0^\beta d\tau \int d^3x\ \mathcal{L}_{PNJL}\right), \tag{A.66}$$

and allows for an easy evaluation of the thermodynamic potential similar to the NJL. The effective Polyakov potential $\mathcal{U}(T,\phi,\bar{\phi})$ will appear with an opposite sign in the thermodynamic potential additional to the NJL mean-field part. The treatment of the gauge field, however, is a little more complicated. For this we have to look at the zeroth component of the covariant derivative that defines the kinetic momentum,

$$\Pi^0 = iD^0 = i\partial^0 + A^0 = i\partial^0 + iA_4. \tag{A.67}$$

We will show for the relativistic mean-field theories in Sec. 5.2 and Appendix A.8 that this translates into an effective chemical potential μ^* with

$$\mu^* = \mu + iA_4, \tag{A.68}$$

where the chemical potential is now a matrix in color space. The evaluation of the thermodynamic potential, except for the color trace, is then the same as in the NJL model in Eq. (A.53), but with an effective chemical potential in addition to the effective mass,

$$\Omega_{PNJL}(T,\mu) = \mathrm{Tr}_c \sum_f \Omega_{0,f}(T,\mu_f^*,M_f) - \mathcal{L}_{MF} + \mathcal{U}(T,\phi,\bar{\phi}). \tag{A.69}$$

We will use Eq. (4.9) to separate the Polyakov loops from the thermal distribution functions:

$$\exp\left(-\frac{\omega-\mu^*}{T}\right) = \exp\left(-\frac{\omega-\mu-iA_4}{T}\right) = L\ \exp\left(-\frac{\omega-\mu}{T}\right), \tag{A.70}$$

$$\exp\left(-\frac{\omega+\mu^*}{T}\right) = \exp\left(-\frac{\omega+\mu+iA_4}{T}\right) = L^\dagger \exp\left(-\frac{\omega+\mu}{T}\right). \tag{A.71}$$

Using the form of the thermodynamic potential for a non-interacting gas of fermions from Eq. (2.29) we find that we have just to evaluate the quantity:

$$\mathrm{Tr}_c\left[\ln\left(1+L\ e^{-\frac{\omega_p-\mu}{T}}\right)+\ln\left(1+L^\dagger e^{-\frac{\omega_p+\mu}{T}}\right)\right]. \tag{A.72}$$

Before we actually do this we will first rewrite the Polyakov loop. It is convenient to work in the Polyakov gauge where the Polyakov loop is diagonal in color space [253]. This implies that only the diagonal Gell-Mann matrices λ_3 and λ_8 contribute to the gauge field A_4:

$$L = \exp\left(i\frac{A_4}{T}\right) = \exp\left(i\begin{pmatrix} a_3+\frac{a_8}{\sqrt{3}} & 0 & 0 \\ 0 & -a_3+\frac{a_8}{\sqrt{3}} & 0 \\ 0 & 0 & -2\frac{a_8}{\sqrt{3}}\end{pmatrix}\right) = \begin{pmatrix} e^{i\alpha} & 0 & 0 \\ 0 & e^{i\tilde{\alpha}} & 0 \\ 0 & 0 & e^{-i(\alpha+\tilde{\alpha})}\end{pmatrix}, \tag{A.73}$$

with $\alpha = a_3 + \frac{a_8}{\sqrt{3}}$ and $\tilde{\alpha} = -a_3 + \frac{a_8}{\sqrt{8}}$. The traced Polyakov loop in this representation reads

$$\phi = \frac{1}{3}\mathrm{Tr}_c\ L\ = \frac{1}{3}\left(e^{i\alpha}+e^{i\tilde{\alpha}}+e^{-i(\alpha+\tilde{\alpha})}\right), \tag{A.74}$$

$$\bar{\phi} = \frac{1}{3}\mathrm{Tr}_c\ L^\dagger = \frac{1}{3}\left(e^{-i\alpha}+e^{-i\tilde{\alpha}}+e^{i(\alpha+\tilde{\alpha})}\right). \tag{A.75}$$

In the confining vacuum we have to get $\mathrm{Tr}_c\ L = 0$ and in the perturbative vacuum $\mathrm{Tr}_c\ L = N_c = 3$ to reproduce the confining properties of QCD. This can be achieved with $\alpha = \frac{2\pi}{\sqrt{3}}$ and $\tilde{\alpha} = 0$ in the confining vacuum and $\alpha = \tilde{\alpha} = 0$ in the perturbative vacuum. Generally assuming $\tilde{\alpha} = 0$ implies that the traces of the Polyakov and the adjoint Polyakov loop are equal $\phi = \mathrm{Tr}_c\ L/3 = \mathrm{Tr}_c\ L^\dagger/3 = \bar{\phi} = \mathrm{Re}\ \phi$. Since the differences between both arise from quantum fluctuations [47], this corresponds to the mean-field approximation. Only a single parameter is then needed to describe the whole Polyakov loop dynamics

$$\phi = \frac{1}{3}\mathrm{Tr}_c\ L = \frac{1+2\cos\alpha}{3}. \tag{A.76}$$

Eq. (A.74) and (A.75) allow to simplify the matrix valued expression (A.72) in the thermodynamic potential. With the explicit form of the Polyakov loop the terms read

$$\begin{aligned}
\mathrm{Tr}_c \ln\left(1 + L\ e^{x}\right) &= \ln\left(1 + e^{i\alpha} e^{x}\right) + \ln\left(1 + e^{i\tilde{\alpha}} e^{x}\right) + \ln\left(1 + e^{-i(\alpha+\tilde{\alpha})} e^{x}\right) \\
&= \ln\left[\left(1 + e^{i\alpha} e^{x}\right)\left(1 + e^{i\tilde{\alpha}} e^{x}\right)\left(1 + e^{-i(\alpha+\tilde{\alpha})} e^{x}\right)\right] \qquad \text{(A.77)} \\
&= \ln\left[1 + \left(e^{i\alpha} + e^{i\tilde{\alpha}} + e^{-i(\alpha+\tilde{\alpha})}\right) e^{x} + \left(e^{-i\alpha} + e^{-i\tilde{\alpha}} + e^{i(\alpha+\tilde{\alpha})}\right) e^{2x} + e^{3x}\right] \\
&= \ln\left[1 + 3\ \phi\ e^{x} + 3\ \bar{\phi}\ e^{2x} + e^{3x}\right]
\end{aligned}$$

and

$$\mathrm{Tr}_c \ln\left(1 + L^{\dagger}\ e^{x}\right) = \ln\left[1 + 3\ \bar{\phi}\ e^{x} + 3\ \phi\ e^{2x} + e^{3x}\right]. \qquad \text{(A.78)}$$

The Dirac part of the thermodynamic potential, after taking the color trace, is then given by:

$$\begin{aligned}
\Omega_{0,PNJL} = -2N_f \int \frac{d^3p}{(2\pi)^3} \Bigg[& N_c\ \omega_p + T \ln\left(1 + 3\ \phi\ e^{-\frac{\omega_p-\mu}{T}} + 3\ \bar{\phi}\ e^{-2\frac{\omega_p-\mu}{T}} + e^{-3\frac{\omega_p-\mu}{T}}\right) \\
& + T \ln\left(1 + 3\ \bar{\phi}\ e^{-\frac{\omega_p+\mu}{T}} + 3\ \phi\ e^{-2\frac{\omega_p+\mu}{T}} + e^{-3\frac{\omega_p+\mu}{T}}\right)\Bigg]. \qquad \text{(A.79)}
\end{aligned}$$

This expression is only valid for the special case of $N_c = 3$. For any other number of colors we have to reevaluate the color trace. We use the same regularization for the divergent vacuum part in Eq. (A.79) as we did for the NJL model in Eq. (A.57) and employ a three dimensional momentum cutoff. Additionally we use partial integration on the logarithm, as we did in Eq. (2.33), to rewrite the potential into a more common form:

$$\begin{aligned}
\frac{\Omega_{0,PNJL}}{V} &= -2N_f \frac{1}{2\pi^2} \int_0^{\infty} dp \Bigg[p^2\ N_c\ \omega_p\ \Theta\left(\Lambda^2 - \mathbf{p}^2\right) \\
&\quad + \frac{p^4}{3\omega_p} \left(\frac{3\ \phi\ e^{-\frac{\omega_p-\mu}{T}} + 6\ \bar{\phi}\ e^{-2\frac{\omega_p-\mu}{T}} + 3\ e^{-3\frac{\omega_p-\mu}{T}}}{1 + 3\ \phi\ e^{-\frac{\omega_p-\mu}{T}} + 3\ \bar{\phi}\ e^{-2\frac{\omega_p-\mu}{T}} + e^{-3\frac{\omega_p-\mu}{T}}} \right. \\
&\quad \left. + \frac{3\ \bar{\phi}\ e^{-\frac{\omega_p+\mu}{T}} + 6\ \phi\ e^{-2\frac{\omega_p+\mu}{T}} + 3\ e^{-3\frac{\omega_p+\mu}{T}}}{1 + 3\ \bar{\phi}\ e^{-\frac{\omega_p+\mu}{T}} + 3\ \phi\ e^{-2\frac{\omega_p+\mu}{T}} + e^{-3\frac{\omega_p+\mu}{T}}} \right) \Bigg] \\
&= -2N_f N_c \frac{1}{2\pi^2} \int_0^{\infty} dp \Bigg[p^2\ \omega_p\ \Theta\left(\Lambda^2 - \mathbf{p}^2\right) \qquad \text{(A.80)} \\
&\quad + \frac{p^4}{3\omega_p} \left(\frac{\phi\ e^{-\frac{\omega_p-\mu}{T}} + 2\ \bar{\phi}\ e^{-2\frac{\omega_p-\mu}{T}} + e^{-3\frac{\omega_p-\mu}{T}}}{1 + 3\ \phi\ e^{-\frac{\omega_p-\mu}{T}} + 3\ \bar{\phi}\ e^{-2\frac{\omega_p-\mu}{T}} + e^{-3\frac{\omega_p-\mu}{T}}} \right. \\
&\quad \left. + \frac{\bar{\phi}\ e^{-\frac{\omega_p+\mu}{T}} + 2\ \phi\ e^{-2\frac{\omega_p+\mu}{T}} + e^{-3\frac{\omega_p+\mu}{T}}}{1 + 3\ \bar{\phi}\ e^{-\frac{\omega_p+\mu}{T}} + 3\ \phi\ e^{-2\frac{\omega_p+\mu}{T}} + e^{-3\frac{\omega_p+\mu}{T}}} \right) \Bigg].
\end{aligned}$$

We see from Eq. (A.80) that it looks very similar to the potential of a non-interacting particle, but with a different distribution function. If one redefines the distribution functions of the quarks according to

$$n_F = \frac{1}{e^{\frac{\omega_p-\mu}{T}}+1} \quad \longrightarrow \quad n_F^{\phi} = \frac{\phi\, e^{-\frac{\omega_p-\mu}{T}} + 2\,\bar{\phi}\, e^{-2\frac{\omega_p-\mu}{T}} + e^{-3\frac{\omega_p-\mu}{T}}}{1+3\,\phi\, e^{-\frac{\omega_p-\mu}{T}} + 3\,\bar{\phi}\, e^{-2\frac{\omega_p-\mu}{T}} + e^{-3\frac{\omega_p-\mu}{T}}}, \tag{A.81}$$

$$n_{\bar{F}} = \frac{1}{e^{\frac{\omega_p+\mu}{T}}+1} \quad \longrightarrow \quad n_{\bar{F}}^{\bar{\phi}} = \frac{\bar{\phi}\, e^{-\frac{\omega_p+\mu}{T}} + 2\,\phi\, e^{-2\frac{\omega_p+\mu}{T}} + e^{-3\frac{\omega_p+\mu}{T}}}{1+3\,\bar{\phi}\, e^{-\frac{\omega_p+\mu}{T}} + 3\,\phi\, e^{-2\frac{\omega_p+\mu}{T}} + e^{-3\frac{\omega_p+\mu}{T}}}, \tag{A.82}$$

one can use the known formulae (2.33), (2.34), (2.35) and (2.36) for a non-interacting gas of fermions to calculate the non-interacting parts of the pressure, the entropy density, the particle density and the energy of the PNJL model [84]. For the full energy and pressure one still has to add the mean-field energy and the effective Polyakov potential and for the full entropy density the temperature derivative of the effective Polyakov potential.

A.7 Hadronic degrees of freedom

We summarize in this section the hadronic particles contained in PHSD. Tab. A.1 shows the mesons and Tab. A.2 baryons. Tab. A.3 shows additionally the scalar 0^+ mesons.

	Mass [MeV]	el. charge	spin	quark content	degeneracy
$\pi^{+/-}$	138	±1	0	ud̄/dū	2
π^0	138	0	0	dd̄/uū	1
η	550	0	0	dd̄/uū	1
$K^{+/-}$	498	±1	0	us̄/sū	2
$K^0/\bar{K}^0$	498	0	0	ds̄/sd̄	2
η'	958	0	0	dd̄/uū	1
$\rho^{+/-}$	770	±1	1	ud̄/dū	6
ρ^0	770	0	1	dd̄/uū	3
$K^{*+/-}$	892	±1	1	us̄/sū	6
$K^{*0}/\bar{K}^{*0}$	892	0	1	ds̄/sū	6
ω	782	0	1	dd̄/uū	3
ϕ	1020	0	1	ss̄	3
a_1	1260	0	1	dd̄/uū	3

Table A.1: Properties of the mesons contained in the PHSD transport approach.

	Mass [MeV]	el. charge	spin	quark content	degeneracy
p	938	$+1$	1/2	uud	2
n	938	0	1/2	udd	2
Λ	1115	0	1/2	uds	2
$\Sigma^{+/0/-}$	1189	$+1/0/-1$	1/2	uus/uds/dds	6
$\Xi^{0/-}$	1315	$0/-1$	1/2	uss/dss	4
$\Delta^{++/+/0/-}$	1232	$+2/+1/0/-1$	3/2	uuu/uud/udd/ddd	16
$\Sigma^{*+/0/-}$	1385	$+1/0/-1$	3/2	uss/uds/dds	12
$\Xi^{*0/-}$	1530	$0/-1$	3/2	uss/dss	8
Ω	1672	-1	3/2	sss	4
N(1440)	1440	$+1/0$	1/2	uud/udd	4
N(1535)	1535	$+1/0$	1/2	uud/udd	4

Table A.2: Properties of the baryons contained in the PHSD transport approach.

	σ	f_0	a_0	κ
Mass [MeV]	500	980	980	720
degeneracy	1	1	3	4
el. charge	0	0	$+1/0/-1$	±1

Table A.3: Properties of the scalar meson nonet. Note that the scalar mesons might not have a normal quark-antiquark structure.

A.8 Density-dependent relativistic mean-field theory

The Lagrangian of the isospin symmetric QHD consists of the free Dirac Lagrangian for the nucleons, the Lagrangian for the σ and the ω-field with selfinteractions and an interaction part of Yukawa type for the nucleon-meson interactions. The couplings are taken as a function of a Lorentz scalar $\hat{\rho}_0$, that depends on the nucleon fields $\bar{\Psi}$ and Ψ.

$$\mathcal{L} = \mathcal{L}_B + \mathcal{L}_M + \mathcal{L}_{int}, \tag{A.83}$$

$$\mathcal{L}_B = \bar{\Psi}\left(i\gamma_\mu\partial^\mu - M\right)\Psi, \tag{A.84}$$

$$\mathcal{L}_M = \frac{1}{2}\partial_\mu\sigma\partial^\mu\sigma - U(\sigma) - \frac{1}{4}F_{\mu\nu}F^{\mu\nu} + O(\omega^\mu\omega_\mu), \tag{A.85}$$

$$\mathcal{L}_{int} = \Gamma_\sigma(\hat{\rho}_0)\bar{\Psi}\sigma\Psi - \Gamma_\omega(\hat{\rho}_0)\bar{\Psi}\gamma^\mu\omega_\mu\Psi. \tag{A.86}$$

The mesonic selfenergies $U(\sigma)$ and $O(\omega^\mu\omega_\mu)$ are not specified here. If the Lorentz scalar is taken as $\hat{\rho}_0 = \bar{\Psi}\Psi$ the couplings will depend on the scalar density (SDD) and if it is taken as $\hat{\rho}_0 = \bar{\Psi}u_\mu\gamma^\mu\Psi$ they will depend on the baryon density (VDD). The equations of motion derived from the Euler-Lagrange equations read,

$$\partial_\mu \partial^\mu \sigma + \frac{\partial U}{\partial \sigma} = \Gamma_\sigma(\hat{\rho}_0)\bar{\Psi}\Psi, \tag{A.87}$$

$$\partial_\nu F^{\mu\nu} + \frac{\partial O}{\partial \omega_\mu} = \Gamma_\omega(\hat{\rho}_0)\bar{\Psi}\gamma^\mu\Psi, \tag{A.88}$$

for the meson fields and

$$\begin{aligned}(i\gamma_\mu\partial^\mu - M)\Psi + \Gamma_\sigma(\hat{\rho}_0)\sigma\Psi - \Gamma_\omega(\hat{\rho}_0)\gamma_\mu\omega^\mu\Psi \\ +\frac{\partial\Gamma_\sigma(\hat{\rho}_0)}{\partial\hat{\rho}_0}\frac{\partial\hat{\rho}_0}{\partial\bar{\Psi}}\bar{\Psi}\sigma\Psi - \frac{\partial\Gamma_\omega(\hat{\rho}_0)}{\partial\hat{\rho}_0}\frac{\partial\hat{\rho}_0}{\partial\bar{\Psi}}\bar{\Psi}\gamma^\nu\omega_\nu\Psi = 0\end{aligned} \tag{A.89}$$

for the nucleon field. One can rearrange the equation of motion for the nucleons and write it in the form of the free Dirac equation as

$$\begin{aligned}0 &= \left(\gamma_\mu\left(i\partial^\mu - \hat{\Sigma}^\mu\right) - \left(M - \hat{\Sigma}^s\right)\right)\Psi \\ &= \left(\gamma_\mu\left(i\partial^\mu - \hat{\Sigma}^{\mu(0)} - \hat{\Sigma}^{\mu(r)}\right) - \left(M - \hat{\Sigma}^{s(0)} - \hat{\Sigma}^{s(r)}\right)\right)\Psi.\end{aligned} \tag{A.90}$$

In (A.90) $\hat{\Sigma}^s$ is the scalar selfenergy and modifies the mass while $\hat{\Sigma}^\mu$ is the vector selfenergy that modifies the four-momentum of the nucleons. The selfenergies are divided into two parts $\hat{\Sigma} = \hat{\Sigma}^{(0)} + \hat{\Sigma}^{(r)}$. The first one is the regular selfenergy $\hat{\Sigma}^{(0)}$, the second is the so called rearrangement selfenergy $\hat{\Sigma}^{(r)}$. The rearrangement selfenergies are the result of the density dependence of the couplings and contain terms that are included in the equations of motion but not in the Lagrangian. They arise from the differentiation of the couplings with respect to the $\bar{\Psi}$-field. The nature of the rearrangement selfenergies depends on the choice of the density $\hat{\rho}_0$. In case of SDD couplings we get

$$\frac{\partial\hat{\rho}_0}{\partial\bar{\Psi}} = \Psi, \tag{A.91}$$

and for VDD couplings

$$\frac{\partial\hat{\rho}_0}{\partial\bar{\Psi}} = u_\mu\gamma^\mu\Psi. \tag{A.92}$$

The first choice leads to a vanishing vector rearrangement selfenergy and the second to a vanishing scalar rearrangement selfenergy. We will specify $\hat{\rho}_0$ later and keep both the vector and the scalar rearrangement selfenergies in the following derivations.

The equations of motion (A.87), (A.88) and (A.90) are too complicated to be solved on the many-body level. We will therefore introduce the mean-field approximation to simplify the equations. In this approximation the quantum fluctuations in the mesonic equations of motion are neglected which is justified if the source terms become large. The right side of Eq. (A.87) and (A.88) are then replaced by their normal ordered expectation values. This leads to

$$\Gamma_\sigma(\hat{\rho}_0)\bar{\Psi}\Psi \to \Gamma_\sigma(\rho_0)\langle :\bar{\Psi}\Psi:\rangle, \qquad \Gamma_\omega(\hat{\rho}_0)\bar{\Psi}\gamma^\mu\Psi \to \Gamma_\omega(\rho_0)\langle :\bar{\Psi}\gamma^\mu\Psi:\rangle, \tag{A.93}$$

where $\langle : \bar{\Psi}\Psi : \rangle = \rho_s$ is the scalar density and $\langle : \bar{\Psi}\gamma^\mu\Psi : \rangle = j^\mu$ is the baryon current with $\langle : \bar{\Psi}\gamma^0\Psi : \rangle = j^0 = \rho_B$ as the baryon density [303]. The couplings depend now on the normal ordered expectation value of $\hat{\rho}_0$.

To further simplify the equations we introduce the local-density approximation (LDA). In the case that the density of the system is locally constant one can neglect the spatial derivatives of the meson fields. Since we are interested in the thermodynamics, this approximation is definitively justified. We can additionally neglect the time derivatives of the meson fields and the spatial components of the baryon current $\langle : \bar{\Psi}\gamma^i\Psi : \rangle$ since we investigate a stationary and homogenous system. The equations of motion (A.87), (A.88) and (A.90) simplify drastically within these approximations. The meson fields drop out as degrees of freedom as they are completely defined by the scalar and the baryon density,

$$\frac{\partial U}{\partial \sigma} = \Gamma_\sigma(\rho_0)\rho_s \tag{A.94}$$

$$\frac{\partial O}{\partial w^0} = \Gamma_\omega(\rho_0)\rho_B, \tag{A.95}$$

The spatial part of the ω-field vanishes $\vec{\omega} = 0$ and the field is defined by its zeroth component, that we denote from here on as ω. The spatial part of the normal vector selfenergy $\Sigma^{\mu(0)}$ will also vanish in this approximation because it is proportional to the $\vec{\omega}$-field and if we choose the nuclear restframe with $u^\mu = (1, 0, 0, 0)$ also the spatial vector rearrangement selfenergies will vanish due to Eq. (A.92). The complete vector selfenergy is then given by its zeroth component.

The selfenergies of the nucleons no longer depend on any field $\hat{\Sigma} \to \Sigma$ and are now simple $\mathbb{C}$-numbers. This allows us to use the known free Dirac spinors in the further evaluation. We write the equation of motion for the nucleons (A.90) as,

$$(\gamma^\mu \Pi_\mu - m^*)\, \Psi(x) = 0, \tag{A.96}$$

with $\Pi^0 = p^{*0} = p^0 - \Sigma^0$, $\vec{\Pi} = \vec{p}$ and $m^* = M - \Sigma^s$. In momentum space the equation reads

$$\left(\gamma^\mu p^*_\mu - m^*\right) u^*(p) = 0, \qquad \left(\gamma^\mu p^*_\mu + m^*\right) v^*(p) = 0 \tag{A.97}$$

with $u^*(p)$ as the effective spinor for particles and $v^*(p)$ as the effective spinor for antiparticles. This leads to the mass-shell condition

$$p^{*\mu} p^*_\mu - m^{*2} = 0 \qquad \Rightarrow \qquad p^{*0} = \pm\sqrt{\mathbf{p}^2 + m^{*2}}. \tag{A.98}$$

The effective spinors are obtained by replacing the mass and the energy with their effective values in the free Dirac spinors $u(p)$ and $v(p)$ and they will fulfill the relations,

$$\bar{u}^*_r u^*_s = \delta_{rs} = -\bar{v}^*_r v^*_s, \qquad \bar{u}^*_s \gamma^\mu u^*_s = \bar{v}^*_s \gamma^\mu v^*_s = \frac{\Pi^\mu}{m^*}. \tag{A.99}$$

With the abbreviations

$$\epsilon^+(\mathbf{p}) = \Pi^{0+} + \Sigma^0 = \sqrt{\mathbf{p}^2 + m^{*2}} + \Sigma^0, \qquad \epsilon^-(\mathbf{p}) = \Pi^{0-} + \Sigma^0 = -\sqrt{\mathbf{p}^2 + m^{*2}} + \Sigma^0 \tag{A.100}$$

the wave function and the conjugated wave function read

$$\Psi(x) = \int \frac{d^3p}{(2\pi)^3} \frac{m^*}{\omega^*(\mathbf{p})} \times \tag{A.101}$$

$$\sum_{\lambda=1}^{2} \Big(c_\lambda(\mathbf{p}) u_\lambda(\mathbf{p}) \exp(-i(\varepsilon^+(\mathbf{p})t - \mathbf{p}\cdot\mathbf{x})) + d_\lambda^\dagger(\mathbf{p}) v_\lambda(\mathbf{p}) \exp(i(\varepsilon^-(\mathbf{p})t - \mathbf{p}\cdot\mathbf{x})) \Big) ,$$

$$\bar{\Psi}(x) = \int \frac{d^3p}{(2\pi)^3} \frac{m^*}{\omega^*(\mathbf{p})} \times \tag{A.102}$$

$$\sum_{\lambda=1}^{2} \Big(c_\lambda^\dagger(\mathbf{p}) \bar{u}_\lambda(\mathbf{p}) \exp(+i(\varepsilon^+(\mathbf{p})t - \mathbf{p}\cdot\mathbf{x})) + d_\lambda(\mathbf{p}) \bar{v}_\lambda(\mathbf{p}) \exp(-i(\varepsilon^-(\mathbf{p})t - \mathbf{p}\cdot\mathbf{x})) \Big)$$

with $\omega^*(\mathbf{p}) = \sqrt{\mathbf{p}^2 + m^{*2}}$ as the always positive defined single-particle energy. This allows us to calculate the baryon density and the scalar density as

$$\rho_B = \langle : \bar{\Psi}\gamma^0\Psi : \rangle = d \int \frac{d^3p}{(2\pi)^3} \Big(\tilde{f}^*(\mathbf{p},T,\mu) - \bar{\tilde{f}}^*(\mathbf{p},T,\mu) \Big) , \tag{A.103}$$

$$\rho_s = \langle : \bar{\Psi}\Psi : \rangle = d \int \frac{d^3p}{(2\pi)^3} \frac{m^*}{\omega^*(\mathbf{p})} \Big(\tilde{f}^*(\mathbf{p},T,\mu) + \bar{\tilde{f}}^*(\mathbf{p},T,\mu) \Big) , \tag{A.104}$$

with the degeneracy factor $d = 4$ for nucleons. The functions $\tilde{f}$ and $\bar{\tilde{f}}$ are the distribution functions for fermions, respectively antifermions

$$\begin{aligned} \tilde{f}(\mathbf{p},T,\mu) &= \big(\exp\big(\big(\epsilon^+ - \mu\big)/T\big) + 1\big)^{-1} = \big(\exp\big(\big(\omega^*(\mathbf{p}) + \Sigma^0 - \mu\big)/T\big) + 1\big)^{-1} \\ &= \left(\exp\left(\left(\omega^*(\mathbf{p}) - \mu^*\right)/T\right) + 1\right)^{-1} = n_F(T,\mu^*,m^*), \end{aligned} \tag{A.105}$$

$$\begin{aligned} \bar{\tilde{f}}(\mathbf{p},T,\mu) &= \big(\exp\big(\big(-\epsilon^- + \mu\big)/T\big) + 1\big)^{-1} = \big(\exp\big(\big(\omega^*(\mathbf{p}) - \Sigma^0 + \mu\big)/T\big) + 1\big)^{-1} \\ &= \left(\exp\left(\left(\omega^*(\mathbf{p}) + \mu^*\right)/T\right) + 1\right)^{-1} = n_{\bar{F}}(T,\mu^*,m^*), \end{aligned} \tag{A.106}$$

and are related to the regular Fermi-distribution functions but with the effective chemical potential $\mu^* = \mu - \Sigma^0$ and the energy $\omega^*(\mathbf{p}) = \omega_p^* = \sqrt{\mathbf{p}^2 + m^{*2}}$.
This allows us to finally evaluate the equations that determine the meson fields, Eqs. (A.94) and (A.95), leaving us with two coupled selfconsistent equations that have to be solved simultaneously:

$$\frac{\partial U}{\partial \sigma} = \Gamma_\sigma(\rho_0)\ d \int \frac{d^3p}{(2\pi)^3} \frac{m^*}{\omega_p^*} \left(n_F(T,\mu^*,m^*) + n_{\bar{F}}(T,\mu^*,m^*) \right) , \tag{A.107}$$

$$\frac{\partial O}{\partial \omega} = \Gamma_\omega(\rho_0)\ d \int \frac{d^3p}{(2\pi)^3} \left(n_F(T,\mu^*,m^*) - n_{\bar{F}}(T,\mu^*,m^*) \right) . \tag{A.108}$$

A.9 Thermodynamic consistency of relativistic mean-field theory

We derive in this section the equation of state of the relativistic mean-field theory and prove the thermodynamic consistency of the approach. We recall that the approximations of a static and homogenous system as well as the local density approximation in Appendix A.8 are exactly fulfilled for a system in thermodynamic equilibrium. We will not derive the equation of state from the path integral formalism, but from the energy-momentum tensor,

$$T^{\mu\nu} = \frac{\partial \mathcal{L}}{\partial \left(\partial_\mu \Psi\right)} \frac{\partial \Psi}{\partial x_\nu} - g^{\mu\nu} \mathcal{L}. \tag{A.109}$$

Both approaches are equivalent, but the path integral formalism becomes more complicated for density-dependent coupling constants as one has to consider the rearrangement selfenergies. The energy density $\mathcal{E}$ and the pressure P of a system are given as normal ordered expectation values from the diagonal elements of the energy-momentum tensor,

$$\mathcal{E} = \langle : T^{00} : \rangle, \tag{A.110}$$

$$P = \langle : T^{ii} : \rangle = \frac{1}{3} \sum_{i=1}^{3} \langle : T^{ii} : \rangle. \tag{A.111}$$

For the following calculations we will write the selfenergies split into the normal and the rearrangement part. This is due to the fact that the rearrangement selfenergies appear in the equation of motion but not in the Lagrangian. The energy density in mean-field approximation is then given by

$$\begin{aligned} \mathcal{E} = \langle : T^{00} : \rangle =& \langle : i\bar{\Psi}\gamma^0 \partial_0 \Psi : \rangle - \langle : \bar{\Psi} \left(\gamma_\mu \left(i\partial^\mu - \Sigma^{\mu(0)} \right) - \left(M - \Sigma^{s(0)} \right) \right) \Psi : \rangle \\ &+ U(\sigma) - O(\omega) \\ =& \langle : i\bar{\Psi}\gamma^0 \partial_0 \Psi : \rangle - \underbrace{\langle : \bar{\Psi} \left(\gamma_\mu \Pi^\mu - m^* \right) \Psi : \rangle}_{=0} \\ &- \langle : \bar{\Psi} \left(\gamma_0 \Sigma^{0(r)} - \Sigma^{s(r)} \right) \Psi : \rangle + U(\sigma) - O(\omega) \\ =& \langle : i\bar{\Psi}\gamma^0 \partial_0 \Psi : \rangle - \Sigma^{0(r)} \rho_B + \Sigma^{s(r)} \rho_s + U(\sigma) - O(\omega), \end{aligned} \tag{A.112}$$

where we have used the equation of motion (A.90) to simplify the expression. With the given solutions for Ψ (A.101) and $\bar{\Psi}$ (A.102) we can further evaluate the first term:

$$\begin{aligned}
\mathcal{E} =& U(\sigma) - O(\omega) - \Sigma^{0(r)}\rho_B + \Sigma^{s(r)}\rho_s \\
&+ d\int \frac{d^3p}{(2\pi)^3}\frac{m^*}{\omega_p^*}\left(\epsilon^+(\mathbf{p})\langle : c_\lambda^\dagger(\mathbf{p})c_\lambda(\mathbf{p}) :\rangle - \epsilon^-(\mathbf{p})\langle : d_\lambda(\mathbf{p})d_\lambda^\dagger(\mathbf{p}) :\rangle\right) \\
=& U(\sigma) - O(\omega) - \Sigma^{0(r)}\rho_B + \Sigma^{s(r)}\rho_s \\
&+ d\int \frac{d^3p}{(2\pi)^3}\left(\left(\omega_p^* + \Sigma^0\right) n_F(T,\mu^*,m^*) - \left(-\omega_p^* + \Sigma^0\right) n_{\bar{F}}(T,\mu^*,m^*)\right) \qquad \text{(A.113)} \\
=& U(\sigma) - O(\omega) - \Sigma^{0(r)}\rho_B + \Sigma^{s(r)}\rho_s + \Sigma^{0(0)}\rho_B + \Sigma^{0(r)}\rho_B \\
&+ d\int \frac{d^3p}{(2\pi)^3}\,\omega_p^*\left(n_F(T,\mu^*,m^*) + n_{\bar{F}}(T,\mu^*,m^*)\right) \\
=& U(\sigma) - O(\omega) + \Sigma^{s(r)}\rho_s + \Sigma^{0(0)}\rho_B + d\int \frac{d^3p}{(2\pi)^3}\,\omega_p^*\left(n_F(T,\mu^*,m^*) + n_{\bar{F}}(T,\mu^*,m^*)\right) \\
=& U(\sigma) - O(\omega) + \Sigma^{s(r)}\rho_s + \Sigma^{0(0)}\rho_B + E_0(T,\mu^*,m^*).
\end{aligned}$$

Note that the vector rearrangement term has been canceled and gives no direct contribution to the energy density. In (A.113) E_0 is the energy density for a non-interacting particle, see Eq. (2.36), but evaluated at the effective chemical potential μ^* and with the effective mass m^*.

We will now calculate the pressure. Using again the equation of motion for the nucleon field (A.90), the pressure in mean-field approximation reads

$$P = \frac{1}{3}\sum_{i=1}^{3}\langle : T^{ii} :\rangle = -U(\sigma) + O(\omega) + \Sigma^{0(r)}\rho_B - \Sigma^{s(r)}\rho_s + \frac{1}{3}\sum_{i=1}^{3}\langle : i\bar{\Psi}\gamma^i\partial_i\Psi :\rangle. \qquad \text{(A.114)}$$

The further evaluation is analogue to the energy density and gives

$$\begin{aligned}
P =& -U(\sigma) + O(\omega) + \Sigma^{0(r)}\rho_B - \Sigma^{s(r)}\rho_s \\
&+ \frac{d}{3}\sum_{i=1}^{3}\int \frac{d^3p}{(2\pi)^3}\left(\frac{m^*}{\omega_p^*}\right)^2\left(\frac{p^i}{m^*}\langle : c_\lambda^\dagger(\mathbf{p})c_\lambda(\mathbf{p}) :\rangle p^i + \frac{p^i}{m^*}\langle : d_\lambda(\mathbf{p})d_\lambda^\dagger(\mathbf{p}) :\rangle p^i\right) \\
=& -U(\sigma) + O(\omega) + \Sigma^{0(r)}\rho_B - \Sigma^{s(r)}\rho_s \qquad \text{(A.115)} \\
&+ \frac{d}{3}\int \frac{d^3p}{(2\pi)^3}\frac{\mathbf{p}^2}{\omega_p^*}\left(n_F(T,\mu^*,m^*) + n_{\bar{F}}(T,\mu^*,m^*)\right) \\
=& -U(\sigma) + O(\omega) + \Sigma^{0(r)}\rho_B - \Sigma^{s(r)}\rho_s + P_0(T,\mu^*,m^*).
\end{aligned}$$

In (A.115) P_0 is the pressure for a non-interacting particle with the effective quantities μ^* and m^*. Contrary to the energy density (A.113) we get a direct contribution from the vector rearrangement term in the pressure. We can also see the basic feature of the path integral formalism, that the field-independent parts of the Lagrangian, in this case the mesonic selfenergies, appear directly in the pressure, cf. Eq. (A.55).

We will now check if the model is thermodynamic consistent. In nuclear matter ($T = 0$) this is tested by comparing the thermodynamic definition of the pressure to the mechanical definition via the energy momentum tensor

$$\rho_B^2 \frac{\partial}{\partial \rho_B} \left(\frac{E}{\rho_B} \right) = P = \frac{1}{3} \sum_{i=1}^{3} \langle : T^{ii} : \rangle . \tag{A.116}$$

This method is only sufficient in the canonical ensemble at $T = 0$ where the energy density is proportional to the thermodynamic potential. In the grand-canonical potential, where the thermodynamic potential is proportional to the pressure $\Omega = -P$, it is better to show that the thermodynamic definition of the energy density is identical to its mechanical definition,

$$E = Ts - P + \mu_B \rho_B \overset{!}{=} \langle : T^{00} : \rangle = \mathcal{E} . \tag{A.117}$$

Another important check concerns the differential form of the grand-canonical potential (2.12). The potential/pressure derived above depends via the selfenergies on the additional parameters σ, ω, ρ_s and ρ_B, that will also enter the differential form. It is therefore necessary that the derivatives of the pressure with respect to these parameters vanish to regain the known differential form of the thermodynamic potential,

$$\frac{\partial P}{\partial \sigma} = \frac{\partial P}{\partial \omega} = \frac{\partial P}{\partial \rho_s} = \frac{\partial P}{\partial \rho_B} = 0 . \tag{A.118}$$

We assume for now that the conditions (A.118) are fulfilled to prove Eq. (A.117). The entropy density is defined as the differential of the pressure with respect to the temperature

$$\begin{aligned} s = \frac{\partial P}{\partial T} &= \left. \frac{\partial P}{\partial T} \right|_{\sigma,\omega} + \underbrace{\frac{\partial P}{\partial \sigma}}_{=0} \frac{\partial \sigma}{\partial T} + \underbrace{\frac{\partial P}{\partial \omega}}_{=0} \frac{\partial \omega}{\partial T} + \underbrace{\frac{\partial P}{\partial \rho_s}}_{=0} \frac{\partial \rho_s}{\partial T} + \underbrace{\frac{\partial P}{\partial \rho_B}}_{=0} \frac{\partial \rho_B}{\partial T} \\ &= \frac{\partial P_0}{\partial T} = s_0(T, \mu^*, m^*) \end{aligned} \tag{A.119}$$

and takes the form of the non-interacting entropy density with the effective quantities μ^* and m^*. The same holds for the particle density,

$$\begin{aligned} n = \frac{\partial P}{\partial \mu} &= \left. \frac{\partial P}{\partial \mu} \right|_{\sigma,\omega} + \underbrace{\frac{\partial P}{\partial \sigma}}_{=0} \frac{\partial \sigma}{\partial \mu} + \underbrace{\frac{\partial P}{\partial \omega}}_{=0} \frac{\partial \omega}{\partial \mu} + \underbrace{\frac{\partial P}{\partial \rho_s}}_{=0} \frac{\partial \rho_s}{\partial \mu} + \underbrace{\frac{\partial P}{\partial \rho_B}}_{=0} \frac{\partial \rho_B}{\partial \mu} \\ &= \frac{\partial P_0}{\partial \mu} = n_0(T, \mu^*, m^*) = \rho_B , \end{aligned} \tag{A.120}$$

which is identical to its definition in Eq. (A.103). The thermodynamical definition of the energy density is then

$$\begin{aligned} E =&Ts - P + \mu n = Ts - P + \mu_B\rho_B \\ =&Ts_0(T,\mu^*,m^*) + U(\sigma) - O(\omega) - \Sigma^{0(r)}\rho_B + \Sigma^{s(r)}\rho_s \\ &- P_0(T,\mu^*,m^*) + \mu^* n_0(T,\mu^*,m^*) + (\mu-\mu^*)\rho_B \\ =&U(\sigma) - O(\omega) - \Sigma^{0(r)}\rho_B + \Sigma^{s(r)}\rho_s + \Sigma^0\rho_B + E_0(T,\mu^*,m^*) \\ =&U(\sigma) - O(\omega) + \Sigma^{s(r)}\rho_s + \Sigma^{0(0)}\rho_B + E_0(T,\mu^*,m^*) = \mathcal{E} \end{aligned} \tag{A.121}$$

and thus equal to the mechanical definition (A.110). This proves the thermodynamic consistency of the theory. Naturally this holds also in the canonical ensemble for $T = 0$. We will now discuss the explicit form of the selfenergies. To cover also the most general cases we assume that the scalar and the vector coupling depend on different densities $\hat{\rho}_\sigma$ and $\hat{\rho}_\omega$, that we take as

$$\hat{\rho}_\sigma = \alpha\bar{\Psi}\Psi + \beta\bar{\Psi}u^\mu\gamma_\mu\Psi, \qquad \hat{\rho}_\omega = \gamma\bar{\Psi}\Psi + \delta\bar{\Psi}u^\mu\gamma_\mu\Psi, \tag{A.122}$$

that translate in mean-field approximation to

$$\rho_\sigma = \alpha\rho_s + \beta\rho_B, \qquad \rho_\omega = \gamma\rho_s + \delta\rho_B. \tag{A.123}$$

The choice $\alpha = \gamma = 1$ and $\beta = \delta = 0$ leads to SDD couplings and the choice $\alpha = \gamma = 0$ and $\beta = \delta = 1$ to VDD couplings. The special case of $\alpha = \beta = \gamma = \delta = 0$ is the standard relativistic mean-field model with constant couplings.

The normal selfenergies are fixed by the Lagrangian and read in mean-field approximation:

$$\Sigma^{s(0)} = \Gamma_\sigma(\rho_\sigma)\sigma, \qquad \Sigma^{\mu(0)} = \Gamma_\omega(\rho_\omega)\omega^\mu = \Gamma_\omega(\rho_\omega)\omega\delta^{\mu 0}. \tag{A.124}$$

The rearrangement selfenergies follow from the equation of motion of the nucleons (A.89) and, using the densities from Eq. (A.122), are given by

$$\hat{\Sigma}^{s(r)} = \alpha\ \hat{\Gamma}'_\sigma\bar{\Psi}\sigma\Psi - \gamma\ \hat{\Gamma}'_\omega\bar{\Psi}\gamma^\mu\omega_\mu\Psi, \tag{A.125}$$

$$\hat{\Sigma}^{\mu(r)} = \left(-\beta\ \hat{\Gamma}'_\sigma\bar{\Psi}\sigma\Psi + \delta\ \hat{\Gamma}'_\omega\bar{\Psi}\gamma^\mu\omega_\mu\Psi\right)u^\mu. \tag{A.126}$$

In mean-field approximation they translate to

$$\Sigma^{s(r)} = \alpha\ \Gamma'_\sigma\sigma\rho_s - \gamma\ \Gamma'_\omega\omega\rho_B, \tag{A.127}$$

$$\Sigma^{0(r)} = -\beta\ \Gamma'_\sigma\sigma\rho_s + \delta\ \Gamma'_\omega\omega\rho_B, \tag{A.128}$$

where Γ' stands for $\partial\Gamma(\rho_0)/\partial\rho_0$. Some comment is useful in the special case of SDD couplings. If α or γ is different from zero the effective mass m^* or the effective chemical potential μ^* will depend on the scalar density. The scalar density ρ_s will therefore depend on itself implicitly and Eq. (A.104) becomes a selfconsistent equation, but unlike the other two selfconsistent equations this one does not follow from the mesonic equations

of motion! Consequently, ρ_s is defined once the selfconsistent equations (A.107) and (A.108) are solved.
With the selfenergies and the densities defined we can finally prove Eq. (A.118) and the thermodynamic consistency of the model. On the level of the selfenergies the derivative of the pressure with respect to $x \in \{\sigma, \omega, \rho_s, \rho_B\}$ is

$$\begin{aligned}
\frac{\partial P}{\partial x} =& - \frac{\partial U}{\partial x} + \frac{\partial O}{\partial x} + \frac{\partial \Sigma^{0(r)}}{\partial x}\rho_B + \Sigma^{0(r)}\frac{\partial \rho_B}{\partial x} - \frac{\partial \Sigma^{s(r)}}{\partial x}\rho_s - \Sigma^{s(r)}\frac{\partial \rho_s}{\partial x} + \frac{\partial P_0}{\partial x} \\
=& - \frac{\partial U}{\partial x} + \frac{\partial O}{\partial x} + \frac{\partial \Sigma^{0(r)}}{\partial x}\rho_B + \Sigma^{0(r)}\frac{\partial \rho_B}{\partial x} - \frac{\partial \Sigma^{s(r)}}{\partial x}\rho_s - \Sigma^{s(r)}\frac{\partial \rho_s}{\partial x} \\
&+ \underbrace{\frac{\partial P_0}{\partial \mu^*}\frac{\partial \mu^*}{\partial x}}_{-\rho_B \partial_x(\Sigma^0)} + \underbrace{\frac{\partial P_0}{\partial m^*}\frac{\partial m^*}{\partial x}}_{\rho_s \partial_x(\Sigma^s)} \\
=& - \frac{\partial U}{\partial x} + \frac{\partial O}{\partial x} + \Sigma^{0(r)}\frac{\partial \rho_B}{\partial x} - \Sigma^{s(r)}\frac{\partial \rho_s}{\partial x} - \rho_B\frac{\partial \Sigma^{0(0)}}{\partial x} + \rho_s\frac{\partial \Sigma^{s(0)}}{\partial x}.
\end{aligned} \tag{A.129}$$

Here we have used the relations $\frac{\partial m^*}{\partial m} = 1 = \frac{\partial \mu^*}{\partial \mu}$, which holds true since we treat ρ_s and ρ_B as variables, as well as $\frac{\partial P_0}{\partial \mu} = \rho_B$ and $\frac{\partial P_0}{\partial m} = -\rho_s$ that correspond to Eq. (A.103) and (A.104). For the further evaluation we have to use the exact forms of the selfenergies. We have to include the density dependence of the couplings while taking the derivatives:

$$\begin{aligned}
\frac{\partial P}{\partial x} =& - \frac{\partial U}{\partial \sigma}\frac{\partial \sigma}{\partial x} + \frac{\partial O}{\partial \omega}\frac{\partial \omega}{\partial x} + \left(-\beta\Gamma'_\sigma\sigma\rho_s + \delta\Gamma'_\omega\omega\rho_B\right)\frac{\partial \rho_B}{\partial x} - \left(\alpha\Gamma'_\sigma\sigma\rho_s - \gamma\Gamma'_\omega\omega\rho_B\right)\frac{\partial \rho_s}{\partial x} \\
&- \rho_B\left(\Gamma_\omega\frac{\partial \omega}{\partial x} + \Gamma'_\omega\omega\left(\gamma\frac{\partial \rho_s}{\partial x} + \delta\frac{\partial \rho_B}{\partial x}\right)\right) + \rho_s\left(\Gamma_\sigma\frac{\partial \sigma}{\partial x} + \Gamma'_\sigma\sigma\left(\alpha\frac{\partial \rho_s}{\partial x} + \beta\frac{\partial \rho_B}{\partial x}\right)\right) \\
=&\frac{\partial \sigma}{\partial x}\left(\Gamma_\sigma\rho_s - \frac{\partial U}{\partial \sigma}\right) + \frac{\partial \omega}{\partial x}\left(\frac{\partial O}{\partial \omega} - \Gamma_\omega\rho_B\right).
\end{aligned} \tag{A.130}$$

The derivatives vanish if the selfconsistent equations (A.107) and (A.108) -following from the mesonic equations of motion (A.87), (A.88)- are fulfilled. This finally proves Eq. (A.118), thus demonstrating the thermodynamic consistency of the model.
A special case is the equation $\partial P/\partial\rho_B = 0$. The conditions (A.118) should maximize the pressure, but $\partial P/\partial\rho_B = 0$ belongs to a saddle point, but this can be a problem if the condition follows only from thermodynamic consistency. This is not the case here as it emerges from the selfconsistent equation (A.108) and is therefore rooted deeper within the theory [43]. We discussed this problem already in Sec. 4.2 for the PNJL model.

A.10 Pion-nucleon σ-term

The pion-nucleon σ-term controls the drop of the chiral condensate as a function of the scalar density in Eq. (5.54). The constant is defined by the matrix element,

$$\sigma_{\pi N} = m_q\langle N|\bar{u}u + \bar{d}d|N\rangle, \tag{A.131}$$

with $|N\rangle$ denoting the nucleon state. One can relate it also to the nucleon mass using the Hellmann-Feynman theorem (5.53),

$$\sigma_{\pi N} = m \frac{\partial m_N(m)}{\partial m}\bigg|_{m=m_q}, \tag{A.132}$$

with the physical light quark mass $m_q = (m_u + m_d)/2 \approx 5$ to 7 MeV. It measures the amount of the nucleon mass, that originates from the explicit chiral symmetry breaking caused by the finite light quark masses. One can extract $\sigma_{\pi N}$ from πN scattering data [410, 411, 412], but one needs the πN scattering amplitude at the so called Cheng-Dashen point [413], that lies outside the physical region so one has to extrapolate the data. This procedure performed in Refs. [410, 411] leads to a value of $\sigma_{\pi N} \approx 59$ MeV.
Using Eq. (A.132) one can also determine $\sigma_{\pi N}$ in the framework of Dyson-Schwinger equations by solving the Faddeev equation and determining the nucleon mass for different quark masses [414, 415]. The most recent result from Ref. [415] is $\sigma_{\pi N} = 60$ MeV, consistent with Refs. [410, 411].
Another possibility to determine $\sigma_{\pi N}$ are lQCD calculations. One can either directly calculate the matrix element (A.131) or determine the baryon mass as a function of the bare quark masses and use the Hellmann-Feynman theorem (A.132). The first approach used in Refs. [416, 417, 418] leads to the values $\sigma_{\pi N} \approx 36$ MeV for an ensemble with two flavors [416, 417] and $\sigma_{\pi N} \approx 45$ MeV for an ensemble with 2+1 flavors [418]. The second approach used in Ref. [419] for a system with $2+1$ flavors leads to the value $\sigma_{\pi N} \approx 38$ MeV.
The results from the different lQCD groups are in the regime $\sigma_{\pi N} \approx 33 - 45$ MeV and therefore inconsistent with the phenomenological determination and the Dyson-Schwinger result. We refer to Ref. [412] for a discussion of this problem.
We will fix the value of the σ-term to $\sigma_{\pi N} = 45$ MeV. This value can be seen as the world average of $\sigma_{\pi N}$ and is in line with the lQCD results for $2+1$ flavors [418, 419]. We used several lattice results as input throughout this thesis and it is therefore consistent to choose $\sigma_{\pi N}$ as determined by the lQCD instead of the phenomenological result.

Bibliography

[1] I. Arsene *et al.* [BRAHMS Collaboration], Nucl. Phys. A **757**, 1 (2005).

[2] B. B. Back *et al.*, Nucl. Phys. A **757**, 28 (2005).

[3] J. Adams *et al.* [STAR Collaboration], Nucl. Phys. A **757**, 102 (2005).

[4] K. Adcox *et al.* [PHENIX Collaboration], Nucl. Phys. A **757**, 184 (2005).

[5] N. Cabibbo and G. Parisi, Phys. Lett. **59B**, 67 (1975).

[6] J. C. Collins and M. J. Perry, Phys. Rev. Lett. **34**, 1353 (1975).

[7] R. A. Lacey, Nucl. Phys. A **774**, 199 (2006).

[8] D. Teaney, J. Lauret and E. V. Shuryak, Phys. Rev. Lett. **86**, 4783 (2001).

[9] P. Huovinen, P. F. Kolb, U. W. Heinz, P. V. Ruuskanen and S. A. Voloshin, Phys. Lett. B **503**, 58 (2001).

[10] S. A. Voloshin, Nucl. Phys. A **715**, 379 (2003).

[11] T. Matsui and H. Satz, Phys. Lett. B **178**, 416 (1986).

[12] M. Gyulassy and M. Plumer, Phys. Lett. B **243**, 432 (1990).

[13] C. Adler *et al.* [STAR Collaboration], Phys. Rev. Lett. **90**, 082302 (2003).

[14] R. Baier, D. Schiff and B. G. Zakharov, Ann. Rev. Nucl. Part. Sci. **50**, 37 (2000).

[15] J. Rafelski and B. Müller, Phys. Rev. Lett. **48**, 1066 (1982) Erratum: [Phys. Rev. Lett. **56**, 2334 (1986)].

[16] P. Koch, B. Müller and J. Rafelski, Phys. Rept. **142**, 167 (1986).

[17] M. Gazdzicki, M. Gorenstein and P. Seyboth, Acta Phys. Polon. B **42**, 307 (2011).

[18] E. V. Shuryak, Phys. Lett. **78B**, 150 (1978) [Sov. J. Nucl. Phys. **28**, 408 (1978)] [Yad. Fiz. **28**, 796 (1978)].

[19] G. Domokos and J. I. Goldman, Phys. Rev. D **23**, 203 (1981).

[20] L. D. McLerran and T. Toimela, Phys. Rev. D **31**, 545 (1985).

[21] O. Linnyk, V. Konchakovski, T. Steinert, W. Cassing and E. L. Bratkovskaya, Phys. Rev. C **92**, no. 5, 054914 (2015).

[22] P. F. Kolb and U. W. Heinz, In *Hwa, R.C. (ed.) et al.: Quark gluon plasma* 634-714 [nucl-th/0305084].

[23] P. Romatschke, Int. J. Mod. Phys. E **19**, 1 (2010).

[24] U. Heinz and R. Snellings, Ann. Rev. Nucl. Part. Sci. **63**, 123 (2013).

[25] P. Kovtun, D. T. Son and A. O. Starinets, Phys. Rev. Lett. **94**, 111601 (2005).

[26] P. Danielewicz, Annals Phys. **152**, 239 (1984).

[27] P. Danielewicz, Annals Phys. **152**, 305 (1984).

[28] H. S. Köhler, Phys. Rev. C **51**, 3232 (1995).

[29] C. Greiner, K. Wagner and P. G. Reinhard, Phys. Rev. C **49**, 1693 (1994).

[30] L. P. Kadanoff and G. Baym, *Quantum Statistical Mechanics*, Benjamin, New York (1962).

[31] W. Cassing, Eur. Phys. J. ST **168**, 3 (2009).

[32] H. Petersen, J. Steinheimer, G. Burau, M. Bleicher and H. Stöcker, Phys. Rev. C **78**, 044901 (2008).

[33] S. A. Bass and A. Dumitru, Phys. Rev. C **61**, 064909 (2000).

[34] T. Hirano, U. W. Heinz, D. Kharzeev, R. Lacey and Y. Nara, Phys. Lett. B **636**, 299 (2006).

[35] Y. Aoki, Z. Fodor, S. D. Katz and K. K. Szabo, JHEP **0601**, 089 (2006).

[36] Y. Aoki, Z. Fodor, S. D. Katz and K. K. Szabo, Phys. Lett. B **643**, 46 (2006).

[37] Y. Aoki, S. Borsanyi, S. Dürr, Z. Fodor, S. D. Katz, S. Krieg and K. K. Szabo, JHEP **0906**, 088 (2009).

[38] S. Borsanyi *et al.* [Wuppertal-Budapest Collaboration], JHEP **1009**, 073 (2010).

[39] A. Bazavov *et al.*, Phys. Rev. D **85**, 054503 (2012).

[40] R. Bellwied, S. Borsanyi, Z. Fodor, J. Gunther, S. D. Katz, A. Pasztor, C. Ratti and K. K. Szabo, Nucl. Phys. A **956**, 797 (2016).

[41] J. Gunther, R. Bellwied, S. Borsanyi, Z. Fodor, S. D. Katz, A. Pasztor and C. Ratti, EPJ Web Conf. **137**, 07008 (2017).

[42] A. Bazavov *et al.*, Phys. Rev. D **95**, no. 5, 054504 (2017).

[43] M. Asakawa and K. Yazaki, Nucl. Phys. A **504**, 668 (1989).

[44] M. Buballa, Phys. Rept. **407**, 205 (2005).

[45] C. Ratti, M. A. Thaler and W. Weise, Phys. Rev. D **73**, 014019 (2006).

[46] P. Costa, C. A. de Sousa, M. C. Ruivo and H. Hansen, EPL **86**, no. 3, 31001 (2009).

[47] S. Roessner, C. Ratti and W. Weise, Phys. Rev. D **75**, 034007 (2007).

[48] B. J. Schaefer and J. Wambach, Phys. Rev. D **75**, 085015 (2007).

[49] B. J. Schaefer and M. Wagner, Phys. Rev. D **79**, 014018 (2009).

[50] T. K. Herbst, J. M. Pawlowski and B. J. Schaefer, Phys. Lett. B **696**, 58 (2011).

[51] R. A. Tripolt, N. Strodthoff, L. von Smekal and J. Wambach, Phys. Rev. D **89**, no. 3, 034010 (2014).

[52] C. E. Detar and T. Kunihiro, Phys. Rev. D **39**, 2805 (1989).

[53] A. Bochkarev and J. I. Kapusta, Phys. Rev. D **54**, 4066 (1996).

[54] O. Scavenius, A. Mocsy, I. N. Mishustin and D. H. Rischke, Phys. Rev. C **64**, 045202 (2001).

[55] J. T. Lenaghan, D. H. Rischke and J. Schaffner-Bielich, Phys. Rev. D **62**, 085008 (2000).

[56] C. D. Roberts and A. G. Williams, Prog. Part. Nucl. Phys. **33**, 477 (1994).

[57] C. D. Roberts and S. M. Schmidt, Prog. Part. Nucl. Phys. **45**, S1 (2000).

[58] R. Alkofer and L. von Smekal, Phys. Rept. **353**, 281 (2001).

[59] C. S. Fischer, J. Luecker and J. A. Mueller, Phys. Lett. B **702**, 438 (2011).

[60] C. S. Fischer and J. Luecker, Phys. Lett. B **718**, 1036 (2013).

[61] J. Berges, N. Tetradis and C. Wetterich, Phys. Rept. **363**, 223 (2002).

[62] J. M. Pawlowski, Annals Phys. **322**, 2831 (2007).

[63] H. Gies, Lect. Notes Phys. **852**, 287 (2012).

[64] J. Braun and H. Gies, JHEP **0606**, 024 (2006).

[65] J. Braun, J. Phys. G **39**, 033001 (2012).

[66] L. Fister and J. M. Pawlowski, Phys. Rev. D **88**, 045010 (2013).

[67] F. Rennecke and B. J. Schaefer, Phys. Rev. D **96**, no. 1, 016009 (2017).

[68] L. Adamczyk *et al.* [STAR Collaboration], Phys. Rev. Lett. **112**, 032302 (2014).

[69] L. Adamczyk *et al.* [STAR Collaboration], Phys. Rev. Lett. **112**, no. 16, 162301 (2014).

[70] L. Adamczyk *et al.* [STAR Collaboration], Phys. Lett. B **750**, 64 (2015).

[71] L. Adamczyk *et al.* [STAR Collaboration], Phys. Rev. C **96**, no. 4, 044904 (2017).

[72] STAR Collaboration, STAR Note 598,
https://drupal.star.bnl.gov/STAR/starnotes/public/sn0598

[73] C. Yang [STAR Collaboration], Nucl. Phys. A **967**, 800 (2017).

[74] B. Friman, C. Höhne, J. Knoll, S. Leupold, J. Randrup, R. Rapp and P. Senger, Lect. Notes Phys. **814**, pp.1 (2011).

[75] V. Kekelidze, R. Lednicky, V. Matveev, I. Meshkov, A. Sorin and G. Trubnikov, Phys. Part. Nucl. Lett. **9**, 313 (2012).

[76] B. J. Schaefer, J. M. Pawlowski and J. Wambach, Phys. Rev. D **76**, 074023 (2007).

[77] J. Braun, Eur. Phys. J. C **64**, 459 (2009).

[78] A. Peshier, Phys. Rev. D **70**, 034016 (2004).

[79] A. Peshier, J. Phys. G **31**, S371 (2005).

[80] A. Peshier, B. Kämpfer and G. Soff, Phys. Rev. C **61**, 045203 (2000).

[81] A. Peshier, B. Kämpfer and G. Soff, Phys. Rev. D **66**, 094003 (2002).

[82] S. Plumari, W. M. Alberico, V. Greco and C. Ratti, Phys. Rev. D **84**, 094004 (2011).

[83] A. Puglisi, S. Plumari and V. Greco, Phys. Lett. B **751**, 326 (2015).

[84] R. Marty, E. Bratkovskaya, W. Cassing, J. Aichelin and H. Berrehrah, Phys. Rev. C **88**, 045204 (2013).

[85] H. Berrehrah, W. Cassing, E. Bratkovskaya and T. Steinert, Phys. Rev. C **93**, no. 4, 044914 (2016).

[86] H. Berrehrah, E. Bratkovskaya, T. Steinert and W. Cassing, Int. J. Mod. Phys. E **25**, no. 07, 1642003 (2016).

[87] R. Dashen, S. K. Ma and H. J. Bernstein, Phys. Rev. **187**, 345 (1969).

[88] S. Borsanyi, Z. Fodor, S. D. Katz, S. Krieg, C. Ratti and K. Szabo, JHEP **1201**, 138 (2012).

[89] A. Bazavov *et al.* [HotQCD Collaboration], Phys. Rev. D **86**, 034509 (2012).

[90] S. Borsanyi, Z. Fodor, C. Hoelbling, S. D. Katz, S. Krieg and K. K. Szabo, Phys. Lett. B **730**, 99 (2014).

[91] A. Bazavov *et al.* [HotQCD Collaboration], Phys. Rev. D **90**, 094503 (2014).

[92] J. D. Walecka, Annals Phys. **83**, 491 (1974).

[93] R. Brockmann and R. Machleidt, Phys. Rev. C **42**, 1965 (1990).

[94] M. R. Anastasio, L. S. Celenza, W. S. Pong and C. M. Shakin, Phys. Rept. **100**, 327 (1983).

[95] B. Ter Haar and R. Malfliet, Phys. Rept. **149**, 207 (1987).

[96] A. Ramos and E. Oset, Nucl. Phys. A **671**, 481 (2000).

[97] L. Tolos, A. Ramos, A. Polls and T. T. S. Kuo, Nucl. Phys. A **690**, 547 (2001).

[98] L. Tolos, D. Cabrera and A. Ramos, Phys. Rev. C **78**, 045205 (2008).

[99] D. Cabrera, L. Tolós, J. Aichelin and E. Bratkovskaya, Phys. Rev. C **90**, no. 5, 055207 (2014).

[100] M. E. Peskin and D. V. Schroeder, *An Introduction to quantum field theory*, Addison-Wesley Publishing Company (2013).

[101] U. Mosel, *Path integrals in field theory: An introduction*, Springer, Berlin (2004).

[102] R. P. Feynman and A. R. Hibbs, *Quantum mechanics and path integrals*, McGraw-Hill, New York (1965).

[103] R. Kubo, J. Phys. Soc. Jap. **12**, 570 (1957).

[104] P. C. Martin and J. Schwinger, Phys. Rev. **115**, 1342 (1959).

[105] L. V. Keldysh, Zh. Eksp. Teor. Fiz. **47**, 1515 (1964) [Sov. Phys. JETP **20**, 1018 (1965)].

[106] R. van Leeuwen, N. E. Dahlen, G. Stefanucci, C. O. Almbladh and U. von Barth, *Introduction to the Keldysh Formalism*, Lect. Notes Phys. **706**, 33-59 (2006).

[107] J. I. Kapusta and C. Gale, *Finite-temperature field theory: Principles and applications*, Cambridge University Press (2006).

[108] T. Muta, World Sci. Lect. Notes Phys. **5**, 1 (1987).

[109] P. Braun-Munzinger and J. Wambach, Rev. Mod. Phys. **81**, 1031 (2009).

[110] D. J. Gross and F. Wilczek, Phys. Rev. Lett. **30**, 1343 (1973).

[111] H. D. Politzer, Phys. Rev. Lett. **30**, 1346 (1973).

[112] S. Klimt, M. F. M. Lutz, U. Vogl and W. Weise, Nucl. Phys. A **516**, 429 (1990).

[113] C. Jung, F. Rennecke, R. A. Tripolt, L. von Smekal and J. Wambach, Phys. Rev. D **95**, no. 3, 036020 (2017).

[114] S. Weinberg, Phys. Rev. Lett. **18**, 507 (1967).

[115] J. I. Kapusta and E. V. Shuryak, Phys. Rev. D **49**, 4694 (1994).

[116] F. Karsch, J. Phys. Conf. Ser. **46**, 122 (2006).

[117] L. D. McLerran and B. Svetitsky, Phys. Rev. D **24**, 450 (1981).

[118] L. D. McLerran and B. Svetitsky, Phys. Lett. **98B**, 195 (1981).

[119] M. A. Stephanov, K. Rajagopal and E. V. Shuryak, Phys. Rev. Lett. **81**, 4816 (1998).

[120] P. de Forcrand, J. Langelage, O. Philipsen and W. Unger, Phys. Rev. Lett. **113**, no. 15, 152002 (2014).

[121] C. S. Fischer, J. Luecker and C. A. Welzbacher, Phys. Rev. D **90**, no. 3, 034022 (2014).

[122] R. Critelli, J. Noronha, J. Noronha-Hostler, I. Portillo, C. Ratti and R. Rougemont, Phys. Rev. D **96**, no. 9, 096026 (2017).

[123] L. McLerran and R. D. Pisarski, Nucl. Phys. A **796**, 83 (2007).

[124] Y. Hidaka, L. D. McLerran and R. D. Pisarski, Nucl. Phys. A **808**, 117 (2008).

[125] H. Suganuma, T. M. Doi, K. Redlich and C. Sasaki, J. Phys. G **44**, 124001 (2017).

[126] B. C. Barrois, Nucl. Phys. B **129**, 390 (1977).

[127] S. B. Ruester, V. Werth, M. Buballa, I. A. Shovkovy and D. H. Rischke, Phys. Rev. D **72**, 034004 (2005).

[128] C. Gattringer and C. B. Lang, Lect. Notes Phys. **788**, 1 (2010).

[129] C. DeTar and U. M. Heller, Eur. Phys. J. A **41**, 405 (2009).

[130] O. Philipsen, Eur. Phys. J. ST **152**, 29 (2007).

[131] N. Metropolis, A. W. Rosenbluth, M. N. Rosenbluth, A. H. Teller and E. Teller, J. Chem. Phys. **21**, 1087 (1953).

[132] W. K. Hastings, Biometrika **57**, 97 (1970).

[133] R. Sommer, PoS LATTICE **2013**, 015 (2014).

[134] S. Muroya, A. Nakamura, C. Nonaka and T. Takaishi, Prog. Theor. Phys. **110**, 615 (2003).

[135] S. Borsanyi, G. Endrodi, Z. Fodor, S. D. Katz, S. Krieg, C. Ratti and K. K. Szabo, JHEP **1208**, 053 (2012).

[136] S. Borsanyi, G. Endrodi, Z. Fodor, A. Jakovac, S. D. Katz, S. Krieg, C. Ratti and K. K. Szabo, JHEP **1011**, 077 (2010).

[137] M. Buballa, A. G. Grunfeld, A. E. Radzhabov and D. Scheffler, Prog. Part. Nucl. Phys. **62**, 365 (2009).

[138] F. Karsch, B. J. Schaefer, M. Wagner and J. Wambach, Phys. Lett. B **698**, 256 (2011).

[139] H. Haug, Statistische Physik - Gleichgewichtstheorie und Kinetik, Vieweg (1997).

[140] W. Botermans and R. Malfliet, Phys. Rept. **198**, 115 (1990).

[141] V. Ozvenchuk, O. Linnyk, M. I. Gorenstein, E. L. Bratkovskaya and W. Cassing, Phys. Rev. C **87**, no. 2, 024901 (2013).

[142] W. Ehehalt and W. Cassing, Nucl. Phys. A **602**, 449 (1996).

[143] W. Cassing and E. L. Bratkovskaya, Phys. Rept. **308**, 65 (1999).

[144] W. Cassing and E. L. Bratkovskaya, Phys. Rev. C **78**, 034919 (2008).

[145] W. Cassing and E. L. Bratkovskaya, Nucl. Phys. A **831**, 215 (2009).

[146] E. L. Bratkovskaya, W. Cassing, V. P. Konchakovski and O. Linnyk, Nucl. Phys. A **856**, 162 (2011).

[147] W. Cassing, A. Palmese, P. Moreau and E. L. Bratkovskaya, Phys. Rev. C **93**, 014902 (2016).

[148] J. P. Blaizot, E. Iancu and A. Rebhan, Phys. Rev. Lett. **83**, 2906 (1999).

[149] J. P. Blaizot, E. Iancu and A. Rebhan, Phys. Lett. B **470**, 181 (1999).

[150] J. P. Blaizot, E. Iancu and A. Rebhan, Phys. Rev. D **63**, 065003 (2001).

[151] A. Peshier, B. Kämpfer, O. P. Pavlenko and G. Soff, Phys. Lett. B **337**, 235 (1994).

[152] A. Peshier, B. Kämpfer, O. P. Pavlenko and G. Soff, Phys. Rev. D **54**, 2399 (1996).

[153] L. Rauber and W. Cassing, Phys. Rev. D **89**, no. 6, 065008 (2014).

[154] E. Braaten and R. D. Pisarski, Nucl. Phys. B **337**, 569 (1990).

[155] F. Karsch, E. Laermann and A. Peikert, Phys. Lett. B **478**, 447 (2000).

[156] P. Levai and U. W. Heinz, Phys. Rev. C **57**, 1879 (1998).

[157] K. Kajantie and J. I. Kapusta, Annals Phys. **160**, 477 (1985).

[158] C. S. Fischer and R. Alkofer, Phys. Rev. D **67**, 094020 (2003).

[159] J. A. Mueller, C. S. Fischer and D. Nickel, Eur. Phys. J. C **70**, 1037 (2010).

[160] R. Bellwied, S. Borsanyi, Z. Fodor, S. D. Katz, A. Pasztor, C. Ratti and K. K. Szabo, Phys. Rev. D **92**, no. 11, 114505 (2015).

[161] A. Bazavov *et al.*, Phys. Rev. D **88**, no. 9, 094021 (2013).

[162] T. Hatsuda and T. Kunihiro, Phys. Rept. **247**, 221 (1994).

[163] M. Albright, J. Kapusta and C. Young, Phys. Rev. C **90**, no. 2, 024915 (2014).

[164] G. D. Moore, JHEP **0210**, 055 (2002).

[165] A. Rebhan and P. Romatschke, Phys. Rev. D **68**, 025022 (2003).

[166] H. Vija and M. H. Thoma, Phys. Lett. B **342**, 212 (1995).

[167] C. Bonati, M. D'Elia, M. Mariti, M. Mesiti, F. Negro and F. Sanfilippo, Phys. Rev. D **92**, no. 5, 054503 (2015).

[168] H. Berrehrah, P. B. Gossiaux, J. Aichelin, W. Cassing, J. M. Torres-Rincon and E. Bratkovskaya, Phys. Rev. C **90**, 051901 (2014).

[169] H. Berrehrah, E. Bratkovskaya, W. Cassing and R. Marty, J. Phys. Conf. Ser. **612**, no. 1, 012050 (2015).

[170] H. Berrehrah, E. Bratkovskaya, W. Cassing, P. B. Gossiaux and J. Aichelin, Phys. Rev. C **91**, no. 5, 054902 (2015).

[171] G. Eichmann, C. S. Fischer and C. A. Welzbacher, Phys. Rev. D **93**, no. 3, 034013 (2016).

[172] M. S. Green, J. Chem. Phys. **22**, 398 (1954).

[173] V. Ozvenchuk, O. Linnyk, M. I. Gorenstein, E. L. Bratkovskaya and W. Cassing, Phys. Rev. C **87**, no. 6, 064903 (2013).

[174] S. Plumari, A. Puglisi, F. Scardina and V. Greco, Phys. Rev. C **86**, 054902 (2012).

[175] C. Wesp, A. El, F. Reining, Z. Xu, I. Bouras and C. Greiner, Phys. Rev. C **84**, 054911 (2011).

[176] A. Muronga, Phys. Rev. C **69**, 044901 (2004).

[177] L. P. Kadanoff and P. C. Martin, Ann. Phys. **24**, 419 (1963).

[178] F. Karsch and H. W. Wyld, Phys. Rev. D **35**, 2518 (1987).

[179] G. Aarts and J. M. Martinez Resco, JHEP **0204**, 053 (2002).

[180] P. Petreczky and D. Teaney, Phys. Rev. D **73**, 014508 (2006).

[181] G. D. Moore and J. M. Robert, hep-ph/0607172.

[182] D. Teaney, Phys. Rev. D **74**, 045025 (2006).

[183] M. Asakawa, T. Hatsuda and Y. Nakahara, Prog. Part. Nucl. Phys. **46**, 459 (2001).

[184] R. K. Bryan, Eur. Biophys. J. **18**, 165 (1990).

[185] P. Chakraborty and J. I. Kapusta, Phys. Rev. C **83**, 014906 (2011).

[186] M. Albright and J. I. Kapusta, Phys. Rev. C **93**, no. 1, 014903 (2016).

[187] A. Nakamura and S. Sakai, Phys. Rev. Lett. **94**, 072305 (2005).

[188] H. B. Meyer, Phys. Rev. D **76**, 101701 (2007).

[189] J. W. Chen and E. Nakano, Phys. Lett. B **647**, 371 (2007).

[190] N. Demir and S. A. Bass, Phys. Rev. Lett. **102**, 172302 (2009).

[191] R. A. Lacey *et al.*, Phys. Rev. Lett. **98**, 092301 (2007).

[192] M. Prakash, M. Prakash, R. Venugopalan and G. Welke, Phys. Rept. **227**, 321 (1993).

[193] N. Astrakhantsev, V. Braguta and A. Kotov, JHEP **1704**, 101 (2017).

[194] M. Bluhm, B. Kämpfer and K. Redlich, Phys. Rev. C **84**, 025201 (2011).

[195] L. P. Csernai, J. I. Kapusta and L. D. McLerran, Phys. Rev. Lett. **97**, 152303 (2006).

[196] A. Adams, L. D. Carr, T. Schäfer, P. Steinberg and J. E. Thomas, New J. Phys. **14**, 115009 (2012).

[197] A. Dobado, F. J. Llanes-Estrada and J. M. Torres-Rincon, Phys. Lett. B **702**, 43 (2011).

[198] C. Sasaki and K. Redlich, Nucl. Phys. A **832**, 62 (2010).

[199] E. Lu and G. D. Moore, Phys. Rev. C **83**, 044901 (2011).

[200] F. Karsch, D. Kharzeev and K. Tuchin, Phys. Lett. B **663**, 217 (2008).

[201] H. B. Meyer, Phys. Rev. Lett. **100**, 162001 (2008).

[202] S. Sakai and A. Nakamura, PoS LATTICE **2007**, 221 (2007) [AIP Conf. Proc. **893**, 5 (2007)].

[203] J. Noronha-Hostler, J. Noronha and C. Greiner, Phys. Rev. Lett. **103**, 172302 (2009).

[204] S. Ghosh, T. C. Peixoto, V. Roy, F. E. Serna and G. Krein, Phys. Rev. C **93**, no. 4, 045205 (2016).

[205] A. Buchel, Phys. Lett. B **663**, 286 (2008).

[206] H. B. Meyer, Nucl. Phys. A **830**, 641C (2009).

[207] N. Christiansen, M. Haas, J. M. Pawlowski and N. Strodthoff, Phys. Rev. Lett. **115**, no. 11, 112002 (2015).

[208] J. E. Bernhard, J. S. Moreland and S. A. Bass, Nucl. Phys. A **967**, 293 (2017).

[209] S. A. Bass, J. E. Bernhard and J. S. Moreland, Nucl. Phys. A **967**, 67 (2017).

[210] Y. Xu, P. Moreau, T. Song, M. Nahrgang, S. A. Bass and E. Bratkovskaya, Phys. Rev. C **96**, no. 2, 024902 (2017).

[211] J. E. Bernhard, P. W. Marcy, C. E. Coleman-Smith, S. Huzurbazar, R. L. Wolpert and S. A. Bass, Phys. Rev. C **91**, no. 5, 054910 (2015).

[212] J. E. Bernhard, J. S. Moreland, S. A. Bass, J. Liu and U. Heinz, Phys. Rev. C **94**, no. 2, 024907 (2016).

[213] H.-T. Ding, A. Francis, O. Kaczmarek, F. Karsch, E. Laermann and W. Soeldner, Phys. Rev. D **83**, 034504 (2011).

[214] A. Amato, G. Aarts, C. Allton, P. Giudice, S. Hands and J. I. Skullerud, Phys. Rev. Lett. **111**, no. 17, 172001 (2013).

[215] W. Cassing, O. Linnyk, T. Steinert and V. Ozvenchuk, Phys. Rev. Lett. **110**, no. 18, 182301 (2013).

[216] T. Steinert and W. Cassing, Phys. Rev. C **89**, no. 3, 035203 (2014).

[217] O. Kaczmarek, E. Laermann, M. Müller, F. Karsch, H. T. Ding, S. Mukherjee, A. Francis and W. Soeldner, PoS ConfinementX , 185 (2012).

[218] G. Aarts, C. Allton, J. Foley, S. Hands and S. Kim, Phys. Rev. Lett. **99**, 022002 (2007).

[219] O. Kaczmarek and M. Müller, PoS LATTICE **2013**, 175 (2014).

[220] P. V. Buividovich, M. N. Chernodub, D. E. Kharzeev, T. Kalaydzhyan, E. V. Luschevskaya and M. I. Polikarpov, Phys. Rev. Lett. **105**, 132001 (2010).

[221] B. B. Brandt, A. Francis, H. B. Meyer and H. Wittig, JHEP **1303**, 100 (2013).

[222] B. B. Brandt, A. Francis, H. B. Meyer and H. Wittig, PoS ConfinementX , 186 (2012).

[223] B. B. Brandt, A. Francis, B. Jäger and H. B. Meyer, Phys. Rev. D **93**, no. 5, 054510 (2016).

[224] G. Aarts, C. Allton, A. Amato, P. Giudice, S. Hands and J. I. Skullerud, JHEP **1502**, 186 (2015).

[225] P. B. Arnold, G. D. Moore and L. G. Yaffe, JHEP **0305**, 051 (2003).

[226] Y. Nambu and G. Jona-Lasinio, Phys. Rev. **122**, 345 (1961).

[227] Y. Nambu and G. Jona-Lasinio, Phys. Rev. **124**, 246 (1961).

[228] U. Vogl and W. Weise, Prog. Part. Nucl. Phys. **27**, 195 (1991).

[229] S. P. Klevansky, Rev. Mod. Phys. **64**, 649 (1992).

[230] G. 't Hooft, Phys. Rept. **142**, 357 (1986).

[231] M. Kobayashi and T. Maskawa, Prog. Theor. Phys. **44**, 1422 (1970).

[232] P. Rehberg, S. P. Klevansky and J. Hüfner, Phys. Rev. C **53**, 410 (1996).

[233] K. Hagiwara *et al.* [Particle Data Group], Phys. Rev. D **66**, 010001 (2002).

[234] B. R. Holstein, Phys. Lett. B **244**, 83 (1990).

[235] K. Fukushima, Phys. Rev. D **77**, 114028 (2008) Erratum: [Phys. Rev. D **78**, 039902 (2008)].

[236] M. Kitazawa, T. Koide, T. Kunihiro and Y. Nemoto, Prog. Theor. Phys. **108**, no. 5, 929 (2002) Erratum: [Prog. Theor. Phys. **110**, no. 1, 185 (2003)].

[237] N. M. Bratovic, T. Hatsuda and W. Weise, Phys. Lett. B **719**, 131 (2013).

[238] E. Quack and S. P. Klevansky, Phys. Rev. C **49**, 3283 (1994).

[239] J. Hüfner, S. P. Klevansky, P. Zhuang and H. Voss, Annals Phys. **234**, 225 (1994).

[240] P. Zhuang, J. Hüfner and S. P. Klevansky, Nucl. Phys. A **576**, 525 (1994).

[241] D. Blaschke, M. Buballa, A. E. Radzhabov and M. K. Volkov, Yad. Fiz. **71**, 2012 (2008) [Phys. Atom. Nucl. **71**, 1981 (2008)].

[242] P. N. Meisinger and M. C. Ogilvie, Nucl. Phys. Proc. Suppl. **47**, 519 (1996).

[243] P. N. Meisinger and M. C. Ogilvie, Phys. Lett. B **379**, 163 (1996).

[244] A. Dumitru, R. D. Pisarski and D. Zschiesche, Phys. Rev. D **72**, 065008 (2005).

[245] K. Fukushima and Y. Hidaka, Phys. Rev. D **75**, 036002 (2007).

[246] W. j. Fu, Z. Zhang and Y. x. Liu, Phys. Rev. D **77**, 014006 (2008).

[247] M. Ciminale, R. Gatto, N. D. Ippolito, G. Nardulli and M. Ruggieri, Phys. Rev. D **77**, 054023 (2008).

[248] G. Boyd, J. Engels, F. Karsch, E. Laermann, C. Legeland, M. Lutgemeier and B. Petersson, Nucl. Phys. B **469**, 419 (1996).

[249] O. Kaczmarek, F. Karsch, P. Petreczky and F. Zantow, Phys. Lett. B **543**, 41 (2002).

[250] C. P. Korthals Altes, R. D. Pisarski and A. Sinkovics, Phys. Rev. D **61**, 056007 (2000).

[251] R. D. Pisarski, Phys. Rev. D **62**, 111501 (2000).

[252] C. Ratti, S. Roessner, M. A. Thaler and W. Weise, Eur. Phys. J. C **49**, 213 (2007).

[253] K. Fukushima, Phys. Lett. B **591**, 277 (2004).

[254] J. M. Torres-Rincon and J. Aichelin, Phys. Rev. C **96**, no. 4, 045205 (2017).

[255] L. M. Haas, R. Stiele, J. Braun, J. M. Pawlowski and J. Schaffner-Bielich, Phys. Rev. D **87**, no. 7, 076004 (2013).

[256] J. M. Torres-Rincon, B. Sintes and J. Aichelin, Phys. Rev. C **91**, no. 6, 065206 (2015).

[257] S. Borsanyi, G. Endrodi, Z. Fodor, S. D. Katz and K. K. Szabo, JHEP **1207**, 056 (2012).

[258] S. S. Xu, Y. Yan, Z. F. Cui and H. S. Zong, Int. J. Mod. Phys. A **30**, no. 36, 1550217 (2015).

[259] J. R. Pelaez, Phys. Rept. **658**, 1 (2016).

[260] C. Patrignani *et al.* [Particle Data Group], Chin. Phys. C **40**, no. 10, 100001 (2016).

[261] W. Heupel, G. Eichmann and C. S. Fischer, Phys. Lett. B **718**, 545 (2012).

[262] R. Venugopalan and M. Prakash, Nucl. Phys. A **546**, 718 (1992).

[263] W. Broniowski, F. Giacosa and V. Begun, Phys. Rev. C **92**, no. 3, 034905 (2015).

[264] V. Bernard, U. G. Meissner and I. Zahed, Phys. Rev. Lett. **59**, 966 (1987).

[265] T. Hatsuda and T. Kunihiro, Phys. Lett. B **185**, 304 (1987).

[266] A. Wergieluk, D. Blaschke, Y. L. Kalinovsky and A. Friesen, Phys. Part. Nucl. Lett. **10**, 660 (2013).

[267] A. Andronic, P. Braun-Munzinger and J. Stachel, Phys. Lett. B **673**, 142 (2009) Erratum: [Phys. Lett. B **678**, 516 (2009)].

[268] G. M. Welke, R. Venugopalan and M. Prakash, Phys. Lett. B **245**, no. 2, 137 (1990).

[269] D. H. Rischke, M. I. Gorenstein, H. Stoecker and W. Greiner, Z. Phys. C **51**, 485 (1991).

[270] G. D. Yen, M. I. Gorenstein, W. Greiner and S. N. Yang, Phys. Rev. C **56**, 2210 (1997).

[271] J. I. Kapusta and K. A. Olive, Nucl. Phys. A **408**, 478 (1983).

[272] R. Hagedorn and J. Rafelski, Phys. Lett. **97B**, 136 (1980).

[273] R. Hagedorn, Nuovo Cim. Suppl. **3**, 147 (1965).

[274] J. Cleymans, H. Satz, E. Suhonen and D. W. von Oertzen, Phys. Lett. B **242**, 111 (1990).

[275] J. Cleymans and H. Satz, Z. Phys. C **57**, 135 (1993).

[276] P. Braun-Munzinger, K. Redlich and J. Stachel, In *Hwa, R.C. (ed.) et al.: Quark gluon plasma* 491-599 [nucl-th/0304013].

[277] A. Andronic, P. Braun-Munzinger and J. Stachel, Nucl. Phys. A **772**, 167 (2006).

[278] J. Letessier and J. Rafelski, Eur. Phys. J. A **35**, 221 (2008).

[279] M. Petrán, J. Letessier, V. Petráček and J. Rafelski, Phys. Rev. C **88**, no. 3, 034907 (2013).

[280] F. Becattini, M. Gazdzicki, A. Keranen, J. Manninen and R. Stock, Phys. Rev. C **69**, 024905 (2004).

[281] F. Becattini, J. Manninen and M. Gazdzicki, Phys. Rev. C **73**, 044905 (2006).

[282] V. Vovchenko, V. V. Begun and M. I. Gorenstein, Phys. Rev. C **93**, no. 6, 064906 (2016).

[283] F. Becattini, P. Castorina, A. Milov and H. Satz, Eur. Phys. J. C **66**, 377 (2010).

[284] A. Andronic, P. Braun-Munzinger, J. Stachel and H. Stöcker, Phys. Lett. B **697**, 203 (2011).

[285] R. Bellwied, S. Borsanyi, Z. Fodor, S. D. Katz and C. Ratti, Phys. Rev. Lett. **111**, 202302 (2013).

[286] J. Noronha-Hostler, J. Noronha and C. Greiner, Phys. Rev. C **86**, 024913 (2012).

[287] V. Vovchenko, D. V. Anchishkin and M. I. Gorenstein, Phys. Rev. C **91**, no. 2, 024905 (2015).

[288] V. V. Begun, M. Gazdzicki and M. I. Gorenstein, Phys. Rev. C **88**, no. 2, 024902 (2013).

[289] A. Andronic, P. Braun-Munzinger, J. Stachel and M. Winn, Phys. Lett. B **718**, 80 (2012).

[290] S. Samanta and B. Mohanty, Phys. Rev. C **97**, no. 1, 015201 (2018).

[291] J. Beringer *et al.* [Particle Data Group], Phys. Rev. D **86**, 010001 (2012).

[292] K. A. Olive *et al.* [Particle Data Group], Chin. Phys. C **38**, 090001 (2014).

[293] K. Weber, B. Blaettel, W. Cassing, H. C. Doenges, V. Koch, A. Lang and U. Mosel, Nucl. Phys. A **539**, 713 (1992).

[294] B. D. Serot and J. D. Walecka, Adv. Nucl. Phys. **16**, 1 (1986).

[295] D. Vretenar, A. V. Afanasjev, G. A. Lalazissis and P. Ring, Phys. Rept. **409**, 101 (2005).

[296] B. D. Serot and J. D. Walecka, Int. J. Mod. Phys. E **6**, 515 (1997).

[297] J. Boguta and A. R. Bodmer, Nucl. Phys. A **292**, 413 (1977).

[298] A. R. Bodmer, Nucl. Phys. A **526**, 703 (1991).

[299] Y. K. Gambhir, P. Ring and A. Thimet, Annals Phys. **198**, 132 (1990).

[300] P. Ring, Prog. Part. Nucl. Phys. **37**, 193 (1996).

[301] T. Klahn *et al.*, Phys. Rev. C **74**, 035802 (2006).

[302] J. Sugano, H. Kouno and M. Yahiro, Phys. Rev. D **94**, 014024 (2016).

[303] C. Fuchs, H. Lenske and H. H. Wolter, Phys. Rev. C **52**, 3043 (1995).

[304] S. Typel and H. H. Wolter, Nucl. Phys. A **656**, 331 (1999).

[305] F. Hofmann, C. M. Keil and H. Lenske, Phys. Rev. C **64**, 034314 (2001).

[306] P. G. Reinhard, M. Rufa, J. Maruhn, W. Greiner and J. Friedrich, Z. Phys. A **323**, 13 (1986).

[307] M. M. Sharma, M. A. Nagarajan and P. Ring, Phys. Lett. B **312**, 377 (1993).

[308] P. G. Reinhard, Z. Phys. A **329**, no. 3, 257 (1988).

[309] G. A. Lalazissis, J. Konig and P. Ring, Phys. Rev. C **55**, 540 (1997).

[310] Y. Sugahara and H. Toki, Nucl. Phys. A **579**, 557 (1994).

[311] T. Tatsumi, T. Maruyama, D. N. Voskresensky, T. Tanigawa and S. Chiba, nucl-th/0502040.

[312] A. Lang, B. Blaettel, W. Cassing, V. Koch, U. Mosel and K. Weber, Z. Phys. A **340**, 287 (1991).

[313] C. J. Horowitz and B. D. Serot, Nucl. Phys. A **464**, 613 (1987) Erratum: [Nucl. Phys. A **473**, 760 (1987)].

[314] P. Danielewicz, R. Lacey and W. G. Lynch, Science **298**, 1592 (2002).

[315] R. C. Tolman, Phys. Rev. **55**, 364 (1939).

[316] J. R. Oppenheimer and G. M. Volkoff, Phys. Rev. **55**, 374 (1939).

[317] L. Lindblom, Astrophys. J. **398**, 569 (1992).

[318] A. W. Steiner, J. M. Lattimer and E. F. Brown, Astrophys. J. **765**, L5 (2013).

[319] P. Demorest, T. Pennucci, S. Ransom, M. Roberts and J. Hessels, Nature **467**, 1081 (2010).

[320] J. Antoniadis *et al.*, Science **340**, 6131 (2013).

[321] A. Palmese, W. Cassing, E. Seifert, T. Steinert, P. Moreau and E. L. Bratkovskaya, Phys. Rev. C **94**, no. 4, 044912 (2016).

[322] C. H. Johnson, D. J. Horen and C. Mahaux, Phys. Rev. C **36**, 2252 (1987).

[323] M. Jaminon and C. Mahaux, Phys. Rev. C **40**, 354 (1989).

[324] C. Fuchs and H. H. Wolter, Eur. Phys. J. A **30**, 5 (2006).

[325] J. Boguta, Phys. Lett. **109B**, 251 (1982).

[326] Z. X. Li, G. J. Mao, Y. Z. Zhuo and W. Greiner, Phys. Rev. C **56**, 1570 (1997).

[327] A. Drago, A. Lavagno and G. Pagliara, Phys. Rev. D **89**, no. 4, 043014 (2014).

[328] D. S. Kosov, C. Fuchs, B. V. Martemyanov and A. Faessler, Phys. Lett. B **421**, 37 (1998).

[329] W. Rarita and J. Schwinger, Phys. Rev. **60**, 61 (1941).

[330] X. m. Jin, Phys. Rev. C **51**, 2260 (1995).

[331] H. Kanzawa, K. Oyamatsu, K. Sumiyoshi and M. Takano, Nucl. Phys. A **791**, 232 (2007).

[332] H. Hellmann, *Einführung in die Quantenchemie*, Leipzig, Franz Deuticke (1937).

[333] R. P. Feynman, Phys. Rev. **56**, 340 (1939).

[334] T. D. Cohen, R. J. Furnstahl and D. K. Griegel, Phys. Rev. Lett. **67**, 961 (1991).

[335] T. D. Cohen, R. J. Furnstahl and D. K. Griegel, Phys. Rev. C **45**, 1881 (1992).

[336] B. Friman, W. Norenberg and V. D. Toneev, Eur. Phys. J. A **3**, 165 (1998).

[337] M. Gell-Mann, R. J. Oakes and B. Renner, Phys. Rev. **175**, 2195 (1968).

[338] R. Rapp and J. Wambach, Adv. Nucl. Phys. **25**, 1 (2000).

[339] R. Rapp, J. Wambach and H. van Hees, Landolt-Bornstein **23**, 134 (2010).

[340] R. Arnaldi *et al.* [NA60 Collaboration], Phys. Rev. Lett. **96**, 162302 (2006).

[341] R. Rapp and J. Wambach, Eur. Phys. J. A **6**, 415 (1999).

[342] D. Adamova *et al.* [CERES/NA45 Collaboration], Phys. Rev. Lett. **91**, 042301 (2003).

[343] D. Adamova *et al.*, Phys. Lett. B **666**, 425 (2008).

[344] J. S. Schwinger, Phys. Rev. **82**, 664 (1951).

[345] B. Andersson, G. Gustafson, G. Ingelman and T. Sjostrand, Phys. Rept. **97**, 31 (1983).

[346] T. Sjostrand, S. Mrenna and P. Z. Skands, JHEP **0605**, 026 (2006).

[347] B. Nilsson-Almqvist and E. Stenlund, Comput. Phys. Commun. **43**, 387 (1987).

[348] B. Andersson, G. Gustafson and H. Pi, Z. Phys. C **57**, 485 (1993).

[349] L. Ahle *et al.* [E-802 Collaboration], Phys. Rev. C **57**, no. 2, R466 (1998).

[350] L. Ahle *et al.* [E-802 and E-866 Collaborations], Phys. Rev. C **60**, 044904 (1999).

[351] J. Barrette *et al.* [E877 Collaboration], Phys. Rev. C **62**, 024901 (2000).

[352] J. Barrette *et al.* [E877 Collaboration], Phys. Rev. C **63**, 014902 (2001).

[353] S. Ahmad *et al.*, Phys. Lett. B **382**, 35 (1996) Erratum: [Phys. Lett. B **386**, 496 (1996)].

[354] S. Albergo *et al.*, Phys. Rev. Lett. **88**, 062301 (2002).

[355] C. Alt *et al.* [NA49 Collaboration], Phys. Rev. C **73**, 044910 (2006).

[356] C. Alt *et al.* [NA49 Collaboration], Phys. Rev. C **77**, 024903 (2008).

[357] C. Alt *et al.* [NA49 Collaboration], Phys. Rev. C **78**, 034918 (2008).

[358] J. L. Klay *et al.* [E-0895 Collaboration], Phys. Rev. C **68**, 054905 (2003).

[359] B. I. Abelev *et al.* [STAR Collaboration], Phys. Rev. C **81**, 024911 (2010).

[360] M. M. Aggarwal *et al.* [STAR Collaboration], Phys. Rev. C **83**, 024901 (2011).

[361] N. K. Glendenning, Phys. Rev. D **46**, 1274 (1992).

[362] J. Cleymans, M. I. Gorenstein, J. Stalnacke and E. Suhonen, Phys. Scripta **48**, 277 (1993).

[363] K. Masuda, T. Hatsuda and T. Takatsuka, PTEP **2013**, no. 7, 073D01 (2013).

[364] M. Albright, J. Kapusta and C. Young, Phys. Rev. C **92**, no. 4, 044904 (2015).

[365] M. Asakawa and T. Hatsuda, Phys. Rev. D **55**, 4488 (1997).

[366] A. Miyahara, Y. Torigoe, H. Kouno and M. Yahiro, Phys. Rev. D **94**, no. 1, 016003 (2016).

[367] C. Shen, Z. Qiu, H. Song, J. Bernhard, S. Bass and U. Heinz, Comput. Phys. Commun. **199**, 61 (2016).

[368] P. Huovinen and H. Petersen, Eur. Phys. J. A **48**, 171 (2012).

[369] Q. f. Li, J. Steinheimer, H. Petersen, M. Bleicher and H. Stöcker, Phys. Lett. B **674**, 111 (2009).

[370] V. P. Konchakovski, E. L. Bratkovskaya, W. Cassing, V. D. Toneev, S. A. Voloshin and V. Voronyuk, Phys. Rev. C **85**, 044922 (2012).

[371] V. P. Konchakovski, W. Cassing and V. D. Toneev, J. Phys. G **42**, no. 5, 055106 (2015).

[372] O. Linnyk, W. Cassing, J. Manninen, E. L. Bratkovskaya, P. B. Gossiaux, J. Aichelin, T. Song and C. M. Ko, Phys. Rev. C **87**, no. 1, 014905 (2013).

[373] O. Linnyk, W. Cassing, J. Manninen, E. L. Bratkovskaya and C. M. Ko, Phys. Rev. C **85**, 024910 (2012).

[374] O. Linnyk, E. L. Bratkovskaya, V. Ozvenchuk, W. Cassing and C. M. Ko, Phys. Rev. C **84**, 054917 (2011).

[375] J. Rafelski and J. Letessier, J. Phys. G **36**, 064017 (2009).

[376] M. Petran and J. Rafelski, Phys. Rev. C **88**, no. 2, 021901 (2013).

[377] K. Masuda, T. Hatsuda and T. Takatsuka, Astrophys. J. **764**, 12 (2013).

[378] J. Cleymans, H. Oeschler, K. Redlich and S. Wheaton, Phys. Rev. C **73**, 034905 (2006).

[379] F. Becattini, M. Bleicher, T. Kollegger, T. Schuster, J. Steinheimer and R. Stock, Phys. Rev. Lett. **111**, 082302 (2013).

[380] F. Becattini, J. Steinheimer, R. Stock and M. Bleicher, Phys. Lett. B **764**, 241 (2017).

[381] L. V. Bravina *et al.*, Nucl. Phys. A **661**, 600 (1999).

[382] S. A. Bass *et al.*, Prog. Part. Nucl. Phys. **41**, 255 (1998) [Prog. Part. Nucl. Phys. **41**, 225 (1998)].

[383] M. Bleicher *et al.*, J. Phys. G **25**, 1859 (1999).

[384] S. Endres, H. van Hees and M. Bleicher, Phys. Rev. C **93**, no. 5, 054901 (2016).

[385] B. Mohanty, Nucl. Phys. A **830**, 899C (2009).

[386] M. M. Aggarwal *et al.* [STAR Collaboration], arXiv:1007.2613 [nucl-ex].

[387] L. Kumar [STAR Collaboration], Nucl. Phys. A **862-863**, 125 (2011).

[388] A. Andronic, P. Braun-Munzinger and J. Stachel, Nucl. Phys. A **834**, 237C (2010).

[389] T. K. Herbst, J. M. Pawlowski and B. J. Schaefer, Phys. Rev. D **88**, no. 1, 014007 (2013).

[390] J. Weyrich, N. Strodthoff and L. von Smekal, Phys. Rev. C **92**, no. 1, 015214 (2015).

[391] J. M. Luttinger and J. C. Ward, Phys. Rev. **118**, 1417 (1960).

[392] G. Baym, Phys. Rev. **127**, 1391 (1962).

[393] B. Vanderheyden and G. Baym, J. Stat. Phys. [J. Statist. Phys. **93**, 843 (1998)].

[394] Y. B. Ivanov, J. Knoll and D. N. Voskresensky, Nucl. Phys. A **657**, 413 (1999).

[395] J. M. Cornwall, R. Jackiw and E. Tomboulis, Phys. Rev. D **10**, 2428 (1974).

[396] A. L. Fetter and J. D. Walecka, *Quantum Theory of Many Particle Systems*, McGraw-Hill, New York (1971).

[397] H. van Hees, Nonequilibrium Relativistic Quantum Many-Body Theory, (2013).

[398] G. Jackson and A. Peshier, Phys. Rev. D **95**, no. 5, 054021 (2017).

[399] P. Cea, L. Cosmai and A. Papa, Phys. Rev. D **89**, no. 7, 074512 (2014).

[400] C. Bonati, M. D'Elia, M. Mariti, M. Mesiti, F. Negro and F. Sanfilippo, Phys. Rev. D **90**, no. 11, 114025 (2014).

[401] R. Bellwied, S. Borsanyi, Z. Fodor, J. Günther, S. D. Katz, C. Ratti and K. K. Szabo, Phys. Lett. B **751**, 559 (2015).

[402] P. Cea, L. Cosmai and A. Papa, Phys. Rev. D **93**, no. 1, 014507 (2016).

[403] O. Kaczmarek *et al.*, Phys. Rev. D **83**, 014504 (2011).

[404] R. Falcone, E. Laermann and M. P. Lombardo, PoS LATTICE **2010**, 183 (2010).

[405] G. Endrodi, Z. Fodor, S. D. Katz and K. K. Szabo, JHEP **1104**, 001 (2011).

[406] A. Bazavov *et al.*, Phys. Rev. D **93**, no. 1, 014512 (2016).

[407] F. Becattini, M. Bleicher, J. Steinheimer and R. Stock, arXiv:1712.03748 [hep-ph].

[408] H. Kohyama, D. Kimura and T. Inagaki, Nucl. Phys. B **896**, 682 (2015).

[409] V. Bernard, R. L. Jaffe and U. G. Meissner, Nucl. Phys. B **308**, 753 (1988).

[410] J. M. Alarcon, J. Martin Camalich and J. A. Oller, Phys. Rev. D **85**, 051503 (2012).

[411] M. Hoferichter, J. Ruiz de Elvira, B. Kubis and U. G. Meißner, Phys. Rev. Lett. **115**, 092301 (2015).

[412] M. Hoferichter, J. Ruiz de Elvira, B. Kubis and U. G. Meißner, Phys. Lett. B **760**, 74 (2016).

[413] T. P. Cheng and R. F. Dashen, Phys. Rev. Lett. **26**, 594 (1971).

[414] H. Sanchis-Alepuz, C. S. Fischer and S. Kubrak, Phys. Lett. B **733**, 151 (2014).

[415] H. Sanchis-Alepuz and R. Williams, Phys. Lett. B **749**, 592 (2015).

[416] A. Abdel-Rehim *et al.* [ETM Collaboration], Phys. Rev. Lett. **116**, no. 25, 252001 (2016).

[417] G. S. Bali *et al.* [RQCD Collaboration], Phys. Rev. D **93**, no. 9, 094504 (2016).

[418] Y. B. Yang *et al.* [xQCD Collaboration], Phys. Rev. D **94**, no. 5, 054503 (2016).

[419] S. Dürr *et al.*, Phys. Rev. Lett. **116**, no. 17, 172001 (2016).

Selbstständigkeitserklärung

Ich erkläre: Ich habe die vorgelegte Dissertation selbstständig und ohne unerlaubte fremde Hilfe und nur mit den Hilfen angefertigt, die ich in der Dissertation angegeben habe. Alle Textstellen, die wörtlich oder sinngemäß aus veröffentlichten Schriften entnommen sind, und alle Angaben, die auf mündlichen Auskünften beruhen, sind als solche kenntlich gemacht. Ich stimme einer evtl. Überprüfung meiner Dissertation durch eine Antiplagiat-Software zu. Bei den von mir durchgeführten und in der Dissertation erwähnten Untersuchungen habe ich die Grundsätze guter wissenschaftlicher Praxis, wie sie in der „Satzung der Justus-Liebig-Universität Gießen zur Sicherung guter wissenschaftlicher Praxis“ niedergelegt sind, eingehalten.

____________________	____________________
Datum	Unterschrift